Pairing geochemistry and sedimentology: an evaluation of Alberta's earliest Triassic deposits and the proxies used to study them

by

Tiffany L. Playter

A thesis submitted in partial fulfillment of the requirements for the degree of

Doctor of Philosophy

Department of Earth and Atmospheric Sciences
University of Alberta

Abstract

The end-Permian mass extinction, 250 million years ago, was the largest in Earth's history, with estimates of faunal species loss up to ~90%. Western Canada plays host to deposits spanning the Permian-Triassic boundary (the Belloy and Montney Formations) allowing for the paleoenvironmental conditions surrounding post-extinction recovery to be evaluated. Utilizing both geochemical methods, such as trace element proxies and carbon isotopes, as well as sedimentology, this thesis has four aims: 1) evaluate the main mechanism facilitating the existence of marine refugia post-extinction, 2) determine if Siberian Trap volcanism was a factor in the delayed faunal recovery in the Early Triassic, 3) ascertain if the geochemical signatures of events within the Early Triassic can be used to correlate deposits across the basin and 4) examine the reliability of the geochemical proxies used to ascertain paleoenvironmental conditions. This thesis demonstrates that, following the end-Permian mass extinction, biotic recovery was facilitated by the monsoon cycle which produced coastal upwelling via Ekman transport and nutrient-rich runoff from increased rainfall. Additionally demonstrated, through the detailed evaluation of trace element proxies, is the subsequent eruption of the Siberian Traps at the end of the Smithian, which resulted in a temperature increase of 10°C, enhanced continental weathering, and a 0.55 unit decrease in seawater pH which resulted in ocean acidification and anoxia. These signatures are correlated, using chemostratigraphy, across the Western Canada Sedimentary Basin, dividing Early Triassic deposits into 13 chemostratigraphic packages. Lastly, by examining the interaction of cyanobacteria and clay during flocculation, this thesis suggests that the geochemical signatures of fine-grained deposits, such as the Triassic Montney Formation, can be altered by biological activity within the water column, in addition to seawater composition and redox state.

Preface

This individual chapters of this thesis, excluding the introductory chapter and conclusions, comprise collaborative research projects which form part of a larger international research effort headed by Dr. Konhuser and Dr. Zonneveld in partnership with the Alberta Geological Survey. The data analysis and manuscript composition of each chapter was conducted by me, with guidance from Dr. Konhauser, Dr. Zonneveld and other coauthors. Specific contributions are outlined as follows:

Chapter 2 of this thesis has been submitted to *Nature Geoscience* as Playter, T., Robbins, L.J., Corlett, H. Gingras, M.K., Zonneveld, J.P., and Konhauser, K.O. "Monsoon cycles, primary productivity, and silica deposition following the end-Permian mass extinction." I was responsible for data collection, analysis and manuscript composition. L.J. Robbins contributed to manuscript edits. H. Corlett assisted with data collection and manuscript editing. M.K. Gingras assisted in data interpretation and manuscript development. J.P. Zonneveld and K.O. Konhauser were supervisory authors and contributed to concept development and manuscript composition.

Chapter 3 of this thesis is currently being submitted to *Geology,* as Playter, T., Konhauser, K., Robbins, L, Lyons, T., Mitrovica, J., Corlett, H., Lalonde, S., Planavsky, N., Cui, Y., Gingras, M., and Zonneveld, J.P. "New evidence for volcanism and its global-scale impacts in the wake of the end-Permian mass extinction." I was responsible for data collection, analysis, interpretation and manuscript composition. K. Konhauser and J.P. Zonneveld were supervisory authors and assisted with concept generation and manuscript composition. L. Robbins assisted with manuscript edits. T.Lyons, J.Mitrovica, S. Lalonde, and M. Gingras assisted with data interpretation and manuscript edits. H. Corlett, S. Lalonde, and N. Planavsky assisted with data generation and manuscript edits. Y.Cui provided computer modelling results and manuscript edits.

Chapter 3 of this thesis has been published as Playter, T., Corlett, H., Konhauser, K., Robbins, L., Rohais, S., Crombez, V., MacCormack, K., Rokosh, D., Prenoslo, D., Furlong, C.M., Pawlowicz, J., Gingras, M., Lalonde, S., Lyster, S., and Zonneveld, J.P., "Clinoform identification and correlation in fine-grained sediments: a case study using the Triassic Montney Formation," *Sedimentology*, v. 65, 263-302. I was responsible for data collection, analysis, interpretation and manuscript composition. K. Konhauser and J.P. Zonneveld were supervisory authors and assisted with concept generation and manuscript composition. S. Rohais, V. Crombez, and Furlong, C.M. assisted in field data gathering and manuscript editing. Corlett, H., MacCormack, K., Rokosh, D., Pawlowicz, J., and Lyster, S. assisted with data generation and manuscript editing. L. Robbins, M. Gingras and S. Lalonde assisted with data interpretation and manuscript edits.

Chapter 4 of this thesis has been published as Playter, T., Konhauser, K., Owttrim, G., Hodgson, C., Warchola, T., Mloszewska, A.M., Sutherland, B., Bekker, A., Zonneveld, J.P., Pemberton, S.G., and Gingras, M. , "Microbe-clay interactions as a mechanism for the preservation of organic matter and trace metal biosignatures in black shales," *Chemical Geology*, v. 459, 65-90. I was responsible for data generation, analysis, interpretation and manuscript composition. K. Konhauser, J.P. Zonneveld, and M. Gingras were supervisory authors and assisted in concept formation, experimental design and manuscript composition. G. Owttrim and Mloszewska, A.M. assisted with cyanobacterial culturing and manuscript editing. C. Hodgson and T. Warchola assisted with data generation and manuscript editing. B. Sutherland and B. Bekkar assisted with data interpretation and manuscript editing.

Dedication

“I can do all things through Christ which strengtheneth me”

Philippians 4:13 KJV

Acknowledgments

I would like to first thank my supervisors, Dr. Kurt Konhauser and Dr. J.P. Zonneveld for their many hours of editing, discussion and general guidance. Their patience and support have been invaluable. I would also like to thank the members of my supervisory committee; Dr. Murray Gingras has provided continuous support and advice and Dr. George Pemberton was a great source of encouragement and knowledge before his untimely passing. Many individuals from both the ichnology research group and the geobiology lab group at the University of Alberta have contributed to the generation of this theses, and I would like to thank all of my lab-mates, both past and present. I would also like to thank everyone at the Alberta Geological Survey for their support and input during the generation of this thesis.

Furthermore, I would like to extend many thanks to my family for their support. Specifically, I thank my husband, Mike, who has helped me in every way possible, and my daughter, Julia, who is a constant source of inspiration.

Lastly, I would like to thank my Lord and Savior Jesus Christ for being my source of strength, joy and peace and who has facilitated the generation of these ideas.

Table of Contents

Chapter 1: Introduction 1

References 5

Chapter 2: Monsoon cycles, primary productivity, and silica deposition following the end-Permian mass extinction 6

The Belloy and Monenty Formations 9

Methods 10

Excess silica and biotic recovery 10

Monsoons in the early Triassic and their effect on productivity 15

References 17

Chapter 3: New evidence for volcanism and its global-scale impacts in the wake of the end-Permian mass extinction 25

Methods 36

References 37

Chapter 4: Clinoform identification and correlation in fine-grained sediments: A case study using the Triassic Montney Formation 46

Geological Setting 49

Methods 53

Elemental Indicators 54

Detrital Indicators 56

Provenance indicators 60

Mineralogical Indicators 61

Results and Interpretation by Category:

Chemofacies descriptions

Results 63

Interpretation 66

Chemostratigraphic correlation

Results 66

Interpretation 67

Elemental Associations and Mineralogy

Results 68

Interpretation 72

Provenance

Results 80

Interpretation 81

Biogenic versus abiotic carbonate

Results 83

Interpretation 84

Hydrothermal indicators and iron mineral phase change

Results 88

Interpretation 92

Discussion

Hydrothermal input and implications 94

Climate change in the Early Triassic 99

Identification of clinoforms and implication for sequence stratigraphy in fine-grained successions 104

Conclusions 109

References 111

Chapter 5: Microbe-clay interactions as a mechanism for preservation of organic matter and trace metal biosignatures in black shales 136

Methods

Culturing 139

Flocculation experiments 140

Trace metal analysis 143

TEM and SEM imaging 145

Results

Chl a measurements 146

SEM/TEM results 149

Trace metal analysis 151

Discussion

Microbe-clay aggregation 152

Organic matter sources in black shales 159

Mechanisms of biomass deposition 162

Organic matter preservation potential 164

Morphology of encased biomass 168

Implications for traditional depositional models of black shales 170

Geochemical implications for organic-rich marine shale 171

Conclusions 175

References 178

Chapter 6: Conclusions 195

References 198

Works Cited 200

Appendix 1: Monsoon cycles, primary productivity, and silica deposition following the end-Permian mass extinction (Supplimentary Material)

Supplimentary Figures 253

Appendix 2: Clinoform identification and correlation in fine-grained sediments: A case study using the Triassic Montney Formation (Supplimentary Material)

Supplimentary Figures 257

Supplimentary Methods 319

List of Tables

Chapter 4

Table 1 56

Table 2 69

Table 3 70

Table 4 72

Table 5 74

Table 6 76

Table 7 80

Table 8 82

Table 9 88

Chapter 5

Table 1 144

Table 2 145

Appendix 2

Table S1 300

Table S2 302

Table S3 306

Table S4 308

Table S5 312

Table S6 315

Table S7 318

List of Figures

Chapter 2

Figure 1 12

Figure 2 13

Figure 3 14

Chapter 3

Figure 1 28

Figure 2 33

Chapter 4

Figure 1 51

Figure 2 58

Figure 3 59

Figure 4 63

Figure 5 65

Figure 6 79

Figure 7 86

Figure 8 90

Figure 9 91

Figure 10 93

Figure 11 94

Figure 12 96

Figure 13 97

Figure 14 98

Figure 15 100

Figure 16 103

Figure 17 105

Chapter 5

Figure 1 142

Figure 2 148

Figure 3 151

Figure 4 155

Figure 5 157

Figure 6 158

Figure 7 161

Appendix 1

Figure S1 253

Figure S2 254

Figure S3 255

Figure S4 256

Appendix 2

Figure S1 257

Figure S2 258

Figure S3 258

Figure S4 259

Figure S5 259

Figure S6 260

Figure S7 260

Figure S8 261

Figure S9 261

Figure S10 262

Figure S11 262

Figure S12 263

Figure S13 263

Figure S14 264

Figure S15 265

Figure S16 265

Figure S17 266

Figure S18 266

Figure S19 267

Figure S20 268

Figure S21 269

Figure S22 270

Figure S23 271

Figure S24 272

Figure S25 273

Figure S26 274

Figure S27 287

Figure S28 293

Figure S29 298

Figure S30 299

Chapter 1: Introduction

The end-Permian biotic crisis at 251 million years ago (Ma) was the largest mass extinction event in the Phanerozoic, with estimates of faunal species loss as high as ~90%. This event was coincident with a number of changes, such as ocean acidification, vegetation loss and soil alteration, sea-level rise. In addition, slower ocean circulation and warmer oceans resulted in decreased levels of dissolved oxygen that led to marine anoxia, and ultimately ocean stratification. Within western Canada, deposits from this critical time period are preserved in both core and outcrop (Belloy and Montney Formations). The following thesis aims to answer numerous questions still remaining regarding this time period and the nature of the rocks which were formed: (1) what was the main mechanism supporting the development of marine refugia immediately following the end-Permian mass extinction; (2) was volcanism an active factor in the punctuated faunal recovery following the end-Permian mass extinction; (3) how do the geochemical signatures of events within the Early Triassic correlate stratigraphically within the Western Canada Sedimentary Basin and (4) how reliable are the geochemical proxies we have employed?

Detailed geochemical and sedimentological analysis of a Permian-Triassic section from western Canada demonstrates systematic trends in weathering and palaeoproductivity proxies, as well as biogenic silica fluxes. These trends, when paired with sedimentological indicators of riverine input and storm episodes, suggest

that seasonal monsoons produced wind-induced upwelling along the northwest margin of Pangea. These intervals of upwelling coincide with intervals of biogenic silica and occur anti-phase to indicators of increased weathering. This suggests that winter storms, in partnership with coastal runoff, were the major factor in supporting biotic recovery in the Griesbachian.

Although it has been postulated that the protracted biotic recovery was slowed by unfavorable environmental conditions following the end-Permian event (Hallam, 1991; Payne et al., 2004; Knoll et al, 2007), other studies contend that the time interval itself records smaller, punctuated extinction events within the Early Triassic (Griesbachian, Dienerian, Smithian and Spathian substages) (Galfetti et al., 2007; Stanley, 2009; Song et al., 2011). Of these subsequent extinctions the end-Smithian (250.7 Ma) event was especially devastating in terms of ammonoid and conodont recovery. While the initial, major mass extinction at the end of the Permian has been linked to extreme climatic change triggered by the eruption of the Siberian Traps, the cause of the end-Smithian extinction remains cryptic and unresolved. Here, in chapter 2, we show that massive CO_2 input at the end of the Smithian resulted in a temperature increase of up to 10°C, enhanced continental weathering, and a 0.55 unit decrease in seawater pH which resulted in ocean acidification and anoxia. The CO_2 increase was sourced from the Siberian Traps, demonstrating that global climate change at that time also caused end-Smithian extinction event.

The earliest Triassic deposits within western Canada (Montney Formation) are very fine-grained. Stratigraphic correlation of fine-grained successions is not always straightforward, making the up-scaling of paleoenvironmental observations (such as

the presence of biogenic silica or volcanism indicators) difficult. Complicating factors, such as unconformities, structural complexity, subsidence and especially minimal grain-size variation, make the application of traditional correlation methods to fine-grained successions problematic. Alternatively, the analysis of detailed geochemical data can allow for the determination of variations in sediment provenance, mineralogy, detrital flux and hydrothermal input. When compared with modelled clay input over time, these geochemical indicators can be used to determine changes in relative sea-level and palaeoclimate, allowing for the identification of clinoform surfaces. As an example, chapter 3 outlines detailed correlations of chemostratigraphic packages within the lower Triassic Montney Formation in Western Canada to demonstrate the effectiveness of chemostratigraphy in defining and correlating fine-grained clinoforms across a sedimentary basin. The data set used includes five wells and one outcrop succession, from which geochemical profiles were generated and tied directly to mineralogical data and well logs. These analyses reveal 13 distinct chemostratigraphic packages that correlate across the basin. Observed elemental and inferred mineralogical changes highlight trends in relative sea-level and palaeoclimate, as well as episodes of inferred hydrothermal input to the Montney basin. Cross-plots of La/Sm and Yb/Sm further suggest hydrothermal input as well as the scavenging of middle rare earth elements by phosphatic fish debris. Additionally, plots of La/Sm versus Yb/Sm, which show volcanic arc input within the Doig Formation, suggest an additional sediment source from the west during the Anisian. Pairing detrital and clay proxies demonstrates changes in relative sea-level and, at the Smithian/Spathian boundary, the lowest

relative sea-level in the Montney Formation is observed, corresponding to a change in climate and the observations of volcanic input from chapter 2.

Geochemical proxies are critical when it comes to evaluating Early Triassic depositional conditions. However, the reliability of proxies, particularly as they relate to marine anoxia, is not entirely established. In general, organic-rich, fine-grained sedimentary rocks are important geochemical archives providing information on the evolution of seawater composition and biological activity over the past 3 billion years. While biological productivity and sedimentation rates greatly affect the organic matter content in these rocks, mechanisms linking these two processes remain poorly resolved. Here in chapter 4, we examine the interactions of clay minerals with the marine planktonic cyanobacterium Synechococcus sp. PCC 7002. We suggest that clays settling through the water column could influence carbon and trace metal burial in three ways: (1) the interaction of reactive clay surfaces with the bacterial cells increases organic matter deposition via mass increase in a seawater growth medium by several orders of magnitude; (2) reactive bacterial cells become completely encased within a clay shroud, enhancing the preservation potential of this organic matter; and (3) the trace metal content of the biomass buried along with metals sorbed to the clay particles contributes to the trace metal concentrations of the black shale precursor sediments. Significantly, our findings imply that the chemical composition of ancient, organic-rich, fine-grained deposits are not only archives of ancient seawater composition and redox state, but they also provide a record of the degree of biological activity in the water column through geological time.

References

Galfetti, T., Hochuli, P.A., Brayard, A., Bucher, H., Weissert, H. and Os Vigran, J. 2007. Smithian-Spathian boundary event: evidence for global climatic change in the wake of the end-Permian biotic crisis. Geology, 35, 291–294.

Hallam, A. & Wignall, P.B. 1999. Mass extinctions and sea-level changes. Earth Sci. Rev. 48, 217-250.

Knoll, A.H., Bambach, R.K., Payne, J.L., Pruss, S., and Fischer, W.W. 2007. Paleophysiology and end-Permian mass extinction. Earth and Planetary Science Letters, v. 256, p. 295-313.

Payne, J.L., Lehrmann, D.J., Wei, J., Orchard, M.J., Schrag, D.P., and Knoll, A.H. 2004. Large perturbations of the carbon cycle during recovery from the end-Permian extinction. Science, v. 305, p. 506-509.

Song, H., Wignall, P.B., Chen, Z.-Q., Tong, J., Bond, D.P.G., Lai, X, Zhau, X., Jiang, H., Yan, C., Niu, Z., Chen, J., Yang, H., and Wang, Y. 2011. Recovery tempo and pattern of marine ecosystems after the end-Permian mass extinction. Geology, v. 39, p. 739-742.

Stanley, S.M. 2009. Evidence from ammonoids and conodonts for multiple Early Triassic mass extinctions. PNAS, v. 106, p. 15264-15267.

Chapter 2: Monsoon cycles, primary productivity, and silica deposition following the end-Permian mass extinction

Introduction

The end-Permian biotic crisis is the largest mass extinction recorded in Earth's history, with species loss approaching ~90% (Erwin, 2006). Increased volcanism led to elevated CO_2 levels and a period of global warming (Kump et al., 2005; Sun et al., 2012), which, in turn, led to vegetation loss and soil alteration (Retallack et al., 1996), ocean acidification (Wignall and Twitchett, 1996; Retallack et al, 1996), and sea-level rise (Hallam and Wignall, 1999). These changes were accompanied by perturbed ocean circulation, stratification, and marine anoxia (Wignall and Twitchett, 1996; Isozaki, 1997; Beauchamp and Baud, 2002). It has been suggested that the decline in marine productivity may have been compounded by a 700% increase in detrital fluxes and a transition to more clay-rich sediment during the Early Triassic (Algeo and Twitchett, 2010). This may have been detrimental for marine organisms as elevated turbidity inhibits necessary biological functions such as feeding, osmoregulation, and larval recruitment (Gingras, et al., 1998; Algeo and Twitchett, 2010), as well as limiting light penetration of light into the photic zone (e.g., Algeo and Twitchett, 2010) and increasing flocculation of planktonic bacteria (e.g., Playter et al., 2017) that may be expected to accompany increased clay mineral supply.

Despite these environmental stressors, there was an abrupt reappearance of warm-water taxa within 4 Myrs of the Permian-Triassic (PT) boundary, the so-called Lazarus taxa (Jablonski and Flessa, 1986; Kozur, 1998; Erwin, 2006). This suggests that organisms, specifically siliceous sponges and radiolarians, remained biologically

active during the Early Triassic (Kozur, 1998; Godbold et al., 2017). Marine refugia, namely isolated pockets of ecologically favorable conditions, such as sheltered near-shore environments, would have provided local environments where marine biota were able to weather the mass extinction (Beatty et al., 2008; Goldbold et al., 2017). While the existence of such refugia is largely uncontested, how the shallow water habitable zone, where these isolated pockets developed, was supplied with organic matter and nutrients in the wake of the collapse of the trophic pyramid has been largely unexplored.

Seasonal monsoons represent a potential and unexplored mechanism that may have driven primary productivity following the PT mass extinction. In modern environments, monsoons have been observed to fuel primary productivity. High winds during the summer monsoon deepen the mixed layer and intensify circulation, leading to the increased upwelling of nutrient-rich deep-waters (Thushara and Vinayachandran, 2016). Monsoons would also contribute to higher rates of physical and chemical weathering on land due to elevated temperatures, greater rainfall, destruction of land plant ecosystems, and enhanced soil erosion (Algeo and Twitchett, 2010). Critical to this hypothesis is whether conditions favorable for the development of monsoons existed during the Early Triassic. The Triassic climate system would have been characterized by cold winters, hot summers, and strong monsoonal circulation, leading to seasonal, abundant rainfall, depressed zonal climate patterns, and a dry equatorial region (Parrish, 1993). Such a climate system would have been supported by the presence of a singular supercontinent, Pangea, that is likely to have already existed at that time (Davies et al., 1997).

Herein we test the link between Early Triassic biogenically sourced silica, an indicator of primary productivity, and monsoonal activity by examining sedimentary core from western Canada that spans the PT boundary. Elsewhere, the Belloy and Montney formations have previously been shown to contain isolated pockets of early Triassic, non-siliceous biota including bivalves and trace fossils. These fossil assemblages suggest that marine refugia existed along the coast despite the shutdown of cold-water upwelling. However, there remains a paucity of direct evidence for primary production in the aftermath of the PT mass extinction (Beatty et al., 2008, Zonneveld et al., 2010; Godbold et al., 2017). Accordingly, we examine carbon isotope and trace element trends over an 18-meter interval, coupling the geochemical measurements to detailed sedimentological observations. Proxies for increased primary productivity such as biogenic silica (e.g. Takiguchi et al., 2006) and higher concentrations of barium (Ba; e.g. Dymond et al, 1992) and phosphorous (P; e.g. Schoepfer et al., 2015) are coincident with the sedimentological expressions of storms, including abrupt increases in grain size, low angle cross lamination and hummocky cross-stratification in recurring intervals, suggesting a relationship between times of increased primary productivity and storm activity. Barium, a refractory element, is particularly useful as a productivity proxy considering that it's preservation as barite ($BaSO_4$) is the result of sulfate and/or barium enrichment during the decay of organic matter (Sternberg et al, 2005). These transient increases in primary productivity provided a basis to support the survival and recovery of marine taxa in the wake of the Earth's most severe mass extinction.

The Belloy and Montney Formations

Western Canada is a unique repository of near-shore Panthalassa deposits. Previous work on biotic recovery has focused on shallow marine environments of the restricted Paleotethys (Algeo, et al., 2007, Cao et al., 2009; Luo et al., 2011) or the deep-water deposits of the Panthalassa (Kato et al., 2002; Takahashi et al., 2009). The Triassic Montney Formation of Western Canada, and the underlying Belloy Formation, however, provide an opportunity to study the Permian-Griesbachian-Dienerian transition in a more proximal setting. Importantly, biotic recovery following the PT boundary has been linked to refugia previously identified within these units (Beatty et al., 2008; Zonneveld et al., 2010). The first appearance of *Hindeodus parvus* marks the boundary between the Permian and Triassic, which occurs along an unconformity in most of the basin; however, there are some areas in the basin where the units are conformable. Chemostratigraphic correlations, sequence stratigraphy, and conodont analysis indicate that these deposits are Griesbachian (Lower Induan) in age (Playter et al 2018). The earliest Triassic deposits within the Montney Formation, dated to the Griesbachian, include cross-stratified sandstones with anomalous patchy calcite cements, referred to as the Calais Sandstone Member (Zonneveld and Moslow, 2018). It forms an amalgamation of shore-parallel sand bodies reminiscent of wave-dominated shoreline deposits, and commonly exhibits storm-related bedforms such as hummocky cross stratification (Zonneveld and Moslow, 2018). Here we construct a chemostratigraphic profile from a Panthalassan near-shore environment (well 2-30-070-24W5), that spans the PT boundary, and includes the Griesbachian-aged Calais sandstone.

Methods

Samples were analyzed for carbonate and organic carbone isotopes ($\delta^{13}C_{carb}$ and $\delta^{13}C_{org}$, respectively) and are reported relative to VPDB. In addition samples were analyzed for major and trace elements by ICP-MS and ICP-OES; detailed analytical procedures are included in the Data Repository. Photomicrographs of samples provided sedimentological context for the geochemical measurements. The drill core examined here is correlative to one that has been dated by conodont biostratigraphy (Golding et al.,2014; Playter et al., 2018), providing clear age constraints for samples presented herein.

Excess silica and biotic recovery

Prior to the Cretaceous, radiolaria, followed by sponges, were the largest sink of biogenic silica in the oceans (Racki, 1999; Ikeda et al., 2017). Radiolarians and sponges were prolific during the Permian and in the Anisian (Middle Triassic), but a notable dearth of deposits has been noted in Panthalassic deposits from Japan and Canada spanning the Permian/Triassic boundary and into the Early Triassic (the Changxingian, Griesbachian, and Dienerian, extending into the Smithian; Isozaki, 1997; Beauchamp and Baud, 2002; Schoepfer et al, 2013). This 'chert gap' is attributed to the intrusion of anoxic bottom waters inhibiting aerobic radiolarian and sponge productivity, as well as the collapse of thermohaline circulation (Isozaki, 1997; Beauchamp and Baud, 2002; Schoepfer, et al., 2013). Indeed, the demise of sponges at the end of the Permian has been linked to bottom water anoxia (Liu et al., 2013). The Early Triassic 'chert gap' has been recognized worldwide and is

estimated to have lasted nearly 10 Ma (Kozur, 1998; Racki, 1999). During the late Permian, just prior to the 'chert gap,' radiolarian fauna of China and Japan show an adaptation and subsequent migration of radiolaria from the deep Panthalassa into the shallower eastern Tethyes, coinciding with the development of anoxic conditions in the deep Panthallassa (Feng and Algeo, 2014). Conditions within the Panthallassa paleoocean are thought to have changed gradually with oxygen-minimum zones rising and anoxic waters inundating the continental shelves during the Late Permian (Feng and Algeo, 2014). Similarly, in the Sverdrup basin of northern Canada, the rising chemocline led to the demise of deep-water siliceous sponges within the late Permian (Algeo et al., 2012). The abundance of sponge spicules in the Belloy Formation and their paucity to absence in the Montney Formation suggests a similar situation on the northwestern margin of Pangaea. Anoxic conditions persisted in deep waters into the Early Triassic (Schoepfer et al., 2013), suggesting that the environment for benthic siliceous organisms, such as sponges, was not ideal. During the Early Triassic, however, shallow water conditions along the western margin of Pangea, in what is now western Canada, became generally oxic, intermittently interrupted by upward incursions of the chemocline (Feng and Algeo, 2014; Zonneveld et al., 2010, Beatty et al. 2008).

While Early Triassic occurrences of biogenic silica are rare, instances of increased biogenic silica deposition have been indirectly identified and interpreted to be from radiolarians in early Triassic (Griesbachian) samples from the Paleotethys by calculating excess silica relative to a shale standard (Shen et al., 2012). Until now, however, biogenic silica has not been identified in deposits from Panthalassa, the largest early Triassic palaeoocean, and there has not been evidence to suggest that

radiolaria remained active in the oxic, shallow waters of Panthalassa during this time period. Our results (Figs 1 and 2) show distinct intervals of biogenic silica.

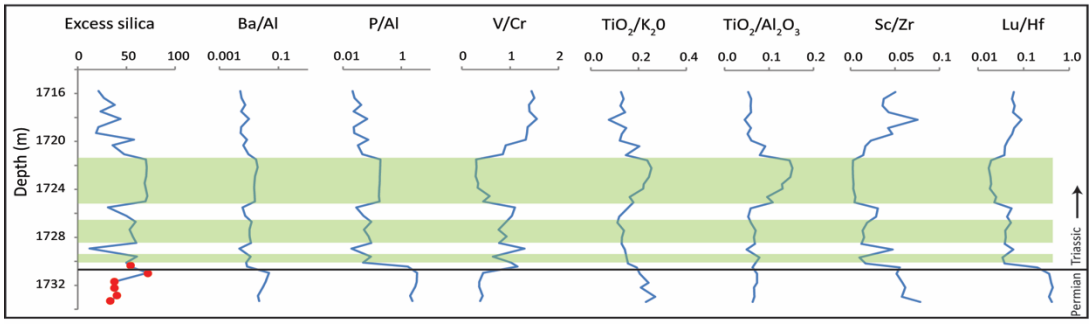

Figure 1 Paleoproductivity Proxies: Depth plot of excess silica (left) as calculated from the formula: Excess SiO_2 (%) = $SiO_{2(measured)}$ – ($Al_{(measured)}$ x (SiO_2/Al_2O_3)$_{PAAS}$) after[39,40]. The Permian/Triassic boundary is indicated on the far right. Red dots indicate hydrothermal influence and are correlated with the red dots in the ternary diagram of Figure 2. Paleoproductivity indicators include Ba/Al and P/Al. Green boxes highlight areas of excess silica which correspond to intervals of high Ba/Al and P/Al. These zones indicate intervals of high paleoproductivity. Excess silica deposited in the Permian is associated with hydrothermal input. When compared with continental input proxies of V/Cr (higher value=increased continental input), TiO_2/K_20 (lower value=increased continental input), TiO_2/Al_2O_3 (lower value=increased continental input) Sc/Zr (higher value=increased continental input) and Lu/Hf (higher value=increased continental input), an anti-phase relationship is evident.

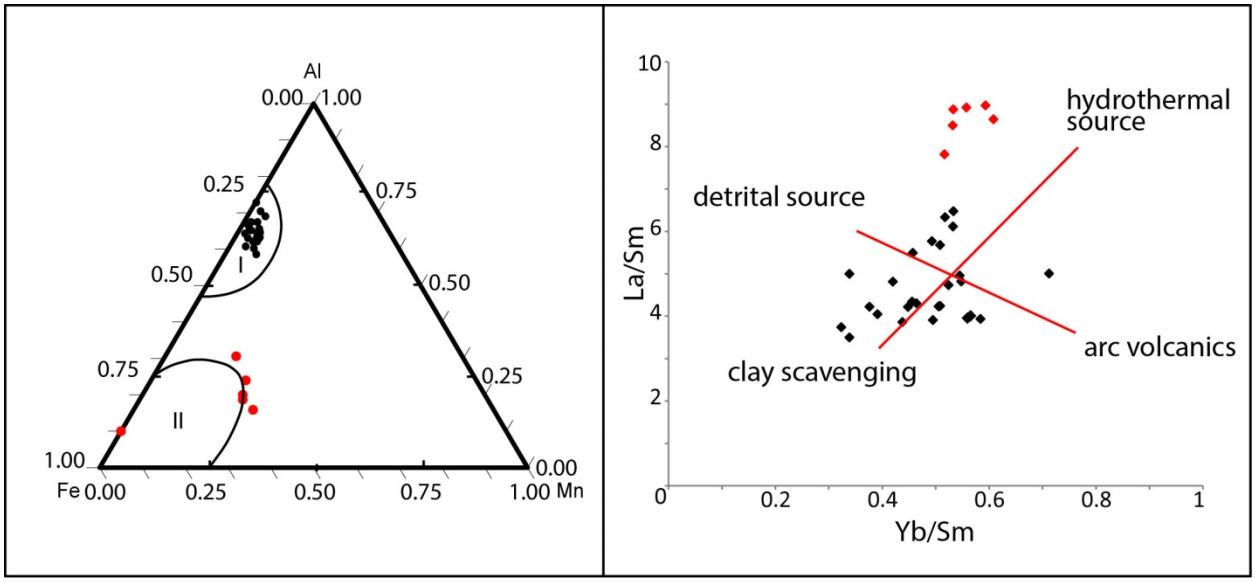

Figure 2 Excess Silica Types: A ternary diagram (left) of Al, Mn and Fe composition highlighting two regions: I) region of biogenic silica, II) region of hydrothermal silica (after [41,42]). Cross plot of La/Sm vs Yb/Sm (right) after[43]. Points in red correspond to both plots and illustrate that data with excess silica have high La/Sm and moderate to high Yb/S; this indicates hydrothermal enrichment.

These intervals were identified by calculating the amount excess silica (silica not associated with detrital components; after Shen et al., 2014; Arsairai et al., 2016), comparing La/Sm and Yb/SM ratios (to determine the contribution of detrital elements, hydrothermal sources, clay scavenging, and arc volcanics; after Plank and Langmuir, 1988), and evaluating Fe, Mn, and Al content (to further distinguish between hydrothermal vs. biogenic silica sourcing; after Adachi et al., 1986; Yamamoto, 1987; Supplementary Information). Intervals of elevated biogenic silica are also characterized by increased P/Al and Ba/Al ratios (Fig 1), photomicrographs that indicate fragmented radiolarian morphologies (Fig 3), and the coupling of carbon isotope trends (($\delta^{13}C_{carb}$ and $\delta^{13}C_{org}$; Supplementary Fig. 1) that suggest minimal diagenetic overprinting. These samples, which correlate to the Griesbachian-aged

sediments from Playter et al. (2018), indicate that radiolarians were active in the shallow western margin of Pangea during the Earliest Triassic. This is highly informative as it has been shown that radiolaria may represent a significant pool of organic matter and may even be the main factor controlling transport of carbon to the deep ocean at that time (De Wever et al. 2014).

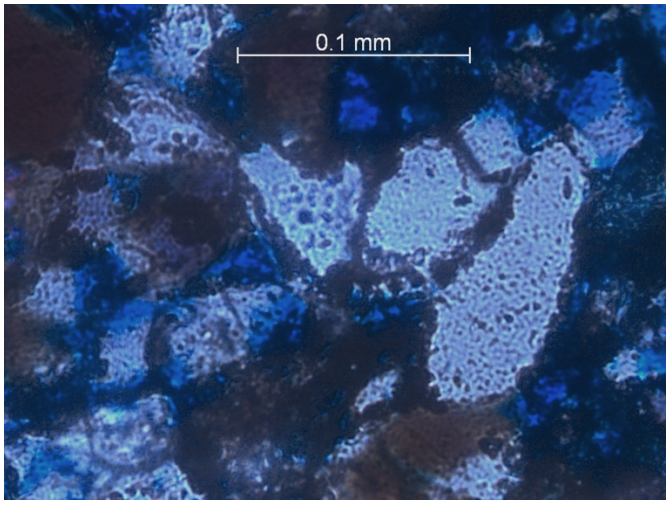

Figure 3 Radiolarian Evidence: Photomicrograph (cross polarized) illustrating fragments of radiolarian tests.

Modern rivers deliver >90% of total dissolved silica to the oceans with only minor contributions from hydrothermal sources, seafloor weathering, and wind-born dust (Ikeda et al., 2017). Thus, weathering is considered the most important factor driving biogenic silica production and burial in the oceans (Ikeda et al., 2017). Given that, chemical and physical weathering following the end-Permian mass extinction would have increased, combined with the elevated atmospheric CO_2 from PT volcanism, it follows that dissolved silica delivery to the oceans must also have

increased, providing an abundant source for siliceous organisms, such as radiolarians and sponges.

Monsoons in the early Triassic and their effect on productivity

Monsoon systems manifest in wind blowing landward from the sea in the summer as the continent warms more quickly than the ocean, while in the winter, the winds shift seaward (De Wever et al., 2014). During the Early Triassic, Pangea was likely dominated by a monsoonal climate (Parrish, 1993), where the supercontinent is thought to have magnified monsoon intensity due to the significant contrast in heat capacity between the Panthallassan ocean and the supercontinent (Kutzback, 1994; Ikeda et al., 2017). Significantly, modelling has demonstrated that Pangea could have increased the latitudinal shift of the Inter-Tropical Convergence Zone (ITCZ), which would have resulted in the ITCZ reaching a latitude of nearly 60°, running in a nearly shore-parallel arc along the northern shores of the Paleotethys with a poleward directed summer monsoon (Kutzback, 1994; Ikeda et al., 2017). This shift in the ITCZ would have also latitudinally shifted the location of precipitation, humidity, and chemical weathering intensity (Ikeda et al., 2017). Climate models suggest that these shifts in the ITCZ could have reached up to 1000 km inland (Ikeda et al., 2017). Collectively, this suggests that northwestern Pangea could have experienced enhanced seasonal continental weathering and runoff.

While coastal runoff increases marine nutrient concentrations such as silica, upwelling may also concentrate nutrients in coastal environments (e.g., Gibbs et al., 2006). Upwelling has been attributed to elevated wind stress from surface winds and

resultant Ekman transport (Ekman, 1905; Shimmield, 1992; Karstensen et al., 2008) and has been observed to correspond to monsoon cycles (Shimmield, 1992; Zhuang et al., 2017; Supplementary Fig. 2). The balance between biogenic silica burial and chemical weathering rates, as noted by Ikeda et al., (2017), suggests that the extent and rate of biogenic silica burial could have been controlled by changes in the intensity of the summer monsoon (Dessert et al., 2001). This monsoon-dependent balance would have ultimately determined the amount and location of biogenic silica precipitation. It has been recognized that within modern diatomites the radiolarian-rich layers reflect periods of increased productivity associated with upwelling, while clay-rich layers are associated with continental run-off (De Wever et al., 2014). Large radiolarian blooms are thought to be related to upwelling (De Wever et al., 1994) and, during the early Triassic, radiolarians were the only planktonic marine organism capable of fixing silica (De Wever et al., 2014). In this study, increases in weathering proxies (Sc/Zr, TiO_2/K_2O and Lu/Hf; Figure 1) occur within the clay-rich, post-monsoon deposits that are bioturbated (Supplementary Figure 3 and 4), indicating the presence of some oxygen, and occur anti-phase to intervals with appreciable biogenic silica, which correspond to storm-influenced, very-fined sandstone with calcite nodules.

Crucially, it is clear that the trophic base in the Early Triassic benefitted from the convergence of monsoon-induced fluvially transported sediments and silica with upwelling-derived nutrients. Given that the Triassic monsoon cycle was reliant on the presence of the supercontinent Pangea, it is possible that tectonic configuration of the continents at this time played a critical role in establishing ecological niches for

recalcitrant marine lineages. In other words, it was a perfect storm – both tectonically and climatically – that led to the rapid recovery of primary productivity, the expansion of shallow-water macrobiota, and ultimately the gradual end of the most severe mass extinction in Earth's history.

References

Algeo, T.J. & Twitchett, R.J. 2010.Anomalous Early Triassic sediment fluxes due to elevated weathering rates and their biological consequences. Geology, 38, 1023-1026.

Algeo, T.J., Ellwood, B., Nguyen, T.K.T., Rowe, H., and Maynard, J.B. 2007. The Permian-Triassic boundary at Nhi Tao, Vietnam: Evidence for recurrent influx of sulfidic watermasses to a shallow-marine carbonate platform. Palaeogeography, Palaeoclimatology, Palaeoecology, v. 252, p. 304-327.

Algeo, T., Henderson, C.M., Ellwood, B., Rowe, H., Elswick, E., Bates, S., Lyons, T., Hower, J.C., Smith, C., Maynard, B., Hays, L.E., Summons, R.E., Fulton, J., and Freeman, K.H. 2012. Evidence for a diachronous Late Permian marine crisis from the Canadian Arctic region. GSA Bulletin, v. 124, p. 1424-1448.

Adachi, M., Yamamoto, K., and Sugisaki, R. 1986. Hydrothermal chert and associated siliceous rocks from the northern Pacific: Their geological significance as indication of ocean ridge activity. Sedimentary Geology, v. 47, p. 125-148.

Arsairai, B., Wannakomol, A., Feng, Q., and Chonglakmani, C. 2016. Paleoproductivity and paleoredox condition of the Huai Hin Lat Formation in Northeastern Thailand. Journal of Earth Science, v. 27, p. 350-364.

Beauchamp, B. & Baud, A. 2002. Growth and demise of Permian biogenic chert along northwest Pangea: evidence for end-Permian collapse of thermohaline circulation. Palaeogeogr., Palaeoclimatol., Palaeoecol. 184, 37-63.

Cao, C., Love, G.D., Hays, L.E., Wang, W., Shen, S., and Summons, R.E. 2009. Biogeochemical evidence for euxinic oceans and ecological disturbance presaging the end-Permian mass extinction event. Earth and Planetary Science Letters, v. 281, p. 188-201.

Davies, G.R., Moslow, T.F., and Sherwin, M.D. 1997. The Lower Triassic Montney Formation, west-central Alberta. Bulletin of Canadian Petroleum Geology, v. 45, p. 474-505.

Dessert, C., Dupre, B., Francois, L.M., Schott, J., Gaillardet, J., Chakrapani, G., and Bajpai, S. 2001. Erosion of Deccan Traps determined by river geochemistry: impact on the global climate and the $^{87}Sr/^{86}Sr$ ratio of seawater. Earth and Planetary Science Letters, v. 188, p. 459-474.

DeWever, P., O'Dogherty, L., Gorican, S. 2014. Monsoon as a cause of radiolarite in the Tethyan realm. Comptes Rendus Geoscience, v. 346, p. 287-297.

Dymond, J., Suess, E., and Lyle, M. 1992. Barium in deep-sea sediment: A geochemical proxy for paleoproductivity. Paleoceanography, v. 7, p. 163-181.

Ekman, V.W. 1905. On the influence of earth's rotation on ocean currents. Ark. Math. Astron. Fys., v. 2, p. 1-53.

Erwin, D.H. *Extinction: How Life on Earth Nearly Ended 250 Million Years Ago* (Princeton Univ. Press, Princeton, 2006).

Feng, Q., and Algeo, T.J. 2014. Evolution of oceanic redox conditions during the Permo-Triassic transition: Evidence form deepwater radiolarian facies. Earth-Science Reviews, v. 137, p. 34-51.

Gibbs, S.J., Bralower, T.J., Bown, P.R., Zachos, J.C., Bybell, L.M. 2006. Shelf and open-ocean calcareous phytoplankton assemblages across the Paleocene-Eocene Thermal Maximum: Implications for global productivity gradients. Geology, v. 34, p. 233-236.

Gingras, M.K., MacEachern, J.A. & Pemberton, S.G. 1998. A comparative analysis of the ichnology of wave- and river-dominated allomembers of the Upper Cretaceous Dunvegan Formation. Bull. Can. Pet. Geol. v. 46, 51-73.

Godbold, A., Schoepfer, S., Shen, S. & Henderson, C.M. 2017. Precarious ephemeral refugia during the earliest Triassic. Geology, v. 45, 607-610.

Golding, M.L., Orchard, M.J., Zonneveld, J.-P., Henderson, C.M., and Dunn, L. 2014. An exceptional record of the sedimentology and biostratigraphy of the Montney and Doig formations in British Columbia. Bulletin of Canadian Petroleum Geology, v. 62, p. 157-176.

Hallam, A. & Wignall, P.B. 1999. Mass extinctions and sea-level changes. Earth Sci. Rev. v. 48, 217-250.

Ikeda, M., Tada, R., and Ozaki, K. 2017. Astronomical pacing of the global silica cycle recorded in Mesozoic bedded cherts. Nature Communications, v. 8, 15532.

Jablonski, D. & Flessa, K.W. 1986. The taxonomic structure of shallow-water marine faunas – implications for Phanerozoic extinctions. Malacologia, v. 27, 43-66.

Karstensen, J., Stramma, L., Visbeck, M. 2005. Oxygen minimum zones in the eastern tropical Atlantic and Pacific oceans. Progress in Oceanography, v. 77, p. 331-350.

Kato, Y., Nakao, K., and Isozaki, Y. 2002. Geochemistry of Late Permian to Early Triassic pelagic cherts from southwest Japan: implications for an oceanic redox change. Chemical Geology, v. 182, p. 15-34.

Kump, L.R., Pavlov, A. & Arthur, M.A. 2005. Massive release of hydrogen sulfide to the surface ocean and atmosphere during intervals of oceanic anoxia. Geology 33, 397-400.

Kutzbach, J.E. 1994. Idealized Pangean climates: sensitivity to orbital change. Geol. Soc. Am. Special Papers, v. 288, p. 41-56.

Kozur, H.W. 1998. Some aspects of the Permian-Triassic boundary (PTB) and of the possible causes for the biotic crisis around this boundary. Palaeogeogr., Palaeoclimatol., Palaeoecol. v.143, 227-272.

Liu. G., Feng, Q., Shen, J., Yu, J., He, W., and Algeo, T.J. 2013. Decline of siliceous sponges and spicule miniaturization induced by marine productivity collapse and expanding anoxia during the Permian-Triassic crisis in south China. Palaios, v. 28, p. 664-679.

Luo, G., Wang, Y., Algeo, T.J., Kump, L.R., Bai, X., Yang, H., Yao, L., and Xie, S. 2011. Enhanced nitrogen fixation in the immediate aftermath of the latest Permian marine mass extinction. Geology, v. 39, 647-650.

Parrish, J.T. 1993. Climate of the Supercontinent Pangea. The Journal of Geology, v. 101, p. 215-233.

Plank, T., Langmuir, C.H. 1998. The chemical composition of subducting sediment and its consequences for the crust and mantle. Chemical Geology, v. 145, p. 325-394.

Playter, T., et al. 2017. Microbe-clay interactions as a mechanism for the preservation of organic matter and trace metal biosignatures in black shales. Chem. Geol., 459, 75-90.

Playter, T., Corlett, H., Konhauser, K., Robbins, L., Rohais, S., Crombez, V., MacCormack, K.M., Rokosh, D., Prenoslo, D., Furlong, C.M., Pawlowicz, J., Gingras, M., Lalonde, S., Lyster, S., and Zonneveld, J.-P. 2018. Clinoform identification and correlation in fine-grained sediments: A case study using the Triassic Montney Formation. Sedimentology, v. 65, p. 263-302.

Racki, G. 1999. Silica-secreting biota and mass extinctions: survival patterns and processes. Palaeogeography, Palaeoclimatology, Palaeoecology, v. 154, p. 107-132.

Retallack, G.J. A 2001. 300-million-year record of atmospheric carbon dioxide from fossil plant cuticles. Nature, v. 411, 287-290.

Schoepfer, S.D., Henderson, C.M., Garrison, G.H., Foriel, J., Ward, P.D., Selby, D., Hower, J.C., Algeo, T.J., and Shen, Y. 2013. Termination of a continent – margin upwelling system at the Permian-Triassic boundary (Opal Creek, Alberta, Canada). Global and Planetary Change, v. 105, p. 21-35.

Schoepfer, S.D., Shen, J., Wei, H., Tyson, T.V., Ingall, E., and Algeo, T.J. 2015. Total organic carbon, organic phosphorus, and biogenic barium fluxes as proxies for paleomarine productivity. Earth-Science Reviews, v. 149, p. 23-52.

Shen, J., Algeo, T.J., Zhou, I., Feng, Q., Yu, J., Ellwood, B. 2012. Volcanic perturbations of the marine environment in South China preceding the latest Permian mass extinction and their biotic effects. Geobiology, v. 10, 82-103.

Shen, J., Zhou, L., Feng, Q., Zhang, M., Kei, Y., Zhang, N., Yu, J., and Gu, S. 2014. Paleo-productivity evolution across the Permian-Triassic boundary and quantitative calculation of primary productivity of black rock series from the Dalong Formation, South China. Science China Earth Science, v. 57, p. 1583-1594.

Shimmield, G.B. 1992. Can sediment geochemistry record changes in coastal upwelling palaeoproductivity? Evidence from northwest Africa and the Arabian Sea. Geological Society Special Publication No. 64, p. 29-46.

Sternberg, E., Tang, D., Ho, T.-Y., Jeandel, C., and Morel, F.M.M. 2005. Barium uptake and adsorption in diatoms. Geochimica et Cosmochimica Acta, v. 69, p. 2745-2752.

Sun, Y., Joachimski, M.M., Wignall, P.B., Yan, C., Chen, Y., Jiang, H., Wang, L. & Lai, X. 2012. Lethally Hot Temperatures During the Early Triassic Greenhouse. Science, v. 338, 366-370.

Takiguchi, T., Sugitani, K., Yamamoto, K., and Suzuki, K. 2006. Biogeochemical signatures preserved in ancient siliceous sediments; new perspectives to Triassic radiolarian bedded chert compositions. Geochemical Journal, v. 40, p. 33-45.

Takahashi, S., Oba, M., Kaiho, K., Yamakita, S., and Sakata, S. 2009. Panthalassic oceanic anoxia at the end of the Early Triassic: A cause of delay in the recovery of life after the end-Permian mass extinction. Palaeogeography, Palaeoclimatology, Palaeoecology, v. 274, p. 185-195.

Thushara, V. & Vinayachandran, P.N. 2016. Formation of summer phytoplankton bloom in the northwestern Bay of Bengal in a coupled physical-ecosystem model. J. Geophys. Res.- Ocean, v. 121 8535-8550.

Wignall, P.B. & Twitchett, R.J. 1996. Oceanic anoxia and the End Permian Mass Extinction. Science, v. 272, 1155-1158.

Yamamoto, K. 1987. Geochemical characteristics and depositional environments of cherts and associated rocks in the Franciscan and Shimanto Terranes. Sedimentary Geology, v. 52, p. 65-108.

Zhuang, G., Pagani, M., Zhange, Y.G. 2017. Monsoonal upwelling in the western Arabian Sea since the middle Miocene. Geology, v. 45, p. 655-658.

Zonneveld, J.-P., Gingras, M.K., and Beatty, T.W. 2010. Diverse ichnofossil assemblages following the P-T Mass Extinction, Lower Triassic, Alberta and British Columbia, Canada: evidence for shallow marine refugia on the northwestern coast of Pangaea. Palaios, v. 25, p. 368-392.

Zonneveld, J.-P., and Moslow, T.F. 2018. Palaeogeographic setting, lithostratigraphy, and sedimentary framework of the Lower Triassic Montney Formation of western Alberta and northeastern British Columbia. Bulletin of Canadian Petroleum Geology, v. 66, p. 93-127.

Chapter 3: New evidence for volcanism and its global-scale impacts in the wake of the end-Permian mass extinction

Volcanism associated with the Siberian Traps in Russia has long been suggested as a possible cause, not only of the end-Permian mass extinction, but the end-Smithian (mid-Olenekian) biotic perturbation as well (Galfetti et al., 2007; Stanley, 2009; Song et al., 2011; Sun et al., 2012). This hypothesis is based primarily upon the correspondence of the end-Smithian extinction with a large negative carbon isotopic excursion that is similar to the negative excursion observed for the end-Permian event (Stanley, 2009). Potential factors contributing to the large negative excursions include; (i) ocean stratification and subsequent overturn (Knoll *et al.* 1996), (ii) the demise of certain primary producers and the oxidation of high levels of terrestrial organic matter transported into the oceans (Erwin, 1994), (iii) the release of methane from clathrates on the ocean floor due to increasing temperatures (Krull and Retallack, 2000), (iv) an ecological shift from cyanobacteria to photosynthetic sulfur-oxidizing bacteria (van Breugel *et al.*, 2005; Riccardi *et al.*, 2007), and (v) the oxidation of coal deposits intruded by igneous bodies (Retallack and Jahren, 2008; Svensen et al., 2018). Regardless of the factors involved in producing the negative carbon excursion, an increase in CO_2 emitted via volcanism likely accompanied the isotopic shift (Renne and Basu, 1991; Galfetti *et al.*, 2007; Payne and Kump, 2007).

Evidence for volcanism at the end-Smithian comes from recent studies demonstrating a fluctuation in carbon isotope values in carbonates coincident with increased mercury (Hg) levels (from 40 up to 100 ppb), total organic carbon (TOC) (from 2 to 3%) and non-acid-volatile sulfur (up to 0.4%) (Hammer et al., 2019; Shen

et al., 2019a; Shen et al., 2019b). However, these studies have not been able to: (1) definitively link this volcanic signal with the Siberian traps or other volcanic sources, (2) quantify the size of the atmospheric gas flux, (3) calculate the change in seawater pH following the volcanic activity and outgassing, and (4) decipher the tempo of the eruption (i.e., when degassing occurred relative to volcanic sediment deposition). In this regard, we provide detailed geochemical data from pristine core samples from the Western Canada Sedimentary Basin correlating with the Smithian/Spathian boundary. To address the above uncertainties, we obtained 240 well-preserved shale and siltstone samples from a 272 meter drill core interval from the Dominion Land Survey location 16-17-083-25W6M in British Columbia, Canada (56.21°N, -121.91°E). This core provides a continuous succession from the latest Permian to the Anisian (Fig. 1); an ideal sample set for examining the end-Smithian's relationship to the Siberian traps volcanism (Fig. 2). Moreover, the samples have undergone minimal diagenesis (Playter *et al.,* 2018) and have been previously dated using conodont biostratigraphy (Golding et al., 2014).

Previous studies on the provenance of shale and pelites often used geochemical cross-plots of incompatible elements (Th/Sc versus Cr/Th) as well as the cobalt (Co), scandium (Sc), nickel (Ni), and chromium (Cr) contents relative to thorium (Th), to distinguish felsic, mafic, and ultramafic sediment sources (e.g., Condie and Wronkiewicz, 1989; Totten, *et al*., 2000; Bracciali *et al.*, 2007; Varga *et al.*, 2007 and references therein). Typical granites have a Th/Sc value of 10 and a Cr/Th value of 0.2; mid-ocean ridge basalts (MORB) have a characteristic Th/Sc ratio of 0.2 and a Cr/Th ratio >500; whereas ultramafic rocks have Th/Sc values between 0.8 to 0.6

and Cr/Th values >200 (Totten *et al*., 2000, Bracciali *et al.*, 2007). Our data plot along a mafic and ultramafic trend in two stratigraphic intervals - the end-Permian and the end-Smithian (Fig 2A). By contrast, data from the remaining stratigraphic intervals indicate a felsic sediment source (low Cr/Th and increasing Th/Sc). The

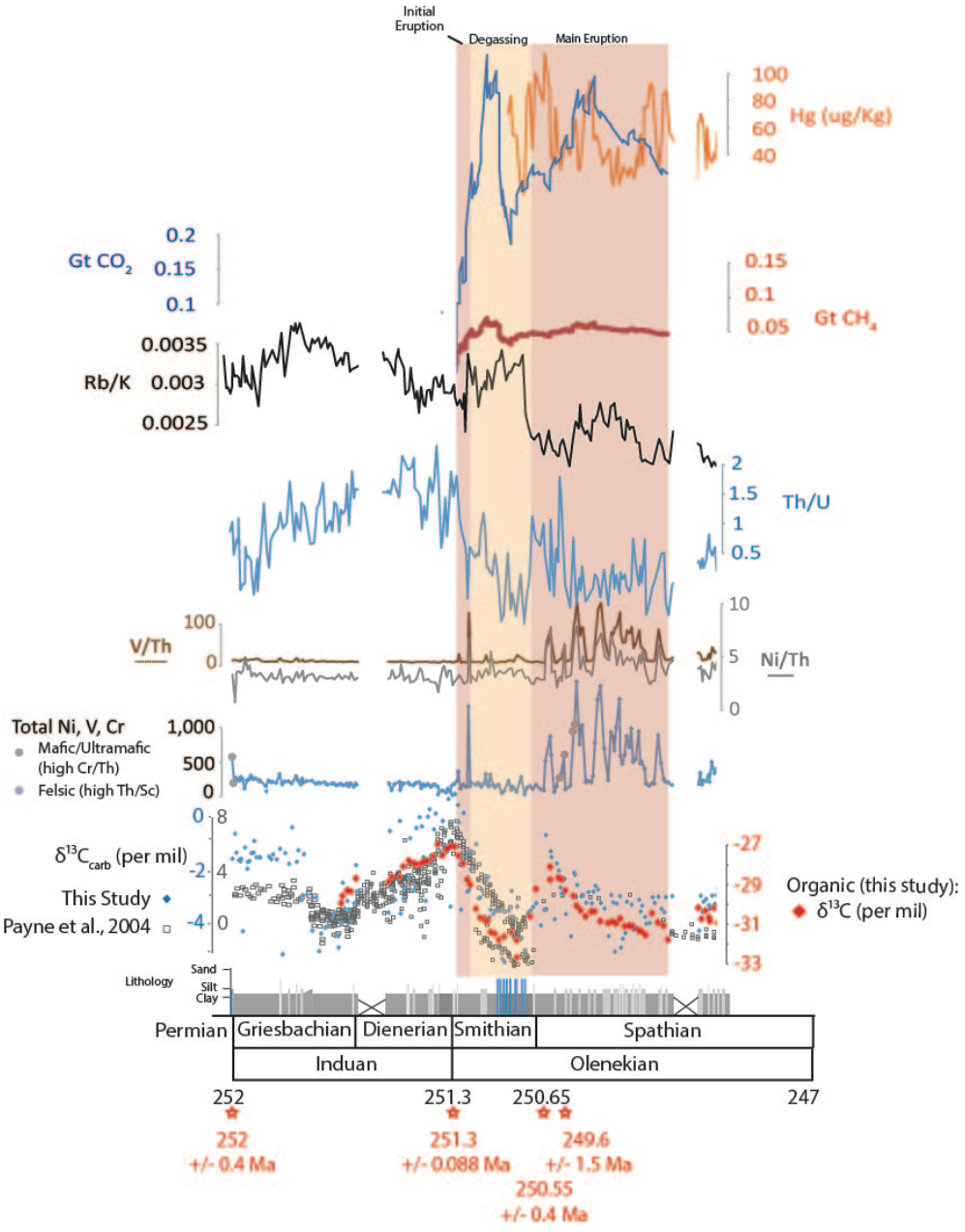

Figure 1: Early Triassic distribution of weathering and volcanic proxies in the context of carbon isotopic signatures. Dates from volcanic ashes or dolerite sills (denoted by volcanoes and red arrows) are sourced from U/Pb dates of Paton et al. (2010; 249.6 +/- 1.5 Ma), Burgess and Bowring (2015; 251.3 +/- 0.088Ma)) and Ovtcharova et al. (2006; 252.0 +/- 0.4; 250.55 +/- 0.5 Ma, 248.12 +/- 0.4 Ma, 246.83 +/- 0.31 Ma). Dates for Triassic Stage boundaries are from Mundil et al. (2010). Stage boundaries are placed in relation to stratigraphic depth based on conodont horizons identified in this core by Golding et al. (2015). A litholog that records grainsize is included with the stage boundaries (blue denotes intervals of bioclastic carbonate). Carbon isotopic data

(reported relative to VPDB) includes data from this study (blue points) and data from Payne et al. (2004; black points), as well as organic carbon isotopic data (this study; red data points) for comparison. Mafic/ultramafic content can be distinguished from felsic input by examining metal cations such as Ni, V, and Cr (high relative contents indicate mafic or ultramafic sources); high ratio values of V/Th and Ni/Th indicate mafic/ultramafic input; cross plots of Cr/Th and Th/Sc distinguish mafic/ultramafic input with high Cr/Th indicating mafic/ultramafic content (Totten et al., 2000; Bracciali et al., 2007; while cross-plot results are indicated by coloured hexagons. The Th/U ratio, used as a redox proxy in clastic sediments, indicates expanded anoxia through an increased value that results from a decrease of U in seawater due to the drawdown of U under anoxic conditions (Brennecka et al., 2011). The ratio of Rb/K indicates weathered sources, while low Rb/K values indicate volcaniclastic input (Plank and Langmuir, 1998). Modelled gigatons of CO_2 (dark blue) and gigatons of CH_4 (red) output are shown in relation to the aforementioned proxy indicators. These outputs were generated from a simple box model built around the carbon isotope data from this study. Mercury concentrations (ppb) can be used as an indicator of volcanic eruptions; prolonged volcanic eruptions emit large fluxes of mercury to the atmosphere and direct deposition of atmospheric mercury to marine sediments can preserve volcanic signatures (Thibodeau et al., 2016).

mafic/ultramafic sourcing is corroborated by large spikes of Ni, Cr, and vanadium (V) concentrations, as well as Ni/Th and V/Th ratios in the same two stratigraphic intervals. These relationships suggest discrete episodes of mafic/ultramafic volcanic output, and crucially, correspond to the extinction events at the end-Permian and end-Smithian. Moreover, a distinct spike in Hg (Fig. 1) at the end-Smithian of over 100 ppb suggests a large-scale volcanic eruption. This anomaly is similar in magnitude to the Hg spikes observed by Thibodeau et al., (2016) at the end of the Triassic that are associated with the emplacement of the Central Atlantic Magmatic Province.

To investigate the origin of the mafic signatures, and ultimately the source of the volcanic input observed, we normalized incompatible elements to normal MORB (N-

MORB) values and compared those values to published signatures (Fig. 2A). Sediment sources that can be identified in this manner include: oceanic island arcs, within plate basalts, continental arcs, or intraplate settings (Fralick, 2003 and references therein). Our data produce incompatible-element ratio plots with a hump from strontium (Sr) to tantalum (Ta) and a diagonal declining trend from Ta to titanium (Ti), with minor perturbations observed for cerium (Ce), zircon (Zr), hafnium (Hf), and samarium (Sm) (Fig. 2A). Yttrium values are high, while ytterbium (Yb) falls along the diagonal trend. These results indicate a within-plate setting where a N-MORB type melt is mixed with subcontinental lithosphere (e.g., Fralick, 2003). The observed pattern is consistent with the proposed models for the origin of the Siberian traps: (1) continental lithosphere and the mantle undergo mixing driven by a mantle plume (Saunders et al., 2005; Allen et al., 2006), or (2) the subduction of oceanic slabs that transported water into the upper mantle, leading to a lowering of the solidus and substantial melting (Ivanov, 2007). The temporally correlated patterns strongly suggest that the observed mafic signatures in our Canadian dataset, and the source of CO_2 influx, are best attributed to volcanic activity in the Siberian Traps. Importantly, U-Pb dating of Siberian Traps extrusive and intrusive rocks indicate two eruption dates of ~251.4 +/- 0.3 Ma and ~250.2 +/- 0.4 Ma (Table 1) within the Early Triassic (Kamo et al., 2003, Paton et al., 2010, Burgess and Bowring, 2015), which correspond to the timing of the volcanic input identified in our samples.

Siberian Trap volcanism would also have impacted the composition of the end-Permian to early Triassic atmosphere. Fluctuations in the carbon isotopic compositions of organic carbon ($\delta^{13}C_{ORG}$) and marine carbonate ($\delta^{13}C_{CARB}$), when

paired, can be used to measure changes in atmospheric pCO_2 (Kump and Arthur, 1999). A simple box model based on Payne and Kump (2007) was developed to investigate the carbon emissions that could account for the observed variations in $\delta^{13}C$ values. For modeling, the initial inorganic carbon content was set to either 500 or 2000 ppm in the atmosphere, and the $\delta^{13}C$ values of the extra carbon source ($\delta^{13}C_{extra}$) was modeled as -12, -22, or -60‰. While this box model assumes a constant ocean-atmosphere mass balance, it allows for an initial estimate of volcanic emissions and comparison with geochemical volcanism proxies. Model outputs include the CO_2 flux (with a range of 0 to 0.4625 Gt) and methane flux (range of 0 to 0.07 Gt; Fig 1), indicating an increase in outgassing during the early-to-mid Smithian. This increase in CO_2 corresponds to a negative excursion in $\delta^{13}C_{ORG}$ values from -27‰ to as low as -33 ‰ and $\delta^{13}C_{CARB}$ from 1‰ to -6 ‰. Calculating

$$\log_2\left(\frac{maximum\ emitted\ carbon\ dioxide}{minimum\ emitted\ carbon\ dioxide}\right)$$

using values of 0.1008 Gt (early Smithian) and 0.4625 Gt (mid Smithian) for the minimum and maximum, respectively, indicates that the CO_2 flux quadrupled in magnitude. This is followed by an abrupt drop to 0.1874 Gt in absolute CO_2 emissions in the late Smithian, which coincides with a drop of approximately 40 ppb in measured Hg. A second gradual increase in the CO_2 flux is observed beginning at the end-Smithian, reaching a maximum of 0.418 Gt within the Spathian. Our data suggest that the degassing phase of CO_2 occurred before the main eruptive event at the end-Smithian. This is similar to what has been postulated to have occurred at the end of the Permian, where initial degassing is thought to have triggered the onset of

the end-Permian mass extinction and was estimated to have occurred over a period of 0.4 Ma (Sobolev et al, 2011). Considering that global temperature increases by 1.5-4.5°C per doubling of atmospheric carbon, using the IPCC 5th assessment report (Collins et al., 2013; Koehler et al., 2010; Holden et al., 2010; Hargreaves et al., 2012; Paleosens, 2012; Aldrin et al., 2012; Bender et al., 2012) and assuming effective radiative forcing, climate sensitivity and climate feedbacks therein, this influx of carbon to the atmosphere would account for a total increase in temperature of up to 10°C. This estimate is considered conservative, as methane converts to CO_2 within 5-7 years (Frieling et al., 2016) and our data indicate an increase in the methane flux to over 0.05 Gt, coincident with increased CO_2 flux (Fig 1). Our results are consistent with Black et al. (2018) who, by modelling the climate at the end of the Permian, found an increase in temperature of 8-10°C

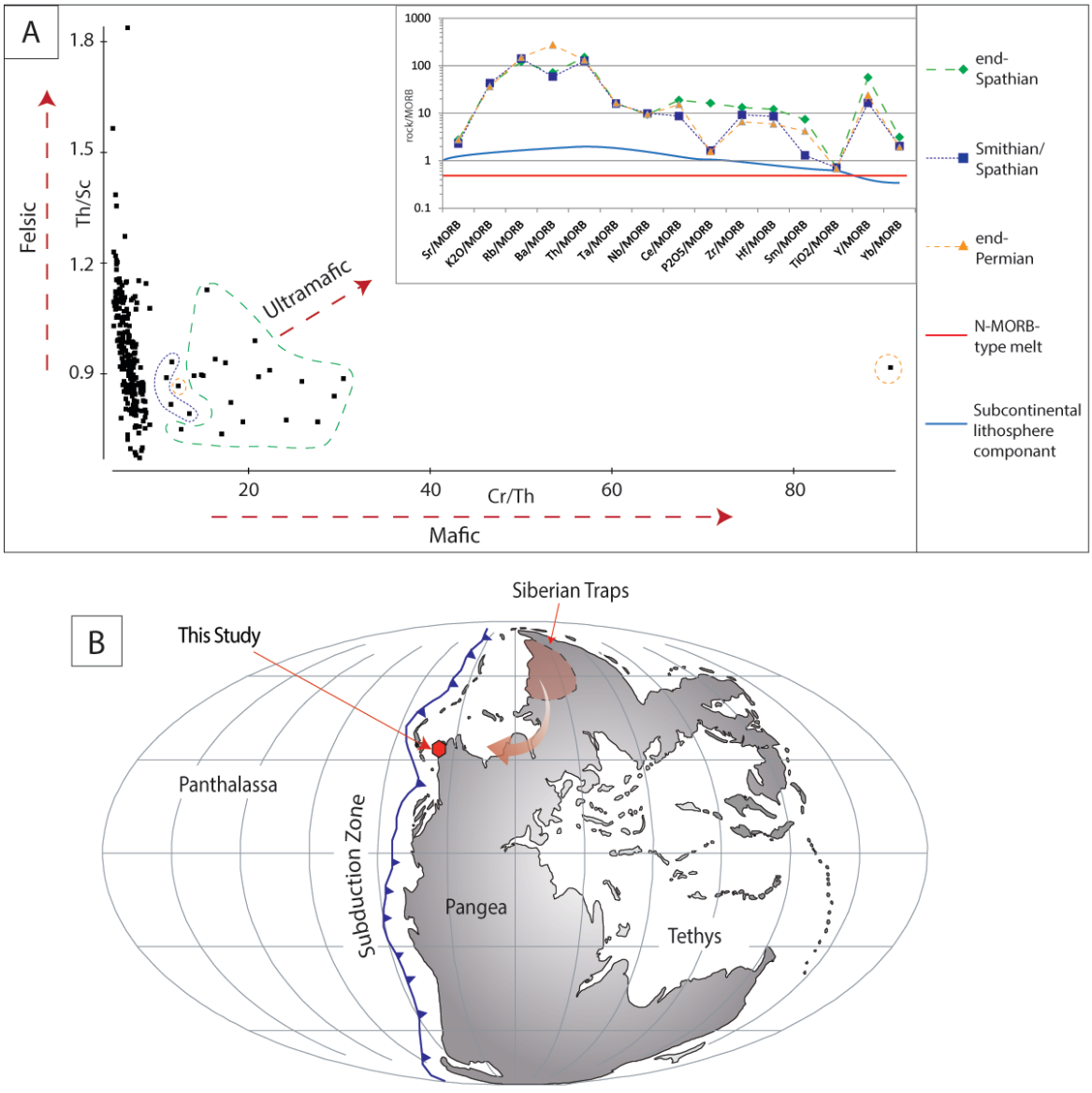

Figure 2: (A) Cross plot of Th/Sc and Cr/Th illustrating samples with high mafic to ultramafic content. Inset shows incompatible element plots for the identified high mafic intervals after Pearce (1983) and Fralick (2003) showing mixing of subcontinental lithosphere (curved line) and subduction zone components (above curved line and N-MORB components – see horizontal line). Values were normalized to MORB values taken from Fralick (2003). (B) Paleogeographic schematic modified from R. Blakey (http://jan.ucc.nau.edu/~rcb7/260moll.jpg) illustrating the approximate location of the Siberian Traps (from Ivanov, 2007) in relation to our sample site. Locations of islands are approximate.

after a threefold increase in CO_2 related to the end-Permian Siberian Trap volcanism.

Our findings also agree with temperature estimates by Sun et al. (2012) who used oxygen isotopes to postulate a Late Smithian thermal maximum between 251 Ma to 250.7 Ma, followed by a global cooling event.

As a doubling of dissolved CO_2 can decrease seawater pH by approximately 0.25 units (Rhein et al., 2013), this suggests that the oceans experienced an acidification event with an initial drop of up to 0.55 pH units (assuming atmosphere-ocean equilibrium). This initial acidification appears to have reversed by the late Smithian, with a sudden decrease in carbon flux (Supplementary Table 2). At the end-Smithian, however, the values of emitted carbon dioxide rise again, suggesting a drop of 0.52 pH units. While ocean acidification has been demonstrated to have been a contributing factor to the end-Permian mass extinction (Hinojosa et al., 2012; Payne et al., 2010; Liang et al., 2002, Clapham and Payne, 2011, Sephton et al., 2015), no evidence has been provided, before now, for acidification contributing to the end-Smithian extinction; although, the possibility of ocean acidification at this time has recently been raised (Shen et al., 2019).

When all geochemical data are considered together, it is possible to elucidate a timeline of volcanic events. An initial, comparably small, eruptive pulse occurred at 251.4 Ma (Phase 1: initial eruption; the start of the Smithian), during which ultramafic derived sediments were delivered to the basin and relatively minor degassing occurred (0.4 Gt CO_2; Fig 1). This initial pulse was short-lived, as indicated by the sudden lack of ultramafic detritus within the mid- to end-Smithian (Phase 2: degassing; Fig. 1). Although ultramafic input to the basin ceased during Phase 2, atmospheric degassing waxed then waned, with the highest volumes of CO_2 (0.418

Gt CO_2) being released during the start of this phase (Fig. 1). A weathering proxy (Rb/K) shows unusually high values (> 0.0035) corresponding to the timing of CO_2 input during Phase 2. The presence of bioclastic debris (Fig. 1) suggests that marine conditions became increasingly favorable as atmospheric degassing declined through the mid- to end-Smithian. The final phase, Phase 3 (the main eruption phase) began at the end-Smithian boundary, 250.2 Ma. While CO_2 degassing increased, ultramafic derived sediment input to the basin increased markedly, as indicated by the highest recorded Ni, V, and Cr values (in excess of 1000 ppm). Mercury also occurs in the highest observed concentrations (in excess of 100 ppb) during this phase. Our Th/U data show a sharp, large positive increase of ~1 at the end-Smithian (Fig. 1). Thorium is redox independent, while anoxic conditions lead to increased U removal, resulting in lower seawater U concentrations and an increased Th/U ratio during periods of anoxia (Elrick et al., 2011). Significantly, the loss of bioclastic material at the end-Smithian is coincident with the start of Phase 3, marking the end-Smithian extinction. Marine anoxia in this case does not appear to correspond to increased weathering, but instead with increased volcanic output (sediment and gas) and the loss of biota at the end-Smithian.

Here, for the first time, we provide sedimentological evidence documenting the influence from an end-Smithian Siberian Trap volcanic eruption in western Canada that coincides with U-Pb dates for two eruption dates of ~251.4 Ma and ~250.2 Ma (Kamo et al., 2003, Paton et al., 2010, Burgess and Bowring, 2015). Following the initial eruptive pulse of volcanic materials (~251.4 Ma), modelling results based on carbon isotope data indicate that a sudden but significant period of CO_2 outgassing

occurred in the Early-Smithian, with calculated temperature fluctuations of up to 10°C and a decrease in pH of 0.55 units. This initial outgassing was accompanied by little eruptive material and, as it declined in volume, gave way to biotic recovery. The second outgassing, which occurred at the end-Smithian, while more gradual, was accompanied by volcanically sourced sediment transported by fluvial, marine and atmospheric process, as well as marine anoxia and the extinction of carbonate-generating biota (~250.2 Ma). This suggests large igneous provinces, such as the Siberian Traps, can produce significant outgassing without coincident ashes or dykes, and that volcanic outgassing of CO_2 alone was not enough to trigger a subsequent extinction event. Instead, it was the combined effects of massive outgassing and eruptive material that triggered the end-Smithian mass extinction. This correlation may be due to the fact that magmas erupted close to the surface, which experience a lower overburden pressure, end up producing more sulfur-enriched gases than magmas sourced deeper in the crust (Gaillard et al., 2011). This leads to increased sulfuric acid production in the atmosphere, and ultimately, acid deposition on land, thereby generating a greater flux of volcanic sediments.

Methods

Samples were analyzed using both inductively coupled plasma mass spectrometry (ICP-MS) and inductively coupled plasma optical emission spectrometry (ICP-OES) at Chemostrat laboratories in Houston, Texas, a laboratory accredited to ISO 17025:2005 (equivalent to ISO 9000). Following procedures outlined in Hildred *et al.* (2010), samples were cleaned using water and solvent to remove surface

contamination. Subsequently, samples were pulverized using an Agate mortar and, in preparation for ICP-MS and ICP-OES, subjected to a Li-metaborate fusion procedure (Jarvis and Jarvis, 1992).

Remnant pulverized sample material was additionally analyzed for $\delta^{13}C_{CARB}$ and $\delta^{18}O$ using a Kiel lll – MAT 252 IRMS at Chemostrat laboratories. Isotopic composition is reported relative to Vienna Pee Dee Bellemnite (VPDB) standard, in delta notation. Analytical precision, +/- 0.18 (2σ), and accuracy, +/- 0.03 (2σ), was determined from replicate measurements of the international standard NBS19 and internal standards. Additionally, pulverized sample material was analyzed for δC^{13}_{ORG} at the Institut Universitaire Européen de la Mer and at Yale University for Hg content following standard methods.

The box model was generated using equations found in Payne and Kump, 2007. Particular inputs are as follows: phosphate weathering was set as 130 x 10^{15} mol/ky; organic carbon weathering was set as 8 x 10^{15} mol/ky; carbonate weathering was set to 24 x 10^{15} mol/ky; silicate weathering was set to 8 x 10^{15} mol/ky after the values used in Payne and Kump, 2007.

References

Aldrin, M., M. Holden, P. Guttorp, R. B. Skeie, G. Myhre, and T. K. Berntsen, 2012: Bayesian estimation of climate sensitivity based on a simple climate model fitted to observations of hemispheric temperatures and global ocean heat content. Environmetrics, v.23, 253–271.

Bender, F. A. M., A. M. L. Ekman, and H. Rodhe, 2010: Response to the eruption of Mount Pinatubo in relation to climate sensitivity in the CMIP3 models. Clim. Dyn., v. 35, 875–886.

Black, B.A., Neely, R.R., L., J.-F., Elkins-Tanton, L.T., Kiehl, J.T., Shields, C.A., Mills, M.J., and Bardeen, C. 2018. Systematic swings in end-Permian climate from Siberian Traps carbon and sulfur outgassing. Nature Geoscience, v. 11, p. 949-954.

Bracciali, L., Marroni, M., Pandolfi, L., and Rocchi, S. 2007. Geochemistry and petrography of Western Tethys Cretaceous sedimentary covers (Corsica and Northern Apennines): From source areas to configuration of margins. In: Sedimentary Provenance and Petrogenesis: Perspectives from Petrography and Geochemistry (Eds J. Arribas, S. Critelli and M.J. Johnsson), GSA Spec. Paper, v. 420, 73-93.

Brennecka, G.A., Herrmann, A.D., Algeo, T.J., and Anbar, A.D. 2011. Rapid expansion of oceanic anoxia immediately before the end-Permian mass extinction. PNAS, v. 108, p. 17631-17634.

Burgess, S.D. and Bowring, S.A. 2015. High-precision geochronology confirms voluminous magmatism before, during, and after Earth's most severe extinction. Science Advances, v. 1. E1500470.

Collins, M., R. Knutti, J. Arblaster, J.-L. Dufresne, T. Fichefet, P. Friedlingstein, X. Gao, W.J. Gutowski, T. Johns, G. Krinner, M. Shongwe, C. Tebaldi, A.J. Weaver and M. Wehner, 2013: Long-term Climate Change: Projections,

Commitments and Irreversibility. In: Climate Change 2013: The Physical Science Basis. Contribution of Working Group I to the Fifth Assessment Report of the Intergovernmental Panel on Climate Change [Stocker, T.F., D. Qin, G.-K. Plattner, M. Tignor, S.K. Allen, J. Boschung, A. Nauels, Y. Xia, V. Bex and P.M. Midgley (eds.)]. Cambridge University Press, Cambridge, United Kingdom and New York, NY, USAErwin, D.H. 1994. The Permo-Triassic extinction. Nature, v. 367, p. 231-236.

Condie, K.C. and Wronkiewicz, D.J. 1989. The Cr/Th ratio in Precambrian pelites from the Kaapvaal Craton as an index of craton evolution. Earth and Planetary Science Letters, v. 97, p. 256-267.

Daag, A.S., B. S. Tubianosa, C. G. Newhall, N. M. Tuñgol, D. Javier, M. T. Dolan, P. J. Delos Reyes, R. A. Arboleda, M. L. Martinez, and T. M. Regalado, in Fire and Mud: Eruptions and Lahars of Mount Pinatubo, Philip- pines, C. G. Newhall and R. S. Punongbayan, Eds. (Univ. of Washington Press, Seattle, 1996), pp. 409-414

Fralick, P.W. 2003. Geochemistry of clastic sedimentary rocks: ratio techniques; in Geochemistry of Sediments and Sedimentary Rocks, Geological Association of Canada, Geotext 4.

Galfetti, T., Hochuli, P.A., Brayard, A., Bucher, H., Weissert, H., Vigran, J.O. 2007. Smithian-Spathian boundary event: evidence for global climatic change in the wake of the end-Permian biotic crisis. Geology, v. 35, p. 291-294.

Gaillard, G., Scaillet, B., and Arndt, N.T. 2011. Atmospheric oxygenation caused by a change in volcanic degassing pressure. Nature, v. 478, p. 229-232.

Gerlach,T.M., H. R. Westrich, R. B. Symonds, in Fire and Mud: Eruptions and Lahars of Mount Pinatubo, Philip- pines, C. G. Newhall and R. S. Punongbayan, Eds. (Univ. of Washington Press, Seattle, 1996), pp. 415-433

Hallam, A. 1991. Why was there a delayed radiation after the end-Palaeozoic extinctions? Historical Biology, v. 5, p. 257-262.

Haugan, P.M. and Drange, H. 1996. Effects of CO_2 on the ocean environment. Energy Conservation Management, v. 37, p. 6-8.

Hargreaves, J. C., J. D. Annan, M. Yoshimori, and A. Abe-Ouchi, 2012: Can the Last Glacial Maximum constrain climate sensitivity? Geophys. Res. Lett., v. 39, L24702.

Hildred, G.V., Ratcliffe, K.T., Wright, A.M., Zaitlin, B.A. and Wray, D.S. (2010) Chemostratigraphic applications to low-accommodation fluvial incised-valley settings: an example from the lower Mannville Formation of Alberta, Canada. J. Sediment. Res., v. 80, 1032–1045.

Holden, P. B., N. R. Edwards, K. I. C. Oliver, T. M. Lenton, and R. D. Wilkinson, 2010: A probabilistic calibration of climate sensitivity and terrestrial carbon change in GENIE-1. Clim. Dyn., v. 35, 785–806

Ivanov, A.V. 2007. Evaluation of different models for the origin of the Siberian Traps, GSA Special Paper 430, p. 669-691.

Jarvis, I. and Jarvis, K. (1992) Plasma spectrometry in the earth sciences: techniques, applications and future trends. Chem. Geol., v. 95, 1–33.

Kamo, S.L., Czamanske, G.K., Amelin, Y., Fedorenko, V.A., Davis, D.W., and Trofimov, V.R. 2003. Rapid eruption of Siberian flood-volcanic rocks and evidence for coincidence with the Permian-Triassic boundary and mass extinction at 251 Ma. Earth and Planetary Science Letters, v. 214, p. 75-91.

Knoll, A.H., Bambach, R.K., Canfield, D.E., and Grotzinger, J.P*.* 1996. Comparative Earth history and Late Permian mass extinction. Science, v. 273, p. 452-457

Knoll, A.H., Bambach, R.K., Payne, J.L., Pruss, S., and Fischer, W.W. 2007. Paleophysiology and end-Permian mass extinction. Earth and Planetary Science Letters, v. 256, p. 295-313.

Koehler, P., R. Bintanja, H. Fischer, F. Joos, R. Knutti, G. Lohmann, and V. MassonDelmotte, 2010: What caused Earth's temperature variations during the last 800,000 years? Data-based evidence on radiative forcing and constraints on climate sensitivity. Quat. Sci. Rev., v. 29, 129–145.

Krull, E.S., and Retallack, G.J. 2000. $\delta^{13}C$ depth profiles from paleosols across the Permian-Triassic boundary: Evidence for methane release. GSA Bulletin, v. 112, p. 1459-1472.

Kump, L.R. and Arthur,M.A. 1999. Interpreting carbon-isotope excursions: carbonates and organic matter. Chemical Geology, v. 11, p. 181-198.

Mathews, H.D., Gillett, N.P., Stott, P.A., and Zickfeld, K. 2009. The proportionality of global warming to cumulative carbon emissions. Nature, v. 459, p. 829-832.

Miller, E.L., Soloviev, A.V., Prokopiev, A.V., Toro, J., Harris, D., Kuzmichev, A.B., and Gehrels, G.E. 2013. Triassic river systems and the paleo-Pacific margin of northwestern Pangea. Gondwana Research, v. 23, p. 1631-1645.

Ovtchrova, M., Bucher, H., Schaltegger, U., Galfetti, T., Brayard, A., and Guex, J. 2006. New Early to Middle Triassic U-Pb ages from South China: calibration with ammonoid biochronozones and implications for the timing of the Triassic biotic recovery. Earth and Planetary Science Letters, v. 243, p. 463-475.

Paleosens Members, 2012: Making sense of palaeoclimate sensitivity. Nature, v. 491, 683–691.

Paton, M.T., Ivanov, A.V., Fiorentini, M.L., McNaughton, N.J., Mudrovska, I., Reznitskii, L.Z., and Demonterova, E.I. 2010. Late Permian and Early Triassic magmatic pulses in the Angara-Taseeva syncline, Southern Siberian Traps and their possible influence on the environment. Russian Geology and Geophysics, v. 51, p. 1012-1020.

Payne, J.L., Lehrmann, D.J., Wei, J., Orchard, M.J., Schrag, D.P., and Knoll, A.H. 2004. Large perturbations of the carbon cycle during recovery from the end-Permian extinction. Science, v. 305, p. 506-509.

Payne, J.L., and Kump, L.R. 2007. Evidence for recurrent Early Triassic massive volcanism from quantitative interpretation of carbon isotope fluctuations. Earth and Planetary Science Letters, v. 256, p. 264-277.

Playter, T., Corlett, H., Konhauser, K., Robbins, L., Rohais, S., Crobez, V., Maccormack, K., Rokosh, D., Prenoslo, D., Furlong, C.M., Pawlowicz, J., Gingras, M., Lalonde, S., Lyster, S., and Zonneveld, JP. 2018. Clinoform identification and correlation in fine-grained sediments: A case study using the Triassic Montney Formation. Sedimentology, v. 65, p. 263-302.

Raup, D.M. 1979. Size of the Permo-Triassic bottleneck and its evolutionary implications. Science, v. 206, p. 217-218.

Renne, P.R., and Basu, A. 1991. Rapid eruption of the Siberian Traps Flood Basalts at the Permo-Triassic Boundary. Science, v. 253, p. 176-179.

Retallack, G.J. and Jahren, A.H. 2008. Methane release from igneous intrusion of coal during Late Permian extinction events. The Journal of Geology, v. 116, p. 1-20.

Rhein, M., S.R. Rintoul, S. Aoki, E. Campos, D. Chambers, R.A. Feely, S. Gulev, G.C. Johnson, S.A. Josey, A. Kostianoy, C. Mauritzen, D. Roemmich, L.D. Talley and F. Wang, 2013: Observations: Ocean. In: Climate Change 2013: The Physical Science Basis. Contribution of Working Group I to the Fifth Assessment Report of the Intergovernmental Panel on Climate Change [Stocker, T.F., D. Qin, G.-K. Plattner, M. Tignor, S.K. Allen, J. Boschung, A.

Nauels, Y. Xia, V. Bex and P.M. Midgley (eds.)]. Cambridge University Press, Cambridge, United Kingdom and New York, NY, USA.

Riccardi, A., Kump, L.R., Arthur, M.A., and D'Hondt, S. 2007. Carbon isotopic evidence for chemocline upward excursions during the end-Permian event. Palaeogeography, Palaeoclimatology, Palaeoecology, v. 248, p. 73-81.

Stanley, S.M. and Yang, X. 1994. A double mass extinction at the end of the Paleozoic Era. Science, v. 266, p. 1340-1344.

Stanley, S.M. 2009. Evidence from ammonoids and conodonts for multiple Early Triassic mass extinctions. PNAS, v. 106, p. 15264-15267.

Sobolev, S.V., Sobolev, A.V., Kuzmin, D.V., Krivolutskaya, N.A., Petrunin, A.G., Arndt, N.T., Radko, V.A., and Vasiliev, Y.R. 2011. Linking mantle plumes, large igneous provinces and environmental catastrophes. Nature, v. 477, p. 312-316.

Song, H., Wignall, P.B., Chen, Z.-Q., Tong, J., Bond, D.P.G., Lai, X, Zhau, X., Jiang, H., Yan, C., Niu, Z., Chen, J., Yang, H., and Wang, Y. 2011. Recovery tempo and pattern of marine ecosystems after the end-Permian mass extinction. Geology, v. 39, p. 739-742.

Sun, Y., Joachimski, M.M., Wignall, P.B., Yan, C., Chen, Y., Jiang, H., Wang, L., and Lai, X. 2012. Lethally hot temperatures during the Early Triassic greenhouse. Science, v. 338, p. 366-370.

Svensen, H.H., Frolov, S., Akhmanov, G.G., Polozov, A.G., Jerram, D.A., Shiganova, O.V., Melnikov, N.V., Iyer, K., Planke, S., 2018. Sills and gas

generation in the Siberian Traps. Philosophical Transactions of the Royal Society A: Mathematical, Physical and Engineering Sciences, v. 376, 20170080.

Totten, M.W., Hanan, M.A., and Weaver, B.L. 2000. Beyond whole-rock geochemistry of shales: The importance of assessing mineralogic controls for revealing tectonic discriminants of multiple sediment sources for the Ouichita Mountain flysch deposits. GSA Bulletin, v. 112, p. 1012-1022.

van Breugel, Y., Schouten, S., Paetzel, M., Ossebaar, J., Sinninghe Damsté. Reconstruction of $\delta^{13}C$ of chemocline CO_2 (aq) in past oceans and lakes using the $\delta^{13}C$ of fossil isorenieratene. Earth and Planetary Science Letters, v. 235, p. 421-434.

Varga A., Szakmány, G., Árgyelán, T., Józsa, S., Raucsik, B., and Máthé, Z. 2007. Complex examination of the Upper Paleozoic siliciclastic rocks from southern Transdanubia, SW Hungary—mineralogical, petrographic, and geochemical study. In: Sedimentary Provenance and Petrogenesis: Perspectives from Petrography and Geochemistry (Eds J. Arribas, S. Critelli and M.J. Johnsson), GSA Spec. Paper, 420, 73-93.

Chapter 4: Clinoform identification and correlation in fine-grained sediments: A case study using the Triassic Montney Formation

Introduction

Correlation of thick, fine-grained lithological successions often poses challenges that are commonly not resolvable through traditional stratigraphic techniques. These include: (i) minimal grain-size variation; (ii) lateral changes in unit thicknesses tied to structural features; (iii) differential subsidence and the occurrence of broad internal clinoforms; and (iv) the occurrence of local and regional unconformities. Elemental chemostratigraphy provides a solution to these challenges by identifying lithological changes that are not apparent under direct observation, and in recent years it has been shown to be an invaluable tool for stratigraphic correlation in a number of successions (e.g. North et al., 2005; Hildred et al., 2010; Wright et al., 2010; Ratcliffe et al., 2015). Questions pertaining to regional anoxia (Retallack et al., 1997; Algeo et al., 2004; Ratcliffe et al., 2012), productivity (e.g. Hays et al., 2007), sediment provenance and source (Armstrong-Altrin et al., 2004; Pearce et al., 2005), as well as palaeoclimate (Armstrong- Altrin et al., 2004; Ratcliffe et al., 2010), have also been successfully investigated using chemostratigraphy.

Despite the wide applicability of chemostratigraphic analysis, it has largely been underutilized in identifying and correlating chronostratigraphic surfaces (such as clinoforms). This paper outlines the application of chemostratigraphic analysis for determining chronostratigraphic surfaces in fine-grained sediments, using the Lower Triassic Montney Formation of Western Canada as an example. The Montney

Formation is a fine-grained, locally organic-rich formation deposited over a wide range of sedimentary environments, from the proximal to distal clastic ramp.

Traditional methods of stratigraphic correlation often focus on lithology and fossil content; however, this method can be challenging in units of apparent lithological homogeneity (such as in thick shale or siltstone successions), especially when fossil evidence is sparse. Analysing chemical trends allows for the identification of subtle mineralogy-based variations that cannot typically be identified by traditional correlation techniques. Geochemical proxies for clay input can be analysed alongside proxies for sediment provenance, mineralogy and detrital influx. This provides a stratigraphic context that allows for genetically related deposits to be correlated.

The determination of provenance or redox specific information requires the use of specific elemental relationships or 'proxies', which can be selected based on demonstrated correlation with specific factors, such as the effects of oxidation state on the formation/alteration of some mineral components (e.g. Wedepohl, 1971; Arthur et al., 1990; Calvert & Pedersen, 1993; Algeo et al., 2004; Algeo & Lyons, 2006; Kendall et al., 2011; Asael et al., 2013; Chappaz et al., 2014; Reinhard et al., 2014; Planavsky et al., 2014), known effects of trace element sequestration due to biological activity and organic matter (e.g. Berner & Westrich, 1985; Rabouille & Gaillard, 1991; Fein et al., 1997; Tribovillard et al., 2006; Lalonde et al., 2008; Anbar & Rouxel, 2007; Gadd, 2010; Liermann et al., 2011; Liang et al., 2013; Pokrovsky et al., 2014), the influence of weathering, palaeogeography and palaeoclimate on mineralogy (e.g. Plank & Langmuir, 1998; Preston et al., 1998; Pearce et al., 1999,

2010; Hofmann et al., 2001; Hofer et al., 2013; Clift et al., 2014; Ratcliffe et al., 2015), the unique compositional signature of mafic/felsic/ultramafic source rocks (e.g. Reategui et al., 2005) and diagenetic reactions (e.g. Froelich et al., 1979; Morton, 1985; Curtis et al., 1986; Canfield et al., 1993).

The overarching goal of this work is a consistent, regional correlative framework of the Triassic Montney Formation. Geochemical elements and ratios used in this study were chosen to reflect indicators that are not: (i) heavily influenced by processes such as oxidation state (which can vary with water depth as well as with diagenesis); and (ii) palaeoproductivity (which can vary geographically). As such, this study used various elemental ratios, including: (i) clay indicators (Cr/Sc, Zr/La, Zn/Sc, SiO_2 / Al2 O3 , Ga/Rb, K2 O/Al2 O3 , K2 O/Rb, Na2 O/Al2 O3 and Rb/Al; Plank & Langmuir, 1998; Preston et al., 1998; Pearce et al., 1999, 2010; Hofmann et al., 2001; Hofer et al., 2013; Clift et al., 2014; Ratcliffe et al., 2015); (ii) detrital input and sediment recycling indicators (TiO_2 /Al2 O3 , TiO_2 / K2 O, Lu/Hf and Sc/Zr; Dean et al., 2002; Croudace et al., 2006; Cuven et al., 2010; Ratcliffe et al., 2006); (iii) provenance indicators (Ni/Al, Cr/Al, Th/Sc, Ti/Zr, MgO/Al2 O3 and Ti/Nb; Amorosi et al., 2007; Dinelli et al., 2007); and (iv) mineralogical indicators (P2 O5 /Al2 O3 and Cr/Nb, Lu/Zr and Cr/Zr; Bhatia & Crook, 1986; Morton & Hallsworth, 1994; Cingolani et al., 2003; Ratcliffe et al., 2004, 2006; Wright et al., 2010; Clift et al., 2014). Some elements used, such as Fe, S, U and P, are redox-sensitive and palaeoproductivity indicators. However, in this study, these elements were analysed in the context of mineralogical and hydrothermal indicators only.

By utilizing these geochemical proxies, this paper outlines correlative chemostratigraphic packages, herein referred to as 'chemofacies', within the Montney Formation and ties them to well logs. Additionally, conodont analyses published by Golding et al. (2014) and Orchard & Tozer (1997), on outcrop and one of the wells used in this study, anchor the geochemical data set of the current study to the existing regional biostratigraphic framework. The identification and correlation of these geochemically distinct packages reveals regional clinoform surfaces within the Montney Formation and provides an initial template for developing regionally consistent stratigraphic and palaeogeographic models for other fine-grained successions. Elemental correlations, analysed through Pearson product moment correlation analysis (PPMC) and eigenvector analysis (EA), support mineralogical data obtained using X-ray diffraction (XRD). When combined with geochemical proxies for provenance, mineralogy, clay and detrital input, these observations highlight trends in sediment sourcing, relative sea-level, climatic effects and identify intervals of inferred hydrothermal input to the basin.

Geological Setting

Within the Western Canada Sedimentary Basin (WCSB), the earliest Triassic deposits in the subsurface are assigned to the Montney Formation. The Montney Formation was deposited on the western margin of Pangaea (eastern Panthalassa margin) and is thickest in the area of the Peace River Embayment (the Peace River Basin) (Fig. 1; Davies et al., 1997). The Peace River Embayment is a broad

structural basin formed during the Carboniferous as a result of the collapse of the Peace River Arch, a structural Precambrian high that remained emergent until the end of the Devonian (Richards et al., 1994; Davies et al., 1997; Moslow & Davies, 1997). During the Early Triassic, Western Canada was rotated approximately 30° clockwise from its current orientation, with the regional shoreline trend approximately parallel to the axis of the modern Rocky Mountains (Golonka et al., 1994; Davies, 1997; Golonka & Ford, 2000).

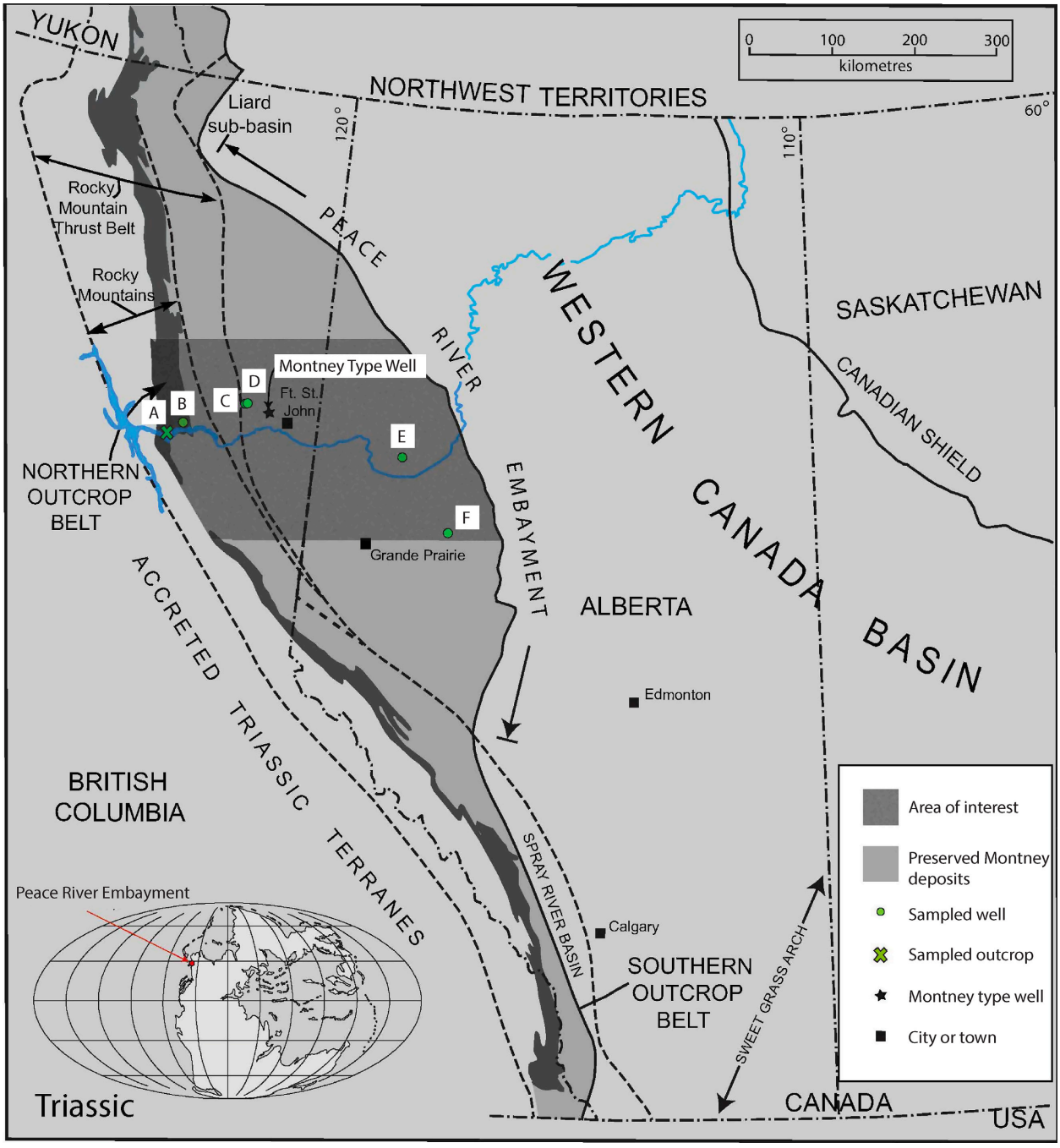

Figure 1: Palaeogeographic map outlining the location of all sample sets. Map after Zonneveld et al. (2011) and Blakey (2006). Sample locations are denoted by circles, an outcrop location is shown by an 'x', and the type well is also marked. Locations of sample sets are as follows: (A) Ursula Creek outcrop; (B) 16-17-083-25W6; (C) c-74-G/ 94-B-9; (D) d-48-A/94-B-9; (E) 11-20-082-02W6; and (F) 2-30-070-24W5.

The Montney Formation is ca. 300 m thick and extends over 150 000 km^2 of north-eastern British Columbia and west-central Alberta (Edwards et al., 1994). It consists of siltstone, sandstone and coquina deposited in environments that range from shoreface to distal offshore, including turbidites (Davies et al., 1997; Moslow & Davies, 1997; Dixon, 2000; Moslow, 2000; Utting et al., 2005; Hays et al., 2007; Zonneveld et al., 2010a). Within the study area, the Montney Formation is unconformably overlain by the Doig Formation and unconformably underlain by the Belloy Formation.

Previous stratigraphic analyses of the Montney Formation have focused on traditional core and well log correlations supported by limited biostratigraphic (conodont) data (Zonneveld et al., 2007; Beatty et al., 2008; Zonneveld et al., 2010a,b; MacNaughton & Zonneveld, 2010; Golding et al., 2014; Sanei et al., 2015; Wood et al., 2015). Temporal constraints on Montney deposition are limited to biostratigraphic analyses in outcrop and subsurface, and demonstrate that deposition occurred from the start of the Triassic (250 Mya) to the Anisian (247 Mya; e.g. Tozer, 1994; Paull et al., 1997; Utting et al., 2005; Orchard & Zonneveld, 2009; Zonneveld et al., 2010a; Golding et al., 2014). Although palynomorphs, bivalves and ammonoids have proven useful in some studies (e.g. Tozer, 1994; Utting et al., 2005), conodont biostratigraphy is the most effective, provided that sufficient material is available to produce diagnostic elements (Paull et al., 1997; Orchard & Zonneveld, 2009; Golding et al., 2014). To this end, the key well used for this study (UWI 16-17-083-25W6; full core) has been lithologically described and dated using conodont analysis (Golding et al., 2014).

Methods

A total of 641 samples were analysed and include core samples (wells c-74-G/94-b-09, d-48-A/94-b-09, 2-30-070-24W5, 16-17-083-25W6 and 11-20-082-02W6) and outcrop samples (Ursula Creek, British Columbia; Fig. 1). The wells and outcrop were chosen to create a transect perpendicular to the Triassic palaeoshoreline. Samples from these locations were analysed using Thermo Scientific XSERIES 2 ICP-MS and iCAP 7000 Series ICP-OES (Thermo Fisher Scientific, Waltham, MA, USA) at Chemostrat and a Perkin Elmer ICP-MS and Spectro ICP-OES (Perkin Elmer, Waltham, MA, USA) at Bureau Veritas Mineral Laboratories. Additionally, one data set, 2-30-070-24W5, was analysed using a Bruker AXS D8 Advance Diffractometer (Bruker, Billerica, MA, USA) at SGS Mineral Services in Lakefield, Ontario.

A statistical evaluation of the correlation between mineralogical and elemental data was conducted using PPMC and EA on DataDesk 6.3.1 (Data Description Inc., Ithaca, NY, USA). Additionally, chemostratigraphic packages were defined using principal component analysis and cluster analysis on the most complete core data set (16-17-083-25W6), which was used as the type section. In total, 84 variables were considered (Table 1). The variables used fall into eight categories: (1) oxides; (2) unaltered trace element data provided by the analytical laboratories; (3) oxide elements, with the calculated elemental portion of the oxides converted to ppm; and (4) to (8) indicators, comprised of ratios of elements or oxides.

Chemofacies were then analysed and summarized using clay indicator ratios (Cr/Sc, Zr/La, Zn/Sc, SiO_2/Al_2O_3 , Ga/Rb, K_2O/Al_2O_3, K_2O/Rb, Na_2O/Al_2O_3 and Rb/Al), provenance indicator ratios (Ni/Al, Cr/Al, Th/Sc, Ti/Zr, MgO/Al_2O_3 and Ti/Nb), detrital input indicators (TiO_2/Al_2O_3, TiO_2/K_2O, Lu/Hf and Sc/Zr) and mineralogical indicators (P_2O_5/Al_2O_3, Cr/Nb, Lu/Zr and Cr/Zr). An average value of each ratio was determined from the type section. These overall average values were compared to the averaged values generated from within each chemofacies in order to make broad interpretations. Due to the low elemental immobility, and the relation to detrital input, subsequent data sets were correlated primarily using the signatures of Sc/Zr, Lu/Hf and Zr/La (see the Elemental indicators section below for a more detailed explanation of the ratios used in this study). For a detailed methodology, refer to the Data S1 (located in Appendix 2).

Elemental indicators

Clay indicators

Some elemental ratios, for example Ga/Rb, are interpreted to reflect the proportion of kaolinite to illite (Ratcliffe et al., 2010, 2015; Hofer et al., 2013) because kaolinite is a major carrier of Ga (Wang et al., 2011; Dai et al., 2012a). Although K/Rb can reflect weathered versus volcanoclastic input (Plank & Langmuir, 1998), when compared to the ratio K_2O/Al_2O_3; K/Rb can also indicate high illite content (i.e. low values of K/Rb paired with high K_2O/Al_2O_3 indicate high illite content; Ratcliffe et al., 2006, 2015; Hofmann et al., 2001; Hofer et al., 2013). Additionally, high Rb/Al_2O_3

ratio values indicate high proportions of illite and mica with little kaolinite (Pearce et al., 2005). The ratio of Na/Al can act as a proxy for smectite content (Hofmann et al., 2001; Hofer et al., 2013). Chromium is associated with chlorite while Sc is associated with kaolinite (Ratcliffe et al., 2015). In general, Sc and Ga are observed to correlate with light rare earth elements (LREE) and Al in kaolinite, although Ga has been observed to adsorb onto illite and montmorillonite under certain pH conditions and can be associated with Cr-spinels (Esser et al., 1991; Paktunc & Cabri, 1995; Takahashi et al., 1999; Hofmann et al., 2003; Tyler, 2004; Dai et al., 2006, 2008, 2012a,b; Pearce et al., 2010; Wang et al., 2011; Benedicto et al., 2014). The ratio of Zr/La can indicate clay and mica content because Zr is often associated with heavy minerals such as garnet and zircon, while La is often bound in the clay and mica fraction (Plank & Langmuir, 1998; Preston et al., 1998; Pearce et al., 1999, 2010). For example, ratios such as Zr/La can be used to assess for elemental dilution (Preston et al., 1998). Pearce et al. (1999) discussed the need to account for elemental dilutions due to elements of a more detrital nature (for example, Si and Al) being 'diluted' in zones that have been highly cemented by carbonate. By comparing the Zr/La ratio to geochemical proxies for carbonate input (such as Ca, Sr and Mg), the dilution effect can be investigated. Because illite fixes Zn much more readily into its structure than kaolinite (Reddy & Perkins, 1974) and Sc (along with Ga) is often sequestered with other REE and Al into kaolinite (Esser et al., 1991; Paktunc & Cabri, 1995; Takahashi et al., 1999; Hofmann et al., 2003; Tyler, 2004; Dai et al., 2006, 2008; Pearce et al., 2010; Wang et al., 2011; Dai et al., 2012a,b; Benedicto et al., 2014), the ratio of Zn/Sc, in the context of other clay proxies, can be used to determine illite/kaolinite proportions (Pearce et al., 1999). Similarly, the

TiO_2/K_2O ratio is representative of the amount of anatase relative to illite (Ratcliffe et al., 2006).

Category	Number of variables
Oxides	10
Oxide Elements	10
Trace Elements	40
Clay Indicators	7
Provenance Indicators	5
Detrital Indicators	4
Mineral Indicators	6
Grain-size Indicators	2
All data	84

Table 1: Summary of the variables used in principal component analysis cluster analysis.

Detrital indicators

Perhaps the most commonly used, the TiO_2/Al_2O_3 ratio can indicate specific sediment flux, in this case aeolian input and also detrital flux associated with relative sea-level change (Chen et al., 2013). Additionally, sediment recycling concentrates heavy minerals, especially zircon, in the sediment, allowing for ratios such as Sc/Zr to be used to indicate the relative intensity of sediment recycling (McLennan et al., 1993; Mongelli et al., 2006). Likewise, the ratio of Lu/Hf, because of the higher concentration of Hf in zircons, can indicate continental shelf versus pelagic clay deposits (Patchett et al., 1984; Plank & Langmuir, 1998). Because the mineralogical products of weathering are often higher in K content, while Ti content largely remains

unchanged during weathering, the ratio of TiO_2/K_2O can be used to determine the relative input of weathered material into the basin over time (Wei et al., 2003).

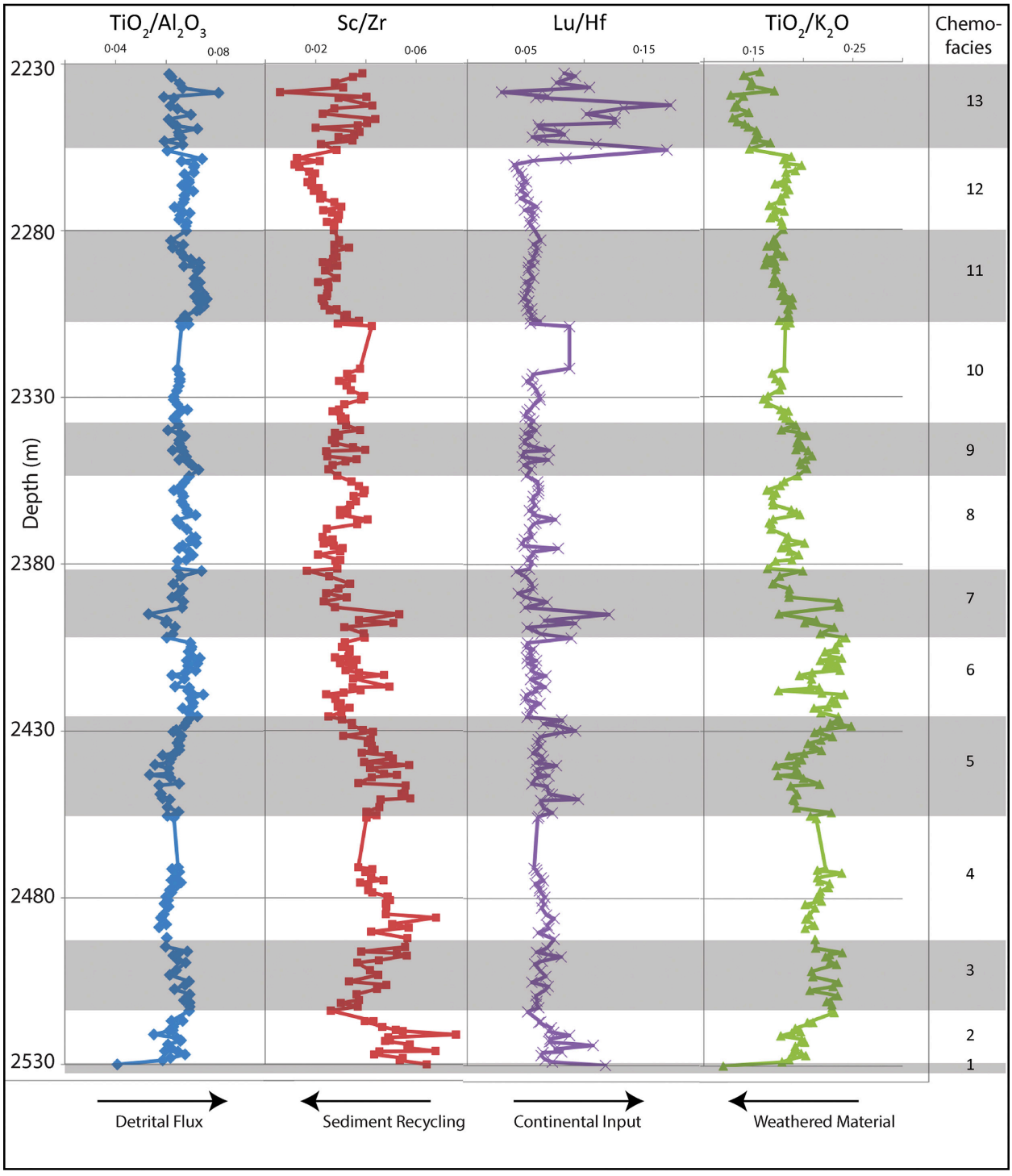

Figure 2: Detrital indicator profiles for well 16-17-083-25W6. Depths are in metres. Chemofacies are numbered from 1 to 13 (right). Simplified interpretations of concentrations are labelled at the base with arrows. For references, refer to the Elemental indicators section in the text.

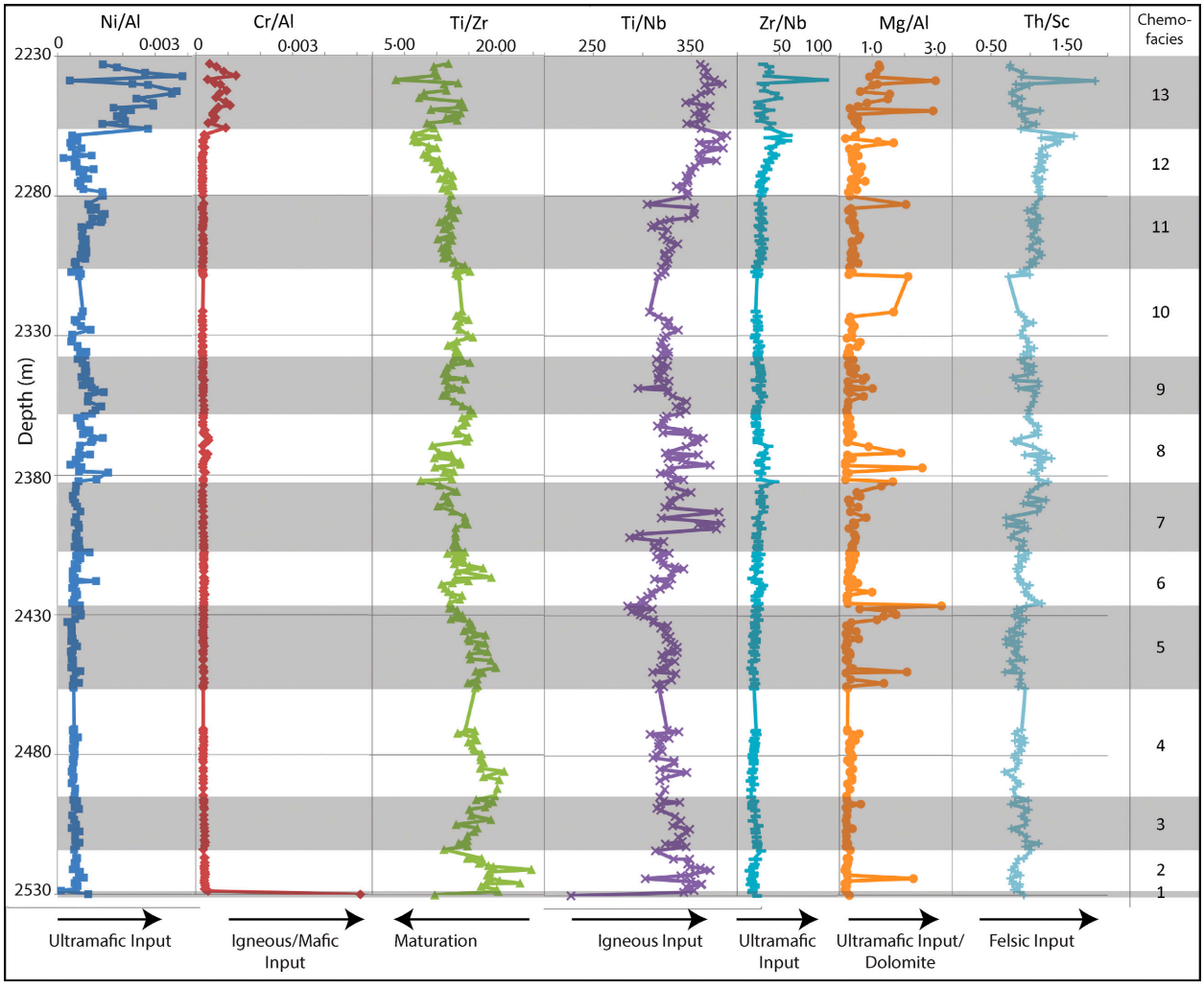

Figure 3: Provenance indicator profiles for well 16-17-083-25W6. Depths are in metres. Chemofacies are numbered from 1 to 13 (right). Simplified interpretations of concentrations are labelled at the base with arrows. For references, refer to the Elemental indicators section in the text.

Provenance indicators

Ratios, such as Cr/Al and Ni/Al, are uninfluenced by grain-size changes (Dinelli et al., 2007). Because Cr can be associated with both heavy minerals and clays (Meinhold et al., 2007), the ratio Cr/Al can indicate Cr enrichment associated with heavy minerals sourced from igneous rocks (Preston et al., 1998; Ratcliffe et al., 2004; Wright et al., 2010). Likewise, an excess of Ni relative to Al can indicate ultramafic provenance (Amorosi et al., 2007). Zirconium/Niobium has been demonstrated to indicate ultramafic igneous input, with Nb being associated with Nb-rich rutile (Ratcliffe et al., 2006). High values of Th/Sc are interpreted as resulting from felsic sediment components, with Th/Sc having been used as a measure of the degree of igneous differentiation (McLennan et al. 1990, 1993; Hofmann et al., 2003; Lopez de Luchi et al., 2003; Bracciali et al., 2007). The ratio Mg/Al (normalized to account for grain-size variation) can indicate ultramafic input or dolomite when associated with Ca (Amorosi et al., 2007; Dinelli et al., 2007). This ratio has also been demonstrated to indicate Mg-rich clay (for example, palygorskite) input in deposits related to the Negev loess (Israel et al., 2015). Additionally, Ti/Nb has been demonstrated to indicate igneous input and has been linked to intraplate settings with basaltic volcanism (Bonjour & Dabard, 1991). The ratio of Ti/Zr has been demonstrated to distinguish turbidites from various tectonic sources and can (when plotted against La/Sc) reveal the tectonic setting of the sediment (Bhatia & Crook, 1986; Cingolani et al., 2003).

Mineralogical indicators

In terms of trace element abundance, Ti, Nb and Ta are related to the presence of heavy minerals (foremost rutile, but also anatase, ilmenite and leucoxene; Pearce et al., 2010). Niobium is associated with Ti in rutile (Preston et al., 1998), and therefore, the TiO_2/Nb ratio can be used to account for rutile-associated Nb. Iron has been linked to the presence of Fe-oxyhydroxides (for example, goethite), pyrite and/or ferroan dolomite (Pearce et al., 2010). Calcium, Mg, Mn and Sr are generally associated with carbonate minerals (for example, calcite, dolomite and siderite; Pearce et al., 2010). In addition to feldspar, Na can be present in the clay fraction as well as in halite (Pearce et al., 2005, 2010). The concentrations of K, Rb and Cs are controlled primarily by the amount of illite and mica present (Pearce et al., 2010). The deposition of P in sediments is related to multiple factors including palaeoproductivity and hydrothermal flux (Feely et al., 1994; Wheat et al., 1996; Tribovillard et al., 2006). Because of the co-occurrence with organic matter, phosphorous is often present in association with clays and can indicate the presence of biogenic phosphatic fish remains and calcareous microfossils (Pearce et al., 2010). When present with Fe, Mn and REE, the presence of P has been linked to siderite (Pearce et al., 2010). Substitutions within apatite include Y and REE for Ca, with Sr balancing the remaining charge (Preston et al., 1998). Chromium (III) occurs within spinel, often substituting for Al (III) or Fe (III) (Preston et al., 1998). Chromium-spinel is found in primitive basic igneous rocks and ultrabasic igneous rocks (Preston et al., 1998). The similar ionic radii of Nb and Ti allow the former to substitute into the

crystal lattice of Ti-bearing minerals such as ilmenite and rutile; however, Nb-rich rutile is generally restricted to ultramafic, alkaline, igneous rocks (Preston et al., 1998). Therefore, the ratio of Cr/Nb can be used to estimate the abundance of Ti-oxide heavy minerals and is thought to reflect variation in the abundance of Ti-oxide heavy minerals with respect to spinel (Ratcliffe et al., 2015). The ratio of Lu/Zr is closely related to the garnet/zircon index (GZi index) and reflects the proportion of garnet to zircon (Wright et al., 2010). The GZi index has been used to fingerprint unique heavy mineral populations related to different sandstone types, which reflect overall lithological differences (Morton & Yaxley, 2007). Likewise, Cr/Zr is a proxy for the chrome-spinel/zircon index (CZI index), which is another provenance-sensitive ratio (Morton & Hallsworth, 1994; Ratcliffe et al., 2006; Morton & Yaxley, 2007; Wright et al., 2010).

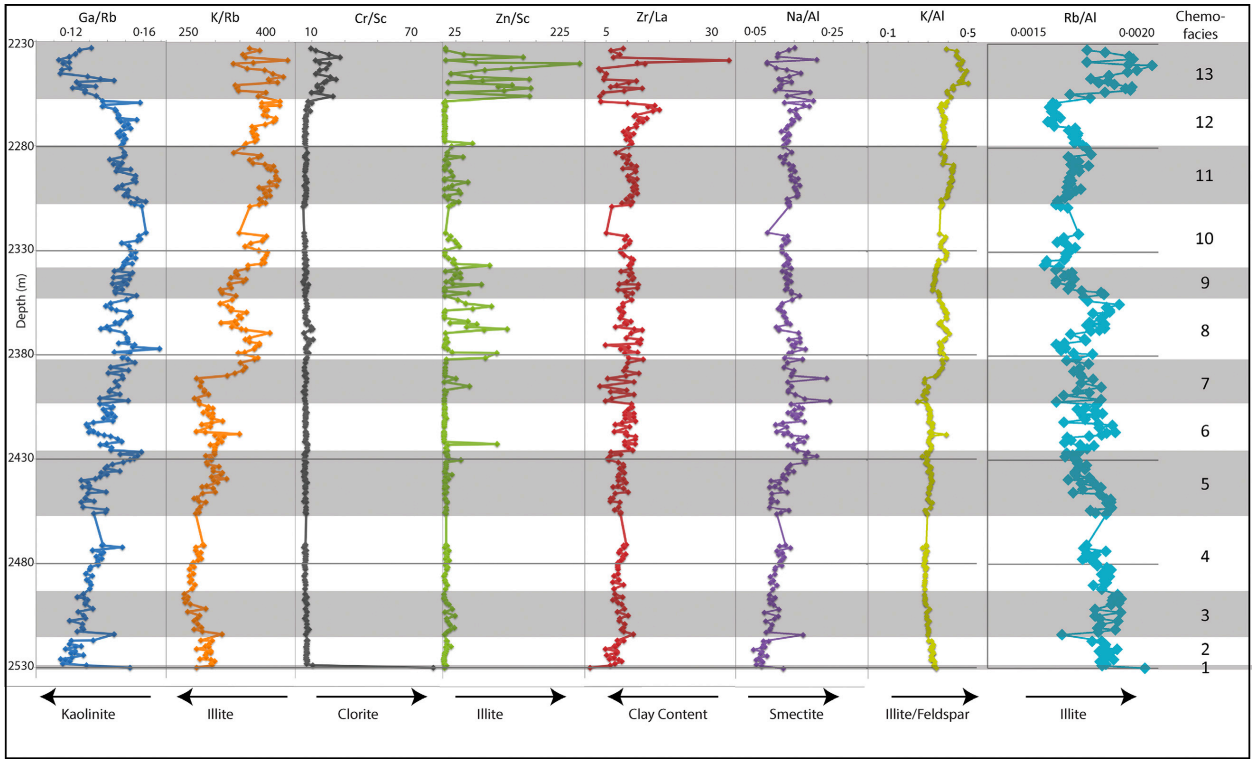

Figure 4: Clay indicator profiles for well 16-17-083-25W6. Depths are in metres. Chemofacies are numbered from 1 to 13 (right). Simplified interpretations of concentrations are labelled at the base with arrows. For references, refer to the Elemental indicators section in the text.

Results and Interpretation by Category

Chemofacies descriptions

Results

Thirteen chemofacies were recognized based on differences in the abundances of major oxides, trace elements and elemental ratios. Twelve packages were first identified and defined in the most complete sample set (16-17-083-25W6; Figs 2 to

5) using cluster and principal component analyses; although only occurring in the basal data point (and thus statistically insignificant), a thirteenth division was added based on the published contact between the Permian Belloy Formation and the Montney Formation in this data set (Golding et al., 2014). Chemofacies are herein defined as distinct bodies of rock characterized by a particular combination of stable isotopic signatures, oxide elemental patterns, trace element signatures or element ratios dependent on underlying mineralogical controls and organic matter that distinguish them from surrounding strata. The chemofacies identified in this study are labelled in stratigraphic order, beginning at the base. Numerical values for each chemical ratio were averaged for the entire 16- 17-083-25W6 data set; this average was compared to the calculated average value for each chemofacies in Tables 2 to 5.

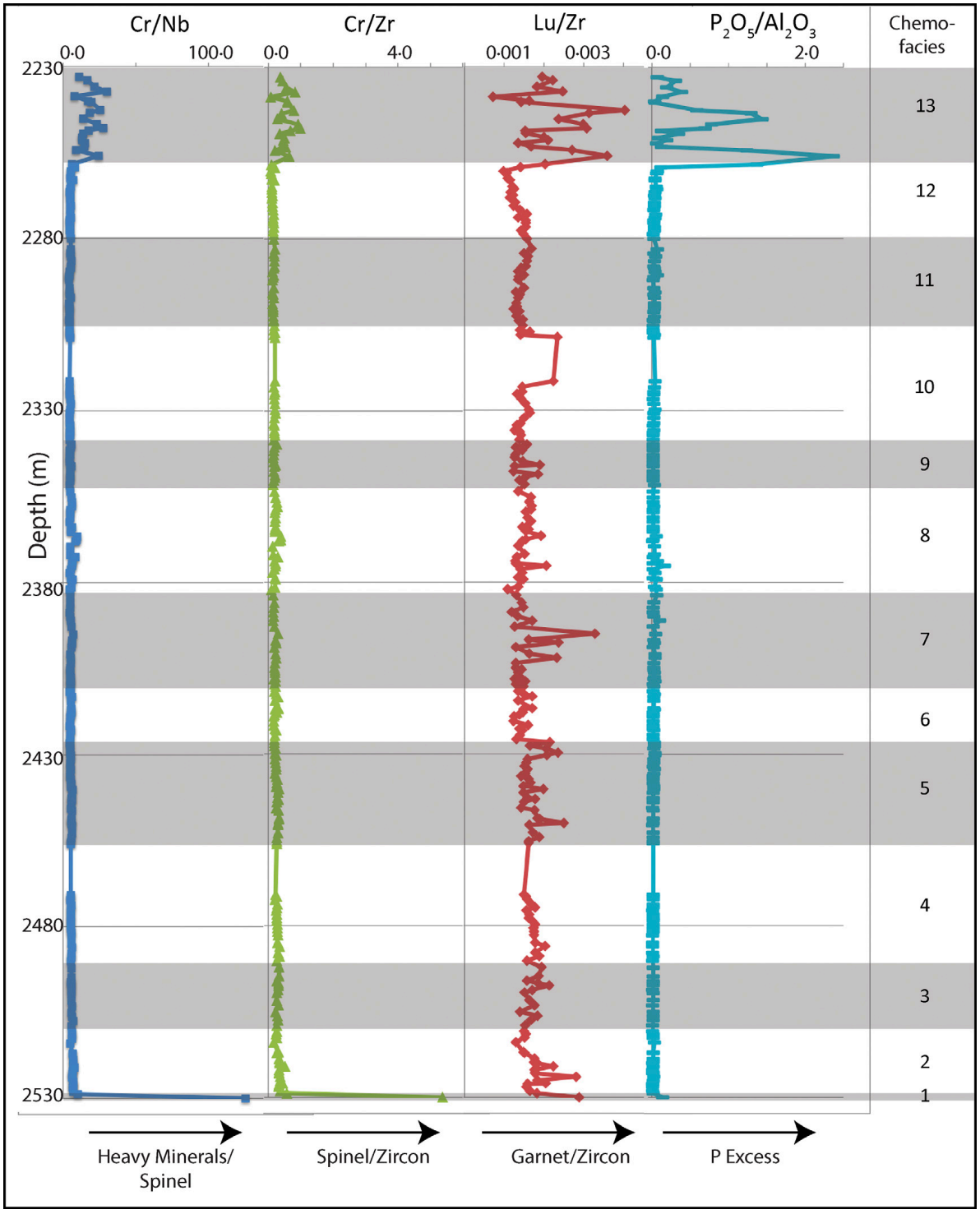

Figure 5: Mineralogical indicator profiles for well 16-17-083-25W6. Depths are in metres. Chemofacies are numbered from 1 to 13 (right). Simplified interpretations of concentrations are labelled at the base with arrows. For references, refer to the Elemental indicators section in the text.

Interpretation

Average values displayed in Tables 2 to 5 were used to guide the interpretation of each chemofacies, the details of which are listed in Table 6. These interpretations highlight perceived changes in clay content throughout the sample set; namely, chemofacies 1 to 5 show high clay input, with low smectite and kaolinite content and greater amounts of illite (Fig. 4). Within chemofacies 5, there is a shift to high smectite content and, by chemofacies 7, a switch from generally high to low clay content. Additionally, illite is replaced by kaolinite and smectite as the more abundant clay phases. Chlorite appears in higher than average proportions in chemofacies 1 (Belloy Formation) and chemofacies 13 (Doig Formation).

Chemostratigraphic correlation

Results

Correlation between wells reveals the presence of various chemofacies within each well or outcrop sample set. Data sets were correlated with the type well using proxy ratios for detrital flux (Sc/Zr and Lu/Hf) and clay input (Zr/La), which should not be affected by fluctuations in redox conditions or diagenesis. Detailed correlation of each data set is visible in Figs S1 to S20; additional supplementary figures illustrate points of correlation between the type data set and each additional well (Figs S21 to S25; see Appendix 2), as well as lithologues for four data sets (Figs S26 to S29; see Appendix 2).

Interpretation

Data from Ursula Creek were found to correspond with all 13 defined chemofacies (Fig. 6). Wells d-48-A/94-B-9 and c-74-G/94-B-9 were found to contain chemofacies 8, 9, 10 and a small portion of 11. This suggests that an unconformity is present, with erosion having removed most of chemofacies 11, and all of chemofacies 12. Data from well 11-20-82-2W6 were found to correspond to chemofacies 2 and 3. Well 2-30- 70-24W5 was interpreted to correspond to chemofacies 1, 2, 3, 7 and 8. Both wells 11-20- 82-2W6 and 2-30-70-24W5 are missing chemofacies 9 to 12, which suggests erosion, and have thicker lower chemofacies. Thicker lower chemofacies in the eastern data sets (wells 11- 20-82-2W6 and 2-30-70-24W5) suggests clinoform deposition from the east. Correlatable conodont intervals, as previously described by Golding et al. (2014) and Orchard & Tozer (1997), occur in chemofacies 7 (well 16-17-083-25W6 and Ursula Creek; Fig. 6). The precise horizons from which the conodont samples were obtained are indicated on the sections identified herein. These samples provide a means of calibrating the chemofacies with the global integrated ammonoid-conodont biostratigraphic zonation, which is based in large part on the British Columbia Triassic succession (Tozer, 1994; Orchard & Tozer, 1997; Orchard & Zonneveld, 2009; Golding et al., 2014). Additionally, P/Fe data from wells 16-17-083-25W6, d-48-A/94-B-9, c-74-G/94-B-9, and the outcrop Ursula Creek all indicate high P/Fe within chemofacies 7 and 8, which supports the interpreted correlations.

Elemental associations and mineralogy

Results

The PPMC for each oxide and element was calculated to determine mineralogical associations for each core and the Ursula Creek outcrop (Table 7 and Tables S1 to S6; Appendix 2). Values exceeding +/-0.8 were considered to represent strong positive or negative correlations, where a value of +/-1 implies perfect positive or negative correlation (Deutsch, 2002). Elements that have a high correlation with one another include SiO_2, Al_2O_3, TiO_2 and K_2O (referred to as the silicate oxides). CaO correlates negatively with SiO_2 and positively with MnO and MgO. Of note, Th, Ta, Nb, Rb, Ga and Sc share a high PPMC with the SiO_2 and negatively correlate with CaO. Nickel and barium also correlate positively with K_2O. Hafnium correlates well with Na_2O and Zr. As would be expected, the REE correlate strongly with one another.

Chemofacies		Ti/Al	Sc/Zr	Lu/Hf	Ti/K
13	Max	0·080849	0·043779	0·173555	0·170706
	Min	0·059138	0·005979	0·029456	0·127007
	Avg	0·064859	0·031454	0·092964	0·145504
12	Max	0·074222	0·030399	0·084082	0·198194
	Min	0·063336	0·011721	0·039973	0·165484
	Avg	0·068147	0·02187	0·051852	0·179885
11	Max	0·076006	0·037303	0·062728	0·18926
	Min	0·06199	0·021035	0·047911	0·161212
	Avg	0·070189	0·027035	0·054473	0·176587
10	Max	0·068321	0·042413	0·087519	0·186066
	Min	0·063022	0·026862	0·049446	0·159848
	Avg	0·064733	0·033378	0·05982	0·17563
9	Max	0·072897	0·039814	0·070306	0·208827
	Min	0·060782	0·024184	0·047167	0·178039
	Avg	0·0666	0·03026	0·054408	0·197164
8	Max	0·071875	0·040722	0·078009	0·201467
	Min	0·063023	0·021032	0·047175	0·163489
	Avg	0·067303	0·031435	0·057197	0·178699
7	Max	0·073922	0·053382	0·120945	0·243106
	Min	0·053016	0·016499	0·041868	0·169261
	Avg	0·063546	0·033181	0·064096	0·203927
6	Max	0·07461	0·049462	0·067065	0·2409
	Min	0·062391	0·024333	0·049591	0·175265
	Avg	0·069363	0·033184	0·055683	0·221709
5	Max	0·068878	0·057641	0·094791	0·24838
	Min	0·053437	0·030539	0·055284	0·172797
	Avg	0·062174	0·043994	0·06734	0·205108
4	Max	0·065819	0·067887	0·074359	0·238807
	Min	0·057334	0·037093	0·056949	0·201989
	Avg	0·061495	0·04671	0·064463	0·21512
3	Max	0·069375	0·056266	0·080454	0·239093
	Min	0·059928	0·026031	0·051332	0·206833
	Avg	0·066101	0·041434	0·063167	0·224788
2	Max	0·06739	0·07577	0·107734	0·2096
	Min	0·055197	0·039477	0·061322	0·177362
	Avg	0·062575	0·052278	0·073085	0·194342
1	Max	0·040829	0·064328	0·118158	0·119407
	Min	0·040829	0·064328	0·118158	0·119407
	Avg	0·040829	0·064328	0·118158	0·119407

Table 2: Calculated values for detrital proxy data within each chemofacies, from the type data set (16-17-083-25W6), including maximum, minimum and average values. These values were compared with the overall average values for this data set (TiO_2/Al_2O_3 = 0.0657, Sc/Zr = 0.0353, Lu/Hf = 0.0632 and TiO_2/K_2O = 0.192). Values above the overall average appear in green; values below the overall calculated average appear in red.

Bulk results of the XRD analysis (detection limit: 0.5 to 2.0%) reveal the presence of quartz (42 to 71%), dolomite (3 to 20%), microcline (4 to 15%), muscovite (2 to 16%), albite (2 to 9%), diopside (1 to 4%) and accessory minerals (Table 8). Accessory minerals include pyrite, clinochlore, calcite, ankerite, kaolinite,

chlorapatite, fluorapatite, brookite, siderite and magnesian calcite. Within the XRD sample set, quartz is consistently the most abundant mineral, followed by dolomite.

Chemofacies		Ga/Rb	K/Rb	Rb/Al	Cr/Sc	Zr/La	Zn/Sc	K/Al	Na/Al
13	Max	0·143721	447·1661	0·002095	27·0123	34·03326	256·8932	0·501256	0·208801
	Min	0·11274	336·8972	0·001549	9·426651	3·325384	5·362664	0·391936	0·081105
	Avg	0·124387	383·7705	0·001835	16·78576	8·952996	86·80913	0·447062	0·128345
12	Max	0·158361	431·9538	0·001658	9·953695	17·63911	55·77653	0·395282	0·200057
	Min	0·137179	357·9692	0·001402	5·623236	3·811868	2·442895	0·358246	0·117733
	Avg	0·147251	394·7814	0·00151	6·68064	11·8819	6·694111	0·379022	0·145489
11	Max	0·161331	429·3171	0·00169	7·216126	12·43012	47·05129	0·427444	0·165247
	Min	0·141334	337·661	0·001456	5·381372	7·386836	3·145944	0·363704	0·114875
	Avg	0·150456	401·2225	0·001556	6·291306	10·76913	14·56291	0·397867	0·144111
10	Max	0·161511	406·3616	0·001606	6·886009	11·44016	88·21825	0·394261	0·138733
	Min	0·147946	348·6106	0·001379	4·760351	5·077812	3·897445	0·345093	0·081716
	Avg	0·154281	387·0522	0·001498	5·86343	9·482	19·74178	0·369222	0·126461
9	max	0·156148	365·6342	0·001775	8·013681	12·59312	72·27645	0·357709	0·164609
	Min	0·14279	310·5874	0·001454	4·635608	7·80944	3·236714	0·321905	0·119659
	Avg	0·148344	336·7473	0·001578	6·207366	10·40401	21·79454	0·337878	0·13732
8	Max	0·169069	410·8626	0·001877	10·79284	13·55448	121·1066	0·40682	0·17951
	Min	0·136376	310·1469	0·001458	5·274246	4·878766	2·680357	0·35415	0·104558
	Avg	0·148075	356·5648	0·001667	7·379145	9·950678	34·14526	0·377362	0·135034
7	Max	0·155409	380·0742	0·001757	6·860339	13·8056	49·99996	0·374848	0·242245
	Min	0·1358	257·8504	0·001459	4·866671	3·586812	2·722726	0·247776	0·1242
	Avg	0·146077	305·9059	0·001622	5·982422	8·915995	9·136538	0·315692	0·158982
6	Max	0·147924	349·1123	0·00185	7·454226	11·99854	102·0715	0·391681	0·183252
	Min	0·128235	261·1168	0·001508	5·726949	6·983901	2·207871	0·295087	0·102822
	Avg	0·138522	294·5231	0·001675	6·469519	10·26135	7·895225	0·31384	0·147736
5	Max	0·158948	322·8516	0·001827	7·189465	10·25548	33·83281	0·321791	0·208736
	Min	0·125228	257·0505	0·001516	4·887892	5·392277	3·200026	0·27117	0·087282
	Avg	0·137639	287·0996	0·001665	6·030078	7·830425	7·40361	0·303945	0·129007
4	Max	0·148307	277·1773	0·001821	6·681185	9·828208	12·21662	0·296667	0·141206
	Min	0·127914	247·7709	0·001632	5·15183	6·630656	2·376812	0·272759	0·089285
	Avg	0·133818	260·103	0·001725	5·999295	8·288536	6·640891	0·285709	0·11043
3	Max	0·143752	313·7154	0·00189	8·334991	11·43834	23·26896	0·30733	0·173565
	Min	0·118853	236·9108	0·001496	5·616258	6·609984	2·241635	0·281845	0·074249
	Avg	0·127163	258·9895	0·001789	6·690059	8·627507	9·621217	0·29415	0·097089
2	Max	0·131944	298·7012	0·001862	10·64945	9·230741	15·66155	0·33304	0·085097
	Min	0·113769	262·1804	0·001695	6·436096	4·89438	1·910621	0·303859	0·046013
	Avg	0·121041	284·3407	0·001777	7·147973	7·126561	5·578249	0·322007	0·066654
1	Max	0·152673	262·0636	0·002047	83·4203	1·287697	3·344827	0·341931	0·122736
	Min	0·152673	262·0636	0·002047	83·4203	1·287697	3·344827	0·341931	0·122736
	Avg	0·152673	262·0636	0·002047	83·4203	1·287697	3·344827	0·341931	0·122736

Table 3: Calculated values for clay proxy data within each chemofacies from the type data set (16-17-083-25W6), including maximum, minimum and average values. These values were compared with the overall average values for this data set (Ga/Rb = 0.14, K/Rb = 330.75, Rb/Al = 0.0017, Cr/Sc = 7.629, Zr/La = 9.40, Zn/Sc = 19.1453, K_2O/Al_2O_3 = 0.347 and Na_2O/Al_2O_3 = 0.129). Values above the overall average appear in green; values below the overall calculated average appear in red.

Principal component analyses were conducted on all data sets, and plots of eigenvector one versus two were produced (Fig. 7). Four major, consistent elemental clusters are observed within the plot series. A cluster of elements, termed the heavy element cluster, occurs in the centre and includes Mo, Zn, V, W, Ni and Cr. The REE and Y occur together in all plots and are referred to as the REE+Y cluster. K_2O, Rb, Al_2O_3, Nb, TiO_2, Ga, Ta, Cs, Be and Sc also occur in close association and comprise the Al_2O_3 cluster. MnO, MgO and CaO generally plot very closely together and are defined as the MgO group. Interestingly, in well c-74-G/94-B-9, CaO occurs in a cluster with Sr, P_2O_5 and U, separate from MgO and MnO (Fig. 7F). Na_2O occurs apart from major clusters and is associated with various other elements (Cr, Cu, Sn, Be, Zn, Co, Ni and Pb). TiO_2 clusters with Nb in all plots. Chromium is observed to occur in association with varying elements (Ni, Sr, Ce and Co) but is often isolated from the major clusters (Fig. 7D). Zirconium occurs in close proximity to Hf in all plots. SiO_2 occurs in isolation in the plots for wells 11-20-082-02W6 and 2-30-070-24W5. In the remaining wells and outcrop, SiO_2 occurs in association with the Al_2O_3 cluster. Fe_2O_3 plots with S in the plots for Ursula Creek and wells 16-17-083-25W6, d-48-A/ 94-B-9 and c-74-G/94-B-9. These two elements are closely associated in well 11-20-082-2W6 and plot near the Al_2O_3 cluster. Strontium is often closely associated with CaO (Fig. 7A, C, D and F).

Chemofacies		P_2O_3/Al_2O_3	Cr/Nb	Lu/Zr	Cr/Zr
13	Max	2·36943706	30·15989	0·004026	1·000416
	Min	0·03037241	7·493004	0·000711	0·07288
	Avg	0·52630791	17·57344	0·002212	0·538475
12	Max	1·36807648	7·943239	0·002026	0·214815
	Min	0·02091007	4·533239	0·000977	0·085984
	Avg	0·10384847	5·1276	0·001343	0·143382
11	Max	0·07377165	5·623304	0·001688	0·211382
	Min	0·01811236	4·107049	0·001226	0·134706
	Avg	0·03213233	4·562836	0·001425	0·169215
10	Max	0·04308528	5·175084	0·002334	0·217686
	Min	0·01845087	4·220701	0·001251	0·165229
	Avg	0·02669023	4·602506	0·001551	0·19396
9	Max	0·0303379	5·624254	0·001886	0·258933
	Min	0·01595749	4·372693	0·001228	0·145316
	Avg	0·01931425	4·820874	0·001442	0·18593
8	Max	0·16003218	9·515539	0·002052	0·394119
	Min	0·01197805	4·48655	0·001272	0·128549
	Avg	0·03224329	5·997805	0·001532	0·232964
7	Max	0·1059192	6·692056	0·00328	0·302098
	Min	0·01863884	4·499245	0·001084	0·103786
	Avg	0·03880327	5·303066	0·001662	0·194837
6	Max	0·04269826	5·897517	0·001705	0·31278
	Min	0·01734135	4·57523	0·00123	0·162611
	Avg	0·02498563	5·07693	0·001408	0·214048
5	Max	0·04443363	6·289217	0·002503	0·339965
	Min	0·01384167	4·527507	0·001419	0·186581
	Avg	0·02240069	5·387552	0·001737	0·264026
4	Max	0·01719659	6·095687	0·00202	0·361694
	Min	0·01202611	4·76272	0·001496	0·204941
	Avg	0·01452501	5·393587	0·001709	0·279008
3	Max	0·02954884	6·688537	0·002132	0·329148
	Min	0·01272907	4·693517	0·001284	0·166474
	Avg	0·01623657	5·717874	0·001641	0·273501
2	Max	0·02746657	9·970311	0·002806	0·569048
	Min	0·01136381	6·134519	0·001482	0·271479
	Avg	0·01511607	6·895471	0·001821	0·372473
1	Max	0·14226455	125·4367	0·002883	5·36628
	Min	0·14226455	125·4367	0·002883	5·36628
	Avg	0·14226455	125·4367	0·002883	5·36628

Table 4: Calculated values for mineralogical proxy data within each chemofacies, from the type data set (16-17-083-25W6), including maximum, minimum and average values. These values were compared with the overall average values for this data set (P_2O_5/Al_2O_3 = 0.074, Cr/Nb = 6.86, Lu/Zr = 0.0016 and Cr/Zr = 0.275). Values above the overall average appear in green; values below the overall calculated average appear in red.

Interpretation

Principal component analysis has been an integral tool for assessing the mineralogy in a number of chemostratigraphic studies (e.g. Pearce et al., 2005, 2010). Mineral

affinities identified by this method (Pearce et al., 2010) are presented in Table 9. The close proximity of Hf and Zr in the eigenvector plot suggests the presence of zircon, despite the apparent lack of zircon in XRD analyses. Hafnium, Zr and Cr are also associated with Cr-spinel; however, this phase was also not identified in the XRD data. It is possible that both zircon and Cr-spinel phases are present but at levels below the detection limit for XRD. The co-occurrence of TiO_2, Nb, Ta and Th is explained by the presence of rutile, detected during XRD analysis. The proximity of U and REE to P_2O_5 suggests scavenging of these elements by phosphatic debris. This is consistent with the identification of both fluorapatite and calcium phosphate in XRD analysis.

Al_2O_3 and Ga are associated with kaolinite, while the close proximity of K_2O, Rb and Cs is accounted for by the presence of illite/smectite. Given that K_2O plots much closer to SiO_2 than to Rb and Cs, it is likely that K-feldspar is present in a higher concentration than these clays. This interpretation is supported by the XRD data, which shows high concentrations of microcline (Table 8).

Chemofacies		Cr/Al	Ni/Al	Th/Sc	Mg/Al	Ti/Nb	Ti/Zr
13	Max	0·0062634	0·003836	1·83846	2·9647	381·107	14·24579
	Min	0·00183892	0·000379	0·736019	0·327647	344·0334	3·628724
	Avg	0·00352918	0·002332	0·930637	1·052833	361·2772	10·80156
12	Max	0·00156774	0·001385	1·565226	1·668002	385·6654	12·55644
	Min	0·0009492	0·000179	1·05759	0·187812	334·4731	6·367101
	Avg	0·00110512	0·000719	1·17332	0·547279	356·9861	10·01036
11	Max	0·00124826	0·001443	1·14847	2·044979	352·8925	15·16116
	Min	0·00098372	0·000424	0·869347	0·27982	304·4002	10·17989
	Avg	0·00110716	0·000867	1·04351	0·479136	326·6818	12·12023
10	Max	0·00112522	0·00102	1·056328	2·114342	336·2982	15·57039
	Min	0·00097965	0·000417	0·720012	0·235856	306·8697	11·75176
	Avg	0·00104771	0·000669	0·93533	0·570821	321·9305	13·57095
9	Max	0·00130002	0·001418	1·108614	1·018683	344·772	15·12734
	Min	0·00103571	0·000615	0·777588	0·254361	295·1303	10·88209
	Avg	0·00113099	0·00091	0·978671	0·464452	321·07	12·33868
8	Max	0·00197769	0·001555	1·274315	2·546412	368·6934	15·66317
	Min	0·00106367	0·000396	0·790063	0·184036	315·0913	9·330922
	Avg	0·00134462	0·000885	1·039495	0·453648	337·5308	13·07144
7	Max	0·00126011	0·000698	1·230906	1·650217	379·5571	14·75287
	Min	0·00101253	0·000466	0·690601	0·275305	286·5369	7·520041
	Avg	0·00112946	0·000577	0·96342	0·616601	336·803	12·20157
6	Max	0·00137507	0·001177	1·149434	1·012248	342·0687	18·46911
	Min	0·00116471	0·000457	0·823138	0·22756	297·907	10·782
	Avg	0·00124966	0·000602	0·920702	0·379105	318·5856	13·37896
5	Max	0·00128589	0·000721	0·954107	3·140037	335·6338	19·16005
	Min	0·00107518	0·000306	0·679658	0·192336	284·6911	11·97982
	Avg	0·00118573	0·000513	0·831798	0·668878	318·8622	15·57781
4	Max	0·00127369	0·000623	0·930612	0·605206	344·8781	20·46371
	Min	0·00111979	0·000437	0·671276	0·244649	307·79	13·24425
	Avg	0·00116571	0·000498	0·834602	0·354241	322·2233	16·63752
3	Max	0·00146115	0·000681	1·11241	0·652266	347·6538	19·04447
	Min	0·00117232	0·000435	0·753515	0·199414	313·157	11·10733
	Avg	0·00129579	0·000553	0·912867	0·269725	329·9038	15·76012
2	Max	0·001939	0·000816	0·919536	2·277989	368·5659	24·7
	Min	0·00129262	0·000109	0·75019	0·169892	302·3913	14·80423
	Avg	0·00140523	0·000568	0·82467	0·353145	346·8148	18·64866
1	Max	0·02554976	0·000939	0·919344	0·315262	227·0059	9·711491
	Min	0·02554976	0·000939	0·919344	0·315262	227·0059	9·711491
	Avg	0·02554976	0·000939	0·919344	0·315262	227·0059	9·711491

Table 5: Calculated values for provenance proxy data within each chemofacies, from the type data set (16-17-083-25W6), including maximum, minimum and average values. These values were compared with the overallaverage values for this data set (Cr/Al = 0.0015, Ni/Al = 0.000812, Th/Sc = 0.952, MgO/Al_2O_3 = 0.523, Ti/Nb = 332.45 and Ti/Zr = 13.58). Values above the overall average appear in green; values below the overall calculated average appear in red.

The association of MnO and MgO is explained by the presence of dolomite, which is consistent with the XRD results. CaO plots slightly away from both MnO and

MgO, suggesting the presence of minor calcite cement. Indeed, calcite, as a distinct phase, occurred only in minor amounts in samples analysed by XRD.

Chemofacies	Provenance signal	Clay content	Detrital input	Mineralogy	Formation	Relative sea-level
13	• igneous, mafic/ ultramafic sediment input • submature sediment	• lower than average clay content • higher than average chlorite and illite • lower than average smectite and kaolinite content	• low detrital input • high pelagic input • weathered material and clays present	• high phosphate • high heavy mineral content (garnet, spinel, rutile)	Doig	Higher than average, sharp sea-level rise
12	• igneous, felsic sediment input • dolomite present • mature sediment	• lower than average clay content • higher than average smectite and kaolinite • lower than average chlorite and illite content	• high detrital input with sediment recycling • high continental input and influx of weathered material	• high phosphate • minor heavy mineral content	Montney	Lower than average, sea-level fall
11	• mature sediment with mixed mafic/ felsic signature	• lower than average clay content • higher than average smectite and kaolinite • lower than average chlorite and illite content	• high detrital input with sediment recycling • high continental input and influx of weathered material	• low phosphate • minor heavy mineral content	Montney	Lower than average, sharp sea-level fall
10	• dolomite present • low mafic/felsic signature • submature sediment	• lower than average clay content • higher than average kaolinite • lower than average chlorite, illite and smectite content	• minor detrital input with sediment recycling • continental input and weathered material present	• low phosphate • minor heavy mineral content	Montney	Higher than average, sea-level rise
9	• mature sediment with mixed mafic/ felsic signature	• lower than average clay content • higher than average kaolinite and smectite • lower than average chlorite and illite content	• high detrital input • high continental input with sediment recycling • low amounts of weathered material/clay	• low phosphate • minor heavy mineral content	Montney	Lower than average, sea -level fall

Table 6: Interpretation of each chemofacies using the average values generated in Table 2. Interpretation is based on the literature cited in the text.

Table 6: (continued)

Chemofacies	Provenance signal	Clay content	Detrital input	Mineralogy	Formation	Relative sea-level
8	• mature sediment with mixed ultramafic/felsic, igneous signature	• lower than average clay content • higher than average smectite and kaolinite • lower than average chlorite and illite content	• high detrital input with sediment recycling • high continental input and influx of weathered material	• low phosphate • minor heavy mineral content	Montney	Lower than average, rising sea-level
7	• igneous, felsic sediment input • dolomite present • mature sediment	• higher than average clay content • higher than average smectite and kaolinite • lower than average chlorite and illite content	• Low detrital input with some evidence of sediment recycling • High pelagic input • low amounts of weathered material	• low phosphate • low heavy mineral content (garnet present)	Montney	Higher than average, sharp rise, then fall
6	• mixed felsic/mafic signatures (low signal strength) • submature sediment	• lower than average clay content • higher than average smectite and illite • lower than average chlorite and kaolinite content	• high detrital input • high continental input with sediment recycling • low amounts of weathered material/clay	• low phosphate • minor heavy mineral content	Montney	Lower than average, sea-level fall
5	• submature sediment with dolomite present • mixed felsic/mafic signatures (low signal strength)	• higher than average smectite and illite • lower than average chlorite and kaolinite content	• low detrital input and sediment recycling • high pelagic input • low amounts of weathered material	• low phosphate • low heavy mineral content (garnet present)	Montney	Higher than average, rise and fall
4	• immature sediment with mixed mafic/ felsic signature (low signal strength)	• higher than average clay content • higher than average illite • lower than average chlorite, smectite and kaolinite content	• low detrital input and sediment recycling • high pelagic input • low amounts of weathered material	• low phosphate • low heavy mineral content (garnet and spinel present)	Montney	Higher than average, falling

Table 6: (continued)

Chemofacies	Provenance signal	Clay content	Detrital input	Mineralogy	Formation	Relative sea-level
3	• immature sediment with mixed mafic/ felsic signature (low signal strength)	• higher than average clay content • higher than average illite • lower than average chlorite, smectite and kaolinite content	• mixed detrital and pelagic input • low sediment recycling, continental material or weathered material	• low phosphate • low heavy mineral content (garnet present)	Montney	Lower than average, rising
2	• igneous input, mixed mafic/felsic signature • immature sediment	• higher than average clay content • higher than average illite • lower than average chlorite, smectite and kaolinite content	• low detrital input and sediment recycling • high pelagic input • low amounts of weathered material	• low phosphate • high heavy mineral content (spinel, garnet, rutile)	Montney	Higher than average but falling
1	mafic/ultramafic input • sediments submature	• higher than average clay content • higher than average chlorite and illite • lower than average smectite and kaolinite content	• low detrital input and sediment recycling • high pelagic input • some weathered material present	• high phosphate • high heavy mineral content (garnet, spinel, rutile)	Belloy	Higher than average

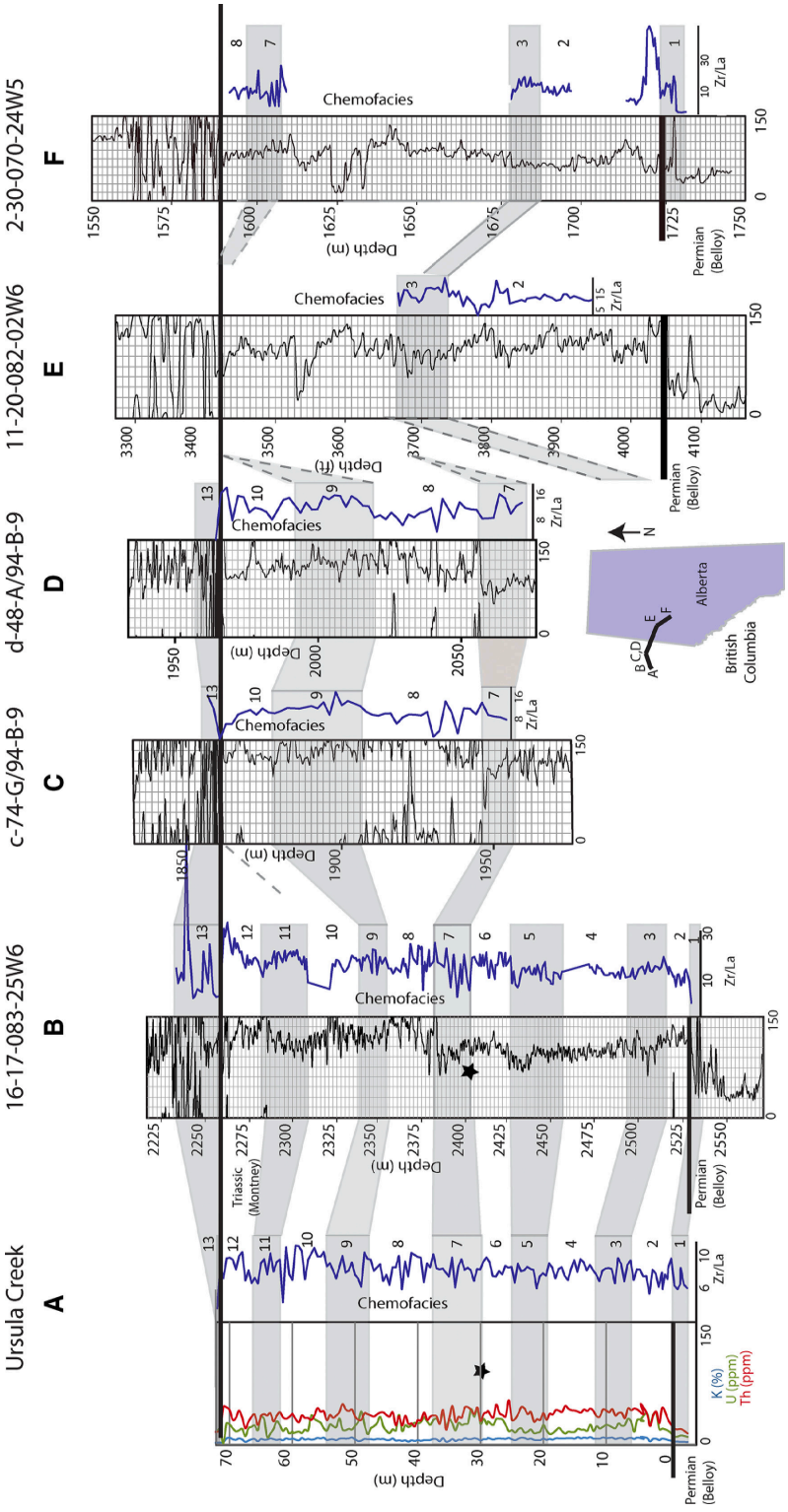

Figure 6: Line of cross-section illustrating the correlation between all sample sets used in this study: (A) Ursula Creek Outcrop; (B) 16-17-083-25W6; (C) c-74-G/94-B-9; (D) d-48-A/94-B-9; (E) 11-20-082-02W6; and (F) 2-30-070-24W5. The Spathian/Anisian (Lower/Middle Triassic) boundary was chosen as the datum as it is a

chronostratigraphic boundary definitively present in all data sets. Gamma ray logs and Zr/La profiles are shown. Zones of correlated conodont horizons are indicated by stars. Of note is the loss of upper chemofacies in wells C and D and in the two Alberta wells (E and F; chemofacies 9 to 13 are not observed). This can be explained by a combination of erosion and clinoform deposition. Also of interest is the thickening of the lower chemofacies in wells E and F, further supporting a clinoform model of deposition.

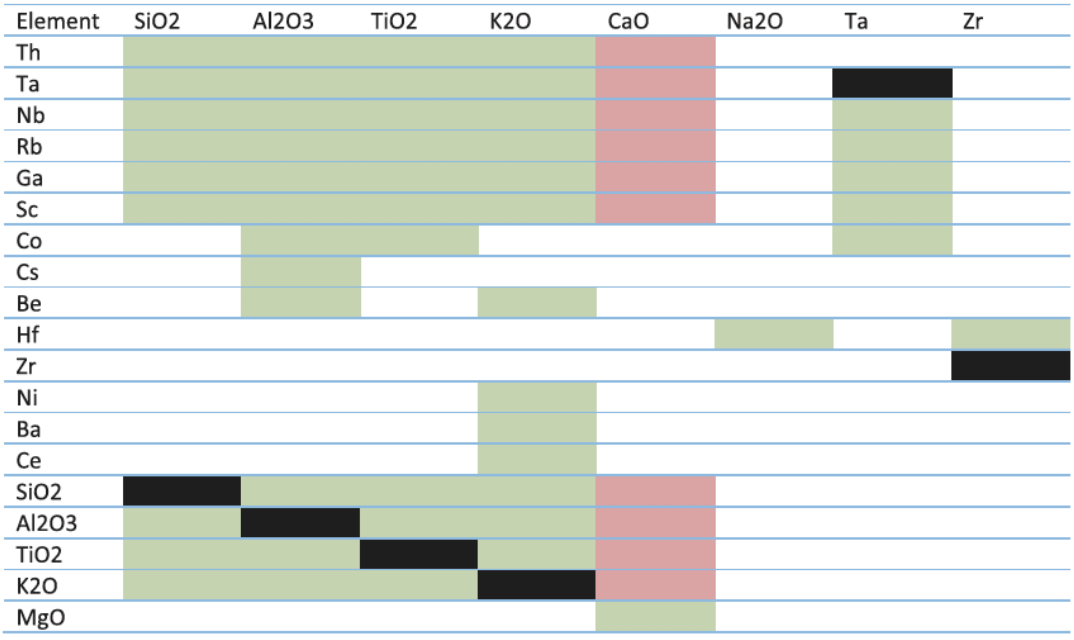

Table 7: Summary table illustrating high (>0.8) and low (<0.8) Pearson product-moment correlation values for certain elements. High correlation values are indicated in green; negative correlation is identified by red.

Provenance

Results

Plotting La/Sm versus Yb/Sm (after Plank & Langmuir, 1998; Fig. 8) reveals a similar trend between the sample sets of 16-17-083-25W6 and Ursula Creek. A strong linear trend is visible, overprinted by a data cluster near the origin. Data points with the highest values of La/Sm and Yb/Sm occur in chemostratigraphic interval 8. Data

from well 2-30-070-24W5 exhibit a clustering trend similar to that seen in 16-17-083-25w6, with a slight vertical spread. Data points from well 11-20-082-02W6 are consistently moderate in La/Sm and Yb/Sm values, and no linear trend is apparent. As observed in the data from 16-17-083-25W6 and Ursula Creek, data for wells d-48-A/94-B9 and c-74-G/94-B-9 display a central cluster and a positive, linear trend.

Plots of Th/Sc (felsic) versus Cr/Th (mafic) after Bracciali et al. (2007) are shown in Figs 9 and 10 and reveal a near vertical trend in all data sets with low values of Cr/Th. Data points from the Belloy Formation (chemofacies 1) exhibit high Cr/Th and low Th/Sc values. Samples from the Doig Formation (chemofacies 13) occur as a spread of points between the main linear trend and the Belloy outliers. Samples from chemostratigraphic interval 8 plot in an arc between the main linear trend and Doig Formation data points. Generally, stratigraphically older Montney data points plot closer to the origin, with increasing Th/Sc content associated with stratigraphically younger points.

Interpretation

Plotting La/Sm versus Yb/Sm can help to differentiate continental, hydrothermal and volcanic arc sediment sources (Plank & Langmuir, 1998). Most data (from all sample sets) plot within the zone of continental detritus and clay scavenging. The exceptions to this are high La/Sm and

Mineral	1715·8 m (wt %)	1717·5 m (wt %)	1719·85 m (wt %)	1721·5 m (wt %)	1723·86 m (wt %)	1725·5 m (wt %)	1727·35 m (wt %)	1728·46 m (wt %)	1730·43 m (wt %)	1732·1 m (wt %)
Quartz	34·7	43·9	54·8	71·8	71·5	50·9	57·6	61·3	73·5	42·4
Dolomite	21·7	18·2	11·3	12·4	10·2	15·1	12·8	11·9	0·6	48·6
Microcline	17·8	8·1	15·1	6·3	5·1	13·1	10·1	8·9	1·1	–
Muscovite	9·1	12·4	5·2	1·9	3·2	6·7	5·4	1·6	2·0	–
Calcite	3·5	5·8	2·1	0·7	1·1	1·1	4·5	6·1	5·3	0·6
Diopside	2·8	3·2	3·1	1·4	1·7	3·1	1·9	2·6	–	–
Albite	2·0	1·5	1·4	1·4	2·0	1·7	2·4	2·7	0·9	1·0
Pyrite	2·8	2·2	2·0	0·5	0·7	2·9	1·0	0·6	3·8	0·3
Clinochlore	1·0	1·6	1·3	0·7	1·1	1·0	1·7	1·4	–	–
Ankerite	0·9	0·8	0·9	0·8	1·0	0·9	0·9	1·0	–	2·3
Kaolinite	2·0	0·3	0·8	0·2	0·3	1·7	0·3	0·4	0·3	–
Chlorapatite	0·5	0·6	0·7	1·0	1·2	0·7	0·5	0·7	—	–
Kutnohorite	0·4	0·7	0·5	0·4	0·3	0·5	0·5	0·5	–	0·8
Brookite	0·4	0·4	0·4	0·3	0·3	0·4	0·3	0·2	–	–
Siderite	0·5	0·3	0·2	0·2	0·2	0·3	0·2	0·2	1·4	0·4
Fluorapatite	–	–	–	–	–	–	–	–	5·2	–
Marcasite	–	–	–	–	–	–	–	–	5·0	–
Calcite magnesian	–	–	–	–	–	–	–	–	0·9	–
Fluorapatite	–	–	–	–	–	–	–	–	–	3·5
Total	100	100	100	100	100	100	100	100	100	100

Table 8: X-ray diffraction (XRD) analysis for select intervals of well 2-30-070-24W5. The limit of detection varies from 0.5 to 2.0% depending on crystallinity.

Yb/Sm data points associated with the sample sets from 16-17-083-25W6 and Ursula Creek, which suggest hydrothermal input. These hydrothermally influenced samples occur within chemofacies 8 and, when compared to the work of Golding et al. (2014), are Spathian in age. Upper crustal (felsic) and mantle (mafic and ultramafic) sources of sediments contain unique geochemical signatures expressed in the Th, Sc and Cr content. Felsic sources are indicated by high Th/Sc and low Cr/Th signatures, while mafic and ultramafic sources have characteristic high Cr/Th and low Th/Sc values (Bracciali et al., 2007). The increase in felsic content in stratigraphically younger samples suggests a gradual change in sediment source over time. This could be attributed to a gradual change in riverine output/sourcing (possibly related to climate and weathering) or could represent the introduction of a completely new sediment source (such as an approaching terrane). The approach of a new terrane is entirely feasible because terrane accretion is thought to have begun by the Early–Middle Triassic (Beranek & Mortensen, 2011).

Biogenic versus abiotic carbonate

Results

The data plots of Sr versus Mg (Fig. 11) reveal a low angle, positive linear trend with Sr levels generally remaining below 400 ppm. A high-Sr, low-Mg outlier (16-17-083-25W6), indicating Sr levels of over 700 ppm, corresponds to a depth of 2440. 2 m. Scatter in the Sr values appears to be related to the low-Mg samples (< 30,000 ppm Mg). Scatter in Mg values occurs in the samples of high-Mg content (30,000 to

60,000 ppm Mg). These values follow the abiotic trend of values published by Carpenter & Lohmann (1992).

Interpretation

Non-skeletal, calcite cements have been shown to contain significantly less Sr than biotic marine calcite (Carpenter & Lohmann, 1992). When Sr–Mg trends are compared, biotic calcite values can be up to five orders of magnitude higher than abiotic calcite, offset by *ca* 1250 ppm (Carpenter & Lohmann, 1992). Biotic calcite trends between low values (Sr = 1400 and Mg = 2000) and high values (Sr = 2600 and Mg = 56 000), while abiotic calcite trends between Sr/Mg of 300/10000 and 1300/50000; abiotic calcite exhibits significantly lower Sr values (Carpenter & Lohmann, 1992).

With the understanding that abiotic calcite is the predominant phase, zones of calcite cement were interpreted to be present where positive excursions in CaO and Sr occurred in association with low concentrations of MgO, MnO, SiO_2, Al_2O_3 and TiO_2 (Fig. 12). Strontium can be associated with minerals such as gypsum, anhydrite, strontianite and celestite, in addition to calcite and aragonite (Banner, 1995). Data from wells examined here demonstrate a close correlation between CaO and Sr in the principal component analysis. Furthermore, XRD analysis did not identify the presence of gypsum, anhydrite, strontianite or celestite, thus supporting the interpretation that calcite is the principal Sr-bearing mineral. Within well 16-17-083-25W6, zones of calcite cement occur within chemofacies 5, 7 and 11; the

highest frequency of calcite occurrence is within chemofacies 7. Calcite is probably a cement phase, as evidenced by the Sr–Mg plot (Fig. 11). The data in this study clearly trend along the abiotic vector, with Sr

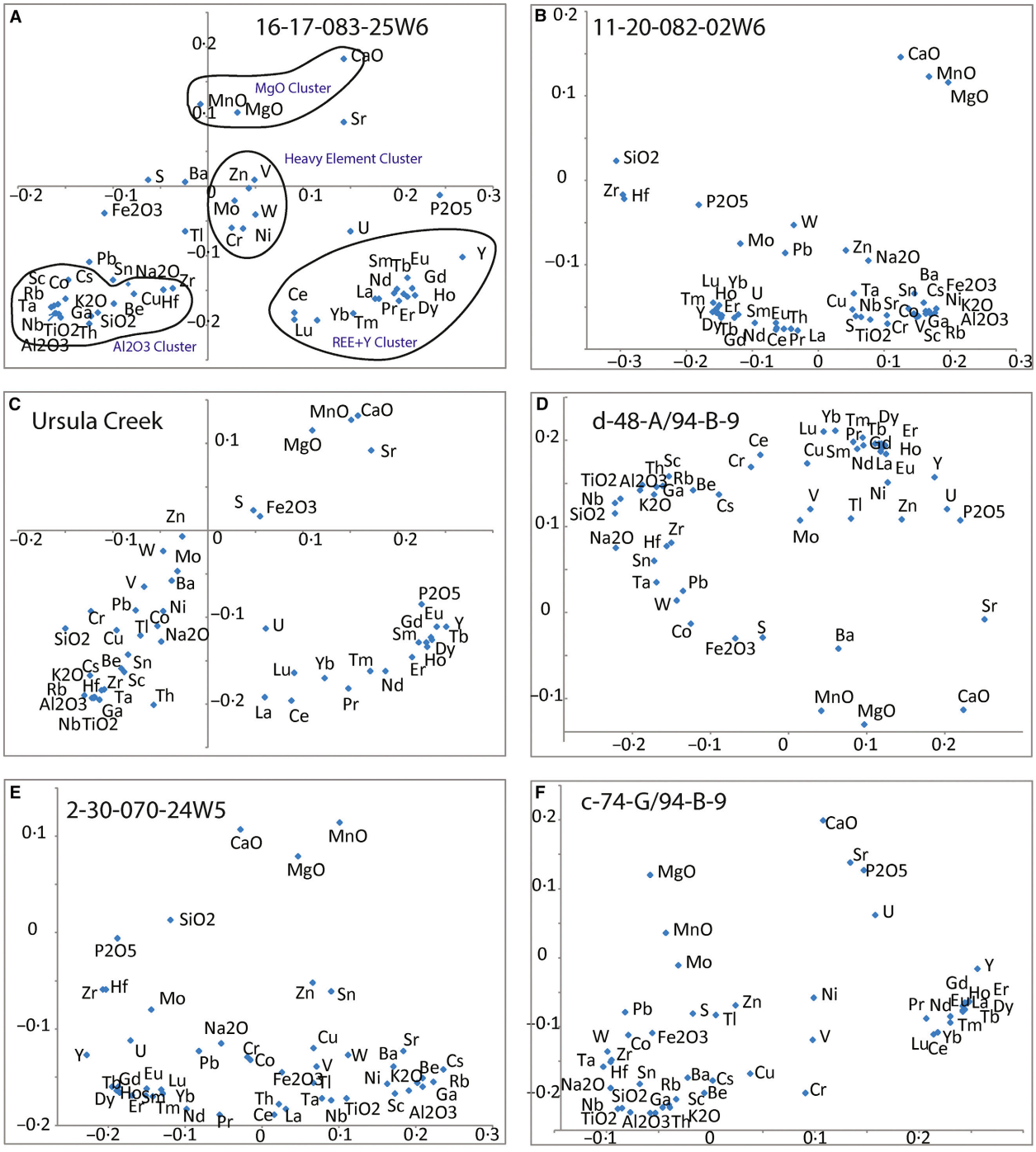

Figure 7: Eigenvector plots of e1 versus e2 for all data sets. (A) Eigenvector plot of well 16-17-083-25W6. Elemental clusters are indicated by black polygons: the MgO cluster (top), the heavy element cluster (central), REE+Y cluster (right) and Al_2O_3 cluster (left). (B) Eigenvector plot of well 11-20-082-02W6. (C) Eigenvector plot of well Ursula Creek. (D) Eigenvector plot of well d-48-A/94-B-9. (E) Eigenvector plot of well 2-30-070-24W5. (F) Eigenvector plot of well c-74-G/94-B-9.

values well below 1000 ppm (cf. Carpenter & Lohmann, 1992). The outlier with the highest Sr content (over 700 ppm) is from an interval identified as having been sourced from high sediment recycling (Fig. 2). Therefore, the high Sr values in this sample may reflect increased weathering input (Pett-Ridge et al., 2009).

Dolomite-rich horizons were identified as having high CaO content and being enriched in MgO and MnO. The presence of MnO within dolomite has been confirmed in cathodoluminescence studies of dolomite (e.g. Pierson, 1981). Dolomite- rich horizons were observed within the majority of chemofacies for well 16-17-083-25W6, with the notable exceptions being chemofacies 4 and a large portion of chemofacies 10 and 11.

Element	Mineral affinity
Si	Quartz
Al	Clay minerals, mica, kaolinite, gibbsite, bauxite
Ti, Nb, Ta	Heavy minerals such as rutile, anatase and Ti-bearing minerals (leucoxene and ilmenite)
Fe	Fe-oxyhydroxides (goethite and haematite), ferroan dolomite, pyrite, siderite
Ca, Mn, Mg, Sr	Siderite, dolomite, calcite, clays (Mg associated with chlorite)
Na	Clay minerals, halite
K, Rb, Cs	Illite, mica, K-feldspar
P	Clays (illite), mica, siderite (in association with Fe, Mn and REEs), biogenic phosphate (associated with U, Mo, Ca and Ce)
Zr and Hf	Zircon
Co, Ni, Zn, V, Cu	Clay minerals and mica; Ni can be associated with Fe-oxyhydroxides
Th	Weathered kaolinite (in association with Al, Ga and Sc), zircon, clay minerals, mica, apatite
U	Organics, zircon (associated with Th and Zr)
REE	Clay and mica, kaolinite or gibbsite (associated with high Al), Fe-oxyhydroxides, diderite, zircon and garnet
Sc and Ga	Kaolinite (in association with Al)
Be, W, and Sn	Heavy minerals (beryl and cassiterite), tonstein
Ba	Clay and drilling fluid

Table 9: Mineral occurrence of elements discussed in Pearce et al. (2010), who also referred to the work of Morton et al. (2005) and Pearce et al. (2005).

Hydrothermal indicators and iron mineral phase changes

Results

Using the data set from well 16-17-083-25W6, a depth plot of P/Fe (Fig. 13) reveals low values overall, below 0.1. Positive excursions in this ratio occur mid-section and also near the top of the section. The two intervals with the highest P/Fe values occur at a depth of 2375 m (values approaching 1) corresponding to chemofacies 8, and within the Doig Formation above 2260 m depth, where values reach as high as 8. The Ursula Creek data set also exhibits values within the range of those observed in

the key data set, 16-17-083-25W6; specifically, high values are observed in chemofacies 7 and 8 (Fig. 14). Samples from wells d-48-A/94-b-9, c-74 g-94-B-9 and 2-30-070-24W5 also exhibit similar P/Fe value ranges for chemofacies 7, 8 and 13 (the Doig Formation). Well 11-20-82-2W6 shows consistently high P/Fe values evident in chemofacies 4, 5 and 6.

To further investigate possible hydrothermal effects, chondrite-normalized plots of REE were constructed for all depths within the most complete sample set (UWI 16-17-083-25W6). This reveals severe middle rare earth element (MREE) depletion at depths of 2367.6 m and 2368 m (Figs 13 and 15). At these intervals, values of Nd, Sm, Eu, Gd, Tb, Dy, Ho and Er plot well below the values observed in surrounding intervals (Fig. 15). A depth plot of Fe/S (Fig. 13) from

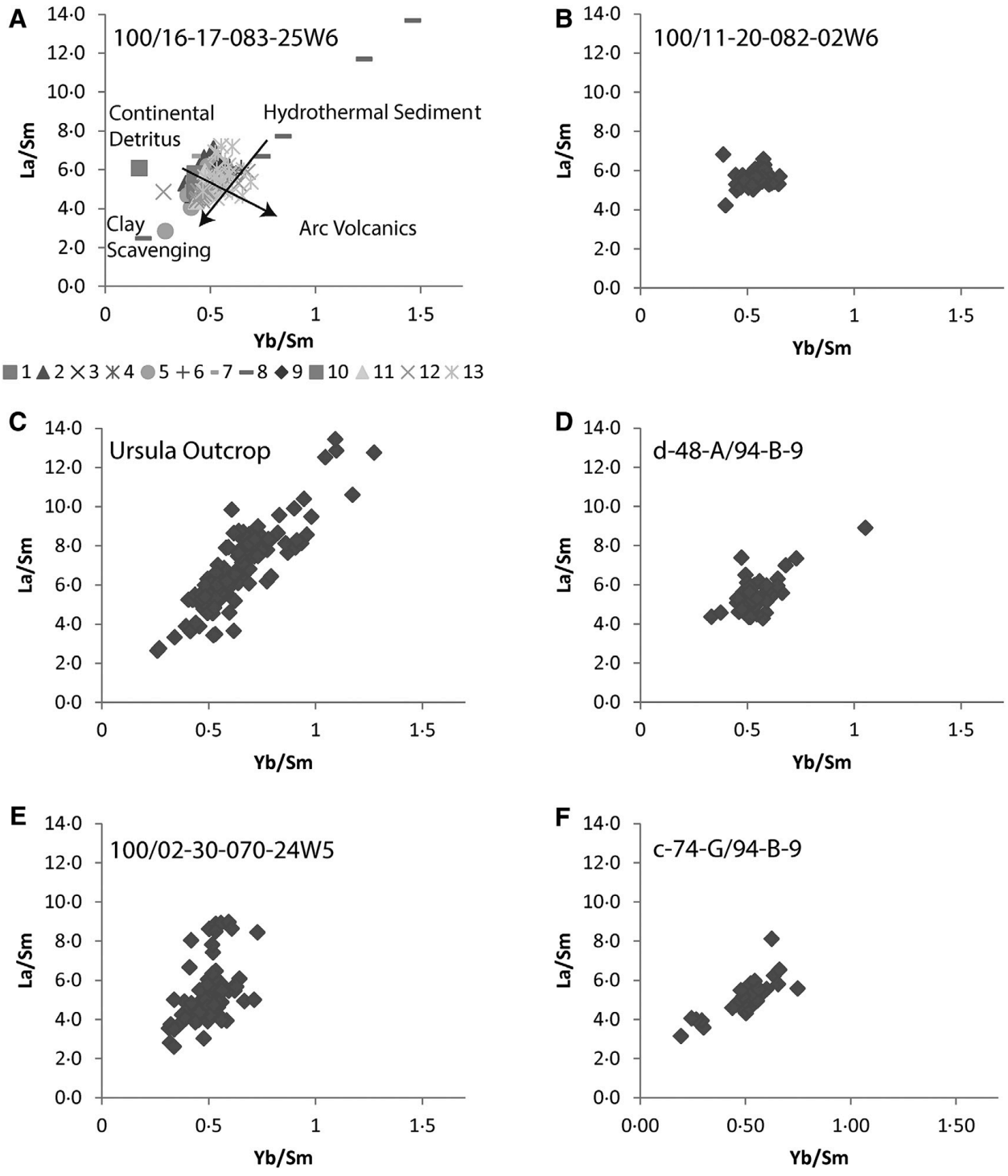

Figure 8: Geochemical plots showing the distribution of light rare earth elements (LREE; y-axis) versus heavy rare earth elements (HREE; x-axis), after Plank & Langmuir (1998). (A) The influence of hydrothermal input, continental detritus, arc volcanics and clay sequestration are illustrated in the plot for well 16-17- 083-25W6

sorted by chemofacies. (B) Plot for well 11-20-082-02W6. (C) Plot for Ursula Creek. (D) Plot for well d-48-A/94-B-9. (E) Plot for well 2-30-070-24W5. (F) Plot for well c-74-G/94-B-9.

the type well 16-17-083-25w6 reveals relatively low ratio values (averaging 20) in samples below 2400 m depth. Negative excursions to values below 5 occur at 2401 m and 2440 m depth. Above 2400 m, the ratio value increases to over 60, remaining high until 2260 m depth. Iron/ sulphur values return to low levels (averaging 20) at 2260 m depth.

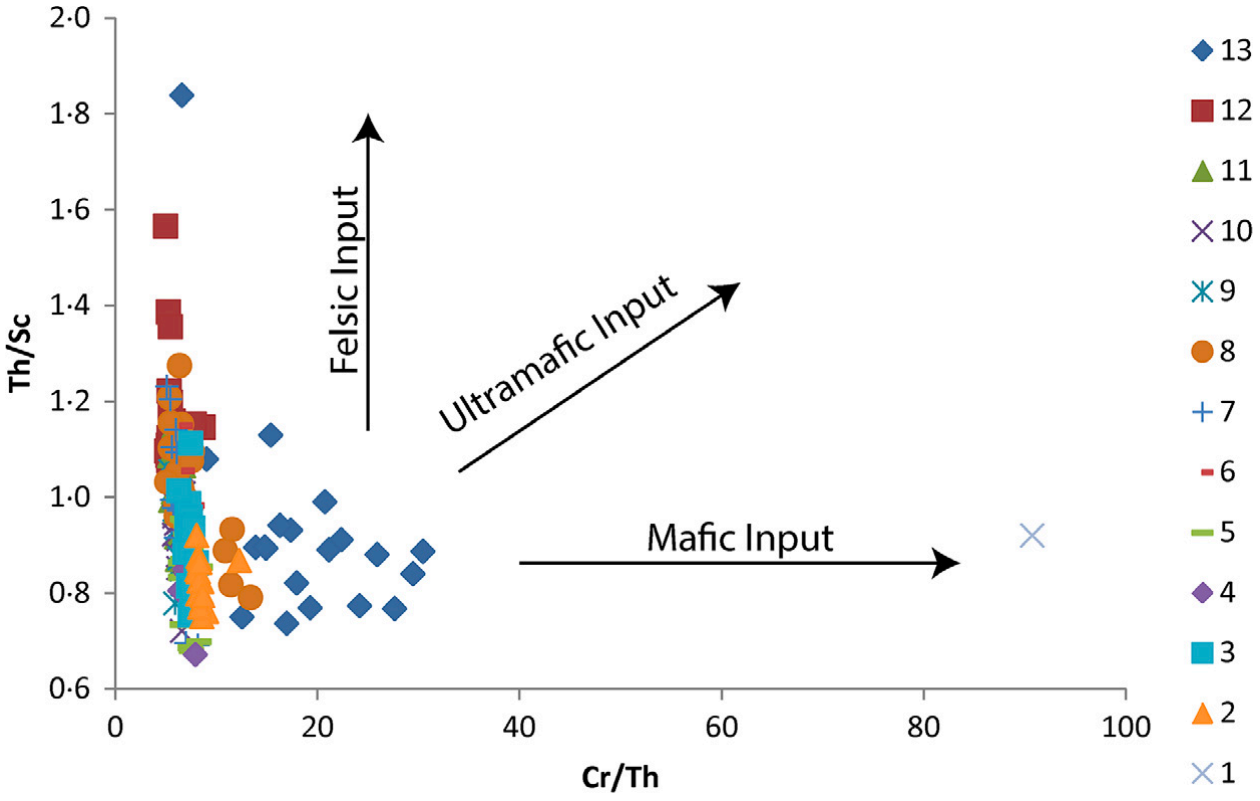

Figure 9: Geochemical plot of the data from well 16-17-083-25W6 illustrating the influence of felsic (Th/Sc) versus mafic (Cr/Th) input (after Bracciali et al., 2007). Felsic, mafic and ultramafic trends are illustrated. Data points are coloured based on chemofacies (legend on the right). Doig samples (chemofacies 13), Belloy samples (chemofacies 1) and chemofacies 8 samples all show mafic, and ultramafic input. Additionally, felsic content increases stratigraphically upward (note change in facies colour along the y-axis).

Interpretation

The ratio of P/Fe has been evaluated in hydrothermal deposits, with hydrothermal plume deposits yielding a P/Fe value of 0.12 to 0.23 (Feely et al., 1994; Wheat et al., 1996). Data sets located proximally to one another, from 16-17-083-25W6, Ursula Creek, c-74-G/94-B-9 and d-48-A/94-B-9, show P/Fe values within chemofacies 7 and 8 that fall within the range identified for hydrothermal plumes (between 0.12 and 0.23) by Feely et al. (1994). High P/Fe values also occur in the Doig phosphate zone (chemofacies 13; Fig. 13), but REE plots within the Doig samples show no evidence for high temperature hydrothermal input. Therefore, this signature is interpreted here to represent the input of hydrothermal plume particles enriched in Fe. This would also explain the P/Fe values observed within data sets 11-20-82-2w6 and 2-30-70-24W5.

Additionally, the molar ratio of Fe/S has been used to determine relative abundance of pyrite; ratio values near 2 signify the dominance of pyrite as the Fe-incorporating phase (Zhao & Zheng, 2015). A change in this ratio can signify a change in the Fe-bearing phase (such as Fe-hydroxide, which can be related to hydrothermal plumes). A depth profile for Fe/S within the key data set (16-17-083-25W6) shows that, at approximately 2400 m, there is a switch in the relative abundance of pyrite as a major iron phase to Fe (III) oxyhydroxides and clays (Fig. 13).

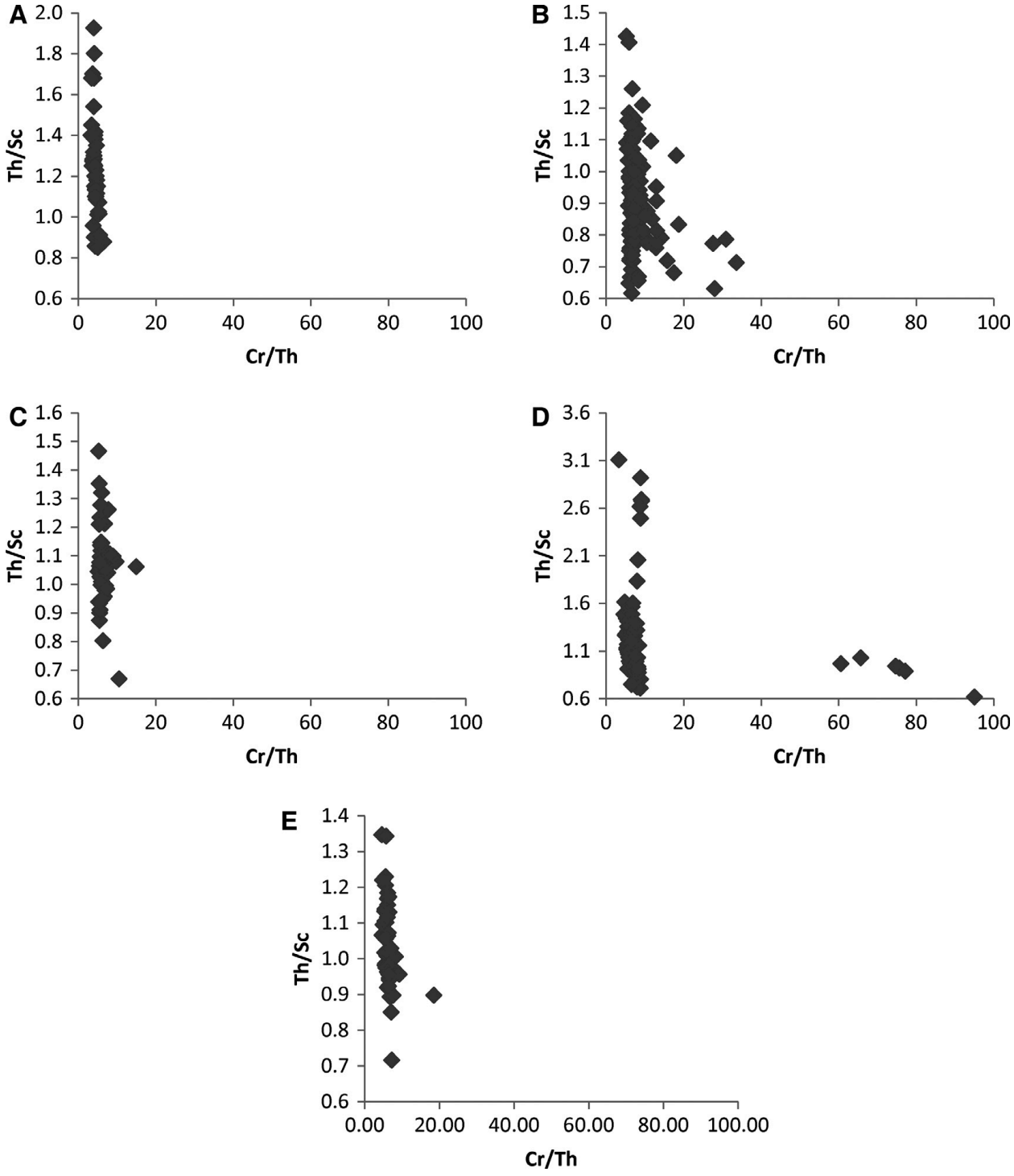

Figure 10: Geochemical plots illustrating the influence of felsic (Th/Sc) versus mafic (Cr/Th) input (after Bracciali et al., 2007) for datasets: (A) 11-20-082-02W6; (B) Ursula Creek; (C) d-48-A/94-B-9; (D) 2-30-070-24W5; and (E) c-74-G/94-B-9.

Increased Fe/S values of this phase occur near the phosphate excursion indicating the possibility of Fe (III) oxyhydroxide plume particles being deposited. Furthermore, the sample sets from 16-17-083-25W6, Ursula Creek and d-48-A/94-B-9 show a strong signature of hydrothermal input, as indicated by high La/Sm and Yb/Sm outliers (Plank & Langmuir, 1998; Fig. 8). These hydrothermal signatures are associated with dolomitization in chemofacies 8.

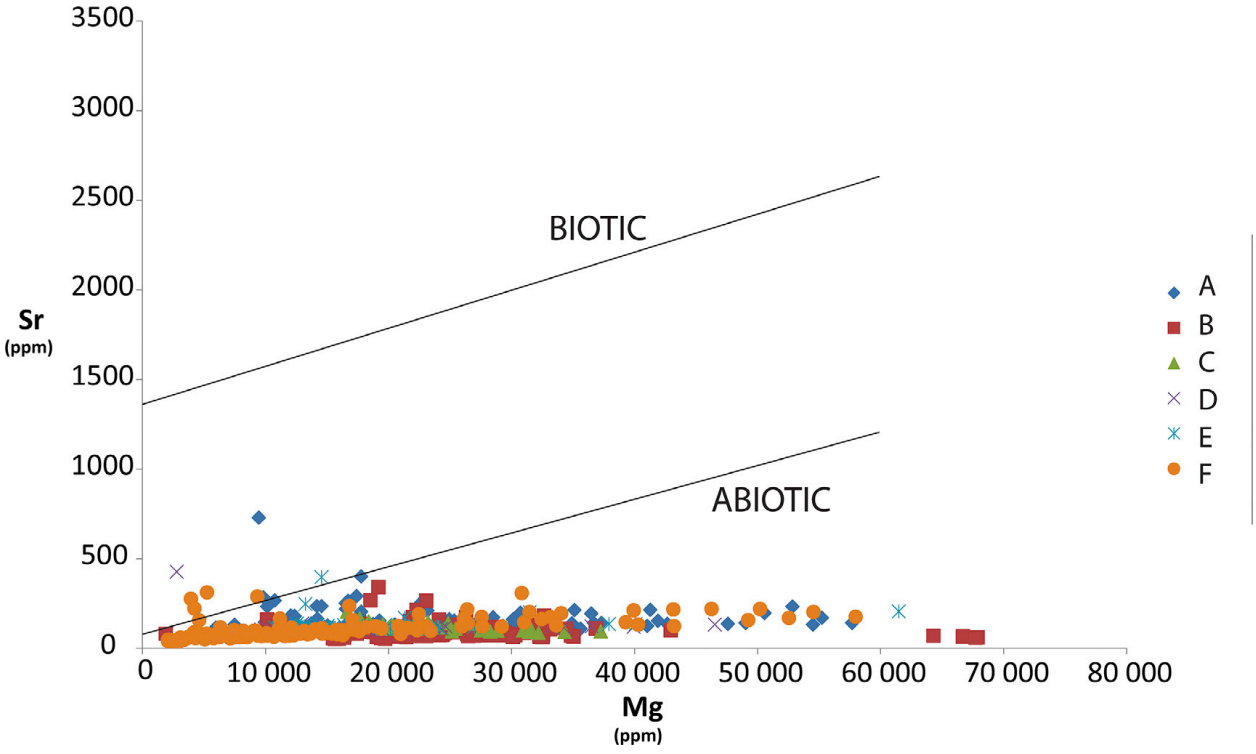

Figure 11: Cross-plot of Sr versus Mg values for well 16-17-083-25W6. Biotic and abiotic trends are shown from Carpenter & Lohmann (1992).

Discussion

Hydrothermal input and implications

The evidence of hydrothermal input co-occurring with dolomitization suggests that hydrothermal input to deeper water regions, possibly associated with basin margin faults, may have been a source of dolomitizing fluids in the Montney Formation. This would necessitate that hydrothermal input occurred post-depositionally. Chondrite-normalized plots for these samples indicate severe depletion of MREE (Fig. 15). A similar depletion was documented by Lev et al. (1999) and attributed to MREE sequestration by phosphate, then subsequent dissolution and a concomitant loss of P and MREE. Dissolution of phosphatic phases (such as apatite) may be promoted when sediments are exposed to hydrothermal fluids. However, evidence for high levels of hydrothermal plume activity complicates the timing of hydrothermal input. An alternative removal pathway for phosphate involves the adsorption onto Fe–Mn oxyhydroxides within hydrothermal plumes, resulting in transport to more distal environments (Wheat et al., 1996). This adsorption severely depletes the seawater phosphate concentrations surrounding the hydrothermal plume and high P/Fe values, observed in this study's data set, can be considered to indicate hydrothermal Fe particle scavenging of P (Feely et al., 1994; Wheat et al., 1996). Hydrothermal plume inputs have also been suggested to explain high levels of trace elements, such as Cu, in Cretaceous black shales (Brumsack, 2006). Such a mechanism would be consistent with the high levels of Cu observed in the present data in association with high P/Fe and depleted MREE.

The timing of this hydrothermal flux is uncertain, although it does appear to coincide with the dolomitization identified in chemofacies 8 (Fig. 12). The involvement of hydrothermal

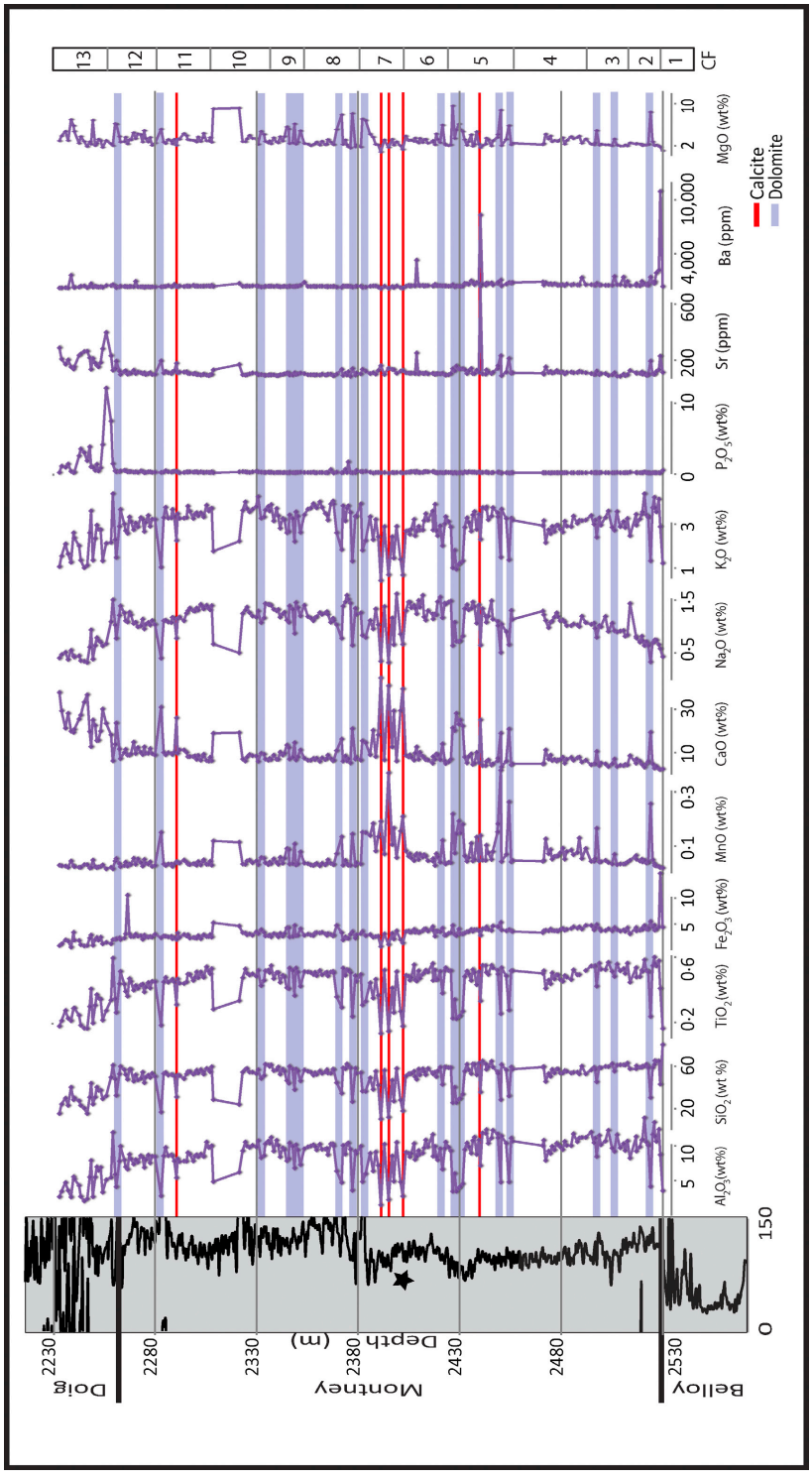

Figure 12: Oxide, Sr and Ba profiles for well 16-17-083-25W6 with calcite cementation zones indicated by red and dolomite-rich zones highlighted in grey. Peaks in Sr correlate with calcite-rich zones. The gamma ray profile is given on the left.

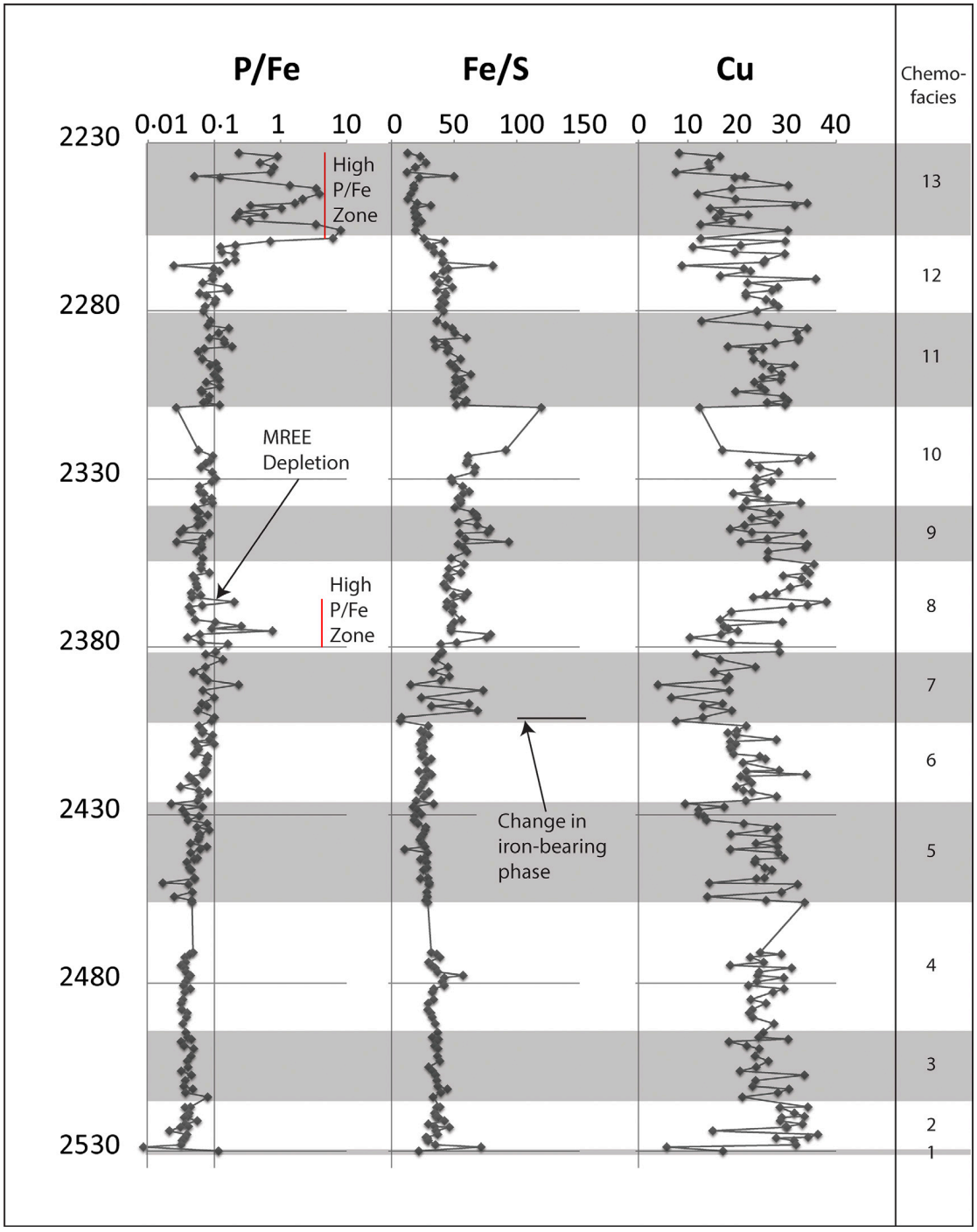

Figure 13: Depth plot illustrating the variation in the ratio of Fe/S, P/Fe (samples showing MREE depletion are shown) and Cu for well 16-17-083-25W6. Zones of high P/Fe are indicated by red bars. Depth is in metres (y-axis). Within the plot of Fe/S, at depth 2400 m, the character of the ratio value changes from low to high, suggesting a switch in the dominant iron-bearing phase from pyrite to iron oxyhydroxide.

fluids has two implications. Firstly, there is the potential for trace element signatures to have been diagenetically altered proximal to this stratigraphic interval. However, hydrothermal

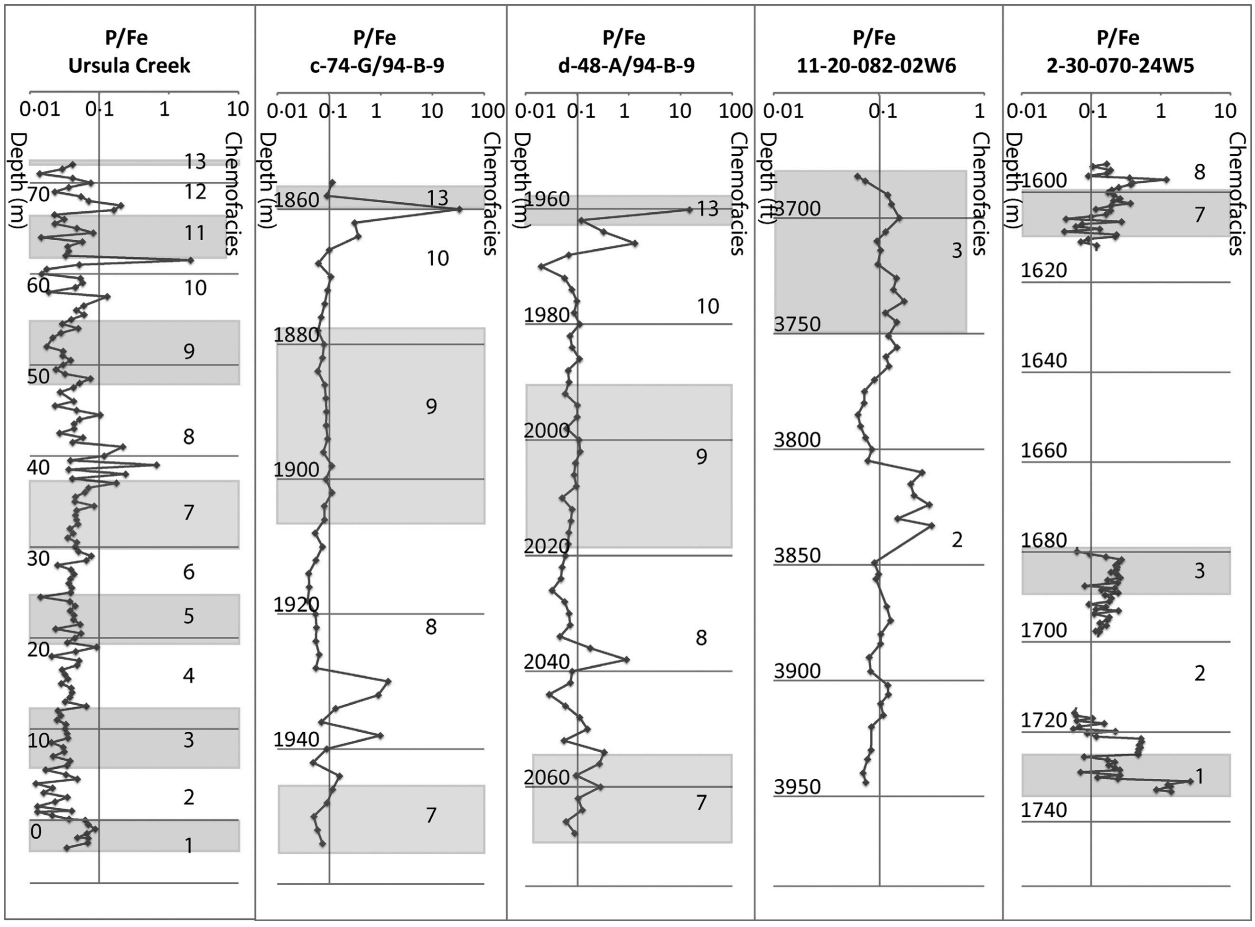

Figure 14: Phosphorus/iron values for wells 2-30-070-24W5, 11-20-082-02W6, c-74-G/94-B-9, d-48-A/94-B-9 and Ursula Creek. Intervals with values greater than 0.12 (the lower limit of hydrothermal influence) are highlighted.

alteration of underlying sediment appears to have been negligible owing to the presence of phosphatic lenses and nodules. The REE signature characteristic of the hydrothermally influenced interval indicates possible phosphate dissolution or scavenging by hydrothermal activity but it seems unlikely that the phosphate would

be preserved at this lower stratigraphic interval if hydrothermal alteration had taken place. Secondly, hydrothermal fluids could also provide a mechanism for the observed dolomitization within the Montney Formation. This is significant because it has implications regarding the propagation of fractures, as dolomite and calcite contribute to the brittleness and hence the ability to generate fractures within a horizon compared to dominantly clay-rich layers (Jin et al., 2015).

Climate change in the Early Triassic

This study demonstrates a marked shift in the nature of the clay component, as indicated by the geochemical proxies, as well as the average amount of clay over time (Fig. 4). There are marked changes in clay proportions, such as the change in abundance of illite to kaolinite and smectite, and the occurrence of chlorite. These transitions are of interest because they correspond to chronostratigraphic boundaries, namely the Permian/Triassic boundary, the Smithian/Spathian boundary and the Early/Middle Triassic boundary (Fig. 16), all of which are

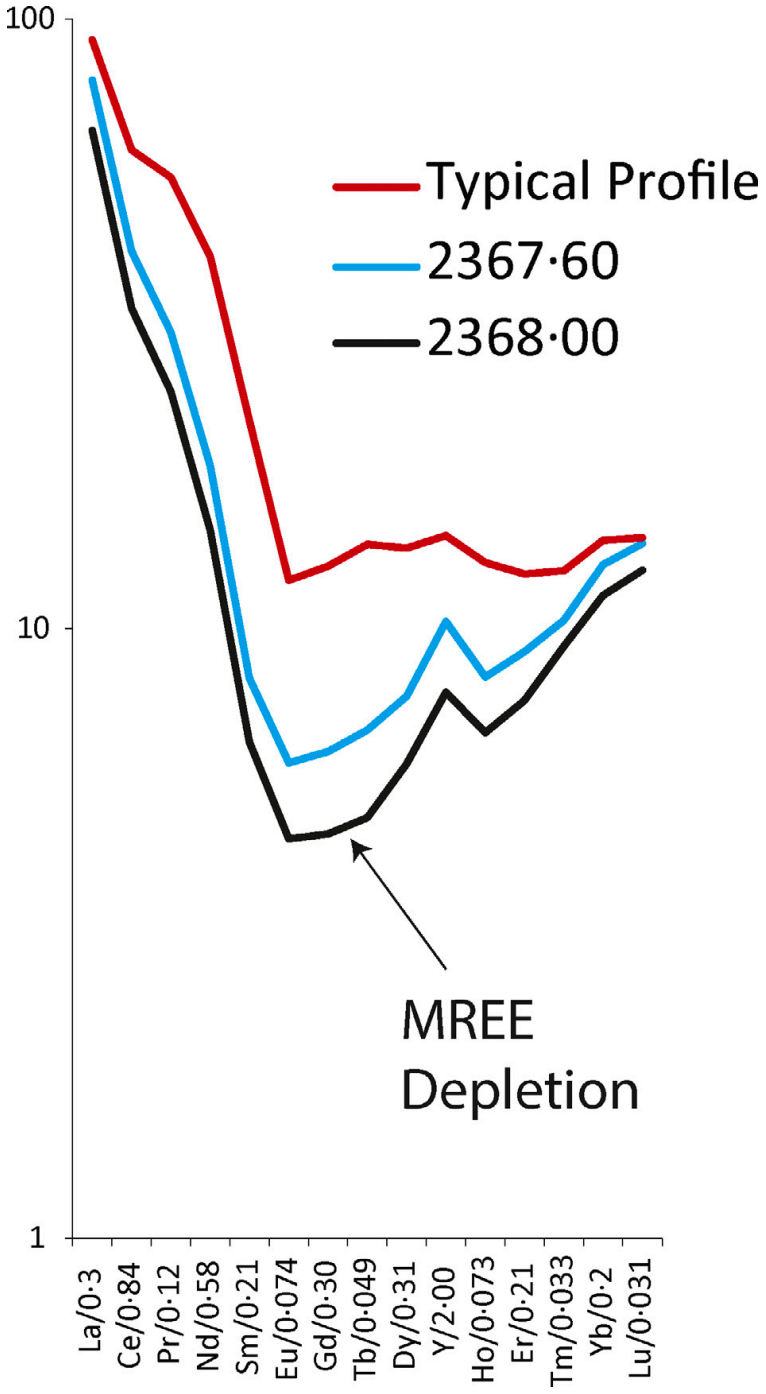

Figure 15: Rare earth element (REE) plots showing the typical pattern observed in the sample set compared to anomalous patterns observed at 2367.6 m and 2368 m: REE data are normalized to chondrite values and MREE deletion is clearly illustrated for depths of 2367.6 m and 2368 m.

important sequence stratigraphic boundaries in the Montney Formation (Davies et al., 1997; Golding et al., 2014).

Li et al. (2000) and Chaudhri & Singh (2012) highlight the lithological and climatic drivers behind changes in clay content, although climate analysis using clay alone should be interpreted with caution (Thiry, 2000). With regard to lithology, illite may be detrital, having been weathered from feldspars and micas, while chlorite is produced from the weathering of crystalline intermediate and basic, or low-grade metamorphic rocks (Chaudhri & Singh, 2012). Detrital illite is attributed to physical erosion being the predominant process within the hinterlands (Ruffell & Batten, 1990; Ruffell et al., 2002a). In contrast, kaolinite forms from the weathering of basic and granitic sources (Chaudhri & Singh, 2012). Additionally, as kaolinite is more prone to flocculation than other clays (e.g. Playter et al., 2017), the relative abundance of detrital kaolinite can indicate the relative source proximity (Ruffell et al., 2002a, b). The abundance of detrital kaolinite also increases with humid weathering (Chamley, 1989; Ruffell et al., 2002a,b). Smectite forms in seasonally dry and wet climates, although smectite and kaolinite can also be a product of volcanic ash deposition (Chamley, 1989; Li et al., 2000; Ruffell et al., 2002a,b).

The high average values of illite, and higher overall clay component in the pre-Smithian/ Spathian boundary samples here, suggest high rates of physical erosion. This is consistent with observations from Early Triassic (Griesbachian) deposits in China, where anomalously high sediment fluxes with clay-rich compositions were observed (Algeo & Twitchett, 2010). These high sedimentation rates have been hypothesized to be related to higher surface temperatures,

increased acid rain and the loss of terrestrial ecosystems owing to the end-Permian Siberian Trap eruptions (Algeo & Twitchett, 2010). The arid Pangean western coastline, where the Montney Formation was deposited, was probably characterized by rare perennial deltas and more numerous ephemeral fluvial sediment sources (Davies et al., 1997). Seasonal or intense periodic rainfall in an arid, sparsely vegetated interior would have resulted in high rates of erosion and sediment delivery during periodic flash floods.

The shift to smectite and kaolinite content at the Smithian/Spathian boundary may correspond to an observed change in the Early Triassic climate regime. At this time within eastern Pangea, a shift in climate from humid, with higher rainfall, to more arid is observed through ammonoid and plant fossil assemblages (Galfetti et al., 2007a,b; Romano et al., 2013). On the west coast of Pangaea, arid conditions already existed, although a shift to an even more arid climate would correlate with an increase in smectite content observed in samples from this study (Ruffell et al., 2002a,b). Additionally, a decrease in rainfall across this boundary, and a concomitant decrease in the proportion of sediment delivered by perennial river systems versus that delivered by ephemeral fluvial systems, is consistent with the observed drop in clay content. Interestingly, the points of highest detrital input, and the lowest relative sea-level, correspond to the climatic shift at the Smithian/Spathian boundary and the Early Triassic/Middle Triassic transition. Generally speaking, climatic changes may then correspond to longer-term shoreline shifts. Although it could be argued that the changes in detrital and clay indicators may reflect fluctuations in the fluvial system due to climate or hinterland changes, the

correspondence of the shoreline (current study) shifts with those of Davies et al. (1997) suggests that these proxies accurately model relative sea-level changes. Additionally, if these changes indeed reflect shifts in fluvial input associated with climate, the observed modelled

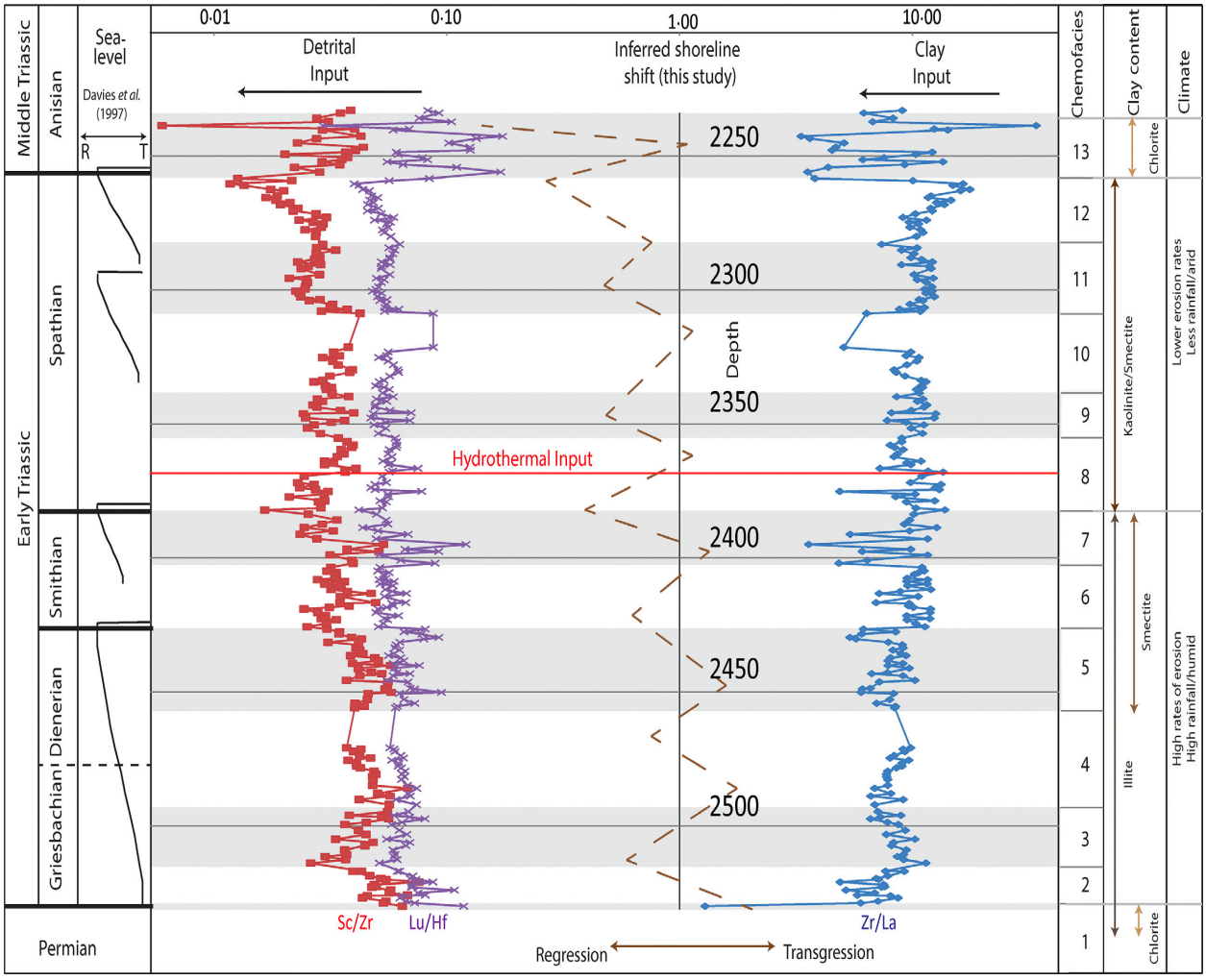

Figure 16: Interpreted sea-level change based off of changes in detrital input proxies and clay indicators. This data set has been biostratigraphically dated (Golding et al., 2014). Additionally, relative sea-level curves from Davies et al. (1997) have been incorporated along the left. These inferred shoreline shifts (central) agree with that of Davies et al. (1997), with the exception of two additional shoreline shifts within the present data during the Griesbachian and Dienerian. Ratio values of Sc/Zr, Lu/Hf and Zr/La are indicated by log-scale along the top of the figure.

climate changes would be expected to correspond to each inferred shoreline shift. Based on these observations, the changes in clay and detrital input are interpreted to be reflective of relative sea-level change.

Identification of clinoforms and implication for sequence stratigraphy in fine-grained successions

The chemostratigraphic correlation presented here implies that the sample sets from western Alberta (11-20-082-2W6 and 2-30-070-27W5) are lacking the uppermost chemostratigraphic intervals observable in British Columbia (Fig. 6). This signifies a significant loss of strata that could be the result of considerable erosion following clinoform deposition, as first suggested by Davies et al. (1997). The Montney/Doig contact has been recognized as being unconformable and chronostratigraphic, corresponding to the Lower/Middle Triassic boundary (Davies et al.,

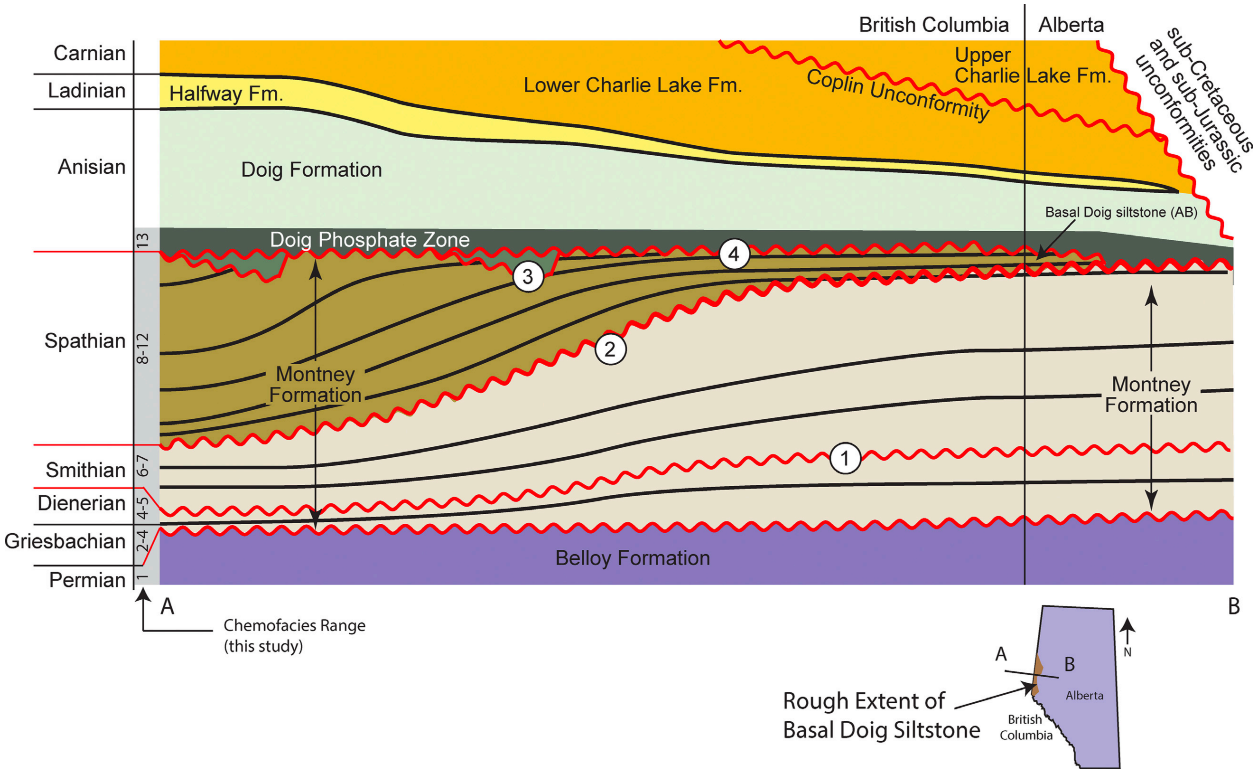

Figure 17: Idealized cross-section highlighting Montney stratigraphy from British Columbia to Alberta (west to east). The clinoform model of Montney deposition is not new, but was first proposed by Davies et al. (1997). However, this new model highlights surfaces of significant erosion, missing from earlier models. These surfaces (such as surface 1) are often associated with sequence boundaries, first described by Davies et al. (1997). Additionally, what is often referred to in Alberta as the 'basal Doig siltstone' is here shown to be equivalent to the upper Montney in British Columbia and is equivalent to chemofacies 8 to 12. The mid-Montney boundary varies across provincial boundaries. Within British Columbia, the mid-Montney boundary corresponds to the Smithian/Spathian boundary, while in Alberta, the mid-Montney boundary occurs at the Dienerian/Smithian transition. Thinning of the upper Montney (denoted by the Smithian/Spathian boundary) eastward results in the loss of Spathian deposits in Alberta. Within this cross-section, the following boundaries of interest are depicted: (1) Alberta mid-Montney sequence boundary – associated with Montney turbidites and Coquinal Dolomite Middle Member. (2) British Columbia mid-Montney sequence boundary/Alberta top-Montney – basal Doig siltstone boundary. This boundary is the Hood Creek Road Cut sequence boundary with the large Thalassinoides. (3) Unconformity below the 'Anisian wedge'. (4) Boundary between the Montney and Doig phosphate zone. The rough extent of the basal Doig siltstone (which marks the presence of Spathian deposits, chemofacies 8 to 12) in Alberta is indicated bottom right.

1997). The model of Montney Formation deposition presented herein shows that the 'Upper Montney' of Alberta is, in fact, temporally equivalent to the lower horizons in British Columbia (Fig. 17).

The identification of clinoform surfaces within the current study's data set suggests that geochemical data, such as detrital and clay proxies, can be used to identify stratigraphic sequences. Because the detrital signatures used for correlation show consistent and correlatable patterns in all of the data sets (which span the palaeobasin), these signatures tie into relative sea-level and climatic changes observed elsewhere, with the chemostratigraphic units appearing to be chronostratigraphic in nature and not merely lithostratigraphic. The identification of stratigraphic sequences using chemostratigraphic analysis in the past has been done largely using isotopic analysis, such as $\delta^{13}C$ or $\delta^{13}N$ (e.g. Pelechaty, 1998; Nance & Rowe, 2015), while correlations have relied heavily on biostratigraphic frameworks (e.g. Bergstrom et al., 2010). In contrast, results in this study suggest that inorganic chemical analysis, which can be generated both non-destructively and in situ using a portable X-ray fluorescence spectrometer (Rowe et al., 2012), allows for the identification of depth-bound chemofacies corresponding to subsurface clinoforms in fine-grained successions on a basinwide scale. Indeed, cyclic variations in sediment provenance have already been identified as allowing for the identification of transgressive surfaces in alluvial, littoral and shallow-marine deposits from Italy (Amorosi et al., 2007). In this case, transgressive surfaces were found to correspond to peaks in Ni/Al content, and maximum flooding surfaces were characterized by high Mg/Al values that correspond to a change in sediment

sourcing during shoreline migration. While Amorosi et al. (2007) focused on two wells, the correlation of these peaks in Ni/Al and Mg/Al within a regional cross-section would, in theory, produce clinoform surfaces.

Perhaps some of the most well-documented and well-studied instances using geochemical data to demonstrate relative sea-level changes in the literature involve Cretaceous deposits. For example, a state of low relative sea-level has been identified in Late Cretaceous deposits that correlates with increased terrigenous input, low kaolinite/chlorite + mica ratios, high Sr/Ca ratios and high TOC; conversely, high relative sea-level may generally be associated with the inverse of these indicators (Li et al., 2000). This correlation of detrital input with relative sea-level has also been demonstrated in Cretaceous deposits (Adatte et al., 2002; Chenot et al., 2016; Keller et al., 2016; Petrash et al., 2016). In fact, changes in clay content and detrital input have been recognized as providing reliable relative sea-level proxies, as well as climate, even in deep marine environments (Li et al., 2000). During periods of transgression and rising sea-level, clay input predominates, while during regression and relative sea-level fall, detrital input increases (Fig. 16).

When compared with second-order and third-order relative sea-level curves for the Early Triassic (Haq et al., 1987; Embry & Gibson, 1995; Davies et al., 1997), these data correlate well by showing instances of relative sea-level fall at the end of the Dienerian, the end of the Smithian, within the Spathian and at the end of the Spathian (Fig. 16). While global correlations of sea-level can be problematic, the proxies used for detrital input (Sc/Zr and Lu/Hf) and clay input (Zr/La) provide reliable information about basin-scale relative sea-level change. Consistency in these

signatures across the basin indicates that causative events were regional in nature, allowing for clinoforms to be delineated. In addition to surfaces inferred to be global in nature (Barclay et al., 1990; Davies et al., 1997), three additional periods of relative sea-level rise and marine transgressions are suggested by the data. Additional relative sea-level rises occur within the Griesbachian, Dienerian and Spathian. Whether these reflect localized tectonic influences or larger-scale sea-level changes remains unclear. It has been suggested that the basin margin was tectonically active during deposition of the Montney Formation, and therefore tectonic activity may be the driving factor. Fault reactivation and subsidence within the graben complexes of the collapsed Peace River Arch is thought to have influenced Montney deposition (Barclay et al., 1990; Davies et al., 1997). The collapsed Peace River Arch forms the basis for the Peace River Embayment, wherein the Montney Formation was deposited. In addition, recent evidence has indicated that accretion of pericratonic terranes to the north-western autochthon was initiated during the Lower Triassic (Beranek et al., 2010). These terrane accretions would have had broad regional influences and may have been a primary driving force in relative sea-level throughout the studied interval (Ferri & Zonneveld, 2008), specifically with regard to the additional sea-level changes noted within the current data set.

An active tectonic margin agrees well with observations in this study of felsic signatures and the pattern of change the data exhibits stratigraphically. Felsic signatures, as recorded by elevated Th/Sc and Cr/Th cross-plots (Condie & Wronkiewicz, 1989; Totten et al., 2000; Bracciali et al., 2007), have been identified in

well 16-17-83-25W6 (Fig. 9). The increase in felsic input up-section (Fig. 9) may be associated with the approach of the Yukon-Tanana terrane from the west (Beranek & Mortensen, 2011) and partial contribution from a western sediment source to Montney sediments. Detrital zircon and monazite analyses (Beranek & Mortensen, 2011) indicate that the Yukon-Tanana terrane was situated just off the west coast of Pangaea by the Early–Middle Triassic and that by the late Triassic the terrane had been fully accreted onto the continental margin. The cross-plots of La/Sm and Yb/Sm in this study suggest volcanic arc signatures within the Doig samples (Fig. 8), indicating that terrain accretion was well underway by the Anisian. This approaching terrane may be linked to fault reactivation and hydrothermal activity, specifically related to the horst and graben complexes associated with the collapsed Peace River Arch within the basin during the Early Triassic (Ferri & Zonneveld, 2008). This, in addition to the migration of the back-bulge associated with the approaching terrane, could explain why the additional relative sea-level changes, identified in this study's data, have not been recognized globally.

Conclusions

The goal of this study was to demonstrate the applicability of chemostratigraphic analysis for determining chronostratigraphic surfaces in finegrained successions, using the Triassic Montney Formation as a field example. Utilizing geochemical trends to highlight changes in provenance, mineralogy, clay and detrital input proved useful for pinpointing changes in relative sea-level, climate change and hydrothermal

input. Analysis of geochemical profiles revealed 13 distinct chemofacies that can be identified across the basin. Correlation of these facies reveals broad clinoform surfaces that indicate that the upper Montney Formation in Alberta is temporally equivalent to lower–mid-Montney deposits in British Columbia. Additionally, analysis of clay proxies indicates high sedimentation rates within the Griesbachian and Dienerian Montney deposits and a correspondent shift in climate and sediment sourcing that is observable at the Smithian/Spathian boundary. This climatic shift is indicated by the point of highest detrital input and lowest relative sea-level within the preserved Montney deposits.

Cross-plots of La/Sm and Yb/Sm probably reveal hydrothermal input during the time immediately following the Smithian/Spathian boundary, as well as the scavenging of middle rare earth elements (MREE) by phosphate. Depleted MREE patterns within these hydrothermally influenced samples are suggestive of either the dissolution of phosphatic debris by hydrothermal fluids and loss of MREE, or the primary scavenging of phosphate by hydrothermal plume particulates and subsequent loss of MREE. These observations coincide with dolomite-rich horizons, suggesting that hydrothermal fluid interaction accounts for at least part of the dolomitization within the Montney Formation. The presence of phosphatic debris immediately below this interval suggests that the diagenetic influence from the hydrothermal fluids was localized.

Additionally, early accretion of the Yukon-Tanana terrane is surmised to have occurred by the Early Anisian. This is supported by crossplots of Th/Sc versus Cr/Th, which indicate increasing felsic input up-section. Moreover, plots of La/Sm versus

Yb/Sm show volcanic arc input within the Doig Formation. Collectively, these lines of evidence imply an additional, western source of sediment input by the Anisian. This is significant because it supports the early terrane accretion model (e.g. Beranek et al., 2010) which argues that accretion began during the Triassic along the western coast of Canada.

Overall, this study demonstrates that geochemical trends can be used to correlate fine-grained successions and highlight detailed, chronostratigraphic changes such as relative sealevel, hydrothermal input and climate when lithological homogeneity and poor palaeontological control exist.

References

Adatte, T., Keller, G. and Stinnesbeck, W. (2002) Late Cretaceous to early Paleocene climate and sea-level fluctuations: the Tunisian record. Palaeogeogr. Palaeoclimatol. Palaeoecol., 178, 165–196.

Algeo, T.J. and Lyons, T.W. (2006) Mo-total organic carbon covariation in modern anoxic marine environments: implications for analysis of paleoredox and paleohydrographic conditions. Paleoceanography, 21, PA1016.

Algeo, T.J. and Twitchett, R.J. (2010) Anomalous Early Triassic sediment fluxes due to elevated weathering rates and their biological consequences. Geology, 38, 1023–1026.

Algeo, T.J., Schwark, L. and Hower, J.C. (2004) Highresolution geochemistry and sequence stratigraphy of the Hushpuckney Shale (Swope Formation, eastern Kansas): implications for climate-environmental dynamics of the Late Pennsylvanian Midcontinent Seaway. Chem. Geol., 206, 259–288.

Amorosi, A., Colalongo, M.L., Dinelli, E., Lucchini, F. and Vaiani, S.C. (2007) Cyclic variations in sediment provenance from late Pleistocene deposits of the eastern Po Plain, Italy. In: Sedimentary Provenance and Petrogenesis: Perspectives from Petrography and Geochemistry (Eds J. Arribas, S. Critelli and M.J. Johnsson), GSA Spec. Paper, 420, 13–24.

Anbar, A.D. and Rouxel, O. (2007) Metal stable isotopes in paleoceanography. Annu. Rev. Earth Planet. Sci., 35, 717– 746.

Armstrong-Altrin, J.S., Lee, Y.I., Verma, S.P. and Ramasamy, S. (2004) Geochemistry of sandstones from the Upper Miocene Kudankulam Formation, southern India: implications for provenance, weathering, and tectonic setting. J. Sediment. Res., 74, 285–297.

Arthur, M.A., Jenkyns, H.C. and Brumsack, H.J. (1990) Stratigraphy, geochemistry, and paleoceanography of organic carbon-rich Cretaceous sequences. In: Cretaceous Resources, Events and Rhythms (Eds. R.N. Ginsburg and B. Beaudoin), pp. 75–119. Kluwer Academic Publishing, Amsterdam.

Asael, D., Tissot, F.L.H., Reinhard, C.T., Rouxel, O., Dauphas, N., Lyons, T., Ponzevera, E., Liorzou, C. and Ch_eron, S. (2013) Coupled molybdenum, iron

and uranium stable isotopes as oceanic paleoredox proxies during the Paleoproterozoic Shunga Event. Chem. Geol., 362, 193–210.

Banner, J.L. (1995) Application of the trace element and isotope geochemistry of strontium to studies of carbonate diagenesis. Sedimentology, 42, 805–824.

Barclay, J.E., Krause, E.E., Campbell, R.I. and Utting, J. (1990) Dynamic casting and growth faulting: Dawson Creek Graben Complex, Carboniferous- Permian Peace River Embayment, western Canada. In: Geology of the Peace River Arch (Eds S.C. O'Connell and J.S. Bell), Bulletin of Canadian Petroleum Geology, 38A, 115–145.

Beatty, T.W., Zonneveld, J.-P. and Henderson, C.M. (2008) Anomalously diverse Early Triassic ichnofossil assemblages in northwest Pangaea: a case for a shallowmarine habitable zone. Geology, 36, 771–774.

Benedicto, A., Degueldre, C. and Missana, T. (2014) Gallium sorption on montmorillonite and illite colloids: experimental study and modeling by ionic exchange and surface complexation. Appl. Geochem., 40, 43–50.

Beranek, L.P. and Mortensen, J.K. (2011) The timing and provenance record of the Late Permian Klondike orogeny in northwestern Canada and arc-continent collision along western North America. Tectonics, 30, TC5017.

Beranek, L.P., Mortensen, J.K., Orchard, M.J. and Ullrich, T. (2010) Provenance of North American Triassic strata from west-central and southeastern Yukon:

correlations with coeval strata in the Western Canada Sedimentary Basin and Canadian Arctic Islands. Can. J. Earth Sci., 47, 53–73.

Bergstrom, S.M., Young, S. and Schmitz, B. (2010) Katian (Upper Ordovician) d13C chemostratigraphy and sequence stratigraphy in the United States and Baltoscandia: a regional comparison. Palaeogeogr. Palaeoclimatol. Palaeoecol., 296, 217–234.

Berner, R.A. and Westrich, J.T. (1985) Bioturbation and the early diagenesis of carbon and sulphur. Am. J. Sci., 285, 193–206.

Bhatia, M.R. and Crook, K.A.W. (1986) Trace element characteristics of graywackes and tectonic setting discrimination of sedimentary basins. Contrib. Miner. Petrol., 92, 181–193.

Blakey, R. (2006) Mollwide plate tectonic maps. Available at: http://jan.ucc.nau.edu/rb7/mollglobe.html

Bonjour, J.L. and Dabard, M.P. (1991) Ti/Nb ratios of clastic terrigenous sediments used as an indicator of provenance. Chem. Geol., 91, 257–267.

Bracciali, L., Marroni, M., Pandolfi, L. and Rocchi, S. (2007) Geochemistry and petrography of Western Tethys Cretaceous sedimentary covers (Corsica and Northern Apennines): from source areas to configuration of margins. In: Sedimentary Provenance and Petrogenesis: Perspectives from Petrography and Geochemistry (Eds J. Arribas, S. Critelli and M.J. Johnsson), GSA Spec. Paper, 420, 73–93.

Brumsack, H.-J. (2006) The trace metal content of recent organic carbon-rich sediments: implications for Cretaceous black shale formation. Palaeogeogr. Palaeoclimatol. Palaeoecol., 232, 344–361.

Calvert, S.E. and Pedersen, T.F. (1993) Geochemistry of recent oxic and anoxic marine sediments: implications for the geological record. Mar. Geol., 113, 67–88.

Canfield, D.E., Thamdrup, B. and Hansen, J.W. (1993) The anaerobic degradation of organic matter in Danish coastal sediments: iron reduction, manganese reduction, and sulfate reduction. Geochim. Cosmochim. Acta, 57, 3867– 3883.

Carpenter, S.J. and Lohmann, K.C. (1992) Sr/Mg ratios of modern marine calcite: empirical indicators of ocean chemistry and precipitation rate. Geochim. Cosmochim. Acta, 56, 1837–1849.

Chamley, H. (1989) Clay Sedimentology. Springer-Verlag, Berlin, Heidelberg, 623 pp.

Chappaz, A., Lyons, T.W., Gregory, D.D., Reinhard, C.T., Gill, B.C., Li, C. and Large, R.R. (2014) Does pyrite act as an important host for molybdenum in modern and ancient euxinic sediments? Geochim. Cosmochim. Acta, 126, 112– 122.

Chaudhri, A.R. and Singh, M. (2012) Clay minerals as climate change indicators-a case study. Am J Climate Change, 1, 231–239.

Chen, Y., Twitchett, R.J., Jiang, H., Richoz, S., Lai, Z., Yan, C., Sun, Y., Liu, X. and Wang, L. (2013) Size variation of conodonts during the Smithian-Spathian (Early Triassic) global warming event. Geology, 41, 823–826.

Chenot, E., Pellenard, P., Martinez, M., Deconinck, J.-F., Amiotte-Suchet, P., Thibault, N., Bruneau, L., Cocquerez, T., Laffont, R., Puc_eat, E. and Robaszynski, R. (2016) Clay mineralogical and geochemical expressions of the "Late Campanian Event" in the Aquitaine and Paris basins (France): palaeoenvironmental implications. Palaeogeogr. Palaeoclimatol. Palaeoecol., 447, 42–52.

Cingolani, C.A., Manassero, M. and Abre, P. (2003) Composition, provenance and tectonic setting of Ordovician siliciclastic rocks in the San Rafael block: southern extension of the Precordillera crustal fragment, Argentina. J. S. Am. Earth Sci., 16, 91–106.

Clift, P.D., Wan, S. and Blusztajn, J. (2014) Reconstructing chemical weathering, physical erosion and monsoon intensity since 25 Ma in the northern South China Sea: a review of competing proxies. Earth Sci. Rev., 130, 86–102.

Condie, K.C. and Wronkiewicz, D.J. (1989) The Cr/Th ratio in Precambrian pelites from the Kaapvaal Craton as an index of craton evolution. Earth Planet. Sci. Lett., 97, 256–267.

Croudace, I.W., Rindby, A. and Rothwell, R.G. (2006) ITRAX: Description and Evaluation of a New Multifunction X-ray Core Scanner. Geological Society Special Publications, London, pp. 51–63.

Curtis, C.D., Coleman, M.L. and Love, L.G. (1986) Pore water evolution during sediment burial from isotopic and mineral chemistry of calcite, dolomite and siderite concretions. Geochim. Cosmochim. Acta, 50, 2321–2334.

Cuven, S., Francus, P. and Lamoureux, S.F. (2010) Estimation of grain size variability with micro X-ray fluorescence in laminated sediments, Cape Bounty, Canadian High Arctic. J. Paleolimnol., 88, 803–817.

Dai, S., Ren, D., Chou, C.-L., Li, S. and Jiang, Y. (2006) Mineralogy and geochemistry of the No. 6 Coal (Pennsylvanian) in the Junger coalfield, Ordos Basin, China. Int. J. Coal Geol., 66, 253–270.

Dai, S., Li, D., Chou, C.-L., Zhao, L., Zhang, Y., Ren, D., Ma, Y. and Sun, Y. (2008) Mineralogy and geochemistry of boehmite-rich coals: new insights from the Haerwusa Surface Mine, Jungar Coalfield, Inner Mongolia, China. Int. J. Coal Geol., 74, 185–202.

Dai, S., Ren, D., Chou, C.-L., Finkelman, R.B., Seredin, V.V. and Zhou, Y. (2012a) Geochemistry of trace elements in Chinese coals: a review of abundances, genetic types, impacts on human health, and industrial utilization. Int. J. Coal Geol., 94, 3–21.

Dai, S., Zhou, J., Jiang, Y., Ward, C.R., Wang, X., Li, T., Xue, W., Liu, S., Tian, H., Sun, X. and Zhou, D. (2012b) Mineralogical and geochemical compositions of the Pennsylvanian coal in the Adaohai Mine, Daqingshan Coalfield, Inner Mongolia, China: modes of occurrence and origin of diaspora, gorceixite, and ammonian illite. Int. J. Coal Geol., 94, 250–270.

Davies, G.R. (1997) The Triassic of the Western Canada Sedimentary Basin: tectonic and stratigraphic framework, paleogeography, paleoclimate and biota. Bull. Can. Pet. Geol., 45, 434–460.

Davies, G.R., Moslow, T.F. and Sherwin, M.D. (1997) The Lower Triassic Montney Formation, west-central Alberta. In: Triassic of the Western Canada Sedimentary Basin (Eds T.F. Moslow and J. Wittenberg), Bulletin of Canadian Petroleum Geology, 45, 474–505.

Dean, W., Anderson, R., Bradbury, J.P. and Anderson, D. (2002) A 1500-year record of climatic and environmental change in Elk Lake, Minnesota-I: a varve thickness and gray-scale density. J. Paleolimnol., 27, 287–299. Deutsch, C.V. (2002) Geostatistical Reservoir Modeling. Oxford University Press, New York, NY, 376 pp.

Dinelli, E., Tateo, F. and Summa, V. (2007) Geochemical and mineralogical proxies for grain size in mudstones and siltstones from the Pleistocene and Holocene of the Po River alluvial plain, Italy. From source areas to configuration of margins. In: Sedimentary Provenance and Petrogenesis: Perspectives from Petrography and Geochemistry (Eds J. Arribas, S. Critelli and M.J. Johnsson), GSA Spec. Paper, 420, 25–36.

Dixon, J. (2000) Regional lithostratigraphic units in the Triassic Montney Formation of western Canada. Bull. Can. Pet. Geol., 48, 80–83.

Edwards, D.E., Barclay, J.E., Gibson, D.W., Kvill, G.E. and Halton, E. (1994) Triassic strata of the Western Canada Sedimentary Basin. In: Geological Atlas of the

Western Canada Sedimentary Basin, Canadian Society of Petroleum Geologists and Alberta Research Council (Eds G.D. Mossop and I. Shetsen). Available at: http://www.ags.gov.ab.ca/publications/wcsb_atlas/atlas.html.

Ellwood, B.B., Tomkin, J.H., Ratcliffe, K.T., Wright, M. and Kafafy, A.M. (2008) High-resolution magnetic susceptibility and geochemistry for the Cenomanian/Turonian boundary GSSP with correlation to time equivalent core. Palaeogeogr. Palaeoclimatol. Palaeoecol., 261, 105–126.

Embry, A.F. and Gibson, D.W. (1995) T-R sequence analysis of the Triassic succession of the Western Canada Sedimentary Basin. In: Proceedings of the Oil and Gas Forum '95 - Energy from Sediments' (Eds J.S. Bell, T.D. Bird, T.L. Hillier and E.L. Greener), Geological Survey of Canada, Open File 3058, 25–32.

Esser, K.B., Bockheim, J.G. and Helmke, P.A. (1991) Trace element distribution in soils formed in the Indiana Dunes, U.S.A. Soil Sci., 152, 340–350.

Feely, R.A., Massoth, G.J., Trefry, J.H., Baker, E.T., Paulson, A.J. and Lebon, G.T. (1994) Composition and sedimentation of hydrothermal plume particles from North Cleft segment, Juan de Fuca Ridge. J. Geophys. Res., 99, 4985–5006.

Fein, J.B., Daughney, C.J., Yee, N. and Davis, T.A. (1997) A chemical equilibrium model for metal adsorption onto bacterial surfaces. Geochim. Cosmochim.Acta, 61, 3319–3328.

Ferri, F. and Zonneveld, J.-P. (2008) Were Triassic rocks of the Western Canada Sedimentary Basin deposited in a Foreland? Can. Soc. Petrol. Geol. Reservoir, 35, 12–14.

Froelich, P.N., Klinkhammer, G.P., Bender, M.L., Luedtke, N.A., Heath, G.R., Cullen, D., Dauphin, P., Hammond, D., Hartman, B. and Maynard, V. (1979) Early oxidation of organic matter in pelagic sediments of the eastern equatorial Atlantic: suboxic diagenesis. Geochim. Cosmochim. Acta, 43, 1075–1090.

Gadd, G.M. (2010) Metals, minerals and microbes: geomicrobiology and bioremediation. Microbiology, 156, 609–643.

Galfetti, T., Hochuli, P.A., Brayard, A., Bucher, H., Weissert, H. and Os Vigran, J. (2007a) Smithian-Spathian boundary event: evidence for global climatic change in the wake of the end-Permian biotic crisis. Geology, 35, 291–294.

Galfetti, T., Bucher, H., Braynard, A., Hochuli, P.A., Weissert, H., Guodun, H., Atudorei, V. and Guex, J. (2007b) Late Early Triassic climate change: insights from carbonate carbon isotopes, sedimentary evolution and ammonoid paleobiogeography. Palaeogeogr. Palaeoclimatol. Palaeoecol., 243, 394–411.

Golding, M.L., Orchard, M.J., Zonneveld, J.-P., Henderson, C.M. and Dunn, L. (2014) An exceptional record of the sedimentology and biostratigraphy of the Montney and Doig formations in British Columbia. Bull. Can. Pet. Geol., 62, 157–176.

Golonka, J. and Ford, D. (2000) Pangean (Late Carboniferous – Middle Jurassic) paleoenvironment and lithofacies. Palaeogeogr. Palaeoclimatol. Palaeoecol., 161, 1–34.

Golonka, J., Ross, M.I. and Scotese, C.R. (1994) Phanerozoic paleogeographic and paleoclimatic modeling maps. In: Pangea: Global Environment and Resources (Eds A.F. Embry, B. Beauchamp and D.J. Glass), CSPG Memoir, 17, 1–47.

Haq, B.V., Hardenbol, J., Vail, R.R., Colin, J.P., Ioannides, N., Stover, L.E., Jan Du Chene, R., Wright, R.C., Sarq, J.F. and Morgan, B.E. (1987) Mesozoic-cenozoic cycle chart, Version 3.IB. American Association of Petroleum Geologists.

Hays, L.E., Beatty, T.W., Henderson, C.M., Love, G.D. and Summons, R.E. (2007) Evidence for photic zone euxinia through the end-Permian mass extinction in the Panthalassic Ocean (Peace River Basin, Western Canada). Palaeoworld, 16, 39–50.

Hildred, G.V., Ratcliffe, K.T., Wright, A.M., Zaitlin, B.A. and Wray, D.S. (2010) Chemostratigraphic applications to low-accommodation fluvial incised-valley settings: an example from the lower Mannville Formation of Alberta, Canada. J. Sediment. Res., 80, 1032–1045.

Hofer, G., Wagreich, M. and Neuhuber, S. (2013) Geochemistry of fine-grained sediments of the upper Cretaceous to Paleogene Gosau Group (Austria, Slovakia): implications for paleoenvironmental and provenance studies. Geosci. Front., 4, 449–468.

Hofmann, A., Bolhar, R., Dirks, P. and Jelsma, H. (2003) The geochemistry of Archaean shales derived from a mafic volcanic sequence, Belingwe greenstone belt, Zimbabwe: provenance, source area unroofing and submarine versus subaerial weathering. Geochim. Cosmochim. Acta, 67, 421–440.

Hofmann, P., Ricken, W., Schwark, L. and Leythaeuser, D. (2001) Geochemical signature and related climateoceanographic processes for early Albian black shales: Site 417D, North Atlantic Ocean. Cretac. Res. 22, 243–257.

Israel, M.B., Enzel, Y., Amit, R. and Erel, Y. (2015) Provenance of the various grain-size fractions in the Negev loess and potential changes in major dust sources to the Eastern Mediterranean. Quatern. Res., 83, 105–115.

Jarvis, I. and Jarvis, K. (1992) Plasma spectrometry in the earth sciences: techniques, applications and future trends. Chem. Geol., 95, 1–33.

Jin, X., Shah, S.N., Roegiers, J.-C. and Zhang, B. (2015) An integrated petrophysics and geomechanics approach for fracability evaluation in shale reservoirs. SPE J., 20, 518–526.

Johnson, R.A. and Wichern, D.W. (1988) Applied Multivariate Statistical Analysis. Prentice Hall, New Jersey, p. 773.

Keller, G., Jaiprakash, B.C. and Reddy, A.N. (2016) Maastrichtian to Eocene subsurface stratigraphy of the Cauvery Basin and correlation with Madagascar. J. Geol. Soc. India, 87, 5–34.

Kendall, B., Gordon, G.W., Poulton, S.W. and Anbar, A.D. (2011) Molybdenum isotope constraints on the extent of late Paleoproterozoic ocean euxinia. Earth Planet. Sci. Lett., 307, 450–460.

Lalonde, S.V., Smith, D.S., Owttrim, G.W. and Konhauser, K.O. (2008) Acid-base properties of cyanobacterial surfaces I: influences of growth phase and nitrogen metabolism on cell surface reactivity. Geochim. Cosmochim. Acta, 72, 1257–1268.

Lev, S.M., McLennan, S.M. and Hanson, G.N. (1999) Mineralogic controls on REE mobility during black-shale diagenesis. J. Sediment. Res., 69, 1071–1082.

Li, L., Keller, G., Adatte, T. and Stinnesbeck, W. (2000) Late Cretaceous sea-level changes in Tunisia: a multidisciplinary approach. J. Geol. Soc. London, 157, 447–458.

Liang, A., Paulo, C., Zhu, Y. and Dittrich, M. (2013) CaCO3 biomineralization on cyanobacterial surfaces: Insights from experiments with three Synechococcus strains. Colloids Surf. B, 111, 600–608.

Liermann, L.J., Mathur, R., Wasylenki, L.E., Nuester, J., Anbar, A.D. and Brantley, S.L. (2011) Extent and isotopic composition of Fe and Mo release from two Pennsylvania shales in the presence of organic ligands and bacteria. Chem. Geol., 281, 167–180.

Lopez de Luchi, M.G., Cerredo, M.E., Siegesmund, S., Steenken, A. and Wemmer, K. (2003) Provenance and tectonic setting of the protoliths of the Metamorphic Complexes of Sierra de San Luis. Rev. Asoc. Geol. Argentina, 58, 525–540.

MacNaughton, R.B. and Zonneveld, J.-P. (2010) Trace-fossil assemblages in the Lower Triassic Toad Formation, La Biche River map area, southeastern Yukon. Bull. Can. Pet. Geol., 58, 100–114.

McLennan, S.M., Hemming, S., McDaniel, D.K. and Hanson, G.N. (1993) Geochemical approaches to sedimentation, provenance, and tectonics. Geol. Soc. Am. Spec. Pap., 284, 21–40.

McLennan, S.M., Taylor, S.R., McCulloch, M.T. and Maynard, J.B. (1990) Geochemical and Nd-Sr isotopic composition of deep-sea turbidites: crustal evolution and plate tectonic associations. Geochem. Cosmochim. Acta, 54, 2015–2050.

Meinhold, G., Kostopoulos, D. and Reischmann, T. (2007) Geochemical constraints on the provenance and depositional setting of sedimentary rocks from the islands of Chios, Inousses and Psara, Aegean Sea, Greece: implications for the evolution of Palaeotethys. J. Geochem. Soc. London, 164, 1145–1163.

Mongelli, G., Critelli, S., Perri, F., Sonnino, M. and Perrone, V. (2006) Sedimentary recycling, provenance and paleoweathering from chemistry and mineralogy of Mesozoic continental red-bed mudrocks, Peloritani mountains, southern Italy. Geochem. J., 40, 197–209.

Morton, J.P. (1985) Rb-Sr evidence for punctuated illite/ smectite diagenesis in the Oligocene Fio Formation, Texas Gulf Coast. Geol. Soc. Am. Bull., 96, 114–122.

Morton, A.C. and Hallsworth, C. (1994) Identifying provenance-specific features of detrital heavy mineral assemblages in sandstones. Sed. Geol., 90, 241–256.

Morton, A.C., Hallsworth, C.R. and Moscariello, A. (2005) Interplay between northern and southern sediment sources during Westphalian deposition in the Silverpit Basin, southern North Sea. In: Carboniferous hydrocarbon geology: the southern North Sea and surrounding onshore areas (Eds J.D. Collinson, D.J. Evans, D.S. Holliday and N.S. Jones). Yorkshire Geological Society Occasional Publication, Vol. 7, 135–146.

Morton, A. and Yaxley, G. (2007) Detrital apatite geochemistry and its application in provenance studies. Geol. Soc. Am. Spec. Pap., 420, 319–344.

Moslow, T.F. (2000) Reservoir architecture of a fine-grained turbidite system: lower Triassic Montney Formation, Western Canada Sedimentary Basin. In: Deep-water Reservoirs of the World (Eds P.Weimer, R.M. Slatt, J. Coleman, N.C. Rosen, H. Nelson, A.H. Bouma, M.J. Styzen and D.T. Lawrence). Conference Proceedings, Gulf Coast SEPM, 686–713.

Moslow, T.F. and Davies, G.R. (1997) Turbidite reservoir facies in the Lower Montney Formation, west-central Alberta. In: Triassic of the Western Canada Sedimentary Basin (Eds T.F. Moslow and J. Wittenberg), Bulletin of Canadian Petroleum Geology, 45, 507–536.

Nance, H.S. and Rowe, H. (2015) Eustatic controls on stratigraphy, chemostratigraphy, and water mass evolution preserved in a Lower Permian mudrock succession, Delaware Basin, west Texas, USA. Interpretation, 3, SH11– SH25.

North, C.P., Hole, M.J. and Jones, D.G. (2005) Geochemical correlation in deltaic successions: a reality check. Geol. Soc. Am. Bull., 117, 620–632.

Orchard, M.J. and Tozer, E.T. (1997) Triassic conodont biochronology, its calibration with the ammonoid standard, and a biostratigraphic summary for the Western Canada Sedimentary Basin. Bull. Can. Pet. Geol., 45, 675– 692.

Orchard, M.J. and Zonneveld, J.-P. (2009) The Lower Triassic Sulphur Mountain Formation in the Wapiti Lake area: lithostratigraphy, conodont biostratigraphy, and a new biozonation for the lower Olenekian (Smithian). Can. J. Earth Sci., 46, 757–790.

Paktunc, A.D. and Cabri, L.J. (1995) A proton- and electronmicroprobe study of gallium, nickel and zinc distribution in chromium spinel. Lithos, 35, 261–282.

Patchett, P.J., White, W.M., Feldmann, H., Kielinczuk, S. and Hofmann, A.W. (1984) Hafnium/rare earth element fractionation in the sedimentary system and crustal recycling into the Earth's mantle. Earth Planet. Sci. Lett., 69, 365–378.

Paull, R.K., Paull, R.A. and Laudon, T.S. (1997) Conodont biostratigraphy of the Lower Triassic Mackenzie Dolomite Lentil, Sulphur Mountain Formation in the Cadomin area, Alberta. Bull. Can. Pet. Geol., 45, 708–714.

Pearce, T.J., Besly, B.M., Wray, D.S. and Wright, D.K. (1999) Chemostratigraphy: a method to improve inter-well correlation in barren sequences – a case study using onshore Duckmantian/Stephanian sequences (West Midlands, U.K.). Sed. Geol., 124, 197–220.

Pearce, T.J., Wray, D., Ratcliffe, K., Wright, D.K. and Moscariello, A. (2005) Chemostratigraphy of the Upper Carboniferous Schooner Formation, southern North Sea. In: Carboniferous Hydrocarbon Resources: The Southern North Sea and Surrounding Onshore Areas (Eds J.D. Collinson, D.J. Evans, D.W. Holliday and N.S. Jones), Occasional Publications Series of the Yorkshire Geological Society, 7, 165–182.

Pearce, T.J., Martin, J.H., Cooper, D. and Wray, D.S. (2010) Chemostratigraphy of Upper Carboniferous (Pennsylvanian) sequences from the southern North Sea (United Kingdom). In: Application of Modern Stratigraphic Techniques: Theory and Case Histories (Eds K. Ratcliffe and B.A. Zaitlin), SEPM Spec. Publ., 94, 109–127.

Pelechaty, S. (1998) Integrated chronostratigraphy of the Vendian system of Siberia: implications for a global stratigraphy. J. Geol. Soc. London, 155, 957–973.

Petrash, D.A., Gueneli, N., Brocks, J.J., M_endez, J.A., Gonzalez-Arismentdi, G., Poulton, S.W. and Konhauser, K.O. (2016) Black shale deposition and early diagenetic dolomite cementation during Oceanic Anoxic Event 1: the mid-Cretaceous Maracaibo Platform, northwestern South America. Am. J. Sci., 316, 669–711.

Pett-Ridge, J.C., Derry, L.A. and Kurtz, A.C. (2009) Sr isotopes as a tracer of weathering processes and dust inputs in a tropical granitoid watershed, Luquillo Mountains, Puerto Rico. Geochim. Cosmochim. Acta, 73, 25–43.

Pierson, B.J. (1981) The control of cathodoluminescence in dolomite by iron and manganese. Sedimentology, 28, 601– 610.

Planavsky, N.J., Asael, D., Hofmann, A., Reinhard, C.T., Lalonde, S.V., Knudsen, A., Wang, X., Ossa Ossa, F., Pecoits, E., Smith, A.J.B., Beukes, N.J., Bekker, A., Johnson, T.M., Konhauser, K.O., Lyons, T.W. and Rouxel, O.J. (2014) Evidence for oxygenic photosynthesis half a billion years before the Great Oxidation Event. Nat. Geosci., 7, 283–286.

Plank, T. and Langmuir, C.H. (1998) The chemical composition of subducting sediment and its consequences for the crust and mantle. Chem. Geol., 145, 325–394.

Playter, T., Konhauser, K., Owttrim, G., Hodgson, C., Warchola, T., Mloszewska, A.M., Sutherland, B., Bekker, A., Zonneveld, J.-P., Pemberton, S.G. and Gingras, M. (2017) Microbe-clay interactions as a mechanism for the preservation of organic matter and trace metal biosignatures in black shales. Chem. Geol., 459, 75–90.

Pokrovsky, O.S., Martinez, R.E., Kompantzeva, E.I. and Shirokova, L.S. (2014) Surface complexation of the phototrophic anoxygenic non-sulfur bacterium Rhodopseudomonas palustris. Chem. Geol., 383, 51–62.

Preston, J., Hartley, A., Hole, M., Buck, S., Bond, J., Mange, M. and Still, J. (1998) Integrated whole-rock trace element geochemistry and heavy mineral chemistry studies: aids to correlation of continental red-bed reservoirs in the Beryl Field, UK North Sea. Petrol. Geosci., 4, 7–16.

Rabouille, C. and Gaillard, J.-F. (1991) Towards the EDGE: Early diagenetic global explanation. A model depicting the early diagenesis of organic matter, O2, NO3, Mn and PO4. Geochim. Cosmochim. Acta, 55, 2511–2525.

Ratcliffe, K.T., Wright, A.M., Hallsworth, C., Morton, A., Zaitlin, B.A., Potocki, D. and Wray, D.S. (2004) An example of alternative correlation techniques in a lowaccommodation setting, non-marine hydrocarbon system: the (Lower Cretaceous) Mannville Basal Quartz succession of southern Alberta. AAPG Bull., 88, 1419–1432.

Ratcliffe, K.T., Martin, J., Pearce, T.J., Hughes, A.D., Lawton, D.E., Wray, D.S. and Bessa, F. (2006) A regional chemostratigraphically – defined correlation framework for the late Triassic TAG – I Formation in Blocks 402 and 405a, Algeria. Petrol. Geosci., 12, 3–12.

Ratcliffe, K.T., Wright, A.M., Montgomery, P., Palfrey, A., Vonk, A., Vermeulen, J. and Barrett, M. (2010) Application of chemostratigraphy to the Mungaroo Formation, the Gorgon Field, offshore Northwest Australia. APPEA Journal, 50th Anniversary Issue, 371–388.

Ratcliffe, K.T., Wright, A.M. and Schmidt, K. (2012) Application of inorganic whole – rock geochemistry to shale resource plays: an example from the Eagle Ford Shale Formation, Texas. Sed. Rec., 10, 4–9.

Ratcliffe, K.T., Wilson, A., Payenberg, T., Rittersbacher, A., Hildred, G.V. and Flint, S.S. (2015) Ground truthing chemostratigraphic correlations in fluvial systems. AAPG Bull., 99, 155–180.

Reategui, K., Mart_ınez, M., Esteves, I., Guti_errez, J.V., Mart_ınez, A., Mel_endez, W. and Urbani, F. (2005) Geochemistry of the Mirador Formation (Late Eocene – Early Oligocene) southwestern Venezuela: chemostratigraphic constraints on provenance and the influence of the sea level. Geochem. J., 39, 213–226.

Reddy, M.R. and Perkins, H.F. (1974) Fixation of zinc by clay minerals. Soil Sci. Soc. Am. J., 38, 229–231. Reinhard, C.T., Planavsky, N.J., Wang, X., Fischer, W.W., Johnson, T.M. and Lyons, T.W. (2014) The isotopic composition of authigenic chromium in anoxic marine sediments: a case study from the Cariaco Basin. Earth Planet. Sci. Lett., 407, 9–18.

Retallack, G.J., Holser, W.T. and Isozaki, Y. (1997) Timing of Permian-Triassic anoxia. Science, 277, 1748–1749.

Richards, B.C., Barclay, J.E., Bryan, D., Hartling, A., Henderson, C.M. and Hinds, R.C. (1994) Carboniferous strata of the Western Canada Sedimentary Basin. In: Geological Atlas of the Western Canada Sedimentary Basin (Eds G.D. Mossop and I. Shetsen), Canadian Society of Petroleum Geologists and Alberta Research Council, 221–250.

Romano, C., Goudemand, N., Vennemann, T.W., Ware, D., Schneebeli-Hermann, E., Hochuli, P.A., Br€uhwiler, T., Brinkmann, W. and Bucher, H. (2013) Climatic and biotic upheavals following the end-Permian mass extinction. Nat. Geosci., 6, 57–60.

Rowe, H., Hughes, N. and Robinson, K. (2012) The quantification and application of handheld energydispersive x-ray fluorescence (ED-XRF) in mudrock chemostratigraphy and geochemistry. Chem. Geol., 324– 325, 122–131.

Ruffell, A.H. and Batten, D.J. (1990) The Barremian-Aptian arid phase in Western-Europe. Palaeogeogr. Palaeoclimatol. Palaeoecol., 80, 197–212.

Ruffell, A.H., Price, G.D., Mutterlose, J., Kessels, K., Baraboshkin, E. and Grocke, D.R. (2002a) Palaeoclimate indicators (clay minerals, calcareous nannofossils, stable isotopes) compared from two successions in the late Jurassic of the Volga Basin (SE Russia). Geol. J., 37, 17–33.

Ruffell, A., McKinley, J.M. and Worden, R.H. (2002b) Comparison of clay mineral stratigraphy to other proxy palaeoclimate indicators in the Mesozoic of NW Europe. Phil. Trans. Roy. Soc. London, 360, 675–693.

Rukhlov, A.S. and Pawlowicz, J.G. (2011) Magmatism and metallic mineralization of the Rocky Mountain Fold-and- Thrust Belt in Southwestern Alberta (NTS 82G, H and J): mineralogy, geochemistry and petrology of selected occurrences. ERCB/AGS Open File Report, 2011-11, 88 pp.

Sanei, H., Haeri-Ardakani, O., Wood, J.M. and Curtis, M.E. (2015) Effects of nano-porosity and surface imperfections on solid bitumen reflectance (BRo) measurements in unconventional reservoirs. Int. J. Coal Geol., 138, 95–102.

Svendsen, J., Friis, H., Stollhofen, H. and Hartley, N. (2007) Facies discrimination in a mixed fluvio-eolian setting using elemental whole-rock geochemistry – applications for reservoir characterization. J. Sediment. Res., 77, 23–33.

Takahashi, Y., Minai, Y., Ambe, S., Makide, Y. and Ambe, F. (1999) Comparison of adsorption behavior of multiple inorganic ions on kaolinite and silica in the presence of humic acid using the multi-tracer technique. Geochim. Cosmochim. Acta, 63, 815–836.

Tan, P., Steinbeck, M. and Kumar, V. (2006) Introduction to Data Mining, 2nd edn. Pearson Education, New York, p. 769.

Thiry, M. (2000) Palaeoclimatic interpretation of clay minerals in marine deposits: an outlook from the continental origin. Earth-Sci. Rev., 49, 201–221.

Totten, M.W., Hanan, M.A. and Weaver, B.L. (2000) Beyond whole-rock geochemistry of shales: the importance of assessing mineralogical controls for revealing tectonic discriminants of multiple sediment sources for the Ouchita Mountain flysch deposits. Geol. Soc. Am. Bull., 112, 1012–1022.

Tozer, E.T. (1994) Canadian Triassic ammonoid faunas. Geol. Sur. Can. Bull., 467, 1–663. Tribovillard, N., Algeo, T.J., Lyons, T. and Ribouleau, A. (2006) Trace

metals as paleoredox and paleoproductivity proxies: an update. Chem. Geol., 232, 12–32.

Tyler, G. (2004) Vertical distribution of major, minor, and rare elements in a Haplic Podzol. Geoderma, 119, 277–290.

Utting, J., MacNaughton, R.B., Zonneveld, J.-P. and Fallas, K. (2005) Palynostratigraphy, organic matter and thermal maturity of the Lower Triassic Toad, Grayling and Montney formations of Yukon, British Columbia and Alberta and comparison with the Sverdrup Basin, Nunavut. Bull. Can. Pet. Geol., 53, 5–24.

Wang, W., Qin, Y., Lui, X., Zhao, J., Wang, J., Wu, G. and Lui, J. (2011) Distribution, occurrence and enrichment causes of gallium in coals from the Jungar Coalfield, Inner Mongolia. Sci. China Earth Sci., 54, 1053–1068.

Ward, J.H., Jr (1963) Hierarchical grouping to optimize an objective function. J. Am. Stat. Assoc., 58, 236–244.

Wedepohl, K.H. (1971) Environmental influences on the chemical composition of shales and clays. In: Physics and Chemistry of Earth (Eds L.H. Ahrens, F. Press, S.K. Runcorn and H.C. Urey), 8, 307–331.

Wei, G., Liu, Y., Li, X., Shao, L. and Liang, X. (2003) Climatic impact on Al, K, Sc and Ti in marine sediments: evidence from ODP Site 1144, South China Sea. Geochem. J., 37, 593–602.

Wheat, C.G., Feely, R.A. and Mottl, M.J. (1996) Phosphate removal by oceanic hydrothermal processes: an update of the phosphorus budget in the oceans. Geochim. Cosmochim. Acta, 60, 3593–3608.

Wood, J.M., Sanei, H., Curtis, M.E. and Clarkson, C.R. (2015) Solid bitumen as a determinant of reservoir quality in an unconventional tight gas siltstone play. Int. J. Coal Geol., 150–151, 287–295.

Wright, A.M., Ratcliffe, K.T., Zaitlin, B.A. and Wray, D.S. (2010) The application of chemostratigraphic techniques to distinguish compound incised valleys in low accommodation incised valley systems in a foreland-basin setting: an example from the Lower Cretaceous Mannville Group and Basal Colorado Sandstone (Colorado Group), Western Canadian Sedimentary Basin. In: Application of Modern Stratigraphic Techniques, Theory and Case Histories (Eds K. Ratcliffe and B.A. Zaitlin), SEPM Spec. Publ., 94, 93–107.

Zhao, M.-Y. and Zheng, Y.-F. (2015) The intensity of chemical weathering: Geochemical constraints from marine detrital sediments of Triassic age in South China. Chem. Geol., 391, 111–122.

Zonneveld, J.-P., Beatty, T.W. and Pemberton, S.G. (2007) Lingulide brachiopods and the trace fossil Lingulichnus from the Triassic of Western Canada: implications for faunal recovery after the end-Permian mass extinction. Palaios, 22, 74–97.

Zonneveld, J.-P., Gingras, M.K. and Beatty, T.W. (2010a) Diverse ichnofossil assemblages following the P-T mass extinction, Lower Triassic, Alberta and

British Columbia, Canada: evidence for shallow marine refugia on the northwestern coast of Pangaea. Palaios, 25, 368–392.

Zonneveld, J.-P., Golding, M., Moslow, T.F., Orchard, M.J., Playter, T. and Wilson, N. (2011) Depositional framework of the lower triassic montney formation, west-central Alberta and northeastern British Columbia. In: Canadian Society of Petroleum Geologists, Canadian Society of Exploration Geophysicists, Joint Annual Meeting, Abstracts 2011, pp. 1–4.

Zonneveld, J.-P., MacNaughton, R.B., Utting, J., Beatty, T.W., Pemberton, S.G. and Henderson, C.M. (2010b) Sedimentology and ichnology of the Lower Triassic Montney Formation in the Pedigree-Ring/Border-Kahntah River area, northwestern Alberta and northwestern British Columbia. Bull. Can. Pet. Geol., 58, 115–140.

Supporting Information

Additional Supporting Information, including details pertaining to methods as well as additional figures, may be found in Appendix 2:

Chapter 5: Microbe-clay interactions as a mechanism for preservation of organic matter and trace metal biosignatures in black shales

Introduction

The lithology of organic-rich, black shales consist of quartz, feldspars, carbonates, sulfides, clay minerals, and at least 1 wt% organic material (Arthur and Sageman, 1994; Aplin and Macquaker, 2011). The organic-rich nature of these rocks requires one of, or a combination of, the following conditions: (i) high primary production rates in the water column (Macquaker et al., 2010), (ii) sedimentation rates high enough to induce rapid burial of organic matter (Betts and Holland, 1991; Canfield, 1994; Tyson, 2001), and/or (iii) low organic matter respiration rates (Smith and Hollibaugh, 1993; Kristensen, 2000; Piper and Calvert, 2009). The latter can occur in several ways, including: (i) limited aerobic respiration due to low O_2 penetration into the sediment (Kristensen, 2000); (ii) reduced anaerobic respiration due to a lack of pore-water sulfate (Canfield et al., 1993a, 1993b); or (iii) the sorption of organic material onto clay particles in the water column preventing its degradation by heterotrophic bacteria (Pedersen and Calvert, 1990; Hedges and Keil, 1995; Ransom et al., 1997, 1998; Bennett et al., 1999; Lünsdorf et al., 2000; Tyson, 2001; Kennedy et al., 2002; Macquaker et al., 2010; Aplin and Macquaker, 2011).

In recent years, black shale deposits have been studied extensively to interpret the seawater trace metal concentrations and redox state of the ancient oceans and atmosphere (e.g., Tribovillard et al., 2006; Anbar and Rouxel, 2007; Scott et al., 2008, 2013; Partin et al., 2013; Reinhard et al., 2013; Swanner et al., 2014). This is because the size of a given trace metal seawater reservoir is determined by the

weathering flux from land and the relative influence of the sulfidic and oxic sinks (e.g., Algeo and Maynard, 2004; Scott et al., 2008). Moreover, the clay and organic fractions in these fine-grained sediments are highly reactive, and as such, they capture and preserve the trace element availability in the seawater from which the aggregates settled.

Planktonic cyanobacteria, such as *Synechococcus* and *Prochlorococcus*, are widely distributed throughout the ocean and can occur in cell densities ranging from 10^3 to 10^8 cells per milliliter, with the highest concentrations occurring during the summer months (e.g., Waterbury et al., 1979; Miyazono et al., 1992; Jacquet et al., 1998; Ohkouchi et al., 2006). They have been observed to contribute significantly to the carbon biomass of the water column, and in some cases, they constitute the majority of the biomass (Campbell et al., 1997). Indeed, biomarker analysis (indicating the presence of 2- methylhopanoids or their diagenetic derivatives, C_{35} homohopanoids) and stable carbon isotopic signatures suggest that cyanobacteria have been major contributors to shale deposition from the Neoproterozoic through to the Phanerozoic (Bechtel and Püttmann, 1997; Köster et al., 1998; Kuypers et al., 2004; Dumitrescu and Brassell, 2005; Olcott et al., 2005; Ohkouchi et al., 2006; Duque-Botero and Maurrasse, 2008; Kashiyama et al., 2008). Recent studies have also demonstrated that planktonic cyanobacterial cell surfaces are highly reactive (Lalonde et al., 2008a, 2008b; Liu et al., 2015) and thus capable of accumulating trace metals from solution (e.g., Dittrich and Sibler, 2005; Hadjoudja et al., 2010). That same reactivity has also been shown to facilitate the adsorption of detrital clay particles and the nucleation of authigenic clay phases (e.g., Konhauser et al., 1993,

1998). In this regard, we propose that live, planktonic cyanobacteria (and indeed any reactive microbial cell), such as *Synechococcus*, could increase clay flocculation, thereby facilitating more rapid deposition of cell-clay aggregates to the seafloor. If rapid burial promotes greater preservation of organic carbon, then this mechanism may very well underpin the formation and preservation of black shale deposits in the rock record, and explain their enrichment in trace metals (e.g. Calvert and Pedersen, 1993; Algeo and Maynard, 2004) as being sourced from the remnants of cell biomass. Furthermore, the increased preservation potential of these cell-clay aggregates suggests that the trace metal signatures of reactive bacterial biomass may become incorporated into the sediments over geologic time-scales.

We test this hypothesis by: (1) observing the depositional rates of *Synechococcus* in the presence of clay (kaolinite and montmorillonite); (2) assessing if clay deposition is influenced by cell metabolism; (3) determining the morphology of the clay-cell aggregates and their preservation potential; and ultimately (4) measuring the trace element composition of *Synechococcus* for the purpose of defining their contribution to the trace metal composition of black shales. These clays were chosen because they are common in near-shore, marine (kaolinite; Thiry, 2000) and fluvial/deltaic (montmorillonite; e.g., Taggart and Kaiser, 1960) environments and encompass both a 1:1 (kaolinite) and 2:1 (montmorillonite) tetrahedral structure. Importantly, these clays encompass a range of structural composition and environments of natural occurrence.

Methods

Culturing

Flocculation experiments (n = 18) were performed using *Synechococcus* sp. PCC 7002 (hereafter simply referred to as *Synechococcus*), a sheathless, planktonic, coccoid marine species. Axenic populations were grown in liquid A+ media (Stevens and Porter, 1980), while stock populations were maintained on A+ agar plates at 30 °C. Experimental cultures were grown in liquid media, shaken at 150 rpm and bubbled with filtered and humidified air (Chamot and Owttrim, 2000). Growth was monitored by measuring optical density at 750 nm and chlorophyll *a* (Chl *a*) concentration, as described by Sakamoto and Bryant (1998). Chl *a* concentration was calculated using the formula (Porra et al., 1989): Chl $a = 16.29OD_{665} - 8.54OD_{652}$. Cell concentration, in grams, were calculated using an additional conversion factor of 7.4×10^{10} cells/L = 10 g/L (Liu et al., 2015). Initial concentrations before clay addition (time −1 on the x-axis of Fig. 1) for all experiments involving kaolinite and montmorillonite were determined using a conversion factor (Liu et al., 2015), to calculate initial cell concentration from OD_{750} nm measurements. This was done to ensure repeatability, as the measurement of OD_{750} nm can be accurately measured during culturing. Cultures were killed by autoclaving for 60 min at 121 °C at 18 psi.

Flocculation experiments

Eighteen experiments were performed with both live and heat-killed biomass in order to ascertain whether metabolic activity was the main driver of clay flocculation and to determine whether surface charge continued to facilitate flocculation after cell lysis. Kaolinite [$Al_2Si_2O_5(OH)_4$] (K Ga-2 from the Source Clay Repository of the Clay Minerals Society; sourced from Warren County, Georgia, USA) was used in this study because it is a common 1:1 clay mineral in which the stacked tetrahedral sheet (Si-O tetrahedrons) are hydrogen bonded directly to the octahedral sheet (mainly Al-O octahedrons) through the sharing of oxygen atoms between silicon and aluminum atoms in adjacent sheets. There is almost no substitution of Al^{3+} for Si^{4+}, or Mg^{2+} for Al^{3+}, therefore, their net surface charge is low (e.g., Ikhsan et al., 1999). Kaolinite is a stable product of either prolonged continental weathering or intense chemical weathering in humid tropical environments, and thus it accumulates in a number of near- shore, marine depositional environments (Thiry, 2000).

Montmorillonite [$(Na,Ca)_{0.33}(Al,Mg)_2(Si_4O_{10})(OH)_2{\cdot}nH_2O$] (SWy-2; Na-rich montmorillonite from Cook County, Wyoming, USA) was also used because it is a common 2:1 clay mineral that consists of two tetrahedral sheets bound to either side of an octahedral sheet (dioctahedral aluminum hydroxide). The structural composition of the sheets allows isomorphic substitutions by lower charge cations, which generates a net negative layer charge and leads to strong colloidal characteristics (e.g., Thomas et al., 1999). Montmorillonite is a common constituent of fluvial and deltaic clay, particularly in catchments with volcanic

rocks, such as the Mississippi River (e.g., Taggart and Kaiser, 1960).

During each experiment, a 400 mL cyanobacterial culture was first diluted with A+ media to create a 1 L volume. A+ media was generated using a standard formulation (A+ Medium Recipe, 2017) based on the work of Stevens and Porter (1980) and McClure et al. (2016). Compared to seawater (at 500 mM NaCl salinity), this media has slightly lower concentrations of cations (e.g. 300 mM NaCl and 8 mM KCl; Ludwig and Bryant, 2012). The diluted bacterial culture was incubated in an acrylic 5.1 cm × 20 cm tank in front of a bank of fluorescent lights in a curtained enclosure (see Sutherland et al., 2014 for experimental setup) at room temperature. Clay (kaolinite or montmorillonite) was added to a final concentration of 0.1 g/L, 5 g/L and 50 g/L, chosen to represent the spectrum of suspended load observed in modern estuaries (Kistner and Pettigrew, 2001; Uncles et al., 2006). The mixture was vigorously stirred to produce a semi-homogeneous mixture, and a HD video camera was used to record each experiment. Sampling for Chl *a* concentrations commenced immediately following clay addition and subsequently at 5, 10, 15, 30, 90, 120, 180 and 240 min.

Controls were performed to independently measure the settling rates of the *Synechococcus* in the absence of clay. Additionally, similar controls were used to measure the rate of clay sedimentation in growth media. To rule out the role of suspended load (resulting in lack of light penetration) on cyanobacterial sedimentation by affecting cell metabolism, an additional tank experiment was conducted whereby *Synechococcus* sedimentation rate (via Chl *a* measurements) was measured over time in complete darkness. During this treatment, all the lights were turned off, the blinds were drawn, and the tank was covered with a black

shroud. The chemical behavior of heat-killed *Synechococcus* biomass compared to live cultures also addresses the effect of turbidity (and inferred cell-death) on sedimentation. If both live and heat-killed biomass behave in a similar chemical manner, cell death due to turbidity would not be a factor.

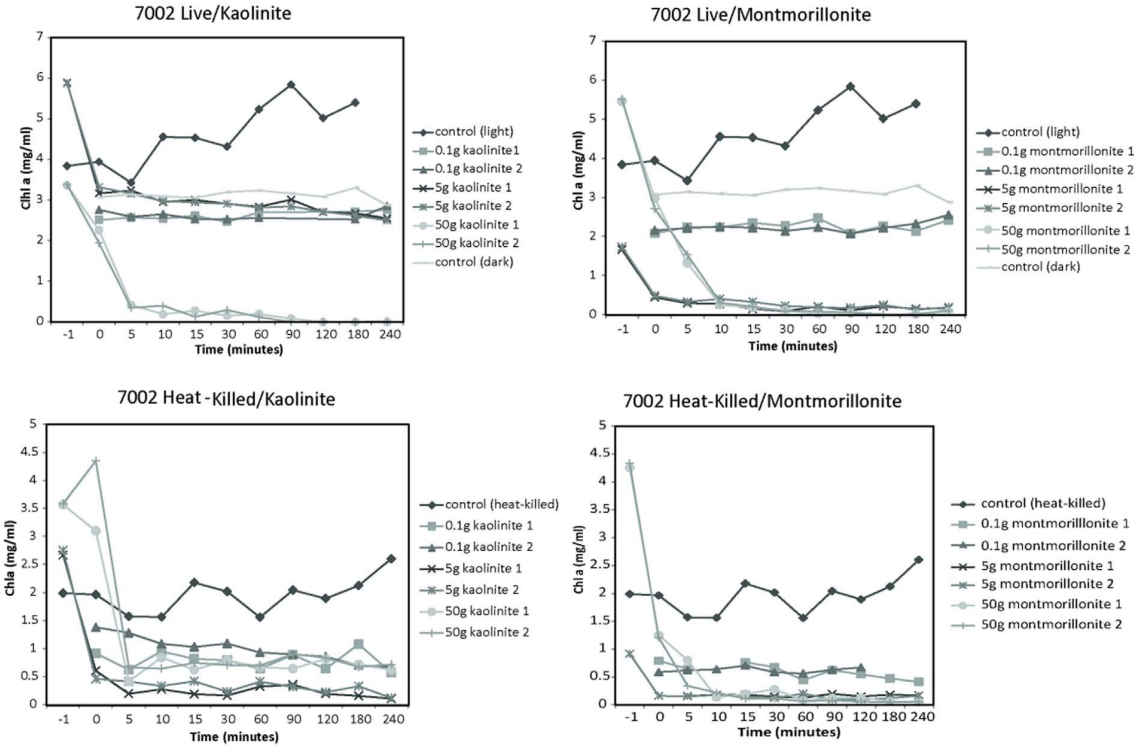

Figure 1: Quantification of Synechococcus sedimentation. Graphical representation of the measured decline of Chl a over time after kaolinite or montmorillonite was added in varying volumes (0.1 g, 5 g or 50 g) to live or dead Synechococcus cells. Time −1 represents initial cell concentration before clay addition. Time 0 represents cell concentrations immediately following clay addition. Controls included were: Synechococcus under normal growth conditions (light), Synechococcus under stressed conditions (darkness) and dead Synechococcus over time (dead).

Trace metal analysis

The trace metal composition of *Synechococcus* was measured using a 1 mL volume with a cell concentration of 3.8×10^7 cells/mL. Analyte values were measured in triplicate for cyanobacteria in growth media (A+) and compared with the average values of A+ media alone (see Table 1 for original data and detection limits; refer to Table 2 for averaged data). The difference between these two values was taken to be the analyte contribution. Trace metal concentrations within a 1 L volume were calculated using two cyanobacterial concentrations that represent both ideal experimental conditions and the modern oceans: (1) the measured bacterial concentration of 3.8×10^7 cells/mL (5.14 g/L wet weight) and (2) the concentration of *Synechococcus* reported by Campbell et al. (1997; Table 2), with values of 10^3 cells/ mL (1.35×10^{-4} g/L wet weight).

Trace metal concentrations were obtained by analyzing samples in triplicate using a Perkin Elmer Elan 6000 quadrupole inductively coupled plasma mass spectrometer (ICPMS) following acid digestion (Nuester et al., 2012). The instrument was calibrated using 5 certified multi-element solutions (CPI International), and instrument drift was corrected using In, Bi, and Sc as internal standards. Running conditions were: a flow rate of approximately 1 mL/min, 35 sweeps/reading, 1 reading/replicate and 3 replicates. Dwell times of 10 ms were used for Na, Al, K, Cu, Zn and Sr and 150 ms for Se. The dwell times of other elements were 20 ms. The integration time (dwell time multiplied by the number of sweeps) was 350 ms for Al, K, Cu, Zn, and Sr; 5250 ms for Se; and 700 ms for the remaining elements. The final

results are the average of 3 replicates. The instrument was set in dual detector mode with the ICP RF power set to 1300 W. Measurements were taken in counts per second (cps) and the blank values were subtracted after the internal standard correction. The auto lens function was turned on and 4 point calibration curves were used (0, 0.25, 0.50, 1.00 ppm for Na, Ca, Mg, Fe, K and P; 0, 0.005, 0.010 and 0.020 ppm for the remaining elements).

Analyte	Detection limits (DL)	Units	A-1	A-2	A-3	S11-6	S11-7	S11-8
Li	0.005	ppm	< DL	0.0060	< DL	0.0070	< DL	< DL
B	0.2	ppm	3.4	3.7	3.8	4.1	5.4	4.9
Na	0.05	ppm	7232	7324	7362	7352	9261	8662
Mg	0.2	ppm	461	471	484	509	630	587
Al	0.02	ppm	0.22	0.22	0.19	0.20	0.20	0.23
P	0.5	ppm	7.9	7.8	7.9	11.3	13.9	12.7
K	0.6	ppm	307	310	318	333	423	394
Ca	3.1	ppm	53.1	52.4	53.8	59.6	75.4	70.3
Ti	0.009	ppm	0.037	0.039	0.040	0.041	0.053	0.054
Cr	0.005	ppm	0.440	0.239	0.238	0.239	0.243	0.244
Fe	0.37	ppm	1.65	0.936	0.732	0.461	0.317	< DL
Mn	0.003	ppm	1.24	1.23	1.25	1.22	1.50	1.39
Co	0.003	ppm	0.023	0.023	0.022	0.015	0.017	0.016
Ni	0.006	ppm	0.406	0.362	0.359	0.357	0.348	0.354
Cu	0.003	ppm	0.281	0.264	0.263	0.260	0.294	0.285
Zn	0.008	ppm	0.515	0.517	0.531	0.500	0.557	0.579
Rb	0.004	ppm	0.012	0.012	0.012	0.025	0.032	0.030
Sr	0.003	ppm	0.027	0.028	0.028	0.034	0.040	0.037
Ba	0.003	ppm	0.005	0.013	0.006	0.009	0.008	0.009

Table 1: Raw ICP-MS data of cyanobacterial cells and A+ media composition. All data is reported in ppm. A- denotes A+ media values only; S11- denotes cyanobacterial cells in A+ media mixture. The value < DL represents a value below detection limits. Elements that occurred below detection limits in both cyanobacterial cells and A+ media include: Be, Ga, Ge, As, Se, Y, Zr, Nb, Mo, Ru, V, Pd, Ag, Cd, Sn, Sb, Te, Cs, La, Ce, Pr, Nd, Sm, Eu, Gd, Tb, Dy, Ho, Er, Tm, Yb, Lu, Hf, Ta, W, Re, Os, Ir, Pt, Au, Tl, Pb, Th, and U.

Table 2

Averaed ICP-MS results in

Analyte	Li	B	Na	Mg	Al	P	K	Ca	Ti	Cr	Fe	Mn	Co	Ni	Cu	Zn	Rb	Sr	Ba
Detection limits (DL)	0.005	0.200	0.050	0.200	0.020	0.500	0.600	3.100	0.009	0.005	0.370	0.003	0.003	0.006	0.003	0.008	0.004	0.003	0.003
Bacteria in media avg																			
A+ avg	0.007	4.776	8425	575.3		12.62	383.4	68.43	0.049			1.371			0.279	0.546	0.029	0.037	0.009
					0.211					0.24	0.38		0.013	0.35					
Bacterial contribution	0.006	3.661	7306	471.9		7.853	311.5	53.11	0.039	2	9	1.238	6	3	0.269	0.521	0.012	0.028	0.008
Value for 3.8×10^{10} cells/L Value for 10^6 cells/L Amount (µg/L)	0.001	1.116	1119.050	103.444	0.212	4.769	71.848	15.321	0.010	0.306	1.107	0.133	0.023	0.376	0.010	0.024	0.017	0.009	0.001
	1.005	1116	1,119,050	103,444	0.003	4769	71,848	15,321	10.453	0.00	0.00	133.42	0.00	0.00	10.32	24.37	17.04	9.48	0.70

TEM and SEM imaging

Synechococcus was imaged using transmission electron microscopy (TEM) and scanning electron microscopy (SEM). For both SEM and TEM imaging, *Synechococcus* cells were fixed over the course of 2 h at room temperature in a mixture of 2.5% glutaraldehyde, 2% paraformalde- hyde, and 0.1 M phosphate buffer. If necessary, the fixed cells were stored in a refrigerator overnight at 4 °C. After fixation, cells were centrifuged at 10,000 rpm, and rinsed 3 × in 0.1 M phosphate buffer saline (PBS) to remove excess fixative.

For SEM imaging, fixed cells were rinsed 3 × in 0.1 M PBS and dehydrated through a graded ethanol series as for TEM sample preparation. Additional dehydration steps were performed in which cells were placed into mixtures of ethanol and hexamethyldisilazane (HMDS) (75:25, 50:50, 25:75), and finally left in 100% HMDS over- night. Dehydrated cells were dried in a desiccation chamber overnight, placed on aluminum SEM stubs and sputter-coated with gold. A Philips FEI XL30 SEM operating at 20 kV was used to image the cells.

Preparation of samples for SEM imaging of *Synechococcus* associated with clay was carried out by mixing a 1 mL aliquot of the A+ medium cell suspension with 1 mg, 10 mg, and 25 mg of kaolinite and mon- tmorillonite, before following the generic SEM procedure described above. The procedure for TEM imaging of the clay-cyanobacterial mixtures was simplified by eliminating all dehydration processing, and simply placing a drop of the fixative containing the bacteria clay mixture onto a TEM grid, and staining with 1% osmium tetroxide. This was done to limit the amount of sample processing that could potentially affect the interaction of the clay and bacteria to provide the most accurate representation of the natural association between the clay and bacteria. In subsequent control experiments, sampling through the entire dehydration process, including multiple centrifugations and re-suspensions, was not observed to significantly affect the resulting clay-bacteria interaction. Again, separate samples were prepared that contained 1 mg, 10 mg, and 25 mg of kaolinite and montmorillonite, in an effort to capture any variation in clay-bacterial interactions dependent on clay concentration.

Results

Chl a measurements

Fig. 1 shows concentrations of the photosynthetic pigment Chl *a* over 18 successive 240-minute growth experiments with *Synechococcus* supplemented with either kaolinite or montmorillonite clay. Chl *a* concentration was used as a measure of cyanobacterial abundance remaining 5 cm below the water surface. In control samples (non-clay

supplemented cultures), Chl *a* increased over time, as would be expected from the cells in exponential growth phase (Fig. 1), or, in the case of darkness, remained constant. In contrast, Chl *a* concentra- tions of kaolinite/montmorillonite-supplemented *Synechococcus* cul- tures showed either unchanging or declining levels at all clay concentrations tested (Fig. 1). For both clays, the rate of decrease in Chl *a* concentration accelerated as the clay concentration increased (Fig. 1). Photographs of representative sedimentation time intervals are shown in Fig. 2. These provide visual representation that the clay-cyanobac- terial mixtures rapidly deposit from the water column, and at a rate that increased with increasing clay concentration.

Heat-killed *Synechococcus* biomass reacted similarly to live cultures, showing a decrease in Chl *a* concentration over time when 5 g or 50 g of kaolinite or montmorillonite was added (Fig. 1). This is in contrast to the live *Synechococcus* control culture kept in complete darkness. The addition of 0.01 g of kaolinite or montmorillonite induced a gradual drop in Chl *a* levels, however, Chl *a* levels fluctuated more in the presence of montmorillonite. The addition of 50 g of kaolinite or montmorillonite induced a sharp drop in Chl *a* levels in dead population of *Synechococcus*.

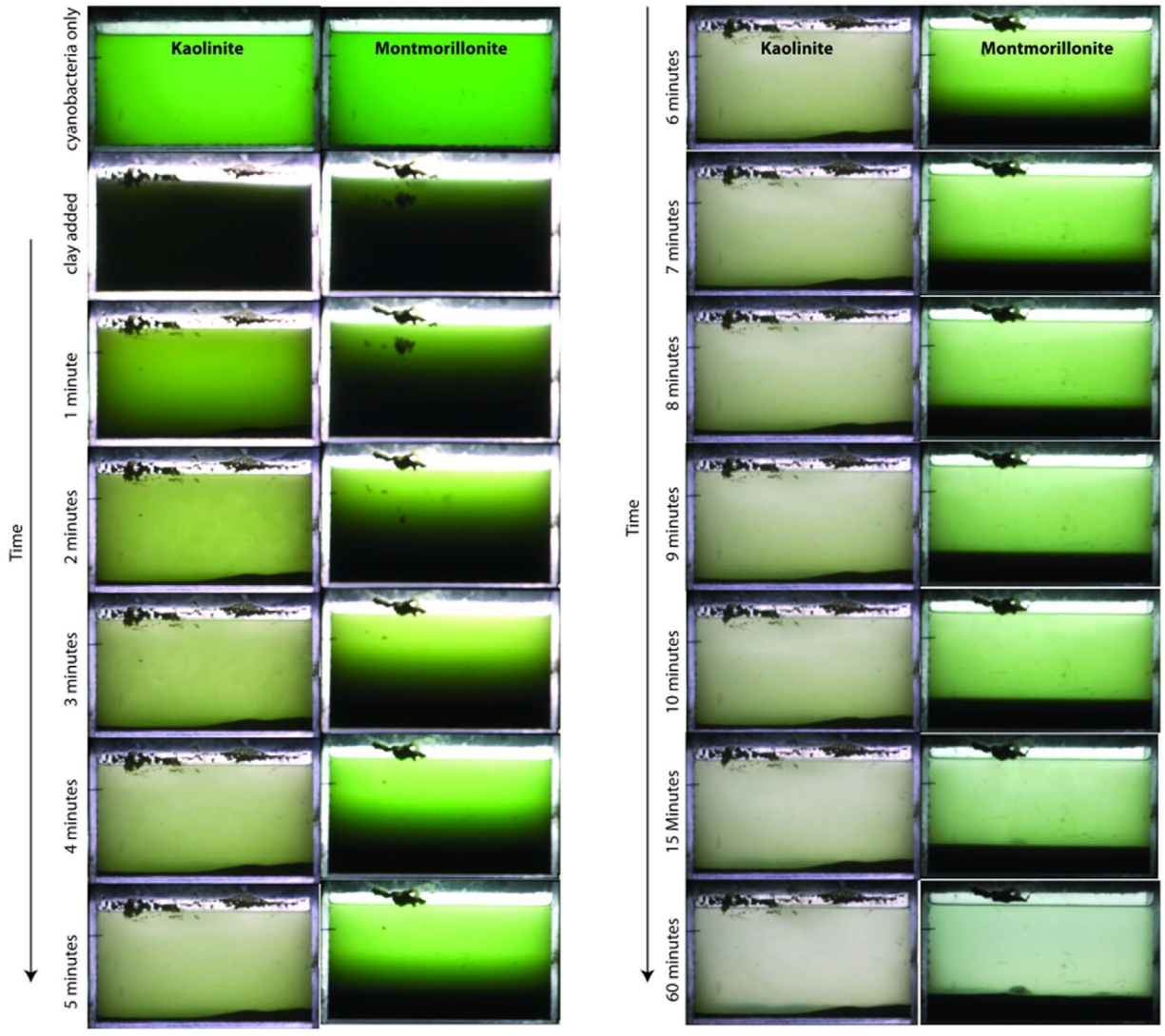

Figure 2: Time course of representative experimental sedimentation tanks illustrating *Synechococcus*-clay deposition. Kaolinite and montmorillonite (50 g) were added to 1 L volume of cyanobacteria. Images include kaolinite-*Synechococcus* and montmorillonite-*Synechococcus* mixtures for comparison. Note that within 15 min, the kaolinite-*Synechococcus* mixture is largely settled, creating a pale green/grey mass at the bottom of the tank. (For interpretation of the references to color in this figure legend, the reader is referred to the web version of this article).

Overall, the trends that we observe pertaining to the live cultures, include: (i) 0 mg/mL of Chl *a* after 10 min when 50 g of kaolinite or montmorillonite is added, (ii) the addition of small amounts of kaolinite, or montmorillonite (0.01 g) produced minimal

deviation from the controls. Data from the heat-killed *Synechococcus* biomass are similar to that obtained from the live cultures. Calculated initial cell concentrations for experiments (using OD_{750} conversion factor from Liu et al. (2015)) involving kaolinite and montmorillonite (time -1 on the x-axis of Fig. 1) may be overestimated when compared to the graphical average trend.

SEM/TEM results

Using SEM imaging, we observed that *Synechococcus* cells, grown under normal conditions in A+ media, are typically spherical to ovoid, unicellular and average 1 μm in diameter, but clump together to form larger cell aggregates (Fig. 3A). The intracellular structures, including the thylakoid membrane and nucleotide, are visible using TEM (Fig. 3B).

SEM analysis of *Synechococcus*-kaolinite (Fig. 4A–D), and *Synechococcus*-montmorillonite (Fig. 4E–H) mixtures clearly indicates that the cells are encrusted with clay. In addition, the kaolinite and montmorillonite-encrusted cells frequently adhere to larger kaolinite or mon- tmorillonite structures to become amorphous masses of cell-clay aggregates whose sizes exceed tens of micrometers (Fig. 4D). When exposed to kaolinite, *Synechococcus* cells become encrusted in micron- sized, plate-like features that generally conform to the morphology of the cyanobacterial cells (Fig. 4A–C). Where hexagonal grains encrusting cyanobacterial cells are discernible, the clay mineral face (the region of largest surface area) appears to be the point of contact with the bacterial cell, while the clay mineral edge (region of small surface area) is the

point of contact with other clay mineral grains (Fig. 4A–C). TEM analysis of *Synechococcus*-kaolinite mixtures reveals the formation of thick kaolinite sheaths, which can be over 1 μm thick, encasing individual cyanobacterial cells (Fig. 5A–B). Imaging of *Synechococcus* in the absence of clay clearly shows extracellular structure such as fimbriae (Fig. 5C). Additionally, when kaolinite is present, the encapsulation of multiple cells is visible (Fig. 5D–E).

Sheet-like structures are common and can be laterally extensive (Fig. 4A). In detail, the kaolinite is seen as hexagonal platelets, with an edge-to-edge (E-E) contact between grains (Fig. 4A). This E-E contact facilitates the formation of large sheet structures (e.g. Du et al., 2009). The kaolinite also forms larger, nodular branching structures (Fig.4D). Stacked kaolinite grains can be seen forming aggregates, which compared to the smooth surface of the larger nodular structure and encrusted cyanobacteria, appear rough and granular (Fig. 5B and D). In the case of these granular aggregates, contacts between kaolinite grains are not confined to grain edges only, but involve the faces of grains as well. Cyanobacterial cells are clearly visible within these aggregates (Fig. 5D, E and F). These nodular structures are also visible when examining montmorillonite-cyanobacterial aggregates (Fig. 4G and H). Upon close inspection, bacterial cells encased in montmorillonite often exhibit a rosette-structure (Fig. 4F), where some clay minerals appear to make contact with the bacterial cell and other clay mineral grains along the clay-mineral edge (edge-to-face contact). Montmorillonite grains also appear to contact the cell along the face (face-to-cell contact). Clay composition measured from *Synechococcus*-kaolinite (Fig. 6), and *Synechococcus*-montmorillonite (Fig. 7) masses are also shown.

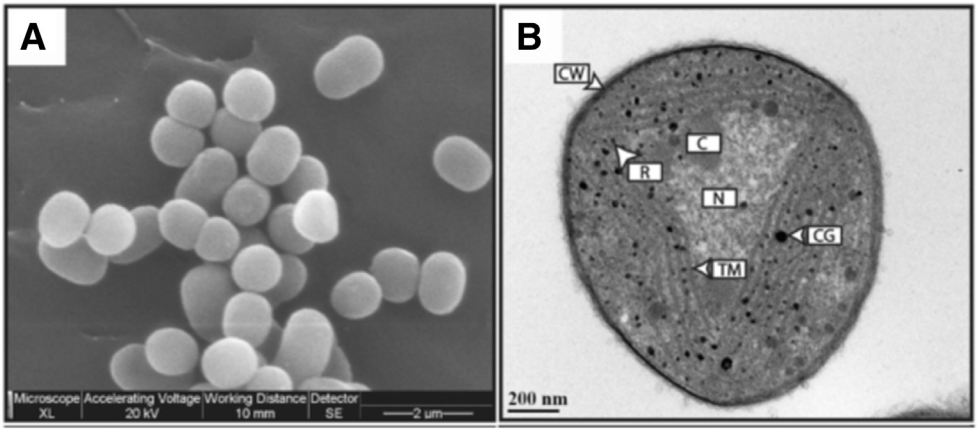

Figure 3: Electron microscopic images showing the ultrastructure of *Synechococcus* sp. PCC 7002 grown in A+ medium. (A) Scanning electron microscope (SEM) micrograph showing the size and morphology of the cyanobacteria. (B) Transmission electron microscope (TEM) micrograph showing the intracellular structure, where CW, cell wall; R, ribosome; C, carboxysome; N, nucleoide region; TM, thylakoid membrane; CG, cyanophycin granule.

Trace metal analysis

Raw trace metal data for all samples are listed in Table 1. The trace metal content, measured in triplicate, was averaged to determine the overall trace metal composition of *Synechococcus* cells (Table 2). Values for certain analytes are relatively high (using a cellular concentration of 10^3 cells/mL): Na (111 ppm), Mg (10 ppm), K (7 ppm), Ca (1.5 ppm), P (0.5 ppm), B (0.1 ppm) and Mn (0.01 ppm; Table 2). Elements with low cellular concentrations (< 0.01 ppm) include: Li, Al, Ti, Cr, Fe, Co, Ni, Cu, Zn, Rb, Sr and Ba (Table 2).

Discussion

Microbe-clay aggregation

Bacterial cells are negatively-charged over a wide range of pH due to the deprotonation of amphoteric organic ligands contained within the polymers of the cell walls (Flemming et al., 1990; Beveridge and Graham, 1991; Fein et al., 1997; Cox et al., 1999; Phoenix et al., 2002; Lalonde et al., 2008a, 2008b; Pokrovsky et al., 2008; Liu et al., 2015). These ligands bind metal cations and serve as nucleation sites for mineral authigenesis (Beveridge, 1989; Beveridge and Graham, 1991; Konhauser et al., 1994; Clarke et al., 1997). Bacteria also have the ability to partially moderate their surface charge (Doyle, 1989; Urrutia et al., 1992; Schultze-Lam et al., 1996). For instance, to generate the proton motive force, protons are continuously pumped into the fabric of the cell wall where they compete with metal cations for binding to the negatively-charged sites (e.g., Urrutia et al., 1992). This mechanism allows live bacteria to reduce detrital mineral adhesion and authigenic mineral formation on their cellular surface by filling up anionic sites with protons (Urrutia et al., 1992; Schultze-Lam et al., 1996; Konhauser and Urrutia, 1999).

The unique surface properties of the bacterial cell facilitate the formation of clay biominerals. For example, in environments where concentrations of dissolved iron proximal to the cell are greater than the solubility product of ferric hydroxide, small mineral aggregates (~100 nm) form, as iron (e.g., Fe^{3+}) initially adsorbs onto the cell surface (Konhauser et al., 1993, 1998; Konhauser and Urrutia, 1999). Additionally, pre-

formed ferric hydroxide particles in suspension can be entrained by the cell (Glasauer et al., 2001). At circumneutral pH, the net positive charge of iron attracts negatively-charged counter-ions, resulting in the formation of (Fe-Al)-silicate phases via hydrogen bonding between the cell-bound iron and the dissolved aluminum, silica or aluminosilicate complexes (e.g., Davis et al., 2002). With further exposure to sufficiently concentrated solutions, poorly ordered clay phases may form as iron attached to the cell surface continues to react with negatively charged solutes (Konhauser, 2007).

In the same way, clay particles in suspension are attracted to cations because incomplete substitution, for example Al^{3+} for Si^{4+} in the tetrahedral sheet or Mg^{2+} for Al^{3+} in the octahedral sheet, results in excess negative charge on either the clay surface (exchangeable cations) or between tetrahedral sheets in 2:1 clays (interlayer cations). This negative surface charge results in a high cation-adsorption capacity for some clays (Guenther and Bozelli, 2004). The adsorption of cations to the clay (e.g., montmorillonite, kaolinite) surface results in a net- positive surface charge, which has an affinity for negatively-charged surfaces, such as bacterial cellular surfaces (Walker et al., 1989;Guenther and Bozelli, 2004). This explains the observation that, in sediments, organic matter and clay particles rarely exist in isolation, occurring instead as microaggregates (Walker et al., 1989).

Similar to the results reported here that demonstrate cyanobacterial enhancement of clay sedimentation, the adhesion of an anionic flocculent to clays in suspension has previously been observed to produce a unique structure. For instance, Du et al. (2009) observed the formation of a honeycomb network structure after the addition of the flocculent (anionic polyacrylamide copolymer FLOPAM AN-910) to a kaolinite

suspension; this was not observed in the absence of the flocculent. The network observed is similar to the honeycomb structures that we observed by SEM analyses (Figs. 3 and 4) after the addition of kaolinite and montmorillonite. This suggests that, in our experiment, the bacteria themselves played the role of an anionic flocculent.

Despite previous studies showing algal cells becoming entrained in settling clay aggregates and flocculating rapidly in the presence of clay particles (e.g., Sengco et al., 2001), there is a paucity of information on the mechanisms underpinning the role of microbes, such as cyanobacteria, in clay deposition. Indeed, clay is used to control harmful algal blooms in environmental rehabilitation projects in many modern environments (e.g., Archambault et al., 2003; Beaulieu et al., 2005). The formation of clay/algal aggregates is influenced by the species of algae, clay/algae concentrations and clay type (Beaulieu et al., 2005). In the case of cyanobacteria, interaction between buoyant species, such as *Microcystis* sp., and clay particles have been observed to form aggregates that rapidly settle out of suspension (Verspagen et al., 2006). The aggregation rates of *Microcystis* sp. and clay particles are directly related to the amount of clay particles in suspension (Verspagen et al., 2006). Similarly, it has been observed that the sinking rates of cyanobacteria, *Anabaena* and *Phormidium*, were in- creased by their adhesion to clay particles (Avnimelech et al., 1982; Guenther and Bozelli, 2004). In fact, addition of clays during our experiments resulted in an increased *Synechococcus* sedimentation rate (Fig. 1). This is in agreement with the work of Verspagen et al. (2006) who observed that the aggregation rate of *Microcystis* and bentonite was linearly proportional to the concentration of clay. Additionally, Chen et al. (2010) reported that, when polysaccharide concentrations were kept constant, the flocculation efficiencies of

cyanobacterial cells increased with increasing doses of kaolinite.

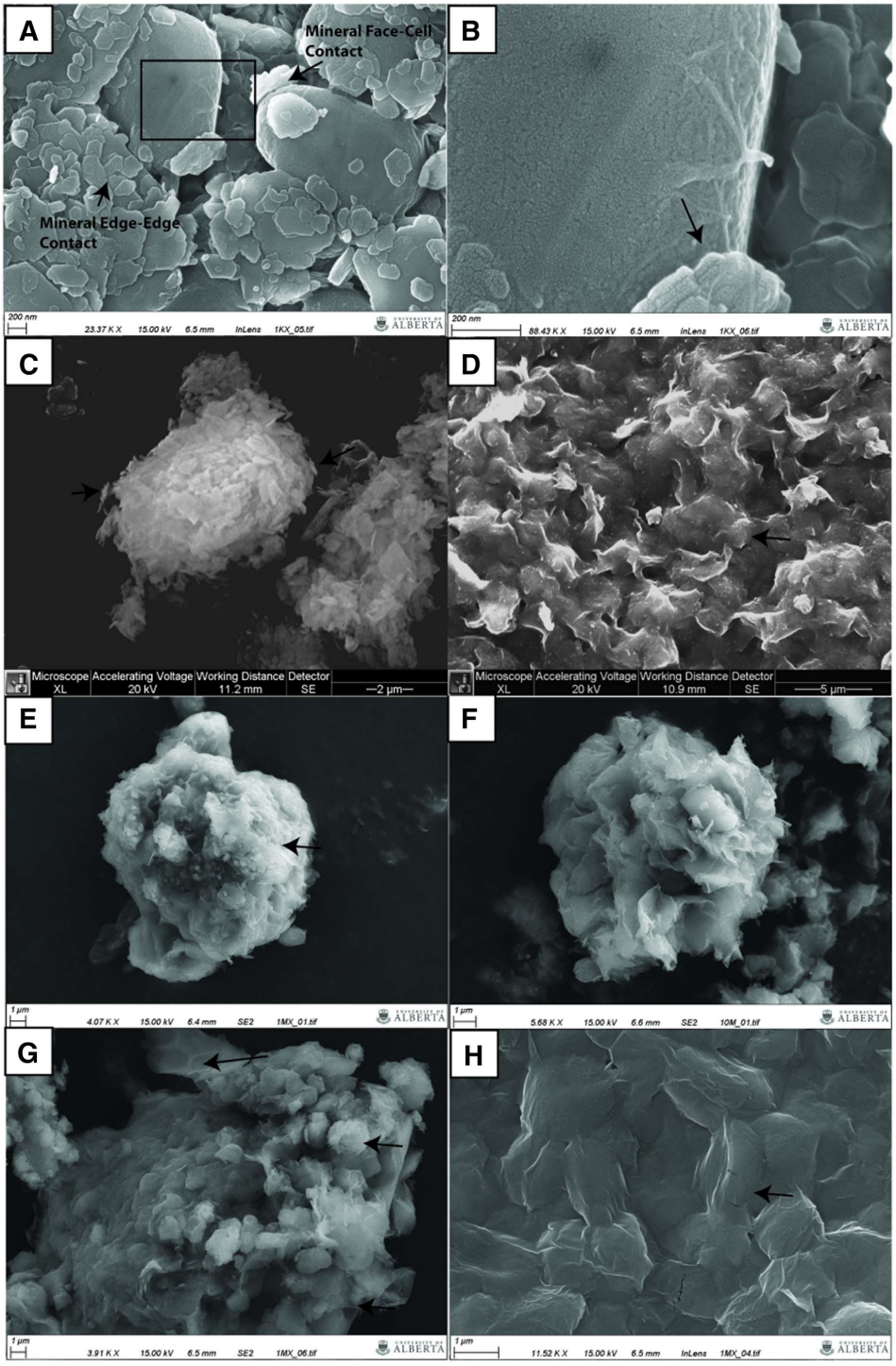

Figure 4: Scanning electron microscope (SEM) images. (A) Kaolinite (1 mg) in the presence of *Synechococcus* sp. PCC 7002. Note the tangential attachment of the kaolinite hexagons and face-on-cell contact with the

bacterial cell. Mineral edge-edge contact of kaolinite grains is also visible. Black box denotes area of inset in (B). B) Inset from (A) showing the tangential attachment of the kaolinite grain to the cell surface (contact is along mineral face). The external structure of the cell is also visible. (C) A *Synechococcus* cell encased in kaolinite. Black arrows highlight the tangential nature of mineral attachment. The cell is completely encased, however, cell morphology is preserved. (D) Large kaolinite-cell network illustrating the complete encasement of cyanobacterial cells (black arrow). Cell encasement produces a nodular morphology. (E) Cell of *Synechococcus* encased in montmorillonite. Although cell morphology is retained (black arrow), the size of the clay-cell aggregate is many times larger than an unattached cell. (F) Although tangential mineral face-to-cell contact is most common, montmorillonite can exhibit edge-to-cell contact, producing a floret-like morphology. (G) Large structure of montmorillonite and cyanobacterial cells illustrating the preservation of cell morphology and nodular textures (black arrows). (H) Complete encasement of cyanobacterial cells in montmorillonite, producing a nodular structure similar to that observed in (D).

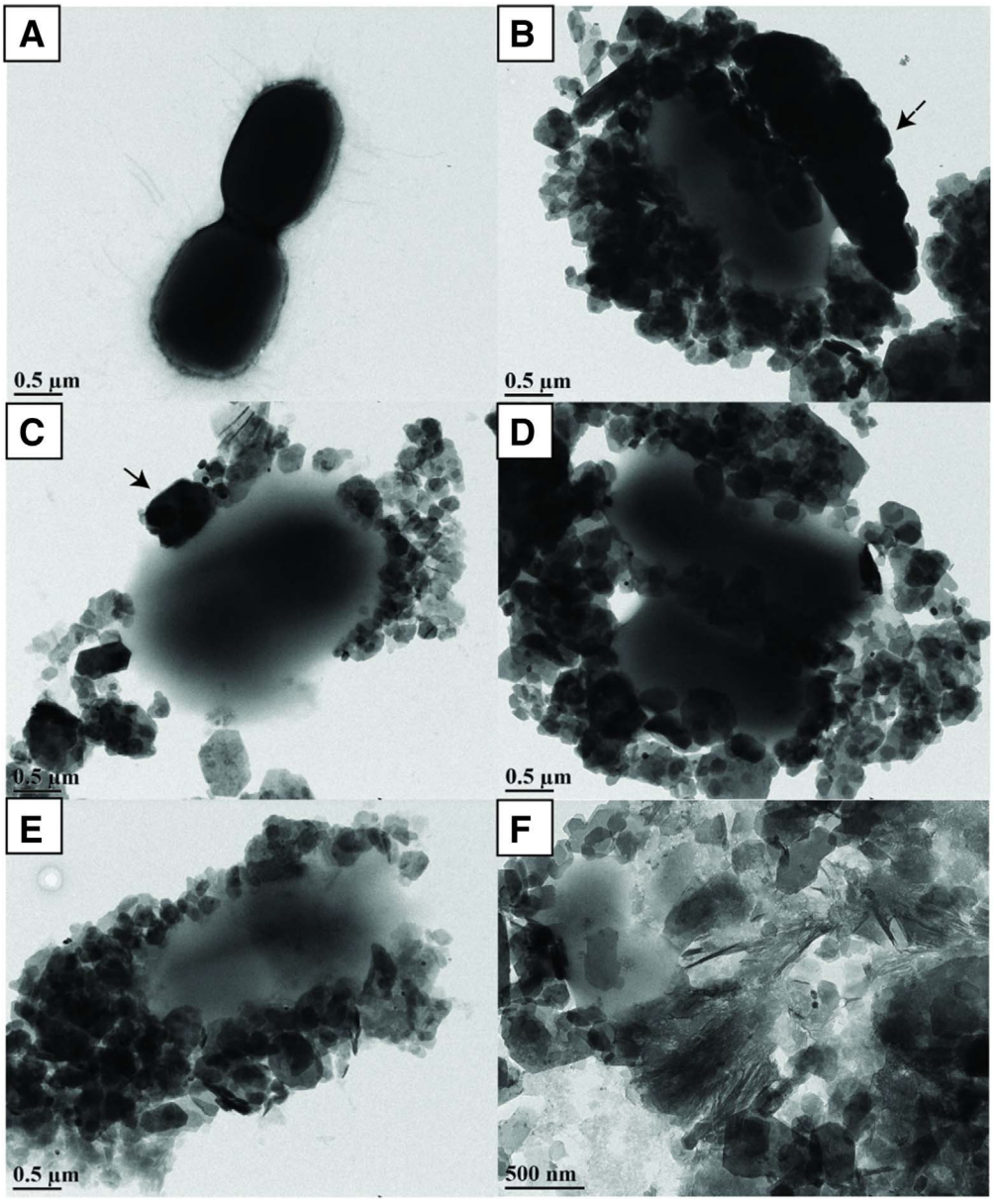

Figure 5: Transmission electron microscope (TEM) images of kaolinite-*Synechococcus* mixtures and *Synechococcus* only. (A) Control *Synechococcus* cells dividing with no clay present. Fimbriae are clearly visible. (B) Kaolinite shells encasing *Synechococcus* cells can be thick (up to 1 µm; black arrow). (C) Kaolinite in the presence of *Synechococcus* sp. PCC 7002. Kaolinite grains can form thick stacks attached tangentially to cell, visible here with a partially covered cell (black arrows). Although the concentration of clay did not appear to influence how the bacteria sorbed to the clay in both the SEM and TEM imaging, the samples containing 1 mg of clay presented rare occurrences in which the bacteria were not completely enshrouded in clay and both the clay and bacteria were visible. This helped to provide convincing evidence that the numerous clay aggregates had a core composed of one or multiple bacteria. (D) Kaolinite grains vary in size, but form an aggregate mass

partially surrounding two cells. (E) Cells of *Synechococcus* encased in kaolinite showing clay stacking. (F) Nodular, aggregate mass of bacterial cells and clay showing complete encasement of the cells.

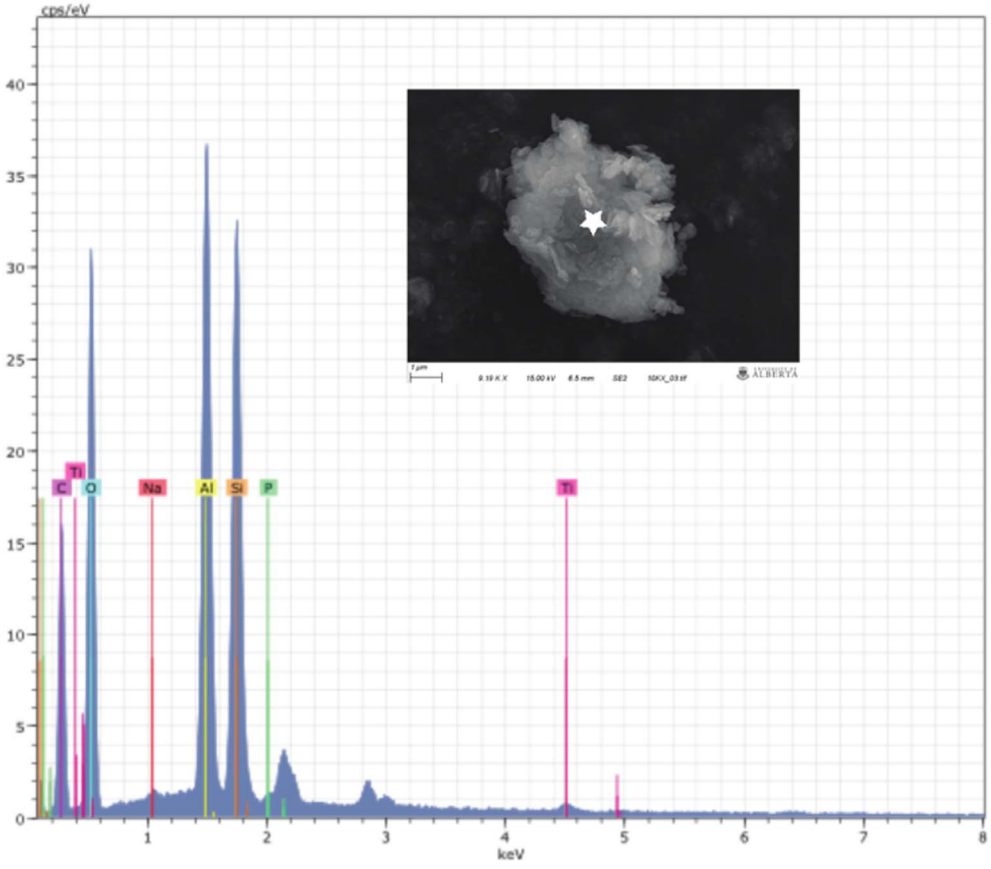

El	AN	Series	unn. C [wt.%]	norm. C [wt.%]	Atom. C [at.%]	Error (1 Sigma) [wt.%]
O	8	K-series	27.34	38.47	38.75	3.36
C	6	K-series	23.89	33.62	45.11	3.18
Si	14	K-series	9.62	13.54	7.77	0.43
Al	13	K-series	9.21	12.96	7.74	0.46
Ti	22	K-series	0.56	0.79	0.27	0.05
P	15	K-series	0.24	0.34	0.18	0.04
Na	11	K-series	0.20	0.28	0.19	0.04
		Total:	71.06	100.00	100.00	

Figure 6: Kaolinite identification on encrusted *Synechococcus*. Insert: SEM image showing a kaolinite-encrusted cyanobacterial cell. The star indicates the point of compositional measurement. The composition of the kaolinite is shown graphically below.

Organic matter sources in black shales

The organic matter found in fine-grained Triassic and Cretaceous sediments (both carbonate and siliciclastic), especially those associated with oceanic anoxic events (OAEs), have largely been attributed to cyanobacteria based on the abundance of 2-methylhopanoids, geoporphyrin distribution and nitrogen isotopic composition (Kuypers et al., 2004; Dumitrescu and Brassell, 2005; Xie et al., 2005; Ohkouchi et al., 2006; Duque-Botero and Maurrasse, 2008; Cao et al., 2009; Jia et al., 2012). For example, during the Triassic, fluctuations in the biomarker 2-methylhopane (in association with negative values of $\delta^{15}N$) have been interpreted as the products of increased cyanobacterial activity following the Permian-Triassic mass extinction, ocean anoxia, denitri- fication and development of oligotrophic conditions (Xie et al., 2005; Cao et al., 2009; Jia et al., 2012). Similarly, the high abundance of cholestanes suggests high rates of planktonic production in association with deposition of early Triassic, organic-rich, fine-grained successions (Suzuki et al., 1998). In Cretaceous sediments, the presence of cyanobacterial biomarkers (2β-methylhopanes and 2β-methylhopanones), in association with sterenes (indicative of algal phytoplankton), also points to a depositional environment characterized by high rates of primary, cyanobacterial production (Dumitrescu and Brassell, 2005).

In the modern oceans, cyanobacteria populations occur in densities large enough to act as major contributors to the organic fraction of marine sediments. Some species occur in concentrations as high as 10^8 cells per mL (Miyazono et al., 1992). Cyanobacteria have been observed to constitute up to 70% of the total phytoplankton

biomass of the northeast Atlantic Ocean (Jardillier et al., 2010). In that study, two genera of cyanobacteria, *Prochlorococcus* and *Synechococcus*, were found to contribute 45 ± 17% and 21 ± 17%, respectively, to the total carbon fixation budget for phytoplankton (Jardillier et al., 2010). In addition to high population potential, cyanobacteria occur in diverse coastal settings; by way of example, *Synechococcus* is a marine coastal genus that occurs in high cell densities within modern estuaries (Pan et al., 2007; Mitbavkar et al., 2012; Rajaneesh and Mitbavkar, 2013), making them major contributors to the estuary's organic carbon pool (Mitbavkar et al., 2012). Indeed, continental margins, where planktonic organisms flourish, have been recognized to be major sites of organic carbon deposition (Burdige, 2007).

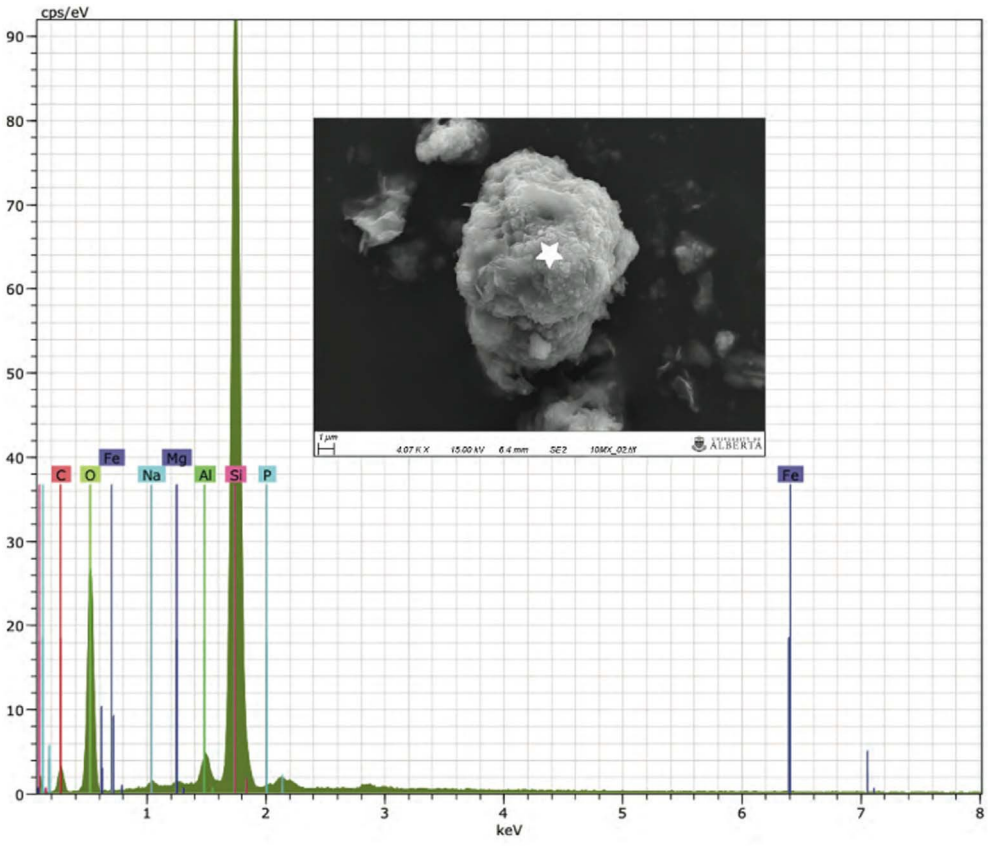

El	AN	Series	unn. C [wt.%]	norm. C [wt.%]	Atom. C [at.%]	Error (1 Sigma) [wt.%]
Si	14	K-series	40.77	45.80	31.32	1.72
O	8	K-series	32.95	37.01	44.43	4.12
C	6	K-series	12.15	13.65	21.82	2.16
Al	13	K-series	1.65	1.85	1.32	0.11
Na	11	K-series	0.52	0.58	0.48	0.07
P	15	K-series	0.37	0.41	0.26	0.05
Fe	26	K-series	0.34	0.39	0.13	0.05
Mg	12	K-series	0.28	0.31	0.25	0.05
		Total:	89.02	100.00	100.00	

Figure 7: Montmorillonite identification on encrusted *Synechococcus*. Insert. SEM image of a montmorillonite-encased cyanobacterial cell. The composition of the clay is indicated below as measured from the point on the clay-cell aggregate indicated by the star. The composition of the montmorillonite is shown graphically below.

Mechanism of biomass deposition

While the contribution of microorganisms (such as cyanobacteria) to the organic matter fraction of black shale deposits is well established, the mechanisms by which large-scale biomass deposition occurred remains extensively debated. Delivery of this reactive carbon pool to the sediment could occur rapidly (Figs. 1 and 2) via flocculation in the presence of considerable clay input. Under normal conditions, the concentration of suspended particulate matter observed in estuaries can vary considerably from 0.1 g/L in the Kennebec Estuary, USA (Kistner and Pettigrew, 2001) to over 200 g/L in the Severn Estuary, UK (Kirby and Parker, 1983; Uncles et al., 2006). Wind-delivered clay was estimated at only 6–11% of the total deposited clay (Wan et al., 2007). In some modern coastal environments, e.g., in the South China Sea, clay (smectite, illite, chlorite, and kaolinite) deposition is attributed to monsoon-induced surface currents originating from the continent (Wan et al., 2007). Considering the abundance of planktonic surface-reactive biomass, such as cyanobacteria, in such coastal settings, it seems plausible that microbes can accentuate mass clay settling in these environments. In fact, in an estuary exposed to seasonal monsoons, *Synechococcus* populations, for example, are shown to flourish during non-monsoonal times and diminish during monsoons due to high turbidity from the increased clay and sediment influx (Rajaneesh and Mitbavkar, 2013). Although the authors conclude that the diminished population is an effect of turbidity, in light of our observations, this population reduction may be reflective of surface-reactive, microbial populations, in this case cyanobacteria, being

stripped from the water column by clay.

Considering the effect of the monsoon cycle on observed populations of *Synechococcus* (Rajaneesh and Mitbavkar, 2013), and the role of monsoons in delivering clay to the basin (Wan et al., 2007), it follows that earlier observations about the link between anomalous fluctuations in the efficiency of organic carbon burial observed in the geological record and environmental conditions (e.g., Kennedy et al., 2014) would hold true. Importantly, monsoonal control on mid-Cretaceous black shale deposition has been postulated (Herrle et al., 2003; Petrash et al., 2016). However, the authors suggested that sediment input (nutrient flux) from the monsoon promoted increased primary productivity and resulted in increased organic matter deposition and water stratification (leading to low oxygen levels and therefore an increase in organic matter preservation potential). The observation that cyanobacterial populations flourish during times of minimal surface runoff and decrease drastically because of turbidity during high monsoonal activity (Rajaneesh and Mitbavkar, 2013), contradicts this idea. In our opinion, monsoon-induced runoff would not promote an increase in primary productivity, but instead would cause the flocculation and deposition of any microorganism in suspension during that time. Combined with our results, these observations regarding clay mobilization and cyanobacterial occurrence, suggest that coastal environments (such as estuaries, prodelta settings and in proximal offshore locations), where large populations of planktonic microorganisms are present and clay input (possibly driven by monsoons) is significant, are optimal for the deposition of fine-grained, organic-rich sediment.

Although it is likely that increased monsoon-driven sedimentation into productive

waters can produce high-TOC bearing stratigraphic intervals, other climatic factors may also influence microbe-mud sedimentation. High pCO_2 in the atmosphere, for example, couples increased primary productivity with enhanced clay weathering which would undoubtedly lead to widespread flocculation and settling of organic-rich mudrocks. This model explains the temporal correspondence shared by large igneous provinces and black shales (i.e. Condie, 2004).

Organic matter preservation potential

While mass organic matter deposition can occur in coastal environments, the question becomes one of preservation potential. In the oceans as a whole, < 1% of the original organic biomass buried into sediment may ultimately contribute to the sedimentary organic geochemical record (e.g., Emerson and Hedges, 1988; Raven and Falkowski, 1999). Of that fraction, most is distributed on the continental shelves because (i) there is greater nutrient supply from both land and upwelling to support primary productivity, and (ii) residence time for the dead biomass in the water column is shorter there and hence lower potential to be aerobically oxidized in the water column (Suess, 1980).

Previous studies that have focused on the preservation of microbial biomass in marine sediments showed that organic-mineral interactions result in the protection of organic matter from heterotrophic micro-organisms (Hedges and Keil, 1995; Ransom et al., 1997, 1998; Bennett et al., 1999; Kennedy et al., 2002; Mayer et al., 2004; Arnarson and Keil, 2005; Aplin and Macquaker, 2011). By contrast, when separated from the

host mineral grains, organic matter decays rapidly (Keil et al., 1994). This degradation occurs regardless of oxygen levels, as decomposition rates by sulfate reduction range from 65 to 85% (Mackin and Swider, 1989). Protection from degradation occurs by: (1) enclosure within pore spaces and between sheets in clay minerals (Kennedy et al., 2002; Mayer et al., 2004); (2) chemical alteration decreasing its susceptibility to chemoheterotrophy (Hedges and Keil, 1995), and (3) a lack of access to energetically favourable terminal electron acceptors (e.g., O_2, NO^-_3) for microbial respiration coupled to organic matter oxidation (see Konhauser, 2007).

The association of organic carbon with minerals, such as clay, can also protect it from bacterial enzymes and other faunal activity (Ransom et al., 1998; Baldock and Skjemstad, 2000; Bennett et al., 1999, 2012). Indeed, two mechanisms have been observed to govern organic-mineral interactions: (1) organic matter may form aggregates with mineral grains (Arnarson and Keil, 2001; Krull et al., 2003), and (2) dissolved solutes may be sorbed onto mineral surfaces (Keil et al., 1994; Baldock and Skjemstad, 2000; Ding and Henrichs, 2002). However, work thus far (e.g. Tietjen et al., 2005) has involved the use of dissolved or decaying organic matter (such as plant material). Therefore, our study shows that complete initial encapsulation of living bacterial cells during deposition is another mechanism facilitating the preservation of organic matter.

Our hypothesis builds on the work of Kennedy et al. (2002, 2014), but differs in two ways. First, those authors argued that it is dissolved organic matter in sedimentary pore fluids that results in TOC adsorption within the interlayer of smectite surfaces. By contrast, our work suggests that live particulate organic matter (such as cyanobacterial

cells) can also interact with clay particles in the water column before deposition. Thus, clay flocculation is likely a combination of both these processes. Second, they suggested that the determining factor regarding organic matter preservation is mineral surface area, where dissolved organic carbon is adsorbed. While mineral surface area is certainly a critical factor (e.g., Ransom et al., 1998), we argue here that the initial encasement of particulate organic matter (such as cyanobacterial cells) by mineral grains is a driving preservational mechanism. In this regard, the surface area of the microbial cells would be of importance.

Clay minerals have been found in association with bacterial cells in modern continental margin sediments (Ransom et al., 1997). However, these microbes were observed to bind sediment using extracellular polysaccharides (EPS) and occurred in patchy distributions within the sediment or marine snow. Encasement that preserved cell morphology was not observed and organic matter was noted to occur in patchy blebs and smears (Ransom et al., 1997). While the association of these microbes with clay minerals was hypothesized to increase organic carbon preservation and sediment cohesion (even in soils; see Baldock and Skjemstad, 2000), a direct relationship between the occurrences of bacterial/cyanobacterial blooms, clay input and mass carbon deposition and preservation was not considered. Indeed, sediment trap and bottom sediment samples were not taken during a cyanobacterial bloom (Ransom et al., 1997), but during steady-state ocean conditions. In this case, the surface area of the clay minerals and the network of EPS were considered preservational factors (Ransom et al., 1997).

Baldock and Skjemstad (2000) suggested that encapsulation of organic matter in

soils by clay protected the organic matter from microbial decay. Similarly, Phoenix and Konhauser (2008) suggested that the encrustation of bacteria by clay – though via biomineralization– protected the cells from toxins, dehydration and ultraviolet irradiation. Building on the work of Kilbertus (1980) and Amelung and Zech (1996), Baldock and Skjemstad (2000) hypothesized that since most bacteria cannot enter pores smaller than 3 μm (Kilbertus, 1980) and that pore size would decrease with increasing clay content in soils, aggregation and encapsulation of organic matter in soils with clay would enhance preservation. Our results show that the pore spaces associated with the clay encapsulating cyanobacterial cells are much smaller than 3 μm and, therefore, would restrict the entrance of heterotrophic microbes that would remineralize the organic matter (Figs. 3 and 4).

Uniform clay-microbial structures ('clay hutches') have been observed to form in acidic freshwater puddles when a floating colonization surface (glass slide) is placed on the water surface and incubated (Lünsdorf et al., 2000). The work of Lünsdorf et al. (2000) showed that soil-dwelling bacteria (*Burkholderia*, *Variovorax*, *Sphingomonas*, *Rhodo- phila*, and *Acidobacterium*), when allowed to colonize a floating substrate (escaping high levels of toxins within the sediment) within low-pH, fresh water puddles (10–15 mm depth), will form biofilms that incorporate clay grains within the exopolymeric substances, forming clay hutches. Initial nucleation appeared to be bacterial adsorption to the substratum surface (glass slide or thin layer of extracellular polysaccharide) and subsequent coverage by clay particles adsorbed from the puddle water column. Empty/hollow clay aggregates suggested that bacteria were able to migrate within the clay aggregates. The clay hutches retained their structure upon the absence of the

bacterial cell and were observed to be held together by extracellular polysaccharides. Clay particles mechanically transported from the soil to the slide (through the water column) were shown to be mechanisms of transport for adsorbed dissolved organic matter and were captured by the extracellular polysaccharides of the bacteria and incorporated into the hutch/biofilm structure. This dissolved organic matter acted as nutrients for the bacteria. These microbial-soil microhabitats were hypothesized to act as 'minimal nutritional spheres' also offering the bacterial cells protection from amoeba or flagellate grazing. These hutches were hypothesized to represent biogeological units in soils, illustrating the role of bacteria in forming clay sediments in soils.

Our work differs on two critical points as it shows: 1) complete encapsulation via direct contact between bacterial cell and clay particles (with no extracellular polysaccharide network) under marine conditions, and 2) that complete encapsulation of planktonic photosynthetic marine bacteria by clay particles brings the bacterial cells out of suspension and induces rapid deposition. In the case of the Lünsdorf et al. (2000) study, the bacteria colonized a substrate and the subsequent incorporation of clay into the bacterial biofilm added important nutrients and protection that facilitated bacterial metabolism. Additionally, the 'clay hutches' did not enclose the bacterial cells, which remained attached to the substrate.

Morphology of encased biomass

With regards to the entrapment of microorganisms, such as cyanobacteria by clay minerals, there has been limited work conducted on the morphology of these aggregates

and their possible role in cellular preservation. In the case of *Anabaena*, Avnimelech et al. (1982) showed that the clay was adsorbed, forming a network-like structure around the cell perimeter, including the cell wall and EPS. Their SEM micrographs revealed that the clay occurred in clusters on the bacteria, while textures that reflected cell morphology were not produced. Studies on the flocculation of kaolinite and the diatom species *Thalassiosira punctigera* showed that the clay particles did not directly attach to the diatom cells but instead they were bound in clusters by the EPS (Hamm, 2002). Interestingly, comparison of this work with the micrographs of *Synechococcus* and kaolinite and montmorillonite aggregates from our study suggests that excessive amounts of EPS actually appeared to impede cell encapsulation. This is similar to the work of Chen et al. (2010) who showed that EPS inhibited microbe and clay flocculation.

Kim et al. (2010) also investigated the adsorption of clay minerals by the cyanobacterium, *Phormidium parchydematicum*. The clay used in that study was unspecified and was sourced from soil. Their findings showed the formation of aggregates from the attachment of clay particles to the bacterial cells. They also observed that the morphology of the cells was preserved. However, in contrast with our results, the bacterial cells were not uniformly coated, but were instead agglomerated with various clay particles of different sizes and orientation. The SEM micrographs of Kim et al. (2010) show the clay infilling spaces between the cyanobacterial filaments, but the cells themselves are not encased and instead remained partly exposed. Although we cannot demonstrate what causes the differences in aggregate textures and the ability to flocculate clay particles as observed between the various cyanobacteria

and diatoms, we suggest that these varieties are a product of the composition of the EPS, and hence cell surface reactivity (*Synechococcus* vs. *Anabaena* vs. *Phormidium* or diatoms), as well as the type of clay used (kaolinite vs. montmorillonite).

Implications for traditional depositional models of black shales

The preservation of microbial organic matter via initial clay encapsulation has important implications for our understanding of the depositional mechanisms of organic-rich, fine-grained sedimentary rocks, such as black shales. High TOC content in these lithologies is not only a function of anoxia (see Arthur and Sageman, 1994), but also a function of the increased preservation potential of the microorganism, such as cyanobacteria, in the presence of a primary mineral coating such as clay. Initial encapsulation would protect the organic carbon from oxidation, regardless of pore water redox conditions, ultimately leading to the development of an organic-rich deposit. This would explain the preservation of organic matter in the presence of limited bioturbation (bioturbation suggests an oxygenated environment; see MacEachern et al., 2010; Aplin and Macquaker, 2011) in fine-grained, organic-rich sediments.

Additionally, our work suggests that sediment input of clay is crucial for the potential preservation of microbes, and so high sedimentation rates could in fact be a key mechanism for enhanced preservation of organic matter in fine-grained sediment. This complicates the view that increased sediment input dilutes the amount of organic carbon within the sediment and leads to organic-poor sediments (e.g., Aplin and Macquaker, 2011), but supports the view (Ransom et al., 1997, 1998) that sediment

composition (amount of clay) is a crucial factor. Considering that, at some point, an increased sedimentation rate will dilute C_{org} content, there is likely a threshold, after which increased sedimentation rates would no longer increase C_{org} content. This threshold could be a product of both microbial cell concentration and amount of clay in suspension.

Geochemical implications for organic-rich marine shale

The increased potential for preservation when kaolinite or montmorillonite and microorganisms, such as cyanobacteria, interact has two major implications regarding elemental analysis: (1) metal cation adsorption and fractionation by clays may record, through cation bridging between the mineral and cell surfaces, a stable isotopic and/or trace metal signature not directly related to the general paleoenvironmental conditions, and (2) the trace metal content of the bacterial cells themselves has an increased likelihood of being preserved and contributing to the trace element content of the sediment. As an example of the former, Ca has been shown to fractionate by as much as −2.76‰ when adsorbing to kaolinite (Ockert et al., 2013). Compared to other clays (such as illite) kaolinite showed one of the largest Ca-isotopic fractionations. Similarly, adsorption of Mg onto kaolinite during weathering has been observed to occur with the preferential adsorption of the heavier isotope onto the clay surface (Huang et al., 2012). What is interesting is that kaolinite (and clay in general) has been observed to bind trace metals in a similar manner to metal oxyhydroxides (Spark et al., 1995), and the preferential

incorporation of light Mo into secondary clay minerals has been suggested as a mechanism for the isotopic fractionation of Mo observed in riverine flux (Archer and Vance, 2008). As such, the question which remains to be addressed is whether the large fractionations of trace metals, such as molybdenum (e.g., Ellis et al., 2002; Barling and Anbar, 2004) might also be observed in association with adsorption onto kaolinite?

In a similar manner, Cr isotopes have been used as a proxy for atmospheric oxygen levels (Frei et al., 2009; Crowe et al., 2013; Reinhard et al., 2014; Planavsky et al., 2014; Cole et al., 2016). Fractionation of Cr is thought to be controlled by redox conditions and is not currently thought to be significantly influenced by other factors, such as sorption (Ellis et al., 2002, 2004; Schauble et al., 2004; Reinhard et al., 2014). However, these studies focused on the effects of Cr absorption onto goethite (Ellis et al., 2004). Work by Buerge and Hug (1999) showed that the presence of kaolinite accelerates the reduction of Cr(VI) by Fe(II). Additionally, Cr(III) has been observed to adsorb onto kaolinite (Ajouyed et al., 2011; Rao et al., 2012). This monolayer adsorption reverses the surface charge of the kaolinite (Rao et al., 2012), which facilitates attachment to negatively-charged cyanobacterial cells. Kaolinite has been shown to absorb hexavalent Cr (Ajouyed et al., 2011) even though chromate (CrO^{2-}) is largely considered to be the mobile form, adsorbing to Fe(III) oxides only at acidic and near neutral pH (Izbicki et al., 2008). The adsorption of Cr (III) and Cr(VI) by montmorillonite (summarized by Bhattacharyya and Gupta, 2008), has been observed to be pH dependent. Cr(III) adsorption has been observed to increase with increasing pH, hypothesized to be a function of metal hydroxide precipitation (Bhattacharyya and

Gupta, 2008). Similarly, the adsorption of Cr(VI) on kaolinite is dependent on pH, with adsorption for kaolinite peaking around pH 7.0 (Bhattacharyya and Gupta, 2008).

Further work is needed to determine the effect of kaolinite (and other clay minerals) and the adsorption of Cr (and other cations) on the isotopic signatures of black shales. The implication resulting from our work is that any isotopic signature associated with preferential adsorption onto clays would have an increased preservation potential if the element in question acted as the bridging cation between the clay mineral and microbial surfaces. This could affect any paleoenvironmental interpretations based on isotopic signatures (such as that of Cr). Trace elements can be enriched in organic-rich shales in three ways: (1) by association with organic matter, (2) adsorption to the detrital clay fraction and (3) through incorporation into sulfide mineral phases. With respect to our data, observations support the idea that the burial of redox-sensitive metals would scale with carbon flux (Algeo and Maynard, 2004; Piper and Perkins, 2004; Dean, 2007; Reinhard et al., 2013). For instance, trace elements, such as Ni, Cd, Zn and Cu, are typically delivered to the sediments via organic matter or organometallic complexes (Calvert and Pedersen, 1993; Murphy et al., 2000; Algeo and Maynard, 2004; Piper and Perkins, 2004; Tribovillard et al., 2006). After organic matter degradation, these elements are liberated into the sediment pore-waters, and then incorporated into pyrite under reducing conditions (Brumsack, 2006; Tribovillard et al., 2006; Xu et al., 2012). This has led to the interpretation that high levels of Ni and Cu signify a high organic matter flux to the sediment and reducing conditions, allowing for the fixation of Ni and Cu into pyrite (Brumsack, 2006; Tribovillard et al., 2006).

Our findings suggest that trace metal content of microbes (specifically Mn, Cu, Zn

and Ba) could contribute directly to the trace metal content of organic-rich, marine shale deposits, assuming preferential preservation of the microbial cells. A number of studies have indeed documented that marine phytoplankton are enriched in various trace elements, close to the approximate extended Redfield formula given by the following average stoichiometry (Ho et al., 2003):

$$(C_{124}N_{16}P_{1}S_{1.3}K_{1.7}Mn_{3.8}Mg_{0.56}Ca_{0.5})_{1000}Sr_{5}Fe_{7.5}Zn_{0.8}Cu_{0.38}Co_{0.19}Cd_{0.21}Mo_{0.03})$$

Although this elemental stoichiometry varies between species, growth rate, and potentially in response to ambient nutrient concentra- tions in seawater (Bruland et al., 1991; Twining et al., 2004), it nevertheless provides a basis for examining the magnitude by which phytoplankton may assimilate trace elements from seawater.

Second, the siliciclastic constituents can also import trace elements. For example, V has been observed to adsorb to kaolinite (Breit and Wanty, 1991). Siliciclastic input can be examined by cross-plotting the element of interest versus Al or Ti, and then comparing the ratios with average published shale values (Dean et al., 1997; Piper and Perkins, 2004; Tribovillard et al., 2006). Our findings suggest that microbial cells, specifically cyanobacteria, contribute Ti directly to the sediment, which potentially makes the normalization to Ti problematic. Additionally, while the adsorption capacity and ability of metal oxyhydroxides to bring trace metals to the sediment has been recognized, the ability of detrital clays, such as kaolinite or montmorillonite, to adsorb trace metals from the water column has been largely ignored. Our results suggest that a primary source of deposited metals originates from the bacterial cells encapsulated by clay minerals. This adds complexity to the notion that the trace element content of organic-rich deposits necessitates chemical deposition in rare environments. For

example, it has been proposed that the development of euxinic conditions in the water column or at the sediment/water interface during deposition acts as a reductant for the fixation of elements such as V (Wanty and Goldhaber, 1992; Brumsack, 2006). In the case of Lower Cambrian black shale deposits from South China, high V/(V + Ni) values (above 0.85) were interpreted as indicating marine euxinia (Xu et al., 2012). However, kaolinite has been observed to adsorb V in the form of VO^{-} (Abd-Allah et al., 2005), and thus has the potential (along with other clays) to contribute to the V content of black shales (as postulated by Kelly et al., 2013). This has implications regarding global mass balance and burial models related to trace element fluxes (e.g. Reinhard et al., 2013), as the reactivity of the depositing sediment (i.e. clays) is not taken into consideration.

Although anoxia can be associated with increased primary productivity, we argue that it is the initial encapsulation of the microbial cells *en masse*, which, along with preserving the organic matter, contributes directly to sedimentary trace element concentrations. Perhaps this is an explanation for the strong association between trace elements (e.g., Cu) and TOC. Cross-plots are generally used to interpret paleoredox conditions (Tribovillard et al., 2006), but may instead reflect the enhanced preservation of marine plankton (e.g., cyanobacteria) and their trace metal components.

Conclusions

This study had a number of aims, one of which was to investigate the role that clay minerals have in flocculating microbial cells from suspension. The addition of montmorillonite or kaolinite (in 5 g/L or 50 g/L concentrations) to a suspension of

Synechococcus cells was found to dramatically increase settling rates of both cells and clay; cells were brought out of suspension within 15 min. In contrast, live *Synechococcus* cells were found to increase in concentration when no clay was added. Cell metabolism was not found to be a factor as both live and dead cell populations behaved in a similar manner in the presence of clay. These findings agree with previous work which reported the ability of clay to sediment microbial cells from suspension (e.g. Beaulieu et al., 2005). As cyanobacteria have been recognized as major contributors to the organic matter content of some organic-rich marine shale deposits (Ohkouchi et al., 2006), this depositional mechanism could account for the deposition of these organic-rich shale deposits. This would suggest an environment of deposition where large microbial populations, such as cyanobacterial blooms, could occur in addition to regular clay input, such as an estuary or other coastal regions, where events such as monsoons could transport large amounts of clay to the basin. In addition, kaolinite is known to be preferentially deposited close to shore and is associated with increased continental weathering (Thiry, 2000). The increased nutrient delivery is conducive to microorganisms (e.g. cyanobacterial blooms), and, in association with the kaolinite from continental weathering, would promote the formation of organic-rich deposits. This supports deltaic, estuarine, or related depositional setting for the formation of these organic-rich deposits. Kaolinite is also stable over long periods of time (compared to other clays, such as smectite; Thiry, 2000), suggesting that long-term cyanobacterial encasement is feasible.

Clay-cell aggregates examined using SEM reveals that, in the presence of surface-reactive microbial cells (e.g. cyanobacteria), kaolinite and montmorillonite form

nodular network structures that incorporate the bacterial cells. Cyanobacterial cells were completely enclosed within a clay envelope, with plates of clay visibly adhering to the negatively-charged cell surface. As the chemical reactivity of cyanobacterial cells has previously been demonstrated (Lalonde et al., 2008a, 2008b; Liu et al., 2015), this suggests that cation bridging likely occurs between the microbial and clay mineral surfaces. This mechanism potentially explains the preservation of large deposits of marine organic matter, with encapsulation of the microbes protecting the biomass from degradation.

Unsurprisingly, the trace metal content of a sample of *Synechococcus* was found to be elevated in bioactive metals (P, Cu, Zn and Ba). However, these trace metals have been thought to be largely liberated during organic matter degradation and only preserved under unique circumstances (anoxia, euxinia or increased sedimentation rates) in sediments (e.g., Algeo and Maynard, 2004; Tribovillard et al., 2006). The rapid deposition and encapsulation of cyanobacterial cells observed during our experiments does not require the development of anoxia or euxinia, suggesting that, while redox controls have been recognized to play a role in numerous organic-rich deposits, rapid deposition with encapsulation of reactive microbial biomass is another important control. This would explain the high levels of bioactive trace elements within some organic-rich deposits (e.g. Tribovillard et al., 2006). Significantly, this depositional model suggests that steady-state, organic-carbon depositional and preservation models may not be entirely accurate. Instead organic-rich, fine-grained deposits may, in some cases, reflect a series of discrete depositional events, which punctuate steady-state conditions.

References

A+ Medium Recipe, 2017. UTEX Culture Collection of Algae at the University of Texas at Austin. http://web.biosci.utexas.edu/utex/Media%20PDF/a%20plus%20medium. pdf (accessed 06.11.16).

Abd-Allah, S.M., El Hussaini, O.M., Mahdy, R.M., 2005. Towards a more safe environment: (4) sorptability of vanadium as a nuclear constructing material by some clay sediments in Egypt. J. Appl. Sci. Res. 1, 168–175.

Ajouyed, O., Hurel, C., Marmier, N., 2011. Evaluation of the adsorption of hexavalent chromium on kaolinite and illite. J. Environ. Prot. 2, 1347–1352.

Algeo, T.J., Maynard, J.B., 2004. Trace-element behavior and redox facies in core shales of Upper Pennsylvanian Kansas-type cyclothems. Chem. Geol. 206, 289–318.

Amelung, W., Zech, W., 1996. Organic species in ped surface and core fractions along a climosequence in the prairie North America. Geoderma 74, 193–206.

Anbar, A.D., Rouxel, O., 2007. Metal stable isotopes in paleoceanography. Annu. Rev. Earth Planet. Sci. 35, 717–746.

Aplin, A.C., Macquaker, J.H., 2011. Mudstone diversity: origin and implications for source, seal, and reservoir properties in petroleum systems. AAPG Bull. 95, 2031–2059.

Archambault, M.-C., Grant, J., Bricelj, V.M., 2003. Removal efficiency of the dinoflagellate *Heterocapsa triquetra* by phosphatic clay and implications for the mitigation of harmful algal blooms. Mar. Ecol. Prog. Ser. 253, 97–109.

Archer, C., Vance, D., 2008. The isotopic signature of the global riverine molybdenum flux and anoxia in the ancient oceans. Nat. Geosci. 1, 597–600.

Arnarson, T.S., Keil, R.G., 2001. Organic-mineral interactions in marine sediments studied using density fractionation and X-ray photoelectron spectroscopy. Org. Geochem. 32, 1401–1415.

Arnarson, T.S., Keil, R.G., 2005. Influence of organic-mineral aggregates on microbial degradation of the dinoflagellate *Scrippsiella trochoidea*. Geochim. Cosmochim. Acta 69, 2111–2117.

Arthur, M.A., Sageman, B.B., 1994. Marine black shales: depositional mechanisms and environments of ancient deposits. Annu. Rev. Earth Planet. Sci. 22, 499–552.

Avnimelech, Y., Troeger, B.W., Reed, L.W., 1982. Mutual flocculation of algae and clay: evidence and implications. Science 216, 63–65.

Baldock, J.A., Skjemstad, J.O., 2000. Role of the soil matrix and minerals in protecting natural organic materials against biological attack. Org. Geochem. 31, 697–710.

Barling, J., Anbar, A.D., 2004. Molybdenum isotope fractionation during adsorption by manganese oxides. Earth Planet. Sci. Lett. 217, 315–329.

Beaulieu, S.E., Sengco, M.R., Anderson, D.M., 2005. Using clay to control harmful algal blooms: deposition and resuspension of clay/algal flocs. Harmful Algae 4, 123–138.

Bechtel, A., Püttmann, W., 1997. Palaeoceanography of the early Zechstein Sea during Kupferschiefer deposition in the Lower Rhine Basin (Germany): a reappraisal from stable isotope an organic geochemical investigations. Palaeogeogr. Palaeoclimatol. Palaeoecol. 136, 331–358.

Bennett, R.H., Ransom, B., Kastner, M., Baerwald, R.J., Hulbert, M.H., Sawyer, W.B., Olsen, H., Lambert, M.W., 1999. Early diagenesis: impact of organic

matter on mass physical properties and processes, California continental margin. Mar. Geol. 159, 7–34.

Bennett, R.H., Hulbert, M.H., Curry, K.J., Curry, A., Douglas, J., 2012. Organic matter sequestered in potential energy fields predicted by 3-D clay microstructure model, direct observations of organo-clay micro- and nanofabric. Mar. Geol. 315–318, 108–114.

Betts, J.N., Holland, H.D., 1991. The oxygen content of ocean bottom waters, the burial efficiency of organic carbon, and the regulation of atmospheric oxygen. Palaeogeogr. Palaeoclimatol. Palaeoecol. 97, 5–18.

Beveridge, T.J., 1989. Role of cellular design in bacterial metal accumulation and mineralization. Annu. Rev. Microbiol. 43, 147–171.

Beveridge, T.J., Graham, L.L., 1991. Surface layers of bacteria. Microbiol. Rev. 55, 684–705.

Bhattacharyya, K.G., Gupta, S.S., 2008. Adsorption of a few heavy metals on natural and modified kaolinite and montmorillonite: a review. Adv. Colloid Interf. Sci. 140, 114–131.

Breit, G.N., Wanty, R.B., 1991. Vanadium accumulation in carbonaceous rocks: a review of geochemical controls during deposition and diagenesis. Chem. Geol. 91, 83–97.

Bruland, K.W., Donat, J.R., Hutchins, D.A., 1991. Interactive influences of bioactive trace metals on biological production in oceanic waters. Limnol. Oceanogr. 36, 1555–1577.

Brumsack, H.J., 2006. The trace metal content of recent organic carbon-rich sediments: implications for Cretaceous black shale formation. Palaeogeogr. Palaeoclimatol. Palaeoecol. 232, 344–361.

Buerge, I.J., Hug, S.J., 1999. Influence of mineral surfaces on chromium(VI) reduction by iron(II). Environ. Sci. Technol. 33, 4285–4291.

Burdige, D.J., 2007. Preservation of organic matter in marine sediments: controls, mechanisms, and an imbalance in sediment organic carbon budgets? Chem. Rev. 107, 467–485.

Calvert, S.E., Pedersen, T.F., 1993. Geochemistry of recent oxic and anoxic marine sediments: implications for the geological record. Mar. Geol. 113, 67–88.

Campbell, L., Liu, H., Nolla, H.A., Vaulot, D., 1997. Annual variability of phytoplankton and bacteria in the subtropical North Pacific Ocean at Station ALOHA during the 1991–1994 ENSO event. Deep-Sea Res. 44, 167–192.

Canfield, D.E., 1994. Factors influencing organic carbon preservation in marine sediments. Chem. Geol. 114, 315–329.

Canfield, D.E., Thamdrup, B., Hansen, J.W., 1993a. The anaerobic degradation of organic matter in Danish coastal sediments: iron reduction, manganese reduction, and sulfate reduction. Geochim. Cosmochim. Acta 57, 3867–3883.

Canfield, D.E., Jørgensen, B.B., Fossing, H., Glud, R., Gundersen, J., Ramsing, N.B., Thamdrup, B., Hansen, J.W., Nielsen, L.P., Hall, P.O.J., 1993b. Pathways of organic carbon oxidation in three continental margin sediments. Mar. Geol. 113, 27–40.

Cao, C., Love, G.D., Hays, L.E., Wang, W., Shen, S., Summons, R.E., 2009. Biogeochemical evidence for euxinic oceans and ecological disturbance presaging the end-Permian mass extinction event. Earth Planet. Sci. Lett. 281, 188–201.

Chamot, D., Owttrim, G.W., 2000. Regulation of cold shock-induced RNA helicase gene expression in the cyanobacterium *Anabaena* sp. strain PCC 7120. J. Bacteriol. 182, 1251–1256.

Chen, L., Men, X., Ma, M., Li, P., Jiao, Q., Lu, S., 2010. Polysaccharide release by *Aphanothece halophytica* inhibits cyanobacteria/clay flocculation. J. Phycol. 46, 417–423.

Clarke, W.A., Konhauser, K.O., Thomas, J.C., Bottrell, S.H., 1997. Ferric hydroxide and ferric hydroxysulfate precipitation by bacteria in an acid mine drainage lagoon. FEMS Microbiol. Rev. 20, 351–361.

Cole, D.B., Reinhard, C.T., Wang, X., Gueguen, B., Halverson, G.P., Gibson, T., Hodgskiss, M.S.W., McKenzie, N.R., Lyons, T.W., Planavsky, N.J., 2016. A shale-hosted Cr istope record of low atmospheric oxygen during the Proterozoic. Geology 44, 555–558.

Condie, K.C., 2004. Supercontinents and superplume events: distinguishing signals in the geological record. Phys. Earth Planet. Inter. 146, 319–332.

Cox, J.S., Smith, D.S., Warren, L.A., Ferris, F.G., 1999. Characterizing heterogeneous bacterial surface functional groups using discrete affinity spectra for proton binding. Environ. Sci. Technol. 33, 4514–4521.

Crowe, S.A., Døssing, L.N., Beukes, N.J., Bau, M., Kruger, S.J., Frei, R., Canfield, D.E., 2013. Atmospheric oxygenation three billion years ago. Nature 501, 535–539.

Davis, C.C., Chen, H.W., Edwards, M., 2002. Modeling silica sorption to iron hydroxide. Environ. Sci. Technol. 36, 582–587.

Dean, W.E., 2007. Sediment geochemical records of productivity and oxygen depletion along the margin of western North America during the past 60,000 years: teleconnections with Greenland ice and the Cariaco Basin. Quat. Sci. Rev. 26, 98–114.

Dean, W.E., Gardner, J.V., Piper, D.Z., 1997. Inorganic geochemical indicators of glacial- interglacial changes in productivity and anoxia on the California continental margin. Geochim. Cosmochim. Acta 61, 4507–4518.

Ding, X., Henrichs, S.M., 2002. Adsorption and desorption of proteins and polyamino acids by clay minerals and marine sediments. Mar. Chem. 77, 225–237.

Dittrich, M., Sibler, S., 2005. Cell surface groups of two picocyanobacteria strains studied by zeta potential investigations, potentiometric titration, and infrared spectroscopy. J. Colloid Interface Sci. 286, 8.

Doyle, R.J., 1989. How cell walls of Gram-positive bacteria interact with metal ions. In: Beveridge, T.J., Doyle, R.J. (Eds.), Metal Ions and Bacteria. Wiley, New York, pp. 275–293.

Du, J., Pushkarova, R.A., Smart, R.St.C., 2009. A cryo-SEM study of aggregate and floc structure changes during clay settling and raking processes. Int. J. Miner. Process. 93, 66–72.

Dumitrescu, M., Brassell, S.C., 2005. Biogeochemical assessment of sources of organic matter and paleoproductivity during the early Aptian Oceanic Anoxic Event at Shatsky Rise, ODP Leg 198. Org. Geochem. 36, 1002–1022.

Duque-Botero, F., Maurrasse, F.J.-M.R., 2008. Role of cyanobacteria in Corg-rich deposits: an example from Indidura Formation (Cenomanian-Turonian), northeastern Mexico. 2008. Cretac. Res. 29, 957–964.

Ellis, A.S., Johnson, T.M., Bullen, T.D., 2002. Chromium isotopes and the fate of hexavalent chromium in the environment. Science 295, 2060–2062.

Ellis, A.S., Johnson, T.M., Bullen, T.D., 2004. Using chromium stable isotope ratios to quantify Cr(VI) reduction: lack of sorption effects. Environ. Sci. Technol. 38, 3604–3607.

Emerson, S., Hedges, J.I., 1988. Processes controlling the organic carbon content of open ocean sediments. Paléo 3, 621–634.

Fein, J.B., Daughney, C.J., Yee, N., Davis, T.A., 1997. A chemical equilibrium model for metal adsorption onto bacterial surfaces. Geochim. Cosmochim. Acta 61, 3319–3328.

Flemming, C.A., Ferris, F.G., Beveridge, T.J., Bailey, G.W., 1990. Remobilization of toxic heavy metals adsorbed to bacterial wall-clay composites. Appl. Environ. Microbiol. 56, 3191–3203.

Frei, R., Dahl, P.S., Frandsson, M.M., Jensen, L.A., Hansen, T.R., Terry, M.P., Frei, K.M., 2009. Lead-isotope and trace-element geochemistry of Paleoproterozoic metasedimentary rocks in the Lead and Rochford basins (Black Hills, South Dakota, USA): implications for genetic models, mineralization ages, and sources of leads in the Homestake gold deposit. Precambrian Res. 172, 1–24.

Glasauer, S., Langley, S., Beveridge, T.J., 2001. Sorption of Fe (hydr)oxides to the surface of *Shewanella putrefaciens*: cell-bound fine-grained minerals are not always formed de novo. Appl. Environ. Microbiol. 67, 5544–5550.

Guenther, M., Bozelli, R., 2004. Factors influencing algae-clay aggregation. Hydrobiologia 523, 217–223.

Hadjoudja, S., Deluchat, V., Baudu, M., 2010. Cell surface characterization of *Microcystis aeruginosa* and *Chlorella vulgaris*. J. Colloid Interface Sci. 342, 293–299.

Hamm, C.E., 2002. Interactive aggregation and sedimentation of diatoms and clay-sized lithogenic material. Limnol. Oceanogr. 47, 1790–1795.

Hedges, J.I., Keil, R.G., 1995. Sedimentary organic matter preservation: an assessment and speculative synthesis. Mar. Chem. 49, 81–115.

Herrle, J.O., Pross, J., Friedrich, O., Kössler, P., Hemleben, C., 2003. Forcing mechanisms for mid-Cretaceous black shale formation: evidence from the Upper Aptian and Lower Albian of the Vocontian Basin (SE France). Palaeogeogr. Palaeoclimatol. Palaeoecol. 190, 399–426.

Ho, T.-Y., Quigg, A., Finkel, Z.V., Milligan, A.J., Wyman, K., Falkowski, P.G., Morel, F.M.M., 2003. The elemental composition of some marine phytoplankton. J. Phycol. 39, 1145–1159.

Huang, K.-J., Teng, F.-Z., Wei, G.-J., Ma, J.-L., Bao, Z.-Y., 2012. Adsorption- and desorption-controlled magnesium isotope fractionation during extreme weathering of basalt in Hainan Island, China. Earth Planet. Sci. Lett. 359–360, 73–83.

Ikhsan, J., Johnson, B.B., Wells, J.D., 1999. A comparative study of the adsorption of transition metals on kaolinite. J. Colloid Interface Sci. 217, 403–410.

Izbicki, J.A., Ball, J.W., Bullen, T.D., Sutley, S.J., 2008. Chromium, chromium isotopes and selected trace elements, western Mojave Desert, USA. Appl. Geochem. 23, 1325–1352.

Jacquet, S., Lennon, J.-F., Marie, D., Vaulot, D., 1998. Picoplankton population dynamics in coastal waters of the northwestern Mediterranean Sea. Limnol. Oceanogr. 43, 1916–1931.

Jardillier, L., Zubkov, M.V., Pearman, J., Scanlan, D.J., 2010. Significant CO_2 fixation by small prymnesiophytes in the subtropical and tropical northeast Atlantic Ocean. ISME J. 4, 1180–1192.

Jia, C., Huang, J., Kershaw, S., Luo, G., Farabegoli, E., Perri, M.C., Chen, L., Bai, X., Xie, S., 2012. Microbial response to limited nutrients in shallow water immediately after the end-Permian mass extinction. Geobiology 10, 60–71.

Kashiyama, Y., Ogawa, N.O., Kuroda, J., Shiro, M., Nomoto, S., Tada, R., Kitazato, H., Ohkouchi, N., 2008. Diazotrophic cyanobacteria as the major photoautotrophs during mid-Cretaceous oceanic anoxic events: nitrogen and carbon isotopic evidence from sedimentary porphyrin. Org. Geochem. 39, 532–549.

Keil, R.G., Montluçon, D.B., Prahl, F.G., Hedges, J.I., 1994. Sorptive preservation of labile organic matter in marine sediments. Nature 370, 549–551.

Kelly, K.D., Benzel, W.M., Pfaff, K., 2013. Preliminary mineralogy and geochemistry of metal-rich (Mo-Ni-V-Zn) oil shale of the Carboniferous Heath Formation, Montana, USA. In: Jonsson, E. (Ed.), Mineral Deposit Research for a High-tech World. 12th SGA Biennial Meeting 2013. Proceedings. 2. pp. 636–639.

Kennedy, M.J., Pevear, D.R., Hill, R.J., 2002. Mineral surface control of organic carbon in black shale. Science 295, 657–660.

Kennedy, M.J., Löhr, S.C., Fraser, S.A., Baruch, E.T., 2014. Direct evidence for organic carbon preservation as clay-organic nanocomposites in a Devonian black shale; from deposition to diagenesis. Earth Planet. Sci. Lett. 388, 59–70.

Kim, C.J., Jung, Y.H., Ahn, C.Y., Lee, Y.K., Oh, H.M., 2010. Adsorption of turbid materials by the cyanobacterium *Phormidium parcydematicum*. J. Appl. Phycol. 22, 181–186.

Kilbertus, G., 1980. Microhabitats in soil aggregates their relationship with bacterial biomass and size of procaryotes present. Rev. Ecol. Biol. Sol 17, 543–557.

Kirby, R., Parker, W.R., 1983. Distribution and behavior of fine sediment in the Severn Estuary and Inner Bristol Channel, UK. Can. J. Fish. Aquat. Sci. 40 (Suppl. 1), 83–95.

Kistner, D.A., Pettigrew, N.R., 2001. A variable turbidity maximum in the Kennebec Estuary. Estuaries 24, 680–687.

Konhauser, K.O., 2007. Introduction to Geomicrobiology. Blackwell Publishing, Oxford, UK (425 pp.).

Konhauser, K.O., Urrutia, M.M., 1999. Bacterial clay authigenesis: a common biochemical process. Chem. Geol. 161, 399–413.

Konhauser, K.O., Fyfe, W.S., Ferris, F.G., Beveridge, T.J., 1993. Metal sorption and mineral precipitation by bacteria in two Amazonian river systems: Rio Solimões and Rio Negro. Geology 21, 1103–1106.

Konhauser, K.O., Fyfe, W.S., Schultze-Lam, S., Ferris, F.G., Beveridge, T.J., 1994. Iron phosphate precipitation by epilithic microbial biofilms in Arctic Canada. Can. J. Earth Sci. 31, 1320–1324.

Konhauser, K.O., Fisher, Q.J., Fyfe, W.S., Longstaffe, F.J., Powell, M.A., 1998. Authigenic mineralization and detrital clay binding by freshwater biofilms: the Brahmani river, India. Geomicrobiol J. 15, 209–222.

Köster, J., Rospondek, M., Schouten, S., Kotarba, M., Zubrzycki, A., Sinninghe Damsté, J.S., 1998. Biomarker geochemistry of a foreland basin: the Oligocene Menilite Formation in the Flysch Carpathians of southeast Poland. Org. Geochem. 29, 649–669.

Kristensen, E., 2000. Organic matter diagenesis at the oxic/anoxic interface in coastal marine sediments, with emphasis on the role of burrowing animals. Hydrobiologia 426, 1–24.

Krull, E.S., Baldock, J.A., Skjemstad, J.O., 2003. Importance of mechanisms and processes of the stabilization of soil organic matter for modeling carbon turnover. Funct. Plant Biol. 30, 207–222.

Kuypers, M.M.M., van Breugel, Y., Schouten, S., Erba, E., Sinninghe-Damsté, J.S.S., 2004. N2-fixing cyanobacteria supplied nutrient N for Cretaceous oceanic anoxic events. Geology 32, 853–856.

Lalonde, S.V., Smith, D.S., Owttrim, G.W., Konhauser, K.O., 2008a. Acid-base properties of cyanobacterial surfaces I: influences of growth phase and nitrogen metabolism on surface reactivity. Geochim. Cosmochim. Acta 72, 1257–1268.

Lalonde, S.V., Smith, D.S., Owttrim, G.W., Konhauser, K.O., 2008b. Acid-base properties of cyanobacterial surfaces II: silica as a chemical stressor influencing cell surface reactivity. Geochim. Cosmochim. Acta 72, 1269–1280.

Liu, Y.X., Alessi, D.S., Owttrim, G.W., Petrash, D.E., Mloszewska, A.M., Lalonde, S.V., Martinez, R.E., Zhou, Q.X., Konhauser, K.O., 2015. Cell surface reactivity

of *Synechococcus* sp. PCC 7002: implications for metal sorption from seawater. Geochim. Cosmochim. Acta 169, 30–44.

Lünsdorf, H., Erb, R.W., Abraham, W.-R., Timmis, K.N., 2000. 'Clay hutches': a novel interaction between bacteria and clay minerals. Environ. Microbiol. 2, 161–168.

Ludwig, M., Bryant, D.A., 2012. Synechococcus sp. strain PCC 7002 transcriptome: acclimation to temperature, salinity, oxidative stress, and mixotrophic growth conditions. Front. Microbiol. 3, 1–14.

MacEachern, J.A., Pemberton, S.G., Gingras, M.K., Bann, K.L., 2010. Ichnology and facies models. In: Dalrymple, R.W., James, N.P. (Eds.), Facies Models 4, Geotext 6.

Geological Association of Canada, St John's Nfld (586 pp.).

Mackin, J.E., Swider, K.T., 1989. Organic matter decomposition pathways and oxygen consumption in coastal marine sediments. J. Mar. Res. 47, 681–716.

Macquaker, H.S., Keller, M.A., Davies, S.J., 2010. Algal blooms and "marine snow": mechanisms that enhance preservation of organic carbon in ancient fine-grained sediments. J. Sediment. Res. 80, 934–942.

Mayer, L.M., Schick, L.L., Hardy, K.R., Wagal, R., MacCarthy, J., 2004. Organic matter in small mesopores in sediments and soils. Geochim. Cosmochim. Acta 68, 3863–3872.

McClure, R.S., Overall, C.C., McDermott, J.E., Hill, E.A., Markillie, L.-M., McCue, L.-A., Taylor, R.C., Ludwig, M., Bryant, D.A., Beliaev, A.S., 2016. Network analysis of transcriptomics expands regulatorylandscapes in *Synechococcus* sp. PCC 7002. Nucleic Acids Res. 44, 1–16.

Mitbavkar, S., Rajaneesh, K.M., Anil, A.C., Sundar, D., 2012. Picophytoplankton community in a tropical estuary: detection of *Prochlorococcus*-like populations. Estuar. Coast. Shelf Sci. 107, 159–164.

Miyazono, A., Odate, T., Maita, Y., 1992. Seasonal fluctuations of cell density of cyanobacteria and other picophytoplankton in Iwanai Bay, Hokkaido, Japan. J. Oceanogr. 48, 257–266.

Murphy, A.E., Sageman, B.B., Hollander, D.J., 2000. Eutrophication by decoupling of the marine biogeochemical cycles of C, N, and P: a mechanism for the Late Devonian mass extinction. Geology 28, 427–430.

Nuester, J., Vogt, S., Newville, M., Kustka, A.B., Twining, B., 2012. The unique biogeochemical signature of the marine diazotroph *Trichodesmium*. Front. Microbiol. 3 (article number 150).

Ockert, C., Gussone, N., Kaufhold, S., Teichert, B.M.A., 2013. Isotope fractionation during Ca exchange on clay minerals in a marine environment. Geochim. Cosmochim. Acta112, 374–388.

Ohkouchi, N., Kashiyama, Y., Kuroda, J., Ogawa, N.O., Kitazato, H., 2006. The importance of diazotrophic cyanobacteria as primary producers during Cretaceous Oceanic Anoxia Event 2. Biogeosciences 3, 467–478.

Olcott, A.N., Sessions, A.L., Corsetti, F.A., Kaufman, A.J., de Oliviera, T.F., 2005. Biomarker evidence for photosynthesis during neoproterozoic glaciation. Science 310, 471–474.

Pan, L., Zhang, J., Zhang, L., 2007. Picophytoplankton, nanophytoplankton, heterotrophic bacteria and viruses in the Changjiang Estuary and adjacent coastal waters. J. Plankton Res. 29, 187–197.

Partin, C.A., Bekker, A., Planovsky, N.J., Scott, C.T., Gill, B.C., Li, C., Podkovyrov, V., Maslov, A., Konhauser, K.O., Lalonde, S.V., Love, G.D., Poulton, S.W., Lyons, T.W., 2013. Large-scale fluctuations in Precambrian atmospheric and oceanic oxygen levels from the record of U in shales. Earth Planet. Sci. Lett. 369, 284–293.

Pedersen, T.F., Calvert, S.E., 1990. Anoxia vs. productivity: what controls the formation of organic-carbon-rich sediments and sedimentary rocks? Am. Assoc. Pet. Geol. Bull. 74, 454–466.

Petrash, D.A., Gueneli, N., Brocks, J.J., Méndez, J.A., Gonzalez-Arismentdi, G., Poulton, S.W., Konhauser, K.O., 2016. Black shale deposition and early diagenetic dolomite cementation during Oceanic Anoxic Event 1: the mid-Cretaceous Maracaibo Platform, northwestern South America. Am. J. Sci. 316, 669–711.

Phoenix, V.R., Konhauser, K.O., 2008. Benefits of bacterial biomineralization. Geobiology 6, 303–308.

Phoenix, V.R., Martinez, R.E., Konhauser, K.O., Ferris, F.G., 2002. Characterization and implications of the cell surface reactivity of *Calothrix* sp. strain KC97. Appl. Environ. Microbiol. 68, 4827–4834.

Piper, D.Z., Calvert, S.E., 2009. A marine biogeochemical perspective on black shale deposition. Earth-Sci. Rev. 95, 63–96.

Piper, D.Z., Perkins, R.B., 2004. A modern vs. Permian black shale-the hydrography, primary productivity, and water-column chemistry of deposition. Chem. Geol. 206, 177–197.

Planavsky, N.J., Reinhard, C.T., Wang, X., Thomson, D., McGoldrick, P., Rainbird, R.H., Johnson, T., Fischer, W.W., Lyons, T.W., 2014. Low Mid-Proterozoic atmospheric oxygen levels and the delayed rise of animals. Science 346, 635–638.

Pokrovsky, O.S., Martinez, R., Golubev, S., Kompantseva, E., Shirokova, L., 2008. Adsorption of metals and protons on *Gloeocapsa* sp. cyanobacteria: a surface speciation approach. Appl. Geochem. 23, 2574–2588.

Porra, R.J., Thompson, W.A., Kriedemann, P.E., 1989. Determination of accurate extinction coefficients and simultaneous equations for assaying chlorophylls *a*

and *b* extracted with four different solvents: verification of the concentration of chlorophyll standards by atomic absorption spectroscopy. Biochim. Biophys. Acta 975, 384–394.

Rajaneesh, K.M., Mitbavkar, S., 2013. Factors controlling the temporal and spatial variations in *Synechococcus* abundance in a monsoonal estuary. Mar. Environ. Res. 92, 133–143.

Ransom, B., Bennett, R.H., Baerwald, R., Shea, K., 1997. TEM study of in situ organic matter on continental margins: occurrence and the "monolayer" hypothesis. Mar. Geol. 138, 1–9.

Ransom, B., Kim, D., Kastner, M., Wainwright, S., 1998. Organic matter preservation on continental slopes: importance of mineralogy and surface area. Geochim.

Cosmochim. Acta 62, 1329–1345.

Rao, R., Song, S., Lopez-Valdivieso, A., 2012. Specific adsorption of chromium species on kaolinite surface. Miner. Process. Extr. Metall. Rev. 33, 180–189.

Raven, J., Falkowski, P., 1999. Oceanic sinks for atmospheric CO_2. Plant Cell Environ. 22, 741–755.

Reinhard, C.T., Planavsky, N.J., Robbins, L.J., Partin, C.A., Gill, B.C., Lalonde, S.V., Bekker, A., Konhauser, K.O., Lyons, T.W., 2013. Proterozoic ocean redox and biogeochemical stasis. Proc. Natl. Acad. Sci. U. S. A. 110, 5357–5362.

Reinhard, C.T., Planavsky, N.J., Wang, X., Fischer, W.W., Johnson, T.M., Lyons, T.W., 2014. The isotopic composition of authogenic chromium in anoxic marine sediments: a case study from the Cariaco Basin. Earth Planet. Sci. Lett. 407, 9–18.

Sakamoto, T., Bryant, D.A., 1998. Growth at low temperature causes nitrogen limitation in the cyanobacterium *Synechococcus* sp. PCC 7002. Arch. Microbiol. 169, 10–19.

Schauble, E., Rossman, G.R., Taylor Jr., H.P., 2004. Theoretical estimates of equilibrium chromium-isotope fractionations. Chem. Geol. 205, 99–114.

Schultze-Lam, S., Fortin, D., Davies, B.S., Beveridge, T.J., 1996. Mineralization of bacterial surfaces. Chem. Geol. 132, 171–181.

Scott, C., Lyons, T.W., Bekker, A., Shen, Y., Poulton, S.W., Chu, X., Anbar, A.D., 2008. Tracing the stepwise oxidation of the Proterozoic ocean. Nature 452, 456–458.

Scott, C.T., Planavsky, N.J., Dupont, C.L., Kendall, B., Gill, B.C., Robbins, L.J., Husband, K.F., Arnold, G.L., Wing, B.A., Poulton, S.W., Bekker, A., Anbar, A.D., Konhauser, K.O., Lyons, T.W., 2013. Bioavailability of zinc in marine systems through time. Nat. Geosci. 6, 125–128.

Sengco, M.R., Li, A.S., Tugend, K., Kulis, D., Anderson, D.M., 2001. Removal of red- and brown-tide cells using clay flocculation I. Laboratory culture experiments with *Gymnodinium breve* and *Aureococcus anophage*ff*erens*. Mar. Ecol. Prog. Ser. 210, 41–53.

Smith, S.V., Hollibaugh, 1993. Coastal metabolism and the oceanic organic carbon balance. Rev. Geophys. 31, 75–89.

Spark, K.M., Wells, J.D., Johnson, B.B., 1995. Eur. J. Soil Sci. 46, 633–640.

Stevens, S.E., Porter, R.D., 1980. Transformation in *Agmenellum quadruplicatum*. Proc. Natl. Acad. Sci. U. S. A. 77, 6052–6056.

Suess, E., 1980. Particulate organic carbon flux in the oceans – surface productivity and oxygen utilization. Nature 288, 260–262.

Sutherland, B.R., Barrett, K.J., Gingras, M.K., 2014. Clay settling in fresh and salt water. Environ. Fluid Mech. 15, 147–160.

Suzuki, N., Ishida, K., Shinomiya, Y., Ishiga, H., 1998. High productivity in the earliest Triassic ocean: black shales, Southwest Japan. Palaeogeogr. Palaeoclimatol. Palaeoecol. 141, 53–65.

Swanner, E.D., Planavsky, N.J., Lalonde, S.V., Robbins, L.J., Bekker, A., Rouxel, O.J., Saito, M.A., Kappler, A., Mojzsis, J., Konhauser, K.O., 2014. Cobalt and marine redox evolution. Earth Planet. Sci. Lett. 390, 253–263.

Taggart Jr., M.S., Kaiser, A.D. Junior, 1960. Clay mineralogy of the Mississippi River deltaic sediments. Geol. Soc. Am. Bull. 71, 521–530.

Thiry, M., 2000. Palaeoclimatic interpretation of clay minerals in marine deposits: an outlook from the continental origin. Earth Sci. Rev. 49, 201–221.

Thomas, F., Michot, L.J., Vantelon, D., Montarges, E., Prelot, B., Cruchaudet, M., Delon, J.-F., 1999. Layer charge and electrophoretic mobility of smectites. Colloids Surf. A Physicochem. Eng. Asp. 159, 351–358.

Tietjen, T., Vähätalo, A.V., Wetzel, R.G., 2005. Effects of clay mineral turbidity on dissolved organic carbon and bacterial production. Aquat. Sci. 67, 51–60.

Tribovillard, N., Algeo, T.J., Lyons, T., Riboulleau, A., 2006. Trace metals as paleoredox and paleoproductivity proxies: an update. Chem. Geol. 232, 12–32.

Twining, B.S., Baines, S.B., Fisher, N.S., 2004. Element stoichiometries of individual plankton cells collected during the southern ocean iron experiment (SOFeX). Limnol. Oceanogr. 49, 2115–2128.

Tyson, R.V., 2001. Sedimentation rate, dilution, preservation and total organic carbon: some results of a modeling study. Org. Geochem. 32, 333–339.

Uncles, R.J., Stephens, J.A., Law, D.J., 2006. Turbidity maximum in the macrotidal, highly turbid Humber Estuary, UK: flocs, fluid mud, stationary suspensions and tidal bores. Estuar. Coast. Shelf Sci. 67, 30–52.

Urrutia, M.M., Kemper, M., Doyle, R., Beveridge, T.J., 1992. The membrane-induced proton motive force influences the metal binding ability of *Bacillus subtilis* cell walls. Appl. Environ. Microbiol. 58, 3837–3844.

Verspagen, J.M.H., Visser, P.M., Huisman, J., 2006. Aggregation with clay causes sedimentation of the buoyant cyanobacteria *Microcystis* spp. Aquat. Microb. Ecol. 44, 165–174.

Walker, S.G., Flemming, C.A., Ferris, F.G., Beveridge, T.J., Bailey, G.W., 1989.

Physiochemical interaction of *Escherichia coli* cell envelopes and *Bacillus subtilis* cell walls with two clays and ability of the composite to immobilize heavy metals from solution. Appl. Environ. Microbiol. 55, 2976–2984.

Wan, S., Li, A., Clift, P.D., Stuut, J.-B.W., 2007. Development of the East Asian monsoon: mineralogical and sedimentological records in the northern South China Sea since 20 Ma. Palaeogeogr. Palaeoclimatol. Palaeoecol. 254, 561–582.

Wanty, R.B., Goldhaber, M.B., 1992. Thermodynamics and kinetics of reactions involving vanadium in sedimentary rocks. Geochim. Cosmochim. Acta 56, 1471–1483.

Waterbury, J.B., Watson, S.W., Guillard, R. R. L. And Brand, L. E., 1979. Widespread occurrence of a unicellular, marine, planktonic, cyanobacterium. Nature 277, 293–294.

Xie, S., Pancost, R.D., Yin, H., Wang, H., Evershed, R.P., 2005. Two episodes of microbial change coupled with Permo/Triassic faunal mass extinction. Nature 434, 494–497.

Xu, L., Lehmann, B., Mao, J., Nägler, T.F., Neubert, N., Böttcher, M.E., Escher, P., 2012. Mo isotope and trace element patterns of Lower Cambrian black shales in South China: multi-proxy constraints on the paleoenvironment. Chem. Geol. 318–319, 45–59.

Chapter 6: Conclusions

This Thesis had four essential aims: 1) to investigate the mechanisms underpinning biotic recovery, namely the source of organic matter, following the end-Permian mass extinction; 2) to evaluate the occurrence and effect of subsequent Siberian Trap volcanism on climate during the Early Triassic; 3) the plausibility of using geochemical signals from Early Triassic climate and biotic recovery to correlate fine-grained deposits across the basin and 4) determine the accuracy of trace metal indicators used in interpreting environmental conditions.

In Chapter 2, the co-occurrence of biogenically derived silica and geochemical proxies for productivity (such as Ba and P) with sedimentological indicators of storm activity is shown to indicate the role of the Early Triassic monsoon climate in biotic recovery following the end-Permian mass extinction. Critically, the monsoon induced an increase in fluvially transported sediments, high in silica, to the shallow marine realm, while wind driven upwelling brought critical nutrients. These combined effects allowed for radiolarian blooms to take place, serving as a source of organic matter to the sea floor and establishing a trophic base for biotic recovery. The continental configuration of the Early Triassic, the supercontinent Pangea, was critical in magnifying these effects, suggesting that biotic recovery was the result of both climatic and tectonic conditions.

In Chapter 3, sedimentological evidence is provided which suggests Siberian Trap volcanism occurred at the end of the Smithian, coinciding with previous U-Pb dates of ~251.4 Ma and ~250.2 Ma (Kamo et al., 2003, Paton et al., 2010, Burgess and Bowring, 2015). After the initial eruptive pulse (~251.4 Ma), modelling of carbon isotope data indictes that CO_2 outgassing occurred during the Early-Smithian and caused

atmospheric temperature to increase by up to 10°C and the pH of the oceans to decrease by 0.55 units. At the end of the Smithian, a second period of outgassing occurred, which was more gradual, but was accompanied by volcanically sourced sediment. This combination of atmospheric outgassing and volcanically derived sediment resulted in marine anoxia and the extinction of carbonate-generating biota. This suggests that outgassing alone did not trigger the end-Smithian extinction, but it was the combined effects of outgassing and eruptive material. This correlation may be owing to the fact that magmas erupted close to surface produce more sulfur-enriched gases (Gaillard et al., 2011), leading to a higher potential for acid rain.

In the 4th chapter, chemostratigraphic analysis is shown to be useful in correlating chronostratigraphic surfaces within the Montney Formation, a fine-grained succession. Geochemical trends can be used to distinguish changes in mineralogy, provenance, clay and detrital input. These trends highlight changes in relative sea-level, hydrothermal input and climate change. Specifically, within the Early Triassic of western Canada, 13 distinct chemofacies were identified and correlated. These correlations reveal broad clinoform surfaces which indicate that the lower-mid Montney deposits of British Columbia are temporally equivalent to upper Montney sediments in Alberta. Clay proxies indicate that a climatic shift occured at the Smithian/Spathian boundary, corresponding to an increase in hydrothermal iput. An increase in felsic input, indicated by cross plots of Th/Sc versus Cr/Th, suggests that early accretion of the Yukon-Tanana terrane occurred by the Early Anisian. Additionally, early terrane accretion is supported by evidence of volcanic arc input in the Early Anisian.

In chapter 5, clay and cyanobacteria are shown to flocculate, providing a mechanism for the deposition of organic-rich, fine-grained deposits. The cyanobacterial cells become encased in a clay shroud, likely due to cation-bridging, providing a mechanism whereby both the cellular organic matter as well as the bioactive metals (such as P, Cu, Zn, and Ba) are preserved. These trace metals have been previously thought to be liberated during organic matter degradation and only retained under conditions of limited oxidation (such as marine anoxia; Algeo and Maynard, 2004; Tribovillard et al., 2006). The rapid deposition of cyanobacterial cells in the presence of clay in a marine environment in addition to cellular encasement suggests that such extreme conditions are not always necessary. While redox controls have been recognized as contributing to the preservation of marine organic matter, encapsulation of reactive microbial biomass is another important mechanism. This suggests that some organic-rich, fine-grained deposits may be the product of discrete depositional events, such as algal blooms exposed to unusually high river discharge, and not the result of steady-state conditions.

Together, these chapters serve as a framework for understanding the complexities of environmental and biotic recovery following the largest mass extinction of all time. These findings point to a setting of extreme monsoonal climate cycles perturbed by volcanic eruption in the Early Triassic in which biota survived in shallow-marine enclaves supplied with organic matter by seasonal planktonic blooms. Sedimentation via flocculation of these blooms allowed for the rapid deposition of planktonic mass to the sea floor. While it has been debated in the past whether biotic recovery occurred gradually as conditions improved, these findings suggest that

environmental conditions continued to be dynamic throughout the Early Triassic. Biota survived in spite of these subsequent environmental challenges.

References

Algeo, T.J., Maynard, J.B., 2004. Trace-element behavior and redox facies in core shales of Upper Pennsylvanian Kansas-type cyclothems. Chem. Geol. 206, 289–318.

Burgess, S.D. and Bowring, S.A. 2015. High-precision geochronology confirms voluminous magmatism before, during, and after Earth's most severe extinction. Science Advances, 1. E1500470.

Gaillard, G., Scaillet, B., and Arndt, N.T. 2011. Atmospheric oxygenation caused by a change in volcanic degassing pressure. Nature, v. 478, p. 229-232.

Kamo, S.L., Czamanske, G.K., Amelin, Y., Fedorenko, V.A., Davis, D.W., and Trofimov, V.R. 2003. Rapid eruption of Siberian flood-volcanic rocks and evidence for coincidence with the Permian-Triassic boundary and mass extinction at 251 Ma. Earth and Planetary Science Letters, v. 214, p. 75-91.

Paton, M.T., Ivanov, A.V., Fiorentini, M.L., McNaughton, N.J., Mudrovska, I., Reznitskii, L.Z., and Demonterova, E.I. 2010. Late Permian and Early Triassic magmatic pulses in the Angara-Taseeva syncline, Southern Siberian Traps and their possible influence on the environment. Russian Geology and Geophysics, v. 51, p. 1012-1020.

Tribovillard, N., Algeo, T.J., Lyons, T., Riboulleau, A., 2006. Trace metals as paleoredox and paleoproductivity proxies: an update. Chem. Geol. 232, 12–32.

Works Cited

A+ Medium Recipe, 2017. UTEX Culture Collection of Algae at the University of Texas at Austin. http://web.biosci.utexas.edu/utex/Media%20PDF/a%20plus%20medium.pdf (accessed 06.11.16).

Abd-Allah, S.M., El Hussaini, O.M., Mahdy, R.M., 2005. Towards a more safe environment: (4) sorptability of vanadium as a nuclear constructing material by some clay sediments in Egypt. J. Appl. Sci. Res. 1, 168–175.

Adatte, T., Keller, G. and Stinnesbeck, W. (2002) Late Cretaceous to early Paleocene climate and sea-level fluctuations: the Tunisian record. Palaeogeogr. Palaeoclimatol. Palaeoecol., 178, 165–196.

Ajouyed, O., Hurel, C., Marmier, N., 2011. Evaluation of the adsorption of hexavalent chromium on kaolinite and illite. J. Environ. Prot. 2, 1347–1352.

Algeo, T.J., Maynard, J.B., 2004. Trace-element behavior and redox facies in core shales of Upper Pennsylvanian Kansas-type cyclothems. Chem. Geol. 206, 289–318.

Algeo, T.J. and Lyons, T.W. (2006) Mo-total organic carbon covariation in modern anoxic marine environments: implications for analysis of paleoredox and paleohydrographic conditions. Paleoceanography, 21, PA1016.

Algeo, T.J. and Twitchett, R.J. (2010) Anomalous Early Triassic sediment fluxes due to elevated weathering rates and their biological consequences. Geology, 38, 1023–1026.

Algeo, T.J., Schwark, L. and Hower, J.C. (2004) Highresolution geochemistry and sequence stratigraphy of the Hushpuckney Shale (Swope Formation, eastern Kansas): implications for climate-environmental dynamics of the Late Pennsylvanian Midcontinent Seaway. Chem. Geol., 206, 259–288.

Algeo, T.J., Ellwood, B., Nguyen, T.K.T., Rowe, H., and Maynard, J.B. 2007. The Permian-Triassic boundary at Nhi Tao, Vietnam: Evidence for recurrent influx of sulfidic watermasses to a shallow-marine carbonate platform. Palaeogeography, Palaeoclimatology, Palaeoecology, v. 252, p. 304-327.

Algeo, T., Henderson, C.M., Ellwood, B., Rowe, H., Elswick, E., Bates, S., Lyons, T., Hower, J.C., Smith, C., Maynard, B., Hays, L.E., Summons, R.E., Fulton, J., and Freeman, K.H. 2012. Evidence for a diachronous Late Permian marine crisis from the Canadian Arctic region. GSA Bulletin, v. 124, p. 1424-1448.

Aldrin, M., M. Holden, P. Guttorp, R. B. Skeie, G. Myhre, and T. K. Berntsen, 2012: Bayesian estimation of climate sensitivity based on a simple climate model fitted to observations of hemispheric temperatures and global ocean heat content. Environmetrics, 23, 253–271.

Adachi, M., Yamamoto, K., and Sugisaki, R. 1986. Hydrothermal chert and associated siliceous rocks from the northern Pacific: Their geological significance as indication of ocean ridge activity. Sedimentary Geology, v. 47, p. 125-148.

Amelung, W., Zech, W., 1996. Organic species in ped surface and core fractions along a climosequence in the prairie North America. Geoderma 74, 193–206.

Amorosi, A., Colalongo, M.L., Dinelli, E., Lucchini, F. and Vaiani, S.C. (2007) Cyclic variations in sediment provenance from late Pleistocene deposits of the eastern Po

Plain, Italy. In: Sedimentary Provenance and Petrogenesis: Perspectives from Petrography and Geochemistry (Eds J. Arribas, S. Critelli and M.J. Johnsson), GSA Spec. Paper, 420, 13–24.

Anbar, A.D. and Rouxel, O. (2007) Metal stable isotopes in paleoceanography. Annu. Rev. Earth Planet. Sci., 35, 717– 746.

Aplin, A.C., Macquaker, J.H., 2011. Mudstone diversity: origin and implications for source, seal, and reservoir properties in petroleum systems. AAPG Bull. 95, 2031–2059.

Archambault, M.-C., Grant, J., Bricelj, V.M., 2003. Removal efficiency of the dinoflagellate *Heterocapsa triquetra* by phosphatic clay and implications for the mitigation of harmful algal blooms. Mar. Ecol. Prog. Ser. 253, 97–109.

Archer, C., Vance, D., 2008. The isotopic signature of the global riverine molybdenum flux and anoxia in the ancient oceans. Nat. Geosci. 1, 597–600.

Armstrong-Altrin, J.S., Lee, Y.I., Verma, S.P. and Ramasamy, S. (2004) Geochemistry of sandstones from the Upper Miocene Kudankulam Formation, southern India: implications for provenance, weathering, and tectonic setting. J. Sediment. Res., 74, 285–297.

Arnarson, T.S., Keil, R.G., 2001. Organic-mineral interactions in marine sediments studied using density fractionation and X-ray photoelectron spectroscopy. Org. Geochem. 32, 1401–1415.

Arnarson, T.S., Keil, R.G., 2005. Influence of organic-mineral aggregates on microbial degradation of the dinoflagellate *Scrippsiella trochoidea*. Geochim. Cosmochim. Acta 69, 2111–2117.

Arsairai, B., Wannakomol, A., Feng, Q., and Chonglakmani, C. 2016. Paleoproductivity and paleoredox condition of the Huai Hin Lat Formation in Northeastern Thailand. Journal of Earth Science, v. 27, p. 350-364.

Arthur, M.A., Jenkyns, H.C. and Brumsack, H.J. (1990) Stratigraphy, geochemistry, and paleoceanography of organic carbon-rich Cretaceous sequences. In: Cretaceous Resources, Events and Rhythms (Eds. R.N. Ginsburg and B. Beaudoin), pp. 75–119. Kluwer Academic Publishing, Amsterdam.

Arthur, M.A., Sageman, B.B., 1994. Marine black shales: depositional mechanisms and environments of ancient deposits. Annu. Rev. Earth Planet. Sci. 22, 499–552.

Asael, D., Tissot, F.L.H., Reinhard, C.T., Rouxel, O., Dauphas, N., Lyons, T., Ponzevera, E., Liorzou, C. and Ch_eron, S. (2013) Coupled molybdenum, iron and uranium stable isotopes as oceanic paleoredox proxies during the Paleoproterozoic Shunga Event. Chem. Geol., 362, 193–210.

Avnimelech, Y., Troeger, B.W., Reed, L.W., 1982. Mutual flocculation of algae and clay: evidence and implications. Science 216, 63–65.

Baldock, J.A., Skjemstad, J.O., 2000. Role of the soil matrix and minerals in protecting natural organic materials against biological attack. Org. Geochem. 31, 697–710.

Banner, J.L. (1995) Application of the trace element and isotope geochemistry of strontium to studies of carbonate diagenesis. Sedimentology, 42, 805–824.

Barclay, J.E., Krause, E.E., Campbell, R.I. and Utting, J. (1990) Dynamic casting and growth faulting: Dawson Creek Graben Complex, Carboniferous- Permian Peace River Embayment, western Canada. In: Geology of the Peace River Arch (Eds S.C. O'Connell and J.S. Bell), Bulletin of Canadian Petroleum Geology, 38A, 115–145.

Barling, J., Anbar, A.D., 2004. Molybdenum isotope fractionation during adsorption by manganese oxides. Earth Planet. Sci. Lett. 217, 315–329.

Beauchamp, B. & Baud, A. Growth and demise of Permian biogenic chert along northwest Pangea: evidence for end-Permian collapse of thermohaline circulation. *Palaeogeogr., Palaeoclimatol., Palaeoecol.* **184**, 37-63 (2002).

Beaulieu, S.E., Sengco, M.R., Anderson, D.M., 2005. Using clay to control harmful algal blooms: deposition and resuspension of clay/algal flocs. Harmful Algae 4, 123–138.

Beatty, T.W., Zonneveld, J.-P. and Henderson, C.M. (2008) Anomalously diverse Early Triassic ichnofossil assemblages in northwest Pangaea: a case for a shallowmarine habitable zone. Geology, 36, 771–774.

Bechtel, A., Püttmann, W., 1997. Palaeoceanography of the early Zechstein Sea during Kupferschiefer deposition in the Lower Rhine Basin (Germany): a reappraisal from stable isotope an organic geochemical investigations. Palaeogeogr. Palaeoclimatol. Palaeoecol. 136, 331–358.

Benedicto, A., Degueldre, C. and Missana, T. (2014) Gallium sorption on montmorillonite and illite colloids: experimental study and modeling by ionic exchange and surface complexation. Appl. Geochem., 40, 43–50.

Bender, F. A. M., A. M. L. Ekman, and H. Rodhe, 2010: Response to the eruption of Mount Pinatubo in relation to climate sensitivity in the CMIP3 models. Clim. Dyn., 35, 875–886.

Bennett, R.H., Ransom, B., Kastner, M., Baerwald, R.J., Hulbert, M.H., Sawyer, W.B., Olsen, H., Lambert, M.W., 1999. Early diagenesis: impact of organic matter on mass physical properties and processes, California continental margin. Mar. Geol. 159, 7–34.

Bennett, R.H., Hulbert, M.H., Curry, K.J., Curry, A., Douglas, J., 2012. Organic matter sequestered in potential energy fields predicted by 3-D clay microstructure model, direct observations of organo-clay micro- and nanofabric. Mar. Geol. 315–318, 108–114.

Beranek, L.P. and Mortensen, J.K. (2011) The timing and provenance record of the Late Permian Klondike orogeny in northwestern Canada and arc-continent collision along western North America. Tectonics, 30, TC5017.

Beranek, L.P., Mortensen, J.K., Orchard, M.J. and Ullrich, T. (2010) Provenance of North American Triassic strata from west-central and southeastern Yukon: correlations with coeval strata in the Western Canada Sedimentary Basin and Canadian Arctic Islands. Can. J. Earth Sci., 47, 53–73.

Bergstrom, S.M., Young, S. and Schmitz, B. (2010) Katian (Upper Ordovician) d13C chemostratigraphy and sequence stratigraphy in the United States and Baltoscandia: a regional comparison. Palaeogeogr. Palaeoclimatol. Palaeoecol., 296, 217–234.

Berner, R.A. and Westrich, J.T. (1985) Bioturbation and the early diagenesis of carbon and sulphur. Am. J. Sci., 285, 193–206.

Betts, J.N., Holland, H.D., 1991. The oxygen content of ocean bottom waters, the burial efficiency of organic carbon, and the regulation of atmospheric oxygen. Palaeogeogr. Palaeoclimatol. Palaeoecol. 97, 5–18.

Beveridge, T.J., 1989. Role of cellular design in bacterial metal accumulation and mineralization. Annu. Rev. Microbiol. 43, 147–171.

Beveridge, T.J., Graham, L.L., 1991. Surface layers of bacteria. Microbiol. Rev. 55, 684–705.

Bhatia, M.R. and Crook, K.A.W. (1986) Trace element characteristics of graywackes and tectonic setting discrimination of sedimentary basins. Contrib. Miner. Petrol., 92, 181–193.

Bhattacharyya, K.G., Gupta, S.S., 2008. Adsorption of a few heavy metals on natural and modified kaolinite and montmorillonite: a review. Adv. Colloid Interf. Sci. 140, 114–131.

Black, B.A., Neely, R.R., L., J.-F., Elkins-Tanton, L.T., Kiehl, J.T., Shields, C.A., Mills, M.J., and Bardeen, C. 2018. Systematic swings in end-Permian climate from Siberian Traps carbon and sulfur outgassing. Nature Geoscience, v. 11, p. 949-954.

Blakey, R. (2006) Mollwide plate tectonic maps. Available at: http://jan.ucc.nau.edu/rb7/mollglobe.html

Bonjour, J.L. and Dabard, M.P. (1991) Ti/Nb ratios of clastic terrigenous sediments used as an indicator of provenance. Chem. Geol., 91, 257–267.

Bracciali, L., Marroni, M., Pandolfi, L. and Rocchi, S. (2007) Geochemistry and petrography of Western Tethys Cretaceous sedimentary covers (Corsica and Northern Apennines): from source areas to configuration of margins. In: Sedimentary Provenance and Petrogenesis: Perspectives from Petrography and Geochemistry (Eds J. Arribas, S. Critelli and M.J. Johnsson), GSA Spec. Paper, 420, 73–93.

Breit, G.N., Wanty, R.B., 1991. Vanadium accumulation in carbonaceous rocks: a review of geochemical controls during deposition and diagenesis. Chem. Geol. 91, 83–97.

Brennecka, G.A., Herrmann, A.D., Algeo, T.J., and Anbar, A.D. 2011. Rapid expansion of oceanic anoxia immediately before the end-Permian mass extinction. PNAS, v. 108, p. 17631-17634.

Bruland, K.W., Donat, J.R., Hutchins, D.A., 1991. Interactive influences of bioactive trace metals on biological production in oceanic waters. Limnol. Oceanogr. 36, 1555–1577.

Brumsack, H.-J. (2006) The trace metal content of recent organic carbon-rich sediments: implications for Cretaceous black shale formation. Palaeogeogr. Palaeoclimatol. Palaeoecol., 232, 344–361.

Buerge, I.J., Hug, S.J., 1999. Influence of mineral surfaces on chromium(VI) reduction by iron(II). Environ. Sci. Technol. 33, 4285–4291.

Burdige, D.J., 2007. Preservation of organic matter in marine sediments: controls, mechanisms, and an imbalance in sediment organic carbon budgets? Chem. Rev. 107, 467–485.

Burgess, S.D. and Bowring, S.A. 2015. High-precision geochronology confirms voluminous magmatism before, during, and after Earth's most severe extinction. Science Advances, 1. E1500470.

Calvert, S.E. and Pedersen, T.F. (1993) Geochemistry of recent oxic and anoxic marine sediments: implications for the geological record. Mar. Geol., 113, 67–88.

Campbell, L., Liu, H., Nolla, H.A., Vaulot, D., 1997. Annual variability of phytoplankton and bacteria in the subtropical North Pacific Ocean at Station ALOHA during the 1991–1994 ENSO event. Deep-Sea Res. 44, 167–192.

Canfield, D.E., 1994. Factors influencing organic carbon preservation in marine sediments. Chem. Geol. 114, 315–329.

Canfield, D.E., Thamdrup, B. and Hansen, J.W. (1993) The anaerobic degradation of organic matter in Danish coastal sediments: iron reduction, manganese reduction, and sulfate reduction. Geochim. Cosmochim. Acta, 57, 3867– 3883.

Canfield, D.E., Jørgensen, B.B., Fossing, H., Glud, R., Gundersen, J., Ramsing, N.B., Thamdrup, B., Hansen, J.W., Nielsen, L.P., Hall, P.O.J., 1993b. Pathways of organic carbon oxidation in three continental margin sediments. Mar. Geol. 113, 27–40.

Cao, C., Love, G.D., Hays, L.E., Wang, W., Shen, S., and Summons, R.E. 2009. Biogeochemical evidence for euxinic oceans and ecological disturbance presaging the end-Permian mass extinction event. Earth and Planetary Science Letters, v. 281, p. 188-201.

Carpenter, S.J. and Lohmann, K.C. (1992) Sr/Mg ratios of modern marine calcite: empirical indicators of ocean chemistry and precipitation rate. Geochim. Cosmochim. Acta, 56, 1837–1849.

Chamley, H. (1989) Clay Sedimentology. Springer-Verlag, Berlin, Heidelberg, 623 pp.

Chamot, D., Owttrim, G.W., 2000. Regulation of cold shock-induced RNA helicase gene expression in the cyanobacterium *Anabaena* sp. strain PCC 7120. J. Bacteriol. 182, 1251–1256.

Chappaz, A., Lyons, T.W., Gregory, D.D., Reinhard, C.T., Gill, B.C., Li, C. and Large, R.R. (2014) Does pyrite act as an important host for molybdenum in modern and ancient euxinic sediments? Geochim. Cosmochim. Acta, 126, 112– 122.

Chaudhri, A.R. and Singh, M. (2012) Clay minerals as climate change indicators-a case study. Am J Climate Change, 1, 231–239.

Chen, L., Men, X., Ma, M., Li, P., Jiao, Q., Lu, S., 2010. Polysaccharide release by *Aphanothece halophytica* inhibits cyanobacteria/clay flocculation. J. Phycol. 46, 417–423.

Chen, Y., Twitchett, R.J., Jiang, H., Richoz, S., Lai, Z., Yan, C., Sun, Y., Liu, X. and Wang, L. (2013) Size variation of conodonts during the Smithian-Spathian (Early Triassic) global warming event. Geology, 41, 823–826.

Chenot, E., Pellenard, P., Martinez, M., Deconinck, J.-F., Amiotte-Suchet, P., Thibault, N., Bruneau, L., Cocquerez, T., Laffont, R., Puc_eat, E. and Robaszynski, R. (2016) Clay mineralogical and geochemical expressions of the “Late Campanian Event” in

the Aquitaine and Paris basins (France): palaeoenvironmental implications. Palaeogeogr. Palaeoclimatol. Palaeoecol., 447, 42–52.

Cingolani, C.A., Manassero, M. and Abre, P. (2003) Composition, provenance and tectonic setting of Ordovician siliciclastic rocks in the San Rafael block: southern extension of the Precordillera crustal fragment, Argentina. J. S. Am. Earth Sci., 16, 91–106.

Clarke, W.A., Konhauser, K.O., Thomas, J.C., Bottrell, S.H., 1997. Ferric hydroxide and ferric hydroxysulfate precipitation by bacteria in an acid mine drainage lagoon. FEMS Microbiol. Rev. 20, 351–361.

Clift, P.D., Wan, S. and Blusztajn, J. (2014) Reconstructing chemical weathering, physical erosion and monsoon intensity since 25 Ma in the northern South China Sea: a review of competing proxies. Earth Sci. Rev., 130, 86–102.

Cole, D.B., Reinhard, C.T., Wang, X., Gueguen, B., Halverson, G.P., Gibson, T., Hodgskiss, M.S.W., McKenzie, N.R., Lyons, T.W., Planavsky, N.J., 2016. A shale-hosted Cr istope record of low atmospheric oxygen during the Proterozoic. Geology 44, 555–558.

Collins, M., R. Knutti, J. Arblaster, J.-L. Dufresne, T. Fichefet, P. Friedlingstein, X. Gao, W.J. Gutowski, T. Johns, G. Krinner, M. Shongwe, C. Tebaldi, A.J. Weaver and M. Wehner, 2013: Long-term Climate Change: Projections, Commitments and Irreversibility. In: Climate Change 2013: The Physical Science Basis. Contribution of Working Group I to the Fifth Assessment Report of the Intergovernmental Panel on Climate Change [Stocker, T.F., D. Qin, G.-K. Plattner, M. Tignor, S.K. Allen, J.

Boschung, A. Nauels, Y. Xia, V. Bex and P.M. Midgley (eds.)]. Cambridge University Press, Cambridge, United Kingdom and New York, NY, USA.

Condie, K.C., 2004. Supercontinents and superplume events: distinguishing signals in the geological record. Phys. Earth Planet. Inter. 146, 319–332.

Condie, K.C. and Wronkiewicz, D.J. (1989) The Cr/Th ratio in Precambrian pelites from the Kaapvaal Craton as an index of craton evolution. Earth Planet. Sci. Lett., 97, 256–267.

Cox, J.S., Smith, D.S., Warren, L.A., Ferris, F.G., 1999. Characterizing heterogeneous bacterial surface functional groups using discrete affinity spectra for proton binding. Environ. Sci. Technol. 33, 4514–4521.

Croudace, I.W., Rindby, A. and Rothwell, R.G. (2006) ITRAX: Description and Evaluation of a New Multifunction X-ray Core Scanner. Geological Society Special Publications, London, pp. 51–63.

Crowe, S.A., Døssing, L.N., Beukes, N.J., Bau, M., Kruger, S.J., Frei, R., Canfield, D.E., 2013. Atmospheric oxygenation three billion years ago. Nature 501, 535–539.

Curtis, C.D., Coleman, M.L. and Love, L.G. (1986) Pore water evolution during sediment burial from isotopic and mineral chemistry of calcite, dolomite and siderite concretions. Geochim. Cosmochim. Acta, 50, 2321–2334.

Cuven, S., Francus, P. and Lamoureux, S.F. (2010) Estimation of grain size variability with micro X-ray fluorescence in laminated sediments, Cape Bounty, Canadian High Arctic. J. Paleolimnol., 88, 803–817.

Daag, A.S., B. S. Tubianosa, C. G. Newhall, N. M. Tuñgol, D. Javier, M. T. Dolan, P. J. Delos Reyes, R. A. Arboleda, M. L. Martinez, and T. M. Regalado, in Fire and Mud: Eruptions and Lahars of Mount Pinatubo, Philip- pines, C. G. Newhall and R. S. Punongbayan, Eds. (Univ. of Washington Press, Seattle, 1996), pp. 409-414

Dai, S., Ren, D., Chou, C.-L., Li, S. and Jiang, Y. (2006) Mineralogy and geochemistry of the No. 6 Coal (Pennsylvanian) in the Junger coalfield, Ordos Basin, China. Int. J. Coal Geol., 66, 253–270.

Dai, S., Li, D., Chou, C.-L., Zhao, L., Zhang, Y., Ren, D., Ma, Y. and Sun, Y. (2008) Mineralogy and geochemistry of boehmite-rich coals: new insights from the Haerwusa Surface Mine, Jungar Coalfield, Inner Mongolia, China. Int. J. Coal Geol., 74, 185–202.

Dai, S., Ren, D., Chou, C.-L., Finkelman, R.B., Seredin, V.V. and Zhou, Y. (2012a) Geochemistry of trace elements in Chinese coals: a review of abundances, genetic types, impacts on human health, and industrial utilization. Int. J. Coal Geol., 94, 3–21.

Dai, S., Zhou, J., Jiang, Y., Ward, C.R., Wang, X., Li, T., Xue, W., Liu, S., Tian, H., Sun, X. and Zhou, D. (2012b) Mineralogical and geochemical compositions of the Pennsylvanian coal in the Adaohai Mine, Daqingshan Coalfield, Inner Mongolia, China: modes of occurrence and origin of diaspora, gorceixite, and ammonian illite. Int. J. Coal Geol., 94, 250–270.

Davis, C.C., Chen, H.W., Edwards, M., 2002. Modeling silica sorption to iron hydroxide. Environ. Sci. Technol. 36, 582–587.

Davies, G.R. (1997) The Triassic of the Western Canada Sedimentary Basin: tectonic and stratigraphic framework, paleogeography, paleoclimate and biota. Bull. Can. Pet. Geol., 45, 434–460.

Davies, G.R., Moslow, T.F. and Sherwin, M.D. (1997) The Lower Triassic Montney Formation, west-central Alberta. In: Triassic of the Western Canada Sedimentary Basin (Eds T.F. Moslow and J. Wittenberg), Bulletin of Canadian Petroleum Geology, 45, 474–505.

Dean, W.E., 2007. Sediment geochemical records of productivity and oxygen depletion along the margin of western North America during the past 60,000 years: teleconnections with Greenland ice and the Cariaco Basin. Quat. Sci. Rev. 26, 98–114.

Dean, W.E., Gardner, J.V., Piper, D.Z., 1997. Inorganic geochemical indicators of glacial- interglacial changes in productivity and anoxia on the California continental margin. Geochim. Cosmochim. Acta 61, 4507–4518.

Dean, W., Anderson, R., Bradbury, J.P. and Anderson, D. (2002) A 1500-year record of climatic and environmental change in Elk Lake, Minnesota-I: a varve thickness and gray-scale density. J. Paleolimnol., 27, 287–299. Deutsch, C.V. (2002) Geostatistical Reservoir Modeling. Oxford University Press, New York, NY, 376 pp.

Dessert, C., Dupre, B., Francois, L.M., Schott, J., Gaillardet, J., Chakrapani, G., and Bajpai, S. 2001. Erosion of Deccan Traps determined by river geochemistry: impact on the global climate and the $^{87}Sr/^{86}Sr$ ratio of seawater. Earth and Planetary Science Letters, v. 188, p. 459-474.

DeWever, P., O'Dogherty, L., Gorican, S. 2014. Monsoon as a cause of radiolarite in the Tethyan realm. Comptes Rendus Geoscience, v. 346, p. 287-297.

Dinelli, E., Tateo, F. and Summa, V. (2007) Geochemical and mineralogical proxies for grain size in mudstones and siltstones from the Pleistocene and Holocene of the Po River alluvial plain, Italy. From source areas to configuration of margins. In: Sedimentary Provenance and Petrogenesis: Perspectives from Petrography and Geochemistry (Eds J. Arribas, S. Critelli and M.J. Johnsson), GSA Spec. Paper, 420, 25–36.

Ding, X., Henrichs, S.M., 2002. Adsorption and desorption of proteins and polyamino acids by clay minerals and marine sediments. Mar. Chem. 77, 225–237.

Dittrich, M., Sibler, S., 2005. Cell surface groups of two picocyanobacteria strains studied by zeta potential investigations, potentiometric titration, and infrared spectroscopy. J. Colloid Interface Sci. 286, 8.

Dixon, J. (2000) Regional lithostratigraphic units in the Triassic Montney Formation of western Canada. Bull. Can. Pet. Geol., 48, 80–83.

Doyle, R.J., 1989. How cell walls of Gram-positive bacteria interact with metal ions. In: Beveridge, T.J., Doyle, R.J. (Eds.), Metal Ions and Bacteria. Wiley, New York, pp. 275–293.

Du, J., Pushkarova, R.A., Smart, R.St.C., 2009. A cryo-SEM study of aggregate and floc structure changes during clay settling and raking processes. Int. J. Miner. Process. 93, 66–72.

Dumitrescu, M., Brassell, S.C., 2005. Biogeochemical assessment of sources of organic matter and paleoproductivity during the early Aptian Oceanic Anoxic Event at Shatsky Rise, ODP Leg 198. Org. Geochem. 36, 1002–1022.

Duque-Botero, F., Maurrasse, F.J.-M.R., 2008. Role of cyanobacteria in Corg-rich deposits: an example from Indidura Formation (Cenomanian-Turonian), northeastern Mexico. 2008. Cretac. Res. 29, 957–964.

Dymond, J., Suess, E., and Lyle, M. 1992. Barium in deep-sea sediment: A geochemical proxy for paleoproductivity. Paleoceanography, v. 7, p. 163-181.

Edwards, D.E., Barclay, J.E., Gibson, D.W., Kvill, G.E. and Halton, E. (1994) Triassic strata of the Western Canada Sedimentary Basin. In: Geological Atlas of the Western Canada Sedimentary Basin, Canadian Society of Petroleum Geologists and Alberta Research Council (Eds G.D. Mossop and I. Shetsen). Available at: http://www.ags.gov.ab.ca/publications/wcsb_atlas/atlas.html.

Ekman, V.W. 1905. On the influence of earth's rotation on ocean currents. Ark. Math. Astron. Fys., v. 2, p. 1-53.

Ellis, A.S., Johnson, T.M., Bullen, T.D., 2002. Chromium isotopes and the fate of hexavalent chromium in the environment. Science 295, 2060–2062.

Ellis, A.S., Johnson, T.M., Bullen, T.D., 2004. Using chromium stable isotope ratios to quantify Cr(VI) reduction: lack of sorption effects. Environ. Sci. Technol. 38, 3604–3607.

Ellwood, B.B., Tomkin, J.H., Ratcliffe, K.T., Wright, M. and Kafafy, A.M. (2008) High-resolution magnetic susceptibility and geochemistry for the Cenomanian/Turonian

boundary GSSP with correlation to time equivalent core. Palaeogeogr. Palaeoclimatol. Palaeoecol., 261, 105–126.

Embry, A.F. and Gibson, D.W. (1995) T-R sequence analysis of the Triassic succession of the Western Canada Sedimentary Basin. In: Proceedings of the Oil and Gas Forum '95 - Energy from Sediments' (Eds J.S. Bell, T.D. Bird, T.L. Hillier and E.L. Greener), Geological Survey of Canada, Open File 3058, 25–32.

Emerson, S., Hedges, J.I., 1988. Processes controlling the organic carbon content of open ocean sediments. Paléo 3, 621–634.

Erwin, D.H. 1994. The Permo-Triassic extinction. Nature, v. 367, p. 231-236.

Erwin, D.H. *Extinction: How Life on Earth Nearly Ended 250 Million Years Ago* (Princeton Univ. Press, Princeton, 2006).

Esser, K.B., Bockheim, J.G. and Helmke, P.A. (1991) Trace element distribution in soils formed in the Indiana Dunes, U.S.A. Soil Sci., 152, 340–350.

Feely, R.A., Massoth, G.J., Trefry, J.H., Baker, E.T., Paulson, A.J. and Lebon, G.T. (1994) Composition and sedimentation of hydrothermal plume particles from North Cleft segment, Juan de Fuca Ridge. J. Geophys. Res., 99, 4985–5006.

Fein, J.B., Daughney, C.J., Yee, N. and Davis, T.A. (1997) A chemical equilibrium model for metal adsorption onto bacterial surfaces. Geochim. Cosmochim.Acta, 61, 3319–3328.

Feng, Q., and Algeo, T.J. 2014. Evolution of oceanic redox conditions during the Permo-Triassic transition: Evidence form deepwater radiolarian facies. Earth-Science Reviews, v. 137, p. 34-51.

Ferri, F. and Zonneveld, J.-P. (2008) Were Triassic rocks of the Western Canada Sedimentary Basin deposited in a Foreland? Can. Soc. Petrol. Geol. Reservoir, 35, 12–14.

Flemming, C.A., Ferris, F.G., Beveridge, T.J., Bailey, G.W., 1990. Remobilization of toxic heavy metals adsorbed to bacterial wall-clay composites. Appl. Environ. Microbiol. 56, 3191–3203.

Fralick, P.W. 2003. Geochemistry of clastic sedimentary rocks: ratio techniques; in Geochemistry of Sediments and Sedimentary Rocks, Geological Association of Canada, Geotext 4.

Frei, R., Dahl, P.S., Frandsson, M.M., Jensen, L.A., Hansen, T.R., Terry, M.P., Frei, K.M., 2009. Lead-isotope and trace-element geochemistry of Paleoproterozoic metasedimentary rocks in the Lead and Rochford basins (Black Hills, South Dakota, USA): implications for genetic models, mineralization ages, and sources of leads in the Homestake gold deposit. Precambrian Res. 172, 1–24.

Froelich, P.N., Klinkhammer, G.P., Bender, M.L., Luedtke, N.A., Heath, G.R., Cullen, D., Dauphin, P., Hammond, D., Hartman, B. and Maynard, V. (1979) Early oxidation of organic matter in pelagic sediments of the eastern equatorial Atlantic: suboxic diagenesis. Geochim. Cosmochim. Acta, 43, 1075–1090.

Gadd, G.M. (2010) Metals, minerals and microbes: geomicrobiology and bioremediation. Microbiology, 156, 609–643.

Gaillard, G., Scaillet, B., and Arndt, N.T. 2011. Atmospheric oxygenation caused by a change in volcanic degassing pressure. Nature, v. 478, p. 229-232.

Galfetti, T., Hochuli, P.A., Brayard, A., Bucher, H., Weissert, H. and Os Vigran, J. (2007a) Smithian-Spathian boundary event: evidence for global climatic change in the wake of the end-Permian biotic crisis. Geology, 35, 291–294.

Galfetti, T., Bucher, H., Braynard, A., Hochuli, P.A., Weissert, H., Guodun, H., Atudorei, V. and Guex, J. (2007b) Late Early Triassic climate change: insights from carbonate carbon isotopes, sedimentary evolution and ammonoid paleobiogeography. Palaeogeogr. Palaeoclimatol. Palaeoecol., 243, 394–411.

Gerlach, T.M., H. R. Westrich, R. B. Symonds, in Fire and Mud: Eruptions and Lahars of Mount Pinatubo, Philip- pines, C. G. Newhall and R. S. Punongbayan, Eds. (Univ. of Washington Press, Seattle, 1996), pp. 415-433

Gibbs, S.J., Bralower, T.J., Bown, P.R., Zachos, J.C., Bybell, L.M. 2006. Shelf and open-ocean calcareous phytoplankton assemblages across the Paleocene-Eocene Thermal Maximum: Implications for global productivity gradients. Geology, v. 34, p. 233-236.

Gingras, M.K., MacEachern, J.A. & Pemberton, S.G. A comparative analysis of the ichnology of wave- and river-dominated allomembers of the Upper Cretaceous Dunvegan Formation. *Bull. Can. Pet. Geol.* **46**, 51-73 (1998).

Godbold, A., Schoepfer, S., Shen, S. & Henderson, C.M. Precarious ephemeral refugia during the earliest Triassic. *Geology* **45,** 607-610 (2017).

Glasauer, S., Langley, S., Beveridge, T.J., 2001. Sorption of Fe (hydr)oxides to the surface of *Shewanella putrefaciens*: cell-bound fine-grained minerals are not always formed de novo. Appl. Environ. Microbiol. 67, 5544–5550.

Golding, M.L., Orchard, M.J., Zonneveld, J.-P., Henderson, C.M. and Dunn, L. (2014) An exceptional record of the sedimentology and biostratigraphy of the Montney and Doig formations in British Columbia. Bull. Can. Pet. Geol., 62, 157–176.

Golonka, J. and Ford, D. (2000) Pangean (Late Carboniferous – Middle Jurassic) paleoenvironment and lithofacies. Palaeogeogr. Palaeoclimatol. Palaeoecol., 161, 1–34.

Golonka, J., Ross, M.I. and Scotese, C.R. (1994) Phanerozoic paleogeographic and paleoclimatic modeling maps. In: Pangea: Global Environment and Resources (Eds A.F. Embry, B. Beauchamp and D.J. Glass), CSPG Memoir, 17, 1–47.

Guenther, M., Bozelli, R., 2004. Factors influencing algae-clay aggregation. Hydrobiologia 523, 217–223.

Hallam, A. 1991. Why was there a delayed radiation after the end-Palaeozoic extinctions? Historical Biology, v. 5, p. 257-262.

Hallam, A. & Wignall, P.B. Mass extinctions and sea-level changes. *Earth Sci. Rev*. **48**, 217-250 (1999).

Hadjoudja, S., Deluchat, V., Baudu, M., 2010. Cell surface characterization of *Microcystis aeruginosa* and *Chlorella vulgaris*. J. Colloid Interface Sci. 342, 293–299.

Hamm, C.E., 2002. Interactive aggregation and sedimentation of diatoms and clay-sized lithogenic material. Limnol. Oceanogr. 47, 1790–1795.

Hargreaves, J. C., J. D. Annan, M. Yoshimori, and A. Abe-Ouchi, 2012: Can the Last Glacial Maximum constrain climate sensitivity? Geophys. Res. Lett., 39, L24702.

Haq, B.V., Hardenbol, J., Vail, R.R., Colin, J.P., loannides, N., Stover, L.E., Jan Du Chene, R., Wright, R.C., Sarq, J.F. and Morgan, B.E. (1987) Mesozoic-cenozoic cycle chart, Version 3.lB. American Association of Petroleum Geologists.

Haugan, P.M. and Drange, H. 1996. Effects of CO_2 on the ocean environment. Energy Conservation Management, v. 37, p. 6-8.

Hays, L.E., Beatty, T.W., Henderson, C.M., Love, G.D. and Summons, R.E. (2007) Evidence for photic zone euxinia through the end-Permian mass extinction in the Panthalassic Ocean (Peace River Basin, Western Canada). Palaeoworld, 16, 39–50.

Hedges, J.I., Keil, R.G., 1995. Sedimentary organic matter preservation: an assessment and speculative synthesis. Mar. Chem. 49, 81–115.

Herrle, J.O., Pross, J., Friedrich, O., Kössler, P., Hemleben, C., 2003. Forcing mechanisms for mid-Cretaceous black shale formation: evidence from the Upper Aptian and Lower Albian of the Vocontian Basin (SE France). Palaeogeogr. Palaeoclimatol. Palaeoecol. 190, 399–426.

Hildred, G.V., Ratcliffe, K.T., Wright, A.M., Zaitlin, B.A. and Wray, D.S. (2010) Chemostratigraphic applications to low-accommodation fluvial incised-valley settings: an example from the lower Mannville Formation of Alberta, Canada. J. Sediment. Res., 80, 1032–1045.

Ho, T.-Y., Quigg, A., Finkel, Z.V., Milligan, A.J., Wyman, K., Falkowski, P.G., Morel, F.M.M., 2003. The elemental composition of some marine phytoplankton. J. Phycol. 39, 1145–1159.

Holden, P. B., N. R. Edwards, K. I. C. Oliver, T. M. Lenton, and R. D. Wilkinson, 2010: A probabilistic calibration of climate sensitivity and terrestrial carbon change in GENIE-1. Clim. Dyn., 35, 785–806

Hofer, G., Wagreich, M. and Neuhuber, S. (2013) Geochemistry of fine-grained sediments of the upper Cretaceous to Paleogene Gosau Group (Austria, Slovakia): implications for paleoenvironmental and provenance studies. Geosci. Front., 4, 449–468.

Hofmann, A., Bolhar, R., Dirks, P. and Jelsma, H. (2003) The geochemistry of Archaean shales derived from a mafic volcanic sequence, Belingwe greenstone belt, Zimbabwe: provenance, source area unroofing and submarine versus subaerial weathering. Geochim. Cosmochim. Acta, 67, 421–440.

Hofmann, P., Ricken, W., Schwark, L. and Leythaeuser, D. (2001) Geochemical signature and related climateoceanographic processes for early Albian black shales: Site 417D, North Atlantic Ocean. Cretac. Res. 22, 243–257.

Huang, K.-J., Teng, F.-Z., Wei, G.-J., Ma, J.-L., Bao, Z.-Y., 2012. Adsorption- and desorption-controlled magnesium isotope fractionation during extreme weathering of basalt in Hainan Island, China. Earth Planet. Sci. Lett. 359–360, 73–83.

Ikeda, M., Tada, R., and Ozaki, K. 2017. Astronomical pacing of the global silica cycle recorded in Mesozoic bedded cherts. Nature Communications, v. 8, 15532.

Ikhsan, J., Johnson, B.B., Wells, J.D., 1999. A comparative study of the adsorption of transition metals on kaolinite. J. Colloid Interface Sci. 217, 403–410.

Israel, M.B., Enzel, Y., Amit, R. and Erel, Y. (2015) Provenance of the various grain-size fractions in the Negev loess and potential changes in major dust sources to the Eastern Mediterranean. Quatern. Res., 83, 105–115.

Ivanov, A.V. 2007. Evaluation of different models for the origin of the Siberian Traps, GSA Special Paper 430, p. 669-691.

Izbicki, J.A., Ball, J.W., Bullen, T.D., Sutley, S.J., 2008. Chromium, chromium isotopes and selected trace elements, western Mojave Desert, USA. Appl. Geochem. 23, 1325–1352.

Jablonski, D. & Flessa, K.W. The taxonomic structure of shallow-water marine faunas – implications for Phanerozoic extinctions. *Malacologia*, **27**, 43-66 (1986).

Jacquet, S., Lennon, J.-F., Marie, D., Vaulot, D., 1998. Picoplankton population dynamics in coastal waters of the northwestern Mediterranean Sea. Limnol. Oceanogr. 43, 1916–1931.

Jardillier, L., Zubkov, M.V., Pearman, J., Scanlan, D.J., 2010. Significant CO_2 fixation by small prymnesiophytes in the subtropical and tropical northeast Atlantic Ocean. ISME J. 4, 1180–1192.

Jarvis, I. and Jarvis, K. (1992) Plasma spectrometry in the earth sciences: techniques, applications and future trends. Chem. Geol., 95, 1–33.

Jia, C., Huang, J., Kershaw, S., Luo, G., Farabegoli, E., Perri, M.C., Chen, L., Bai, X., Xie, S., 2012. Microbial response to limited nutrients in shallow water immediately after the end-Permian mass extinction. Geobiology 10, 60–71.

Jin, X., Shah, S.N., Roegiers, J.-C. and Zhang, B. (2015) An integrated petrophysics and geomechanics approach for fracability evaluation in shale reservoirs. SPE J., 20, 518–526.

Johnson, R.A. and Wichern, D.W. (1988) Applied Multivariate Statistical Analysis. Prentice Hall, New Jersey, p. 773.

Kamo, S.L., Czamanske, G.K., Amelin, Y., Fedorenko, V.A., Davis, D.W., and Trofimov, V.R. 2003. Rapid eruption of Siberian flood-volcanic rocks and evidence for coincidence with the Permian-Triassic boundary and mass extinction at 251 Ma. Earth and Planetary Science Letters, v. 214, p. 75-91.

Karstensen, J., Stramma, L., Visbeck, M. 2005. Oxygen minimum zones in the eastern tropical Atlantic and Pacific oceans. Progress in Oceanography, v. 77, p. 331-350.

Kashiyama, Y., Ogawa, N.O., Kuroda, J., Shiro, M., Nomoto, S., Tada, R., Kitazato, H., Ohkouchi, N., 2008. Diazotrophic cyanobacteria as the major photoautotrophs during mid-Cretaceous oceanic anoxic events: nitrogen and carbon isotopic evidence from sedimentary porphyrin. Org. Geochem. 39, 532–549.

Kato, Y., Nakao, K., and Isozaki, Y. 2002. Geochemistry of Late Permian to Early Triassic pelagic cherts from southwest Japan: implications for an oceanic redox change. Chemical Geology, v. 182, p. 15-34.

Keil, R.G., Montluçon, D.B., Prahl, F.G., Hedges, J.I., 1994. Sorptive preservation of labile organic matter in marine sediments. Nature 370, 549–551.

Keller, G., Jaiprakash, B.C. and Reddy, A.N. (2016) Maastrichtian to Eocene subsurface stratigraphy of the Cauvery Basin and correlation with Madagascar. J. Geol. Soc. India, 87, 5–34.

Kelly, K.D., Benzel, W.M., Pfaff, K., 2013. Preliminary mineralogy and geochemistry of metal-rich (Mo-Ni-V-Zn) oil shale of the Carboniferous Heath Formation, Montana, USA. In: Jonsson, E. (Ed.), Mineral Deposit Research for a High-tech World. 12th SGA Biennial Meeting 2013. Proceedings. 2. pp. 636–639.

Kendall, B., Gordon, G.W., Poulton, S.W. and Anbar, A.D. (2011) Molybdenum isotope constraints on the extent of late Paleoproterozoic ocean euxinia. Earth Planet. Sci. Lett., 307, 450–460.

Kennedy, M.J., Pevear, D.R., Hill, R.J., 2002. Mineral surface control of organic carbon in black shale. Science 295, 657–660.

Kennedy, M.J., Löhr, S.C., Fraser, S.A., Baruch, E.T., 2014. Direct evidence for organic carbon preservation as clay-organic nanocomposites in a Devonian black shale; from deposition to diagenesis. Earth Planet. Sci. Lett. 388, 59–70.

Kim, C.J., Jung, Y.H., Ahn, C.Y., Lee, Y.K., Oh, H.M., 2010. Adsorption of turbid materials by the cyanobacterium *Phormidium parcydematicum*. J. Appl. Phycol. 22, 181–186.

Kilbertus, G., 1980. Microhabitats in soil aggregates their relationship with bacterial biomass and size of procaryotes present. Rev. Ecol. Biol. Sol 17, 543–557.

Kirby, R., Parker, W.R., 1983. Distribution and behavior of fine sediment in the Severn Estuary and Inner Bristol Channel, UK. Can. J. Fish. Aquat. Sci. 40 (Suppl. 1), 83–95.

Kistner, D.A., Pettigrew, N.R., 2001. A variable turbidity maximum in the Kennebec Estuary. Estuaries 24, 680–687.

Knoll, A.H., Bambach, R.K., Canfield, D.E., and Grotzinger, J.P*.* 1996. Comparative Earth history and Late Permian mass extinction. Science, v. 273, p. 452-457.

Knoll, A.H., Bambach, R.K., Payne, J.L., Pruss, S., and Fischer, W.W. 2007. Paleophysiology and end-Permian mass extinction. Earth and Planetary Science Letters, v. 256, p. 295-313.

Koehler, P., R. Bintanja, H. Fischer, F. Joos, R. Knutti, G. Lohmann, and V. MassonDelmotte, 2010: What caused Earth's temperature variations during the last 800,000 years? Data-based evidence on radiative forcing and constraints on climate sensitivity. Quat. Sci. Rev., 29, 129–145.

Konhauser, K.O., 2007. Introduction to Geomicrobiology. Blackwell Publishing, Oxford, UK (425 pp.).

Konhauser, K.O., Urrutia, M.M., 1999. Bacterial clay authigenesis: a common biochemical process. Chem. Geol. 161, 399–413.

Konhauser, K.O., Fyfe, W.S., Ferris, F.G., Beveridge, T.J., 1993. Metal sorption and mineral precipitation by bacteria in two Amazonian river systems: Rio Solimões and Rio Negro. Geology 21, 1103–1106.

Konhauser, K.O., Fyfe, W.S., Schultze-Lam, S., Ferris, F.G., Beveridge, T.J., 1994. Iron phosphate precipitation by epilithic microbial biofilms in Arctic Canada. Can. J. Earth Sci. 31, 1320–1324.

Konhauser, K.O., Fisher, Q.J., Fyfe, W.S., Longstaffe, F.J., Powell, M.A., 1998. Authigenic mineralization and detrital clay binding by freshwater biofilms: the Brahmani river, India. Geomicrobiol J. 15, 209–222.

Köster, J., Rospondek, M., Schouten, S., Kotarba, M., Zubrzycki, A., Sinninghe Damsté, J.S., 1998. Biomarker geochemistry of a foreland basin: the Oligocene Menilite Formation in the Flysch Carpathians of southeast Poland. Org. Geochem. 29, 649–669.

Kristensen, E., 2000. Organic matter diagenesis at the oxic/anoxic interface in coastal marine sediments, with emphasis on the role of burrowing animals. Hydrobiologia 426, 1–24.

Krull, E.S., and Retallack, G.J. 2000. $\delta^{13}C$ depth profiles from paleosols across the Permian-Triassic boundary: Evidence for methane release. GSA Bulletin, v. 112, p. 1459-1472.

Krull, E.S., Baldock, J.A., Skjemstad, J.O., 2003. Importance of mechanisms and processes of the stabilization of soil organic matter for modeling carbon turnover. Funct. Plant Biol. 30, 207–222.

Kump, L.R. and Arthur,M.A. 1999. Interpreting carbon-isotope excursions: carbonates and organic matter. Chemical Geology, v. 11, p. 181-198.

Kump, L.R., Pavlov, A. & Arthur, M.A. Massive release of hydrogen sulfide to the surface ocean and atmosphere during intervals of oceanic anoxia. *Geology* **33**, 397-400 (2005).

Kutzbach, J.E. 1994. Idealized Pangean climates: sensitivity to orbital change. Geol. Soc. Am. Special Papers, v. 288, p. 41-56.

Kozur, H.W. Some aspects of the Permian-Triassic boundary (PTB) and of the possible causes for the biotic crisis around this boundary. *Palaeogeogr., Palaeoclimatol., Palaeoecol*. **143**, 227-272 (1998).

Kuypers, M.M.M., van Breugel, Y., Schouten, S., Erba, E., Sinninghe-Damsté, J.S.S., 2004. N2-fixing cyanobacteria supplied nutrient N for Cretaceous oceanic anoxic events. Geology 32, 853–856.

Lalonde, S.V., Smith, D.S., Owttrim, G.W. and Konhauser, K.O. (2008) Acid-base properties of cyanobacterial surfaces I: influences of growth phase and nitrogen metabolism on cell surface reactivity. Geochim. Cosmochim. Acta, 72, 1257–1268.

Lalonde, S.V., Smith, D.S., Owttrim, G.W., Konhauser, K.O., 2008b. Acid-base properties of cyanobacterial surfaces II: silica as a chemical stressor influencing cell surface reactivity. Geochim. Cosmochim. Acta 72, 1269–1280.

Lev, S.M., McLennan, S.M. and Hanson, G.N. (1999) Mineralogic controls on REE mobility during black-shale diagenesis. J. Sediment. Res., 69, 1071–1082.

Li, L., Keller, G., Adatte, T. and Stinnesbeck, W. (2000) Late Cretaceous sea-level changes in Tunisia: a multidisciplinary approach. J. Geol. Soc. London, 157, 447–458.

Liang, A., Paulo, C., Zhu, Y. and Dittrich, M. (2013) CaCO3 biomineralization on cyanobacterial surfaces: Insights from experiments with three Synechococcus strains. Colloids Surf. B, 111, 600–608.

Liermann, L.J., Mathur, R., Wasylenki, L.E., Nuester, J., Anbar, A.D. and Brantley, S.L. (2011) Extent and isotopic composition of Fe and Mo release from two Pennsylvania shales in the presence of organic ligands and bacteria. Chem. Geol., 281, 167–180.

Liu. G., Feng, Q., Shen, J., Yu, J., He, W., and Algeo, T.J. 2013. Decline of siliceous sponges and spicule miniaturization induced by marine productivity collapse and expanding anoxia during the Permian-Triassic crisis in south China. Palaios, v. 28, p. 664-679.

Liu, Y.X., Alessi, D.S., Owttrim, G.W., Petrash, D.E., Mloszewska, A.M., Lalonde, S.V., Martinez, R.E., Zhou, Q.X., Konhauser, K.O., 2015. Cell surface reactivity of *Synechococcus* sp. PCC 7002: implications for metal sorption from seawater. Geochim. Cosmochim. Acta 169, 30–44.

Lünsdorf, H., Erb, R.W., Abraham, W.-R., Timmis, K.N., 2000. 'Clay hutches': a novel interaction between bacteria and clay minerals. Environ. Microbiol. 2, 161–168.

Ludwig, M., Bryant, D.A., 2012. Synechococcus sp. strain PCC 7002 transcriptome: acclimation to temperature, salinity, oxidative stress, and mixotrophic growth conditions. Front. Microbiol. 3, 1–14.

Lopez de Luchi, M.G., Cerredo, M.E., Siegesmund, S., Steenken, A. and Wemmer, K. (2003) Provenance and tectonic setting of the protoliths of the Metamorphic Complexes of Sierra de San Luis. Rev. Asoc. Geol. Argentina, 58, 525–540.

Luo, G., Wang, Y., Algeo, T.J., Kump, L.R., Bai, X., Yang, H., Yao, L., and Xie, S. 2011. Enhanced nitrogen fixation in the immediate aftermath of the latest Permian marine mass extinction. Geology, v. 39, 647-650.

MacEachern, J.A., Pemberton, S.G., Gingras, M.K., Bann, K.L., 2010. Ichnology and facies models. In: Dalrymple, R.W., James, N.P. (Eds.), Facies Models 4, Geotext 6. Geological Association of Canada, St John's Nfld (586 pp.).

Mackin, J.E., Swider, K.T., 1989. Organic matter decomposition pathways and oxygen consumption in coastal marine sediments. J. Mar. Res. 47, 681–716.

MacNaughton, R.B. and Zonneveld, J.-P. (2010) Trace-fossil assemblages in the Lower Triassic Toad Formation, La Biche River map area, southeastern Yukon. Bull. Can. Pet. Geol., 58, 100–114.

Macquaker, H.S., Keller, M.A., Davies, S.J., 2010. Algal blooms and “marine snow”: mechanisms that enhance preservation of organic carbon in ancient fine-grained sediments. J. Sediment. Res. 80, 934–942.

Mathews, H.D., Gillett, N.P., Stott, P.A., and Zickfeld, K. 2009. The proportionality of global warming to cumulative carbon emissions. Nature, v. 459, p. 829-832.

Mayer, L.M., Schick, L.L., Hardy, K.R., Wagal, R., MacCarthy, J., 2004. Organic matter in small mesopores in sediments and soils. Geochim. Cosmochim. Acta 68, 3863–3872.

McClure, R.S., Overall, C.C., McDermott, J.E., Hill, E.A., Markillie, L.-M., McCue, L.-A., Taylor, R.C., Ludwig, M., Bryant, D.A., Beliaev, A.S., 2016. Network analysis of transcriptomics expands regulatorylandscapes in *Synechococcus* sp. PCC 7002. Nucleic Acids Res. 44, 1–16.

McLennan, S.M., Hemming, S., McDaniel, D.K. and Hanson, G.N. (1993) Geochemical approaches to sedimentation, provenance, and tectonics. Geol. Soc. Am. Spec. Pap., 284, 21–40.

McLennan, S.M., Taylor, S.R., McCulloch, M.T. and Maynard, J.B. (1990) Geochemical and Nd-Sr isotopic composition of deep-sea turbidites: crustal evolution and plate tectonic associations. Geochem. Cosmochim. Acta, 54, 2015–2050.

Meinhold, G., Kostopoulos, D. and Reischmann, T. (2007) Geochemical constraints on the provenance and depositional setting of sedimentary rocks from the islands of Chios, Inousses and Psara, Aegean Sea, Greece: implications for the evolution of Palaeotethys. J. Geochem. Soc. London, 164, 1145–1163.

Miller, E.L., Soloviev, A.V., Prokopiev, A.V., Toro, J., Harris, D., Kuzmichev, A.B., and Gehrels, G.E. 2013. Triassic river systems and the paleo-Pacific margin of northwestern Pangea. Gondwana Research, v. 23, p. 1631-1645.

Mitbavkar, S., Rajaneesh, K.M., Anil, A.C., Sundar, D., 2012. Picophytoplankton community in a tropical estuary: detection of *Prochlorococcus*-like populations. Estuar. Coast. Shelf Sci. 107, 159–164.

Miyazono, A., Odate, T., Maita, Y., 1992. Seasonal fluctuations of cell density of cyanobacteria and other picophytoplankton in Iwanai Bay, Hokkaido, Japan. J. Oceanogr. 48, 257–266.

Mongelli, G., Critelli, S., Perri, F., Sonnino, M. and Perrone, V. (2006) Sedimentary recycling, provenance and paleoweathering from chemistry and mineralogy of Mesozoic continental red-bed mudrocks, Peloritani mountains, southern Italy. Geochem. J., 40, 197–209.

Morton, J.P. (1985) Rb-Sr evidence for punctuated illite/ smectite diagenesis in the Oligocene Fio Formation, Texas Gulf Coast. Geol. Soc. Am. Bull., 96, 114–122.

Morton, A.C. and Hallsworth, C. (1994) Identifying provenance-specific features of detrital heavy mineral assemblages in sandstones. Sed. Geol., 90, 241–256.

Morton, A.C., Hallsworth, C.R. and Moscariello, A. (2005) Interplay between northern and southern sediment sources during Westphalian deposition in the Silverpit Basin, southern North Sea. In: Carboniferous hydrocarbon geology: the southern North Sea and surrounding onshore areas (Eds J.D. Collinson, D.J. Evans, D.S. Holliday and N.S. Jones). Yorkshire Geological Society Occasional Publication, Vol. 7, 135–146.

Morton, A. and Yaxley, G. (2007) Detrital apatite geochemistry and its application in provenance studies. Geol. Soc. Am. Spec. Pap., 420, 319–344.

Moslow, T.F. (2000) Reservoir architecture of a fine-grained turbidite system: lower Triassic Montney Formation, Western Canada Sedimentary Basin. In: Deep-water Reservoirs of the World (Eds P.Weimer, R.M. Slatt, J. Coleman, N.C. Rosen, H.

Nelson, A.H. Bouma, M.J. Styzen and D.T. Lawrence). Conference Proceedings, Gulf Coast SEPM, 686–713.

Moslow, T.F. and Davies, G.R. (1997) Turbidite reservoir facies in the Lower Montney Formation, west-central Alberta. In: Triassic of the Western Canada Sedimentary Basin (Eds T.F. Moslow and J. Wittenberg), Bulletin of Canadian Petroleum Geology, 45, 507–536.

Murphy, A.E., Sageman, B.B., Hollander, D.J., 2000. Eutrophication by decoupling of the marine biogeochemical cycles of C, N, and P: a mechanism for the Late Devonian mass extinction. Geology 28, 427–430.

Nance, H.S. and Rowe, H. (2015) Eustatic controls on stratigraphy, chemostratigraphy, and water mass evolution preserved in a Lower Permian mudrock succession, Delaware Basin, west Texas, USA. Interpretation, 3, SH11– SH25.

North, C.P., Hole, M.J. and Jones, D.G. (2005) Geochemical correlation in deltaic successions: a reality check. Geol. Soc. Am. Bull., 117, 620–632.

Nuester, J., Vogt, S., Newville, M., Kustka, A.B., Twining, B., 2012. The unique biogeochemical signature of the marine diazotroph *Trichodesmium*. Front. Microbiol. 3 (article number 150).

Ockert, C., Gussone, N., Kaufhold, S., Teichert, B.M.A., 2013. Isotope fractionation during Ca exchange on clay minerals in a marine environment. Geochim. Cosmochim. Acta112, 374–388.

Ohkouchi, N., Kashiyama, Y., Kuroda, J., Ogawa, N.O., Kitazato, H., 2006. The importance of diazotrophic cyanobacteria as primary producers during Cretaceous Oceanic Anoxia Event 2. Biogeosciences 3, 467–478.

Olcott, A.N., Sessions, A.L., Corsetti, F.A., Kaufman, A.J., de Oliviera, T.F., 2005. Biomarker evidence for photosynthesis during neoproterozoic glaciation. Science 310, 471–474.

Orchard, M.J. and Tozer, E.T. (1997) Triassic conodont biochronology, its calibration with the ammonoid standard, and a biostratigraphic summary for the Western Canada Sedimentary Basin. Bull. Can. Pet. Geol., 45, 675– 692.

Orchard, M.J. and Zonneveld, J.-P. (2009) The Lower Triassic Sulphur Mountain Formation in the Wapiti Lake area: lithostratigraphy, conodont biostratigraphy, and a new biozonation for the lower Olenekian (Smithian). Can. J. Earth Sci., 46, 757–790.

Ovtchrova, M., Bucher, H., Schaltegger, U., Galfetti, T., Brayard, A., and Guex, J. 2006. New Early to Middle Triassic U-Pb ages from South China: calibration with ammonoid biochronozones and implications for the timing of the Triassic biotic recovery. Earth and Planetary Science Letters, v. 243, p. 463-475.

Paktunc, A.D. and Cabri, L.J. (1995) A proton- and electronmicroprobe study of gallium, nickel and zinc distribution in chromium spinel. Lithos, 35, 261–282.

Paleosens Members, 2012: Making sense of palaeoclimate sensitivity. Nature, 491, 683–691.

Pan, L., Zhang, J., Zhang, L., 2007. Picophytoplankton, nanophytoplankton, heterotrophic bacteria and viruses in the Changjiang Estuary and adjacent coastal waters. J. Plankton Res. 29, 187–197.

Parrish, J.T. 1993. Climate of the Supercontinent Pangea. The Journal of Geology, v. 101, p. 215-233.

Partin, C.A., Bekker, A., Planovsky, N.J., Scott, C.T., Gill, B.C., Li, C., Podkovyrov, V., Maslov, A., Konhauser, K.O., Lalonde, S.V., Love, G.D., Poulton, S.W., Lyons, T.W., 2013. Large-scale fluctuations in Precambrian atmospheric and oceanic oxygen levels from the record of U in shales. Earth Planet. Sci. Lett. 369, 284–293.

Patchett, P.J., White, W.M., Feldmann, H., Kielinczuk, S. and Hofmann, A.W. (1984) Hafnium/rare earth element fractionation in the sedimentary system and crustal recycling into the Earth's mantle. Earth Planet. Sci. Lett., 69, 365–378.

Paton, M.T., Ivanov, A.V., Fiorentini, M.L., McNaughton, N.J., Mudrovska, I., Reznitskii, L.Z., and Demonterova, E.I. 2010. Late Permian and Early Triassic magmatic pulses in the Angara-Taseeva syncline, Southern Siberian Traps and their possible influence on the environment. Russian Geology and Geophysics, v. 51, p. 1012-1020.

Paull, R.K., Paull, R.A. and Laudon, T.S. (1997) Conodont biostratigraphy of the Lower Triassic Mackenzie Dolomite Lentil, Sulphur Mountain Formation in the Cadomin area, Alberta. Bull. Can. Pet. Geol., 45, 708–714.

Payne, J.L., and Kump, L.R. 2007. Evidence for recurrent Early Triassic massive volcanism from quantitative interpretation of carbon isotope fluctuations. Earth and Planetary Science Letters, v. 256, p. 264-277.

Payne, J.L., Lehrmann, D.J., Wei, J., Orchard, M.J., Schrag, D.P., and Knoll, A.H. 2004. Large perturbations of the carbon cycle during recovery from the end-Permian extinction. Science, v. 305, p. 506-509.

Pearce, T.J., Besly, B.M., Wray, D.S. and Wright, D.K. (1999) Chemostratigraphy: a method to improve inter-well correlation in barren sequences – a case study using onshore Duckmantian/Stephanian sequences (West Midlands, U.K.). Sed. Geol., 124, 197–220.

Pearce, T.J., Wray, D., Ratcliffe, K., Wright, D.K. and Moscariello, A. (2005) Chemostratigraphy of the Upper Carboniferous Schooner Formation, southern North Sea. In: Carboniferous Hydrocarbon Resources: The Southern North Sea and Surrounding Onshore Areas (Eds J.D. Collinson, D.J. Evans, D.W. Holliday and N.S. Jones), Occasional Publications Series of the Yorkshire Geological Society, 7, 165–182.

Pearce, T.J., Martin, J.H., Cooper, D. and Wray, D.S. (2010) Chemostratigraphy of Upper Carboniferous (Pennsylvanian) sequences from the southern North Sea (United Kingdom). In: Application of Modern Stratigraphic Techniques: Theory and Case Histories (Eds K. Ratcliffe and B.A. Zaitlin), SEPM Spec. Publ., 94, 109–127.

Pelechaty, S. (1998) Integrated chronostratigraphy of the Vendian system of Siberia: implications for a global stratigraphy. J. Geol. Soc. London, 155, 957–973.

Pedersen, T.F., Calvert, S.E., 1990. Anoxia vs. productivity: what controls the formation of organic-carbon-rich sediments and sedimentary rocks? Am. Assoc. Pet. Geol. Bull. 74, 454–466.

Petrash, D.A., Gueneli, N., Brocks, J.J., M_endez, J.A., Gonzalez-Arismentdi, G., Poulton, S.W. and Konhauser, K.O. (2016) Black shale deposition and early diagenetic dolomite cementation during Oceanic Anoxic Event 1: the mid-Cretaceous Maracaibo Platform, northwestern South America. Am. J. Sci., 316, 669–711.

Pett-Ridge, J.C., Derry, L.A. and Kurtz, A.C. (2009) Sr isotopes as a tracer of weathering processes and dust inputs in a tropical granitoid watershed, Luquillo Mountains, Puerto Rico. Geochim. Cosmochim. Acta, 73, 25–43.

Phoenix, V.R., Konhauser, K.O., 2008. Benefits of bacterial biomineralization. Geobiology 6, 303–308.

Phoenix, V.R., Martinez, R.E., Konhauser, K.O., Ferris, F.G., 2002. Characterization and implications of the cell surface reactivity of *Calothrix* sp. strain KC97. Appl. Environ. Microbiol. 68, 4827–4834.

Pierson, B.J. (1981) The control of cathodoluminescence in dolomite by iron and manganese. Sedimentology, 28, 601– 610.

Piper, D.Z., Calvert, S.E., 2009. A marine biogeochemical perspective on black shale deposition. Earth-Sci. Rev. 95, 63–96.

Piper, D.Z., Perkins, R.B., 2004. A modern vs. Permian black shale-the hydrography, primary productivity, and water-column chemistry of deposition. Chem. Geol. 206, 177–197.

Planavsky, N.J., Asael, D., Hofmann, A., Reinhard, C.T., Lalonde, S.V., Knudsen, A., Wang, X., Ossa Ossa, F., Pecoits, E., Smith, A.J.B., Beukes, N.J., Bekker, A.,

Johnson, T.M., Konhauser, K.O., Lyons, T.W. and Rouxel, O.J. (2014) Evidence for oxygenic photosynthesis half a billion years before the Great Oxidation Event. Nat. Geosci., 7, 283–286.

Plank, T. and Langmuir, C.H. (1998) The chemical composition of subducting sediment and its consequences for the crust and mantle. Chem. Geol., 145, 325–394.

Playter, T., Konhauser, K., Owttrim, G., Hodgson, C., Warchola, T., Mloszewska, A.M., Sutherland, B., Bekker, A., Zonneveld, J.-P., Pemberton, S.G. and Gingras, M. (2017) Microbe-clay interactions as a mechanism for the preservation of organic matter and trace metal biosignatures in black shales. Chem. Geol., 459, 75–90.

Playter, T., Corlett, H., Konhauser, K., Robbins, L., Rohais, S., Crombez, V., MacCormack, K.M., Rokosh, D., Prenoslo, D., Furlong, C.M., Pawlowicz, J., Gingras, M., Lalonde, S., Lyster, S., and Zonneveld, J.-P. 2018. Clinoform identification and correlation in fine-grained sediments: A case study using the Triassic Montney Formation. Sedimentology, v. 65, p. 263-302.

Pokrovsky, O.S., Martinez, R., Golubev, S., Kompantseva, E., Shirokova, L., 2008. Adsorption of metals and protons on *Gloeocapsa* sp. cyanobacteria: a surface speciation approach. Appl. Geochem. 23, 2574–2588.

Pokrovsky, O.S., Martinez, R.E., Kompantzeva, E.I. and Shirokova, L.S. (2014) Surface complexation of the phototrophic anoxygenic non-sulfur bacterium Rhodopseudomonas palustris. Chem. Geol., 383, 51–62.

Porra, R.J., Thompson, W.A., Kriedemann, P.E., 1989. Determination of accurate extinction coefficients and simultaneous equations for assaying chlorophylls *a* and *b*

extracted with four different solvents: verification of the concentration of chlorophyll standards by atomic absorption spectroscopy. Biochim. Biophys. Acta 975, 384–394.

Preston, J., Hartley, A., Hole, M., Buck, S., Bond, J., Mange, M. and Still, J. (1998) Integrated whole-rock trace element geochemistry and heavy mineral chemistry studies: aids to correlation of continental red-bed reservoirs in the Beryl Field, UK North Sea. Petrol. Geosci., 4, 7–16.

Rabouille, C. and Gaillard, J.-F. (1991) Towards the EDGE: Early diagenetic global explanation. A model depicting the early diagenesis of organic matter, O2, NO3, Mn and PO4. Geochim. Cosmochim. Acta, 55, 2511–2525.

Racki, G. 1999. Silica-secreting biota and mass extinctions: survival patterns and processes. Palaeogeography, Palaeoclimatology, Palaeoecology, v. 154, p. 107-132.

Rajaneesh, K.M., Mitbavkar, S., 2013. Factors controlling the temporal and spatial variations in *Synechococcus* abundance in a monsoonal estuary. Mar. Environ. Res. 92, 133–143.

Ransom, B., Bennett, R.H., Baerwald, R., Shea, K., 1997. TEM study of in situ organic matter on continental margins: occurrence and the “monolayer” hypothesis. Mar. Geol. 138, 1–9.

Ransom, B., Kim, D., Kastner, M., Wainwright, S., 1998. Organic matter preservation on continental slopes: importance of mineralogy and surface area. Geochim. Cosmochim. Acta 62, 1329–1345.

Rao, R., Song, S., Lopez-Valdivieso, A., 2012. Specific adsorption of chromium species on kaolinite surface. Miner. Process. Extr. Metall. Rev. 33, 180–189.

Ratcliffe, K.T., Wright, A.M., Hallsworth, C., Morton, A., Zaitlin, B.A., Potocki, D. and Wray, D.S. (2004) An example of alternative correlation techniques in a lowaccommodation setting, non-marine hydrocarbon system: the (Lower Cretaceous) Mannville Basal Quartz succession of southern Alberta. AAPG Bull., 88, 1419–1432.

Ratcliffe, K.T., Martin, J., Pearce, T.J., Hughes, A.D., Lawton, D.E., Wray, D.S. and Bessa, F. (2006) A regional chemostratigraphically – defined correlation framework for the late Triassic TAG – I Formation in Blocks 402 and 405a, Algeria. Petrol. Geosci., 12, 3–12.

Ratcliffe, K.T., Wright, A.M., Montgomery, P., Palfrey, A., Vonk, A., Vermeulen, J. and Barrett, M. (2010) Application of chemostratigraphy to the Mungaroo Formation, the Gorgon Field, offshore Northwest Australia. APPEA Journal, 50th Anniversary Issue, 371–388.

Ratcliffe, K.T., Wright, A.M. and Schmidt, K. (2012) Application of inorganic whole – rock geochemistry to shale resource plays: an example from the Eagle Ford Shale Formation, Texas. Sed. Rec., 10, 4–9.

Ratcliffe, K.T., Wilson, A., Payenberg, T., Rittersbacher, A., Hildred, G.V. and Flint, S.S. (2015) Ground truthing chemostratigraphic correlations in fluvial systems. AAPG Bull., 99, 155–180.

Raup, D.M. 1979. Size of the Permo-Triassic bottleneck and its evolutionary implications. Science, v. 206, p. 217-218.

Raven, J., Falkowski, P., 1999. Oceanic sinks for atmospheric CO_2. Plant Cell Environ. 22, 741–755.

Reategui, K., Mart_ınez, M., Esteves, I., Guti_errez, J.V., Mart_ınez, A., Mel_endez, W. and Urbani, F. (2005) Geochemistry of the Mirador Formation (Late Eocene – Early Oligocene) southwestern Venezuela: chemostratigraphic constraints on provenance and the influence of the sea level. Geochem. J., 39, 213–226.

Reddy, M.R. and Perkins, H.F. (1974) Fixation of zinc by clay minerals. Soil Sci. Soc. Am. J., 38, 229–231. Reinhard, C.T., Planavsky, N.J., Wang, X., Fischer, W.W., Johnson, T.M. and Lyons, T.W. (2014) The isotopic composition of authigenic chromium in anoxic marine sediments: a case study from the Cariaco Basin. Earth Planet. Sci. Lett., 407, 9–18.

Reinhard, C.T., Planavsky, N.J., Robbins, L.J., Partin, C.A., Gill, B.C., Lalonde, S.V., Bekker, A., Konhauser, K.O., Lyons, T.W., 2013. Proterozoic ocean redox and biogeochemical stasis. Proc. Natl. Acad. Sci. U. S. A. 110, 5357–5362.

Reinhard, C.T., Planavsky, N.J., Wang, X., Fischer, W.W., Johnson, T.M., Lyons, T.W., 2014. The isotopic composition of authogenic chromium in anoxic marine sediments: a case study from the Cariaco Basin. Earth Planet. Sci. Lett. 407, 9–18.

Renne, P.R., and Basu, A. 1991. Rapid eruption of the Siberian Traps Flood Basalts at the Permo-Triassic Boundary. Science, v. 253, p. 176-179.

Retallack, G.J. A 300-million-year record of atmospheric carbon dioxide from fossil plant cuticles. *Nature* **411**, 287-290 (2001).

Retallack, G.J. and Jahren, A.H. 2008. Methane release from igneous intrusion of coal during Late Permian extinction events. The Journal of Geology, v. 116, p. 1-20.

Retallack, G.J., Holser, W.T. and Isozaki, Y. (1997) Timing of Permian-Triassic anoxia. Science, 277, 1748–1749.

Rhein, M., S.R. Rintoul, S. Aoki, E. Campos, D. Chambers, R.A. Feely, S. Gulev, G.C. Johnson, S.A. Josey, A. Kostianoy, C. Mauritzen, D. Roemmich, L.D. Talley and F. Wang, 2013: Observations: Ocean. In: Climate Change 2013: The Physical Science Basis. Contribution of Working Group I to the Fifth Assessment Report of the Intergovernmental Panel on Climate Change [Stocker, T.F., D. Qin, G.-K. Plattner, M. Tignor, S.K. Allen, J. Boschung, A. Nauels, Y. Xia, V. Bex and P.M. Midgley (eds.)]. Cambridge University Press, Cambridge, United Kingdom and New York, NY, USA.

Riccardi, A., Kump, L.R., Arthur, M.A., and D'Hondt, S.2007. Carbon isotopic evidence for chemocline upward excursions during the end-Permian event. Palaeogeography, Palaeoclimatology, Palaeoecology, v. 248, p. 73-81.

Richards, B.C., Barclay, J.E., Bryan, D., Hartling, A., Henderson, C.M. and Hinds, R.C. (1994) Carboniferous strata of the Western Canada Sedimentary Basin. In: Geological Atlas of the Western Canada Sedimentary Basin (Eds G.D. Mossop and I. Shetsen), Canadian Society of Petroleum Geologists and Alberta Research Council, 221–250.

Romano, C., Goudemand, N., Vennemann, T.W., Ware, D., Schneebeli-Hermann, E., Hochuli, P.A., Br€uhwiler, T., Brinkmann, W. and Bucher, H. (2013) Climatic and biotic upheavals following the end-Permian mass extinction. Nat. Geosci., 6, 57–60.

Rowe, H., Hughes, N. and Robinson, K. (2012) The quantification and application of handheld energydispersive x-ray fluorescence (ED-XRF) in mudrock chemostratigraphy and geochemistry. Chem. Geol., 324– 325, 122–131.

Ruffell, A.H. and Batten, D.J. (1990) The Barremian-Aptian arid phase in Western-Europe. Palaeogeogr. Palaeoclimatol. Palaeoecol., 80, 197–212.

Ruffell, A.H., Price, G.D., Mutterlose, J., Kessels, K., Baraboshkin, E. and Grocke, D.R. (2002a) Palaeoclimate indicators (clay minerals, calcareous nannofossils, stable isotopes) compared from two successions in the late Jurassic of the Volga Basin (SE Russia). Geol. J., 37, 17–33.

Ruffell, A., McKinley, J.M. and Worden, R.H. (2002b) Comparison of clay mineral stratigraphy to other proxy palaeoclimate indicators in the Mesozoic of NW Europe. Phil. Trans. Roy. Soc. London, 360, 675–693.

Rukhlov, A.S. and Pawlowicz, J.G. (2011) Magmatism and metallic mineralization of the Rocky Mountain Fold-and- Thrust Belt in Southwestern Alberta (NTS 82G, H and J): mineralogy, geochemistry and petrology of selected occurrences. ERCB/AGS Open File Report, 2011-11, 88 pp.

Sakamoto, T., Bryant, D.A., 1998. Growth at low temperature causes nitrogen limitation in the cyanobacterium *Synechococcus* sp. PCC 7002. Arch. Microbiol. 169, 10–19.

Sanei, H., Haeri-Ardakani, O., Wood, J.M. and Curtis, M.E. (2015) Effects of nano-porosity and surface imperfections on solid bitumen reflectance (BRo) measurements in unconventional reservoirs. Int. J. Coal Geol., 138, 95–102.

Schauble, E., Rossman, G.R., Taylor Jr., H.P., 2004. Theoretical estimates of equilibrium chromium-isotope fractionations. Chem. Geol. 205, 99–114.

Schoepfer, S.D., Henderson, C.M., Garrison, G.H., Foriel, J., Ward, P.D., Selby, D., Hower, J.C., Algeo, T.J., and Shen, Y. 2013. Termination of a continent – margin upwelling system at the Permian-Triassic boundary (Opal Creek, Alberta, Canada). Global and Planetary Change, v. 105, p. 21-35.

Schoepfer, S.D., Shen, J., Wei, H., Tyson, T.V., Ingall, E., and Algeo, T.J. 2015. Total organic carbon, organic phosphorus, and biogenic barium fluxes as proxies for paleomarine productivity. Earth-Science Reviews, v. 149, p. 23-52.

Schultze-Lam, S., Fortin, D., Davies, B.S., Beveridge, T.J., 1996. Mineralization of bacterial surfaces. Chem. Geol. 132, 171–181.

Scott, C., Lyons, T.W., Bekker, A., Shen, Y., Poulton, S.W., Chu, X., Anbar, A.D., 2008. Tracing the stepwise oxidation of the Proterozoic ocean. Nature 452, 456–458.

Scott, C.T., Planavsky, N.J., Dupont, C.L., Kendall, B., Gill, B.C., Robbins, L.J., Husband, K.F., Arnold, G.L., Wing, B.A., Poulton, S.W., Bekker, A., Anbar, A.D., Konhauser, K.O., Lyons, T.W., 2013. Bioavailability of zinc in marine systems through time. Nat. Geosci. 6, 125–128.

Sengco, M.R., Li, A.S., Tugend, K., Kulis, D., Anderson, D.M., 2001. Removal of red- and brown-tide cells using clay flocculation I. Laboratory culture experiments with

Gymnodinium breve and *Aureococcus anophage*ff*erens*. Mar. Ecol. Prog. Ser. 210, 41–53.

Shen, J., Algeo, T.J., Zhou, I., Feng, Q., Yu, J., Ellwood, B. 2012. Volcanic perturbations of the marine environment in South China preceding the latest Permian mass extinction and their biotic effects. Geobiology, v. 10, 82-103.

Shen, J., Zhou, L., Feng, Q., Zhang, M., Kei, Y., Zhang, N., Yu, J., and Gu, S. 2014. Paleo-productivity evolution across the Permian-Triassic boundary and quantitative calculation of primary productivity of black rock series from the Dalong Formation, South China. Science China Earth Science, v. 57, p. 1583-1594.

Shimmield, G.B. 1992. Can sediment geochemistry record changes in coastal upwelling palaeoproductivity? Evidence from northwest Africa and the Arabian Sea. Geological Society Special Publication No. 64, p. 29-46.

Smith, S.V., Hollibaugh, 1993. Coastal metabolism and the oceanic organic carbon balance. Rev. Geophys. 31, 75–89.

Sobolev, S.V., Sobolev, A.V., Kuzmin, D.V., Krivolutskaya, N.A., Petrunin, A.G., Arndt, N.T., Radko, V.A., and Vasiliev, Y.R. 2011. Linking mantle plumes, large igneous provinces and environmental catastrophes. Nature, v. 477, p. 312-316.

Song, H., Wignall, P.B., Chen, Z.-Q., Tong, J., Bond, D.P.G., Lai, X, Zhau, X., Jiang, H., Yan, C., Niu, Z., Chen, J., Yang, H., and Wang, Y. 2011. Recovery tempo and pattern of marine ecosystems after the end-Permian mass extinction. Geology, v. 39, p. 739-742.

Spark, K.M., Wells, J.D., Johnson, B.B., 1995. Eur. J. Soil Sci. 46, 633–640.

Stanley, S.M. 2009. Evidence from ammonoids and conodonts for multiple Early Triassic mass extinctions. PNAS, v. 106, p. 15264-15267.

Stanley, S.M. and Yang, X. 1994. A double mass extinction at the end of the Paleozoic Era. Science, v. 266, p. 1340-1344.

Sternberg, E., Tang, D., Ho, T.-Y., Jeandel, C., and Morel, F.M.M. 2005. Barium uptake and adsorption in diatoms. Geochimica et Cosmochimica Acta, v. 69, p. 2745-2752.

Sun, Y., Joachimski, M.M., Wignall, P.B., Yan, C., Chen, Y., Jiang, H., Wang, L. & Lai, X. 2012. Lethally Hot Temperatures During the Early Triassic Greenhouse. *Science* **338**, 366-370 (2012).

Stevens, S.E., Porter, R.D., 1980. Transformation in *Agmenellum quadruplicatum*. Proc. Natl. Acad. Sci. U. S. A. 77, 6052–6056.

Suess, E., 1980. Particulate organic carbon flux in the oceans – surface productivity and oxygen utilization. Nature 288, 260–262.

Sutherland, B.R., Barrett, K.J., Gingras, M.K., 2014. Clay settling in fresh and salt water. Environ. Fluid Mech. 15, 147–160.

Suzuki, N., Ishida, K., Shinomiya, Y., Ishiga, H., 1998. High productivity in the earliest Triassic ocean: black shales, Southwest Japan. Palaeogeogr. Palaeoclimatol. Palaeoecol. 141, 53–65.

Svendsen, J., Friis, H., Stollhofen, H. and Hartley, N. (2007) Facies discrimination in a mixed fluvio-eolian setting using elemental whole-rock geochemistry – applications for reservoir characterization. J. Sediment. Res., 77, 23–33.

Svensen, H.H., Frolov, S., Akhmanov, G.G., Polozov, A.G., Jerram, D.A., Shiganova, O.V., Melnikov, N.V., Iyer, K., Planke, S., 2018. Sills and gas generation in the

Siberian Traps. Philosophical Transactions of the Royal Society A: Mathematical, Physical and Engineering Sciences 376, 20170080.

Swanner, E.D., Planavsky, N.J., Lalonde, S.V., Robbins, L.J., Bekker, A., Rouxel, O.J., Saito, M.A., Kappler, A., Mojzsis, J., Konhauser, K.O., 2014. Cobalt and marine redox evolution. Earth Planet. Sci. Lett. 390, 253–263.

Takahashi, Y., Minai, Y., Ambe, S., Makide, Y. and Ambe, F. (1999) Comparison of adsorption behavior of multiple inorganic ions on kaolinite and silica in the presence of humic acid using the multi-tracer technique. Geochim. Cosmochim. Acta, 63, 815–836.

Takahashi, S., Oba, M., Kaiho, K., Yamakita, S., and Sakata, S. 2009. Panthalassic oceanic anoxia at the end of the Early Triassic: A cause of delay in the recovery of life after the end-Permian mass extinction. Palaeogeography, Palaeoclimatology, Palaeoecology, v. 274, p. 185-195.

Takiguchi, T., Sugitani, K., Yamamoto, K., and Suzuki, K. 2006. Biogeochemical signatures preserved in ancient siliceous sediments; new perspectives to Triassic radiolarian bedded chert compositions. Geochemical Journal, v. 40, p. 33-45.

Taggart Jr., M.S., Kaiser, A.D. Junior, 1960. Clay mineralogy of the Mississippi River deltaic sediments. Geol. Soc. Am. Bull. 71, 521–530.

Tan, P., Steinbeck, M. and Kumar, V. (2006) Introduction to Data Mining, 2nd edn. Pearson Education, New York, p. 769.

Thiry, M. (2000) Palaeoclimatic interpretation of clay minerals in marine deposits: an outlook from the continental origin. Earth-Sci. Rev., 49, 201–221.

Thomas, F., Michot, L.J., Vantelon, D., Montarges, E., Prelot, B., Cruchaudet, M., Delon, J.-F., 1999. Layer charge and electrophoretic mobility of smectites. Colloids Surf. A Physicochem. Eng. Asp. 159, 351–358.

Thushara, V. & Vinayachandran, P.N. Formation of summer phytoplankton bloom in the northwestern Bay of Bengal in a coupled physical-ecosystem model. *J. Geophys. Res.- Ocean* **121** 8535-8550 (2016).

Tietjen, T., Vähätalo, A.V., Wetzel, R.G., 2005. Effects of clay mineral turbidity on dissolved organic carbon and bacterial production. Aquat. Sci. 67, 51–60.

Totten, M.W., Hanan, M.A. and Weaver, B.L. (2000) Beyond whole-rock geochemistry of shales: the importance of assessing mineralogical controls for revealing tectonic discriminants of multiple sediment sources for the Ouchita Mountain flysch deposits. Geol. Soc. Am. Bull., 112, 1012–1022.

Tozer, E.T. (1994) Canadian Triassic ammonoid faunas. Geol. Sur. Can. Bull., 467, 1–663. Tribovillard, N., Algeo, T.J., Lyons, T. and Ribouleau, A. (2006) Trace metals as paleoredox and paleoproductivity proxies: an update. Chem. Geol., 232, 12–32.

Tribovillard, N., Algeo, T.J., Lyons, T., Riboulleau, A., 2006. Trace metals as paleoredox and paleoproductivity proxies: an update. Chem. Geol. 232, 12–32.

Twining, B.S., Baines, S.B., Fisher, N.S., 2004. Element stoichiometries of individual plankton cells collected during the southern ocean iron experiment (SOFeX). Limnol. Oceanogr. 49, 2115–2128.

Tyler, G. (2004) Vertical distribution of major, minor, and rare elements in a Haplic Podzol. Geoderma, 119, 277–290.

Tyson, R.V., 2001. Sedimentation rate, dilution, preservation and total organic carbon: some results of a modeling study. Org. Geochem. 32, 333–339.

Uncles, R.J., Stephens, J.A., Law, D.J., 2006. Turbidity maximum in the macrotidal, highly turbid Humber Estuary, UK: flocs, fluid mud, stationary suspensions and tidal bores. Estuar. Coast. Shelf Sci. 67, 30–52.

Urrutia, M.M., Kemper, M., Doyle, R., Beveridge, T.J., 1992. The membrane-induced proton motive force influences the metal binding ability of *Bacillus subtilis* cell walls. Appl. Environ. Microbiol. 58, 3837–3844.

Utting, J., MacNaughton, R.B., Zonneveld, J.-P. and Fallas, K. (2005) Palynostratigraphy, organic matter and thermal maturity of the Lower Triassic Toad, Grayling and Montney formations of Yukon, British Columbia and Alberta and comparison with the Sverdrup Basin, Nunavut. Bull. Can. Pet. Geol., 53, 5–24.

Varga A., Szakmány, G., Árgyelán, T., Józsa, S., Raucsik, B., and Máthé, Z. 2007. Complex examination of the Upper Paleozoic siliciclastic rocks from southern Transdanubia, SW Hungary—mineralogical, petrographic, and geochemical study. In: Sedimentary Provenance and Petrogenesis: Perspectives from Petrography and Geochemistry (Eds J. Arribas, S. Critelli and M.J. Johnsson), GSA Spec. Paper, 420, 73-93.

van Breugel, Y., Schouten, S., Paetzel, M., Ossebaar, J., Sinninghe Damsté. Reconstruction of $\delta^{13}C$ of chemocline CO_2 (aq) in past oceans and lakes using the $\delta^{13}C$ of fossil isorenieratene. Earth and Planetary Science Letters, v. 235, p. 421-434.

Verspagen, J.M.H., Visser, P.M., Huisman, J., 2006. Aggregation with clay causes sedimentation of the buoyant cyanobacteria *Microcystis* spp. Aquat. Microb. Ecol. 44, 165–174.

Walker, S.G., Flemming, C.A., Ferris, F.G., Beveridge, T.J., Bailey, G.W., 1989. Physiochemical interaction of *Escherichia coli* cell envelopes and *Bacillus subtilis* cell walls with two clays and ability of the composite to immobilize heavy metals from solution. Appl. Environ. Microbiol. 55, 2976–2984.

Wan, S., Li, A., Clift, P.D., Stuut, J.-B.W., 2007. Development of the East Asian monsoon: mineralogical and sedimentological records in the northern South China Sea since 20 Ma. Palaeogeogr. Palaeoclimatol. Palaeoecol. 254, 561–582.

Wang, W., Qin, Y., Lui, X., Zhao, J., Wang, J., Wu, G. and Lui, J. (2011) Distribution, occurrence and enrichment causes of gallium in coals from the Jungar Coalfield, Inner Mongolia. Sci. China Earth Sci., 54, 1053–1068.

Wanty, R.B., Goldhaber, M.B., 1992. Thermodynamics and kinetics of reactions involving vanadium in sedimentary rocks. Geochim. Cosmochim. Acta 56, 1471–1483.

Ward, J.H., Jr (1963) Hierarchical grouping to optimize an objective function. J. Am. Stat. Assoc., 58, 236–244.

Waterbury, J.B., Watson, S.W., Guillard, R. R. L. And Brand, L. E., 1979. Widespread occurrence of a unicellular, marine, planktonic, cyanobacterium. Nature 277, 293–294.

Wedepohl, K.H. (1971) Environmental influences on the chemical composition of shales and clays. In: Physics and Chemistry of Earth (Eds L.H. Ahrens, F. Press, S.K. Runcorn and H.C. Urey), 8, 307–331.

Wei, G., Liu, Y., Li, X., Shao, L. and Liang, X. (2003) Climatic impact on Al, K, Sc and Ti in marine sediments: evidence from ODP Site 1144, South China Sea. Geochem. J., 37, 593–602.

Wheat, C.G., Feely, R.A. and Mottl, M.J. (1996) Phosphate removal by oceanic hydrothermal processes: an update of the phosphorus budget in the oceans. Geochim. Cosmochim. Acta, 60, 3593–3608.

Wignall, P.B. & Twitchett, R.J. Oceanic anoxia and the End Permian Mass Extinction. *Science* **272**, 1155-1158 (1996).

Wood, J.M., Sanei, H., Curtis, M.E. and Clarkson, C.R. (2015) Solid bitumen as a determinant of reservoir quality in an unconventional tight gas siltstone play. Int. J. Coal Geol., 150–151, 287–295.

Wright, A.M., Ratcliffe, K.T., Zaitlin, B.A. and Wray, D.S. (2010) The application of chemostratigraphic techniques to distinguish compound incised valleys in low accommodation incised valley systems in a foreland-basin setting: an example from the Lower Cretaceous Mannville Group and Basal Colorado Sandstone (Colorado Group), Western Canadian Sedimentary Basin. In: Application of Modern Stratigraphic Techniques, Theory and Case Histories (Eds K. Ratcliffe and B.A. Zaitlin), SEPM Spec. Publ., 94, 93–107.

Xie, S., Pancost, R.D., Yin, H., Wang, H., Evershed, R.P., 2005. Two episodes of microbial change coupled with Permo/Triassic faunal mass extinction. Nature 434, 494–497.

Xu, L., Lehmann, B., Mao, J., Nägler, T.F., Neubert, N., Böttcher, M.E., Escher, P., 2012. Mo isotope and trace element patterns of Lower Cambrian black shales in South China: multi-proxy constraints on the paleoenvironment. Chem. Geol. 318–319, 45–59.

Yamamoto, K. 1987. Geochemical characteristics and depositional environments of cherts and associated rocks in the Franciscan and Shimanto Terranes. Sedimentary Geology, v. 52, p. 65-108.

Zhao, M.-Y. and Zheng, Y.-F. (2015) The intensity of chemical weathering: Geochemical constraints from marine detrital sediments of Triassic age in South China. Chem. Geol., 391, 111–122.

Zhuang, G., Pagani, M., Zhange, Y.G. 2017. Monsoonal upwelling in the western Arabian Sea since the middle Miocene. Geology, v. 45, p. 655-658.

Zonneveld, J.-P., and Moslow, T.F. 2018. Palaeogeographic setting, lithostratigraphy, and sedimentary framework of the Lower Triassic Montney Formation of western Alberta and northeastern British Columbia. Bulletin of Canadian Petroleum Geology, v. 66, p. 93-127.

Zonneveld, J.-P., Beatty, T.W. and Pemberton, S.G. (2007) Lingulide brachiopods and the trace fossil Lingulichnus from the Triassic of Western Canada: implications for faunal recovery after the end-Permian mass extinction. Palaios, 22, 74–97.

Zonneveld, J.-P., Gingras, M.K. and Beatty, T.W. (2010a) Diverse ichnofossil assemblages following the P-T mass extinction, Lower Triassic, Alberta and British Columbia, Canada: evidence for shallow marine refugia on the northwestern coast of Pangaea. Palaios, 25, 368–392.

Zonneveld, J.-P., Golding, M., Moslow, T.F., Orchard, M.J., Playter, T. and Wilson, N. (2011) Depositional framework of the lower triassic montney formation, west-central Alberta and northeastern British Columbia. In: Canadian Society of Petroleum Geologists, Canadian Society of Exploration Geophysicists, Joint Annual Meeting, Abstracts 2011, pp. 1–4.

Zonneveld, J.-P., MacNaughton, R.B., Utting, J., Beatty, T.W., Pemberton, S.G. and Henderson, C.M. (2010b) Sedimentology and ichnology of the Lower Triassic Montney Formation in the Pedigree-Ring/Border-Kahntah River area, northwestern Alberta and northwestern British Columbia. Bull. Can. Pet. Geol., 58, 115–140.

Appendix 1

Monsoon cycles, primary productivity, and silica deposition following the end-Permian mass extinction

Supplimentary Figures

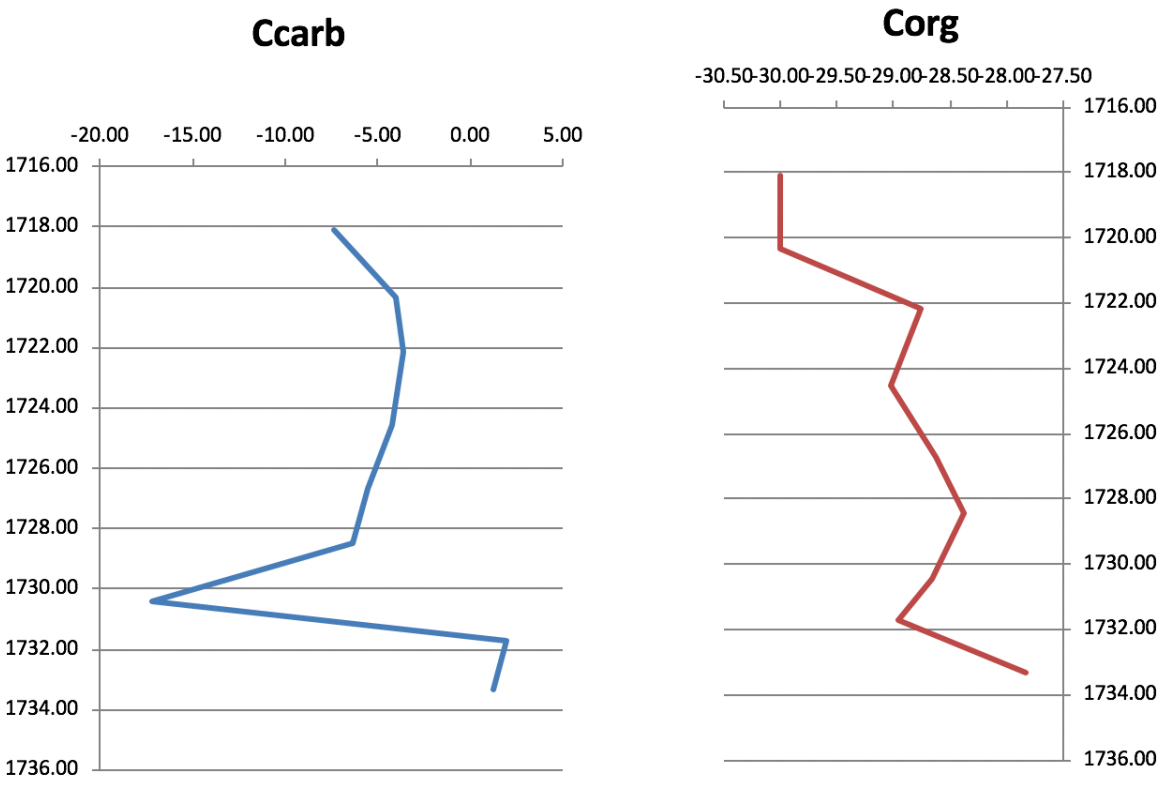

Supplementary Figure 1: Carbon isotopes measured from the carbonate (left) and organic (right) fractions. Values are reported with reference to V-PDB. The similarity in trend between the two data sets illustrates that they are not decoupled, suggesting that diagenetic overprinting has not affected the isotope data.

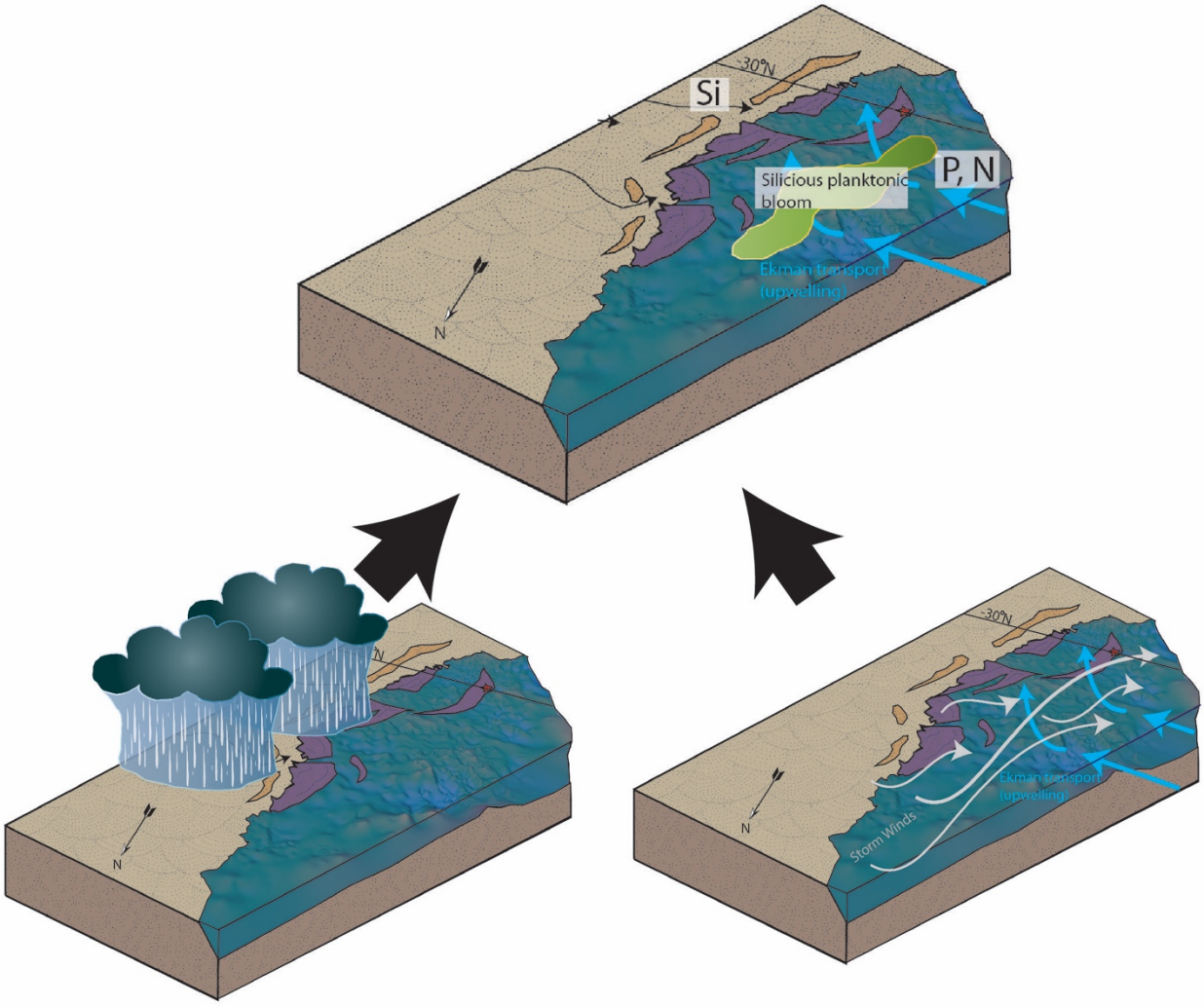

Supplementary Figure 2: Block diagrams illustrating the effect of seasonal monsoon rains on continental weathering and Si input into the basin operating in partnership with seasonal monsoon storms and winds, which cause Ekman transport and upwelling. This brings P and N to the surface and increases water mixing and oxygenation. The combined result is increased Si, P, and N in the basin which are conducive to siliceous planktonic blooms. These blooms result in the deposition of organic matter and siliceous tests.

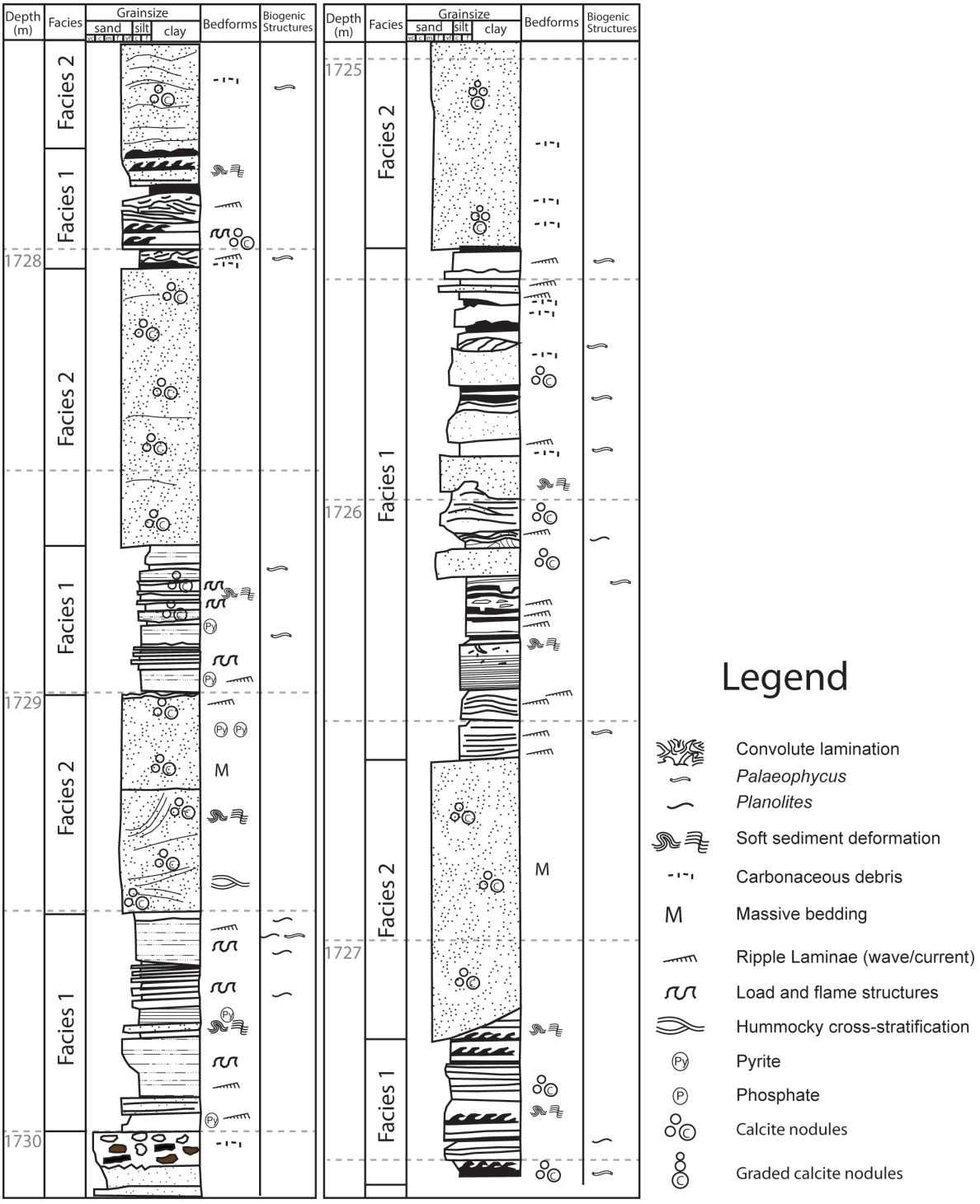

Supplementary Figure 3: Litholog of drill core from well 2-30-070-24W5. Depth is given in meters and facies occurrences are indicated. The Permian/Triassic boundary occurs at 1730 m. Two facies were identified: The first is composed of wavy to lenticular bedded siltstone and mudstone with bidirectional ripples and occasional trace fossils (Planolites) (Facies 1). The second facies consists of hummocky cross stratified very fine sandstone with randomly distributed calcite cemented spheroids, approximately 5mm in diameter on average (Facies 2). The distribution of the hummocky cross stratified sandstone coincides with the zones of biogenically sourced excess silica and paleoproductivity indicators.

Supplementary Figure 4: Close up images of Facies 1 (left) and Facies 2 (right). Facies 1 consists of wavy to lenticular bedded siltstone and mudstone with bidirectional ripples and occasional Planolites. This is interpreted as being formed in a distal, tidally-influenced, delta front. Facies 2 comprises hummocky cross stratified fine sandstone with randomly distributed calcite spheres. This facies is interpreted as storm deposits with diagenetic calcite cementation after burial from the consumption of organic matter by sulphate reduction.

Appendix 2

Clinoform identification and correlation in fine-grained sediments: A case study using the Triassic Montney Formation (Supplimentary Material)

Supplimentary Figures

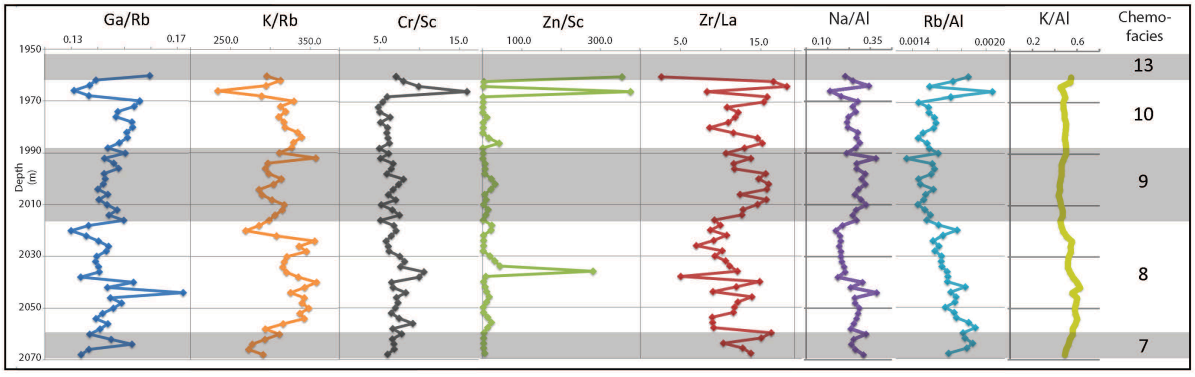

Figure S1: Clay indicator profiles for well d-48-A/ 94-B-9. Depths are in metres. Chemofacies are numbered on the right. Simplified interpretations of concentrations are labelled at the base with arrows. For references, refer to the Elemental indicators section in the text.

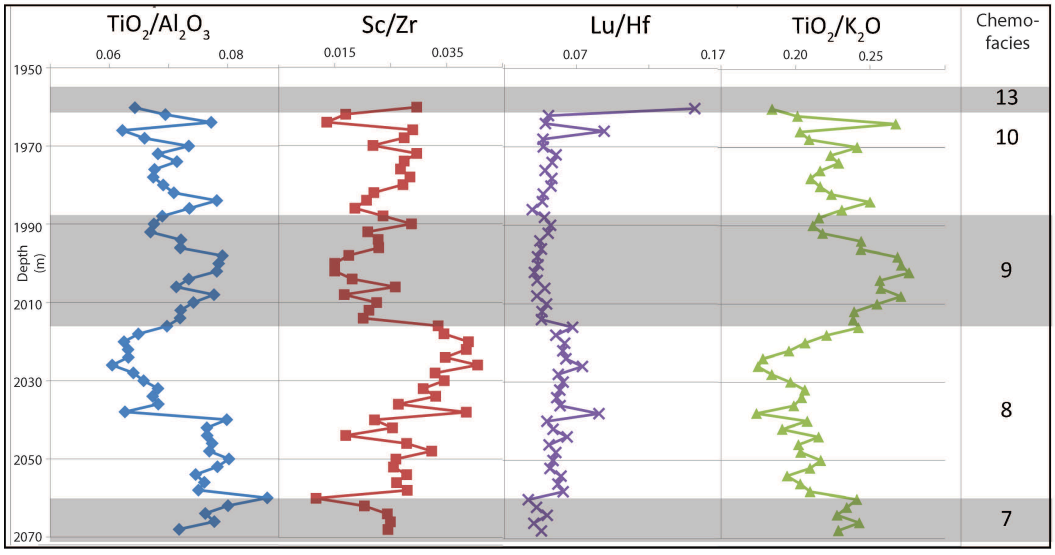

Figure S2: Detrital indicator profiles for well d-48- A/94-B-9. Depths are in metres. Chemofacies are numbered on the right. Simplified interpretations of concentrations are labelled at the base with arrows. For references, refer to the Elemental indicators section in the text.

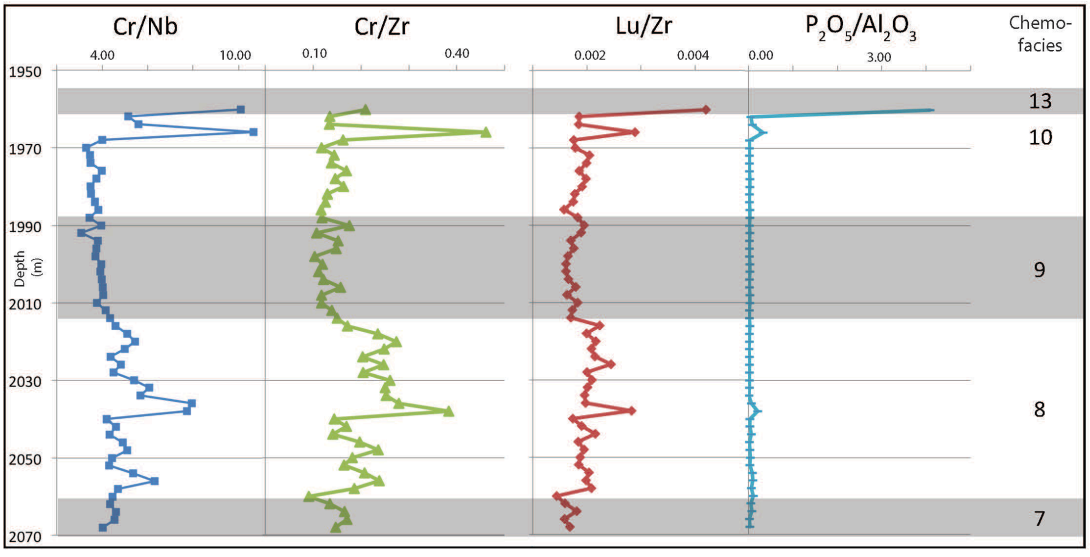

Figure S3: Mineralogical indicator profiles for well d-48-A/94-B-9. Depths are in metres. Chemofacies are numbered on the right. Simplified interpretations of concentrations are labelled at the base with arrows. For references, refer to the Elemental indicators section in the text.

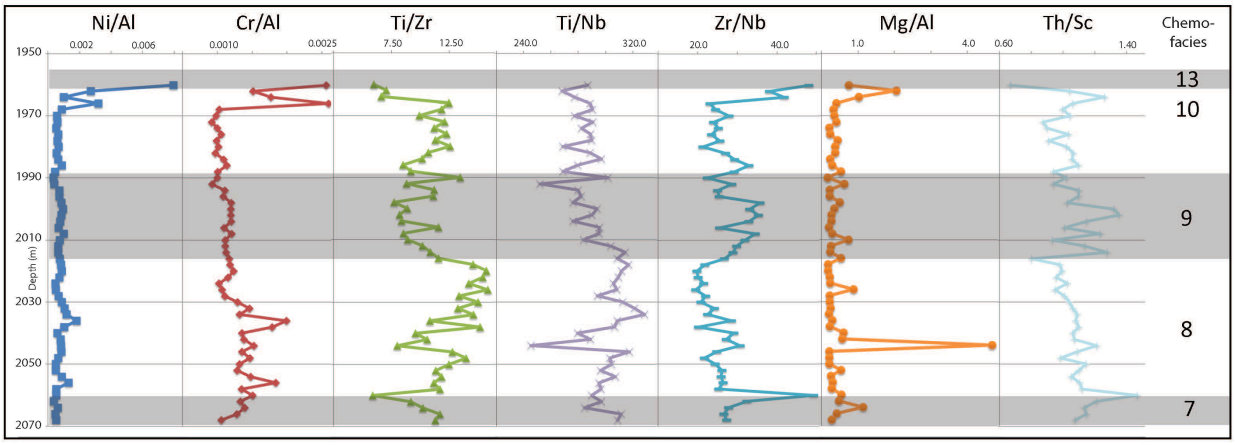

Figure S4: Provenance indicator profiles for well d- 48-A/94-B-9. Depths are in metres. Chemofacies are numbered on the right. Simplified interpretations of concentrations are labelled at the base with arrows. For references, refer to the Elemental indicators section in the text.

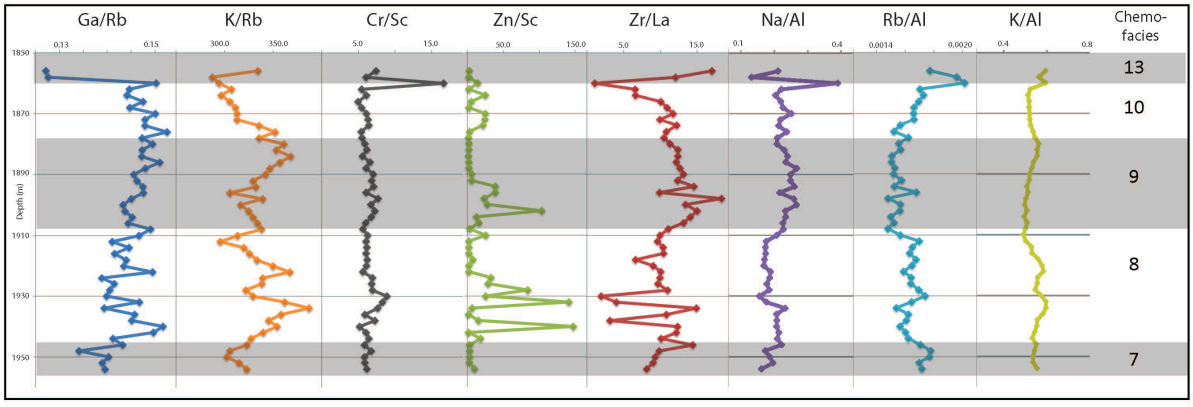

Figure S5: Clay indicator profiles for well c-74-G/ 94-B-9. Depths are in metres. Chemofacies are numbered on the right. Simplified interpretations of concentrations are labelled at the base with arrows. For references, refer to the Elemental indicators section in the text.

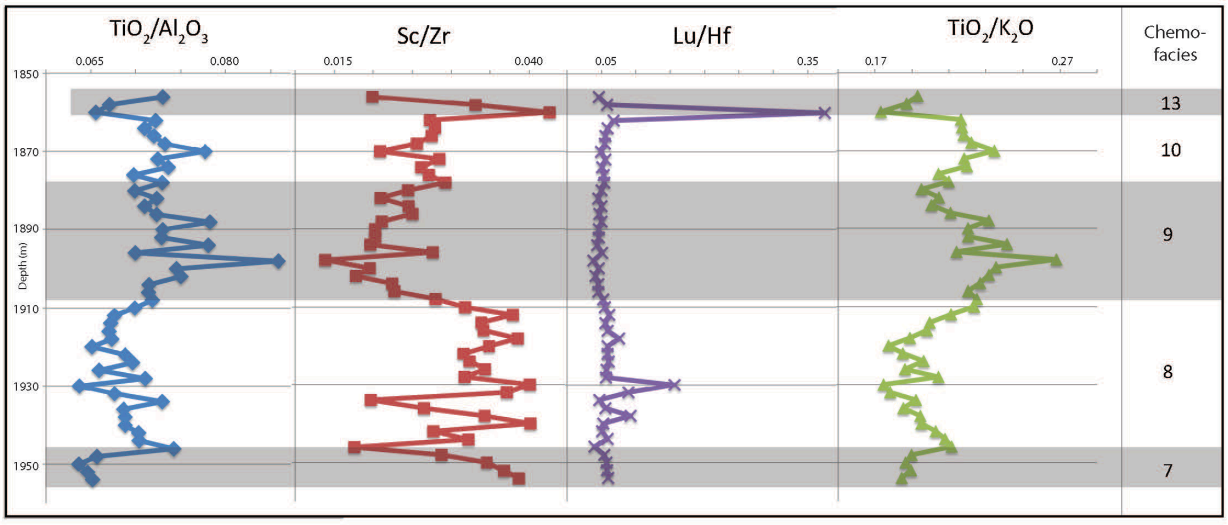

Figure S6: Detrital indicator profiles for well c-74- G/94-B-9. Depths are in metres. Chemofacies are numbered on the right. Simplified interpretations of concentrations are labelled at the base with arrows. For references, refer to the Elemental indicators section in the text.

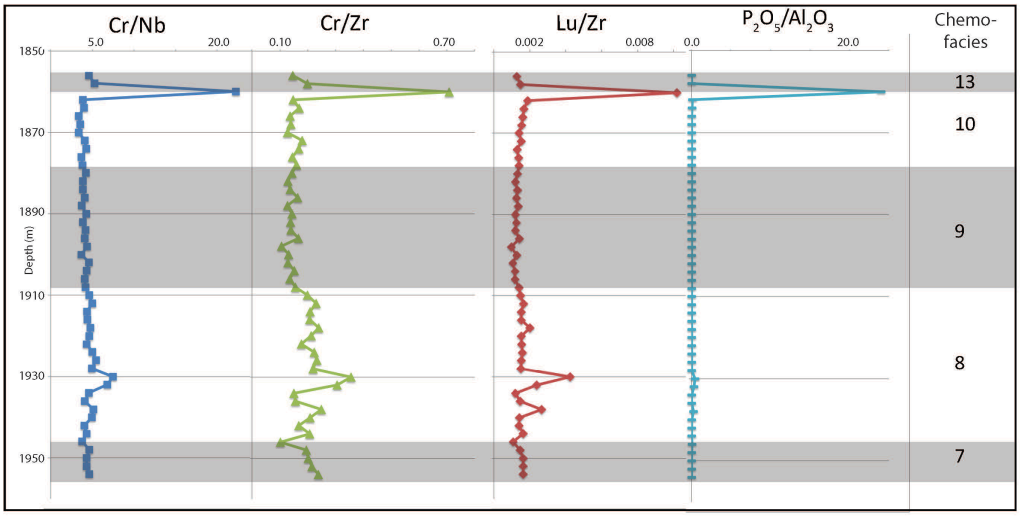

Figure S7: Mineralogical indicator profiles for well c-74-G/94-B-9. Depths are in metres. Chemofacies are numbered on the right. Simplified interpretations of concentrations are labelled at the base with arrows. For references, refer to the Elemental indicators section in the text.

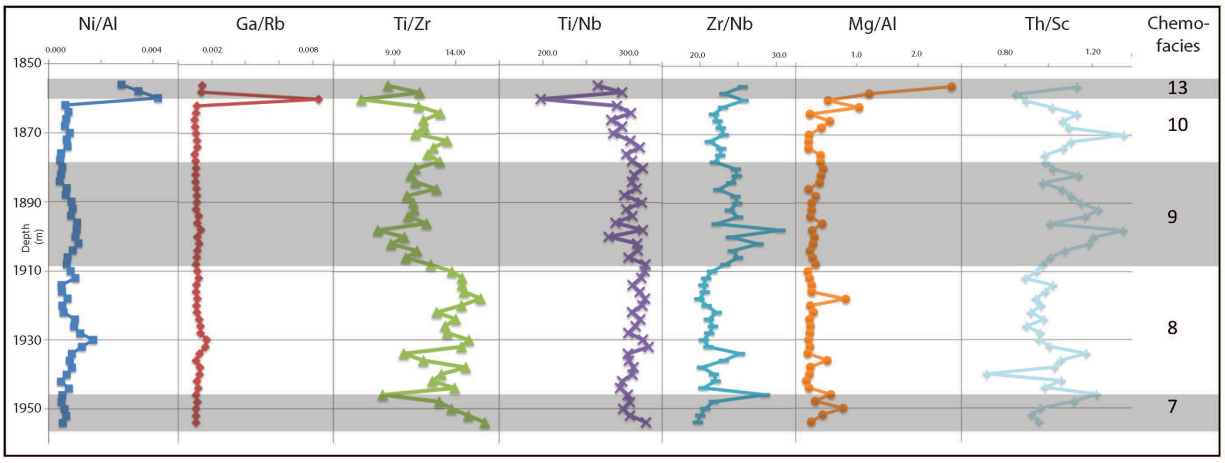

Figure S8: Provenance indicator profiles for well c- 74-G/94-B-9. Depths are in metres. Chemofacies are numbered on the right. Simplified interpretations of concentrations are labelled at the base with arrows. For references, refer to the Elemental indicators section in the text.

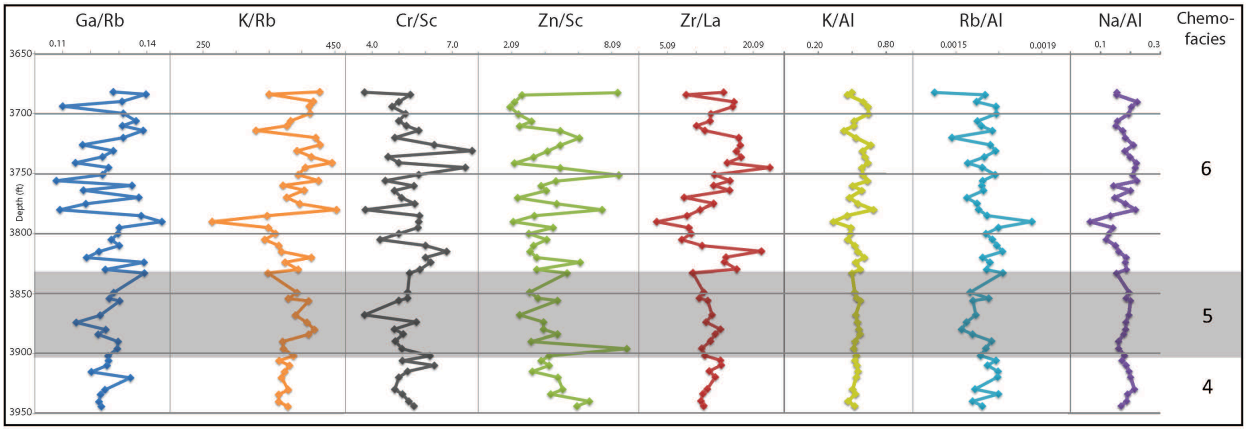

Figure S9: Clay indicator profiles for well 11-20-082- 02W6. Depths are in feet. Chemofacies are numbered on the right. Simplified interpretations of concentrations are labelled at the base with arrows. For references, refer to the Elemental indicators section in the text.

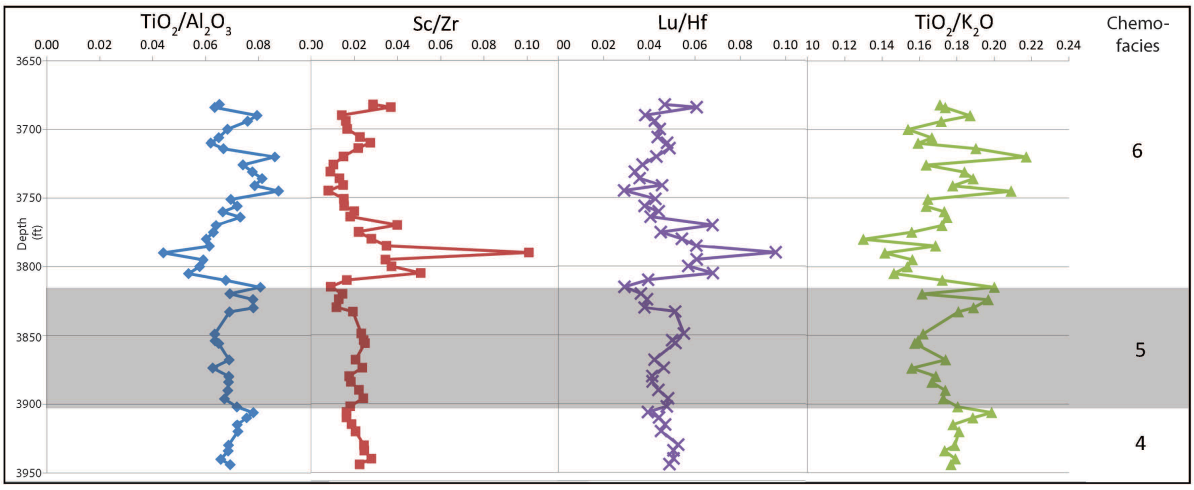

Figure S10: Detrital indicator profiles for well 11- 20-082-02W6. Depths are in feet. Chemofacies are numbered on the right. Simplified interpretations of concentrations are labelled at the base with arrows. For references, refer to the Elemental indicators section in the text.

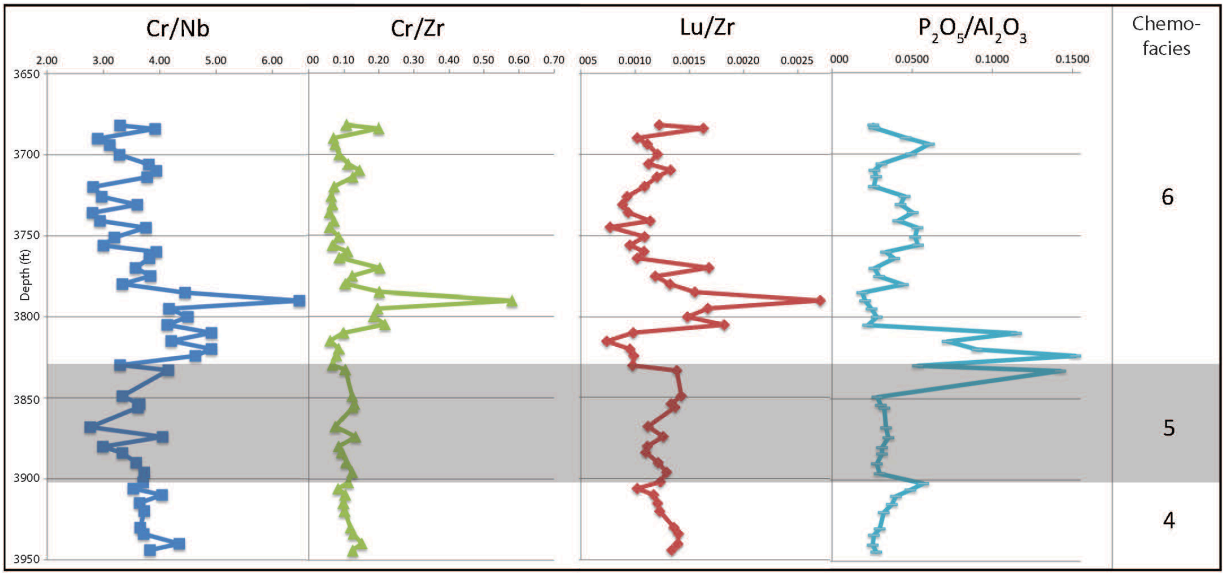

Figure S11: Mineralogical indicator profiles for well 11-20-082-02W6. Depths are in feet. Chemofacies are numbered on the right. Simplified interpretations of concentrations are labelled at the base with arrows. For references, refer to the Elemental indicators section in the text.

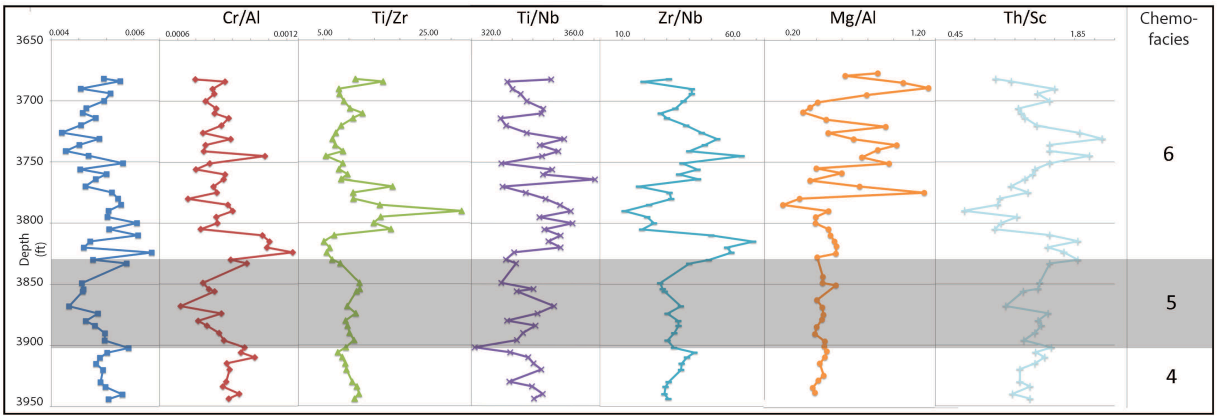

Figure S12: Provenance indicator profiles for well 11-20-082-02W6. Depths are in feet. Chemofacies are numbered on the right. Simplified interpretations of concentrations are labelled at the base with arrows. For references, refer to the Elemental indicators section in the text.

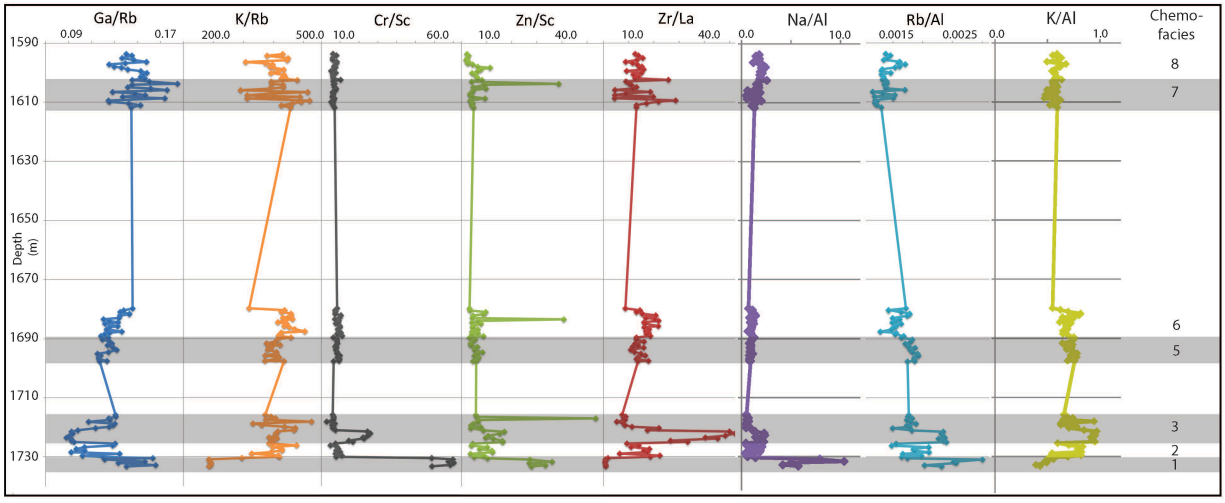

Figure S13: Clay indicator profiles for well 2-30- 070-24W5. Depths are in metres. Chemofacies are numbered on the right. Simplified interpretations of concentrations are labelled at the base with arrows. For references, refer to the Elemental indicators section in the text.

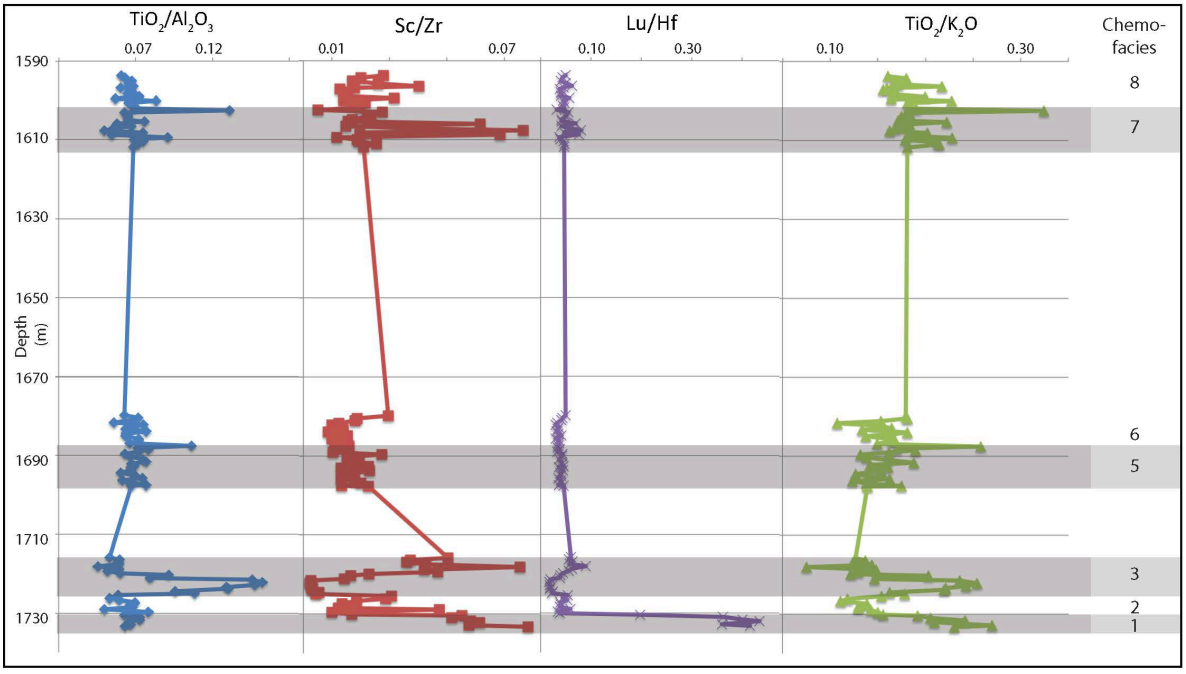

Figure S14: Detrital indicator profiles for well 2-30- 070-24W5. Depths are in metres. Chemofacies are numbered on the right. Simplified interpretations of concentrations are labelled at the base with arrows. For references, refer to the Elemental indicators section in the text.

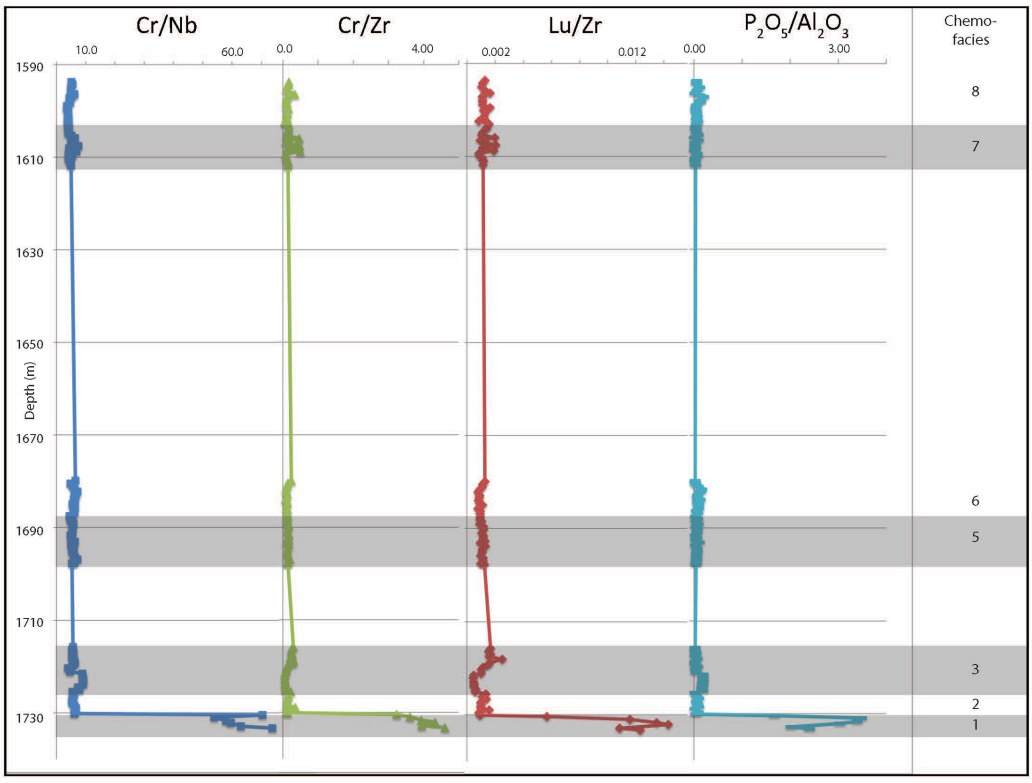

Figure S15: Mineralogical indicator profiles for well 2-30-070-24W5. Depths are in metres. Chemofacies are numbered on the right. Simplified interpretations of concentrations are labelled at the base with arrows. For references, refer to the Elemental indicators section in the text.

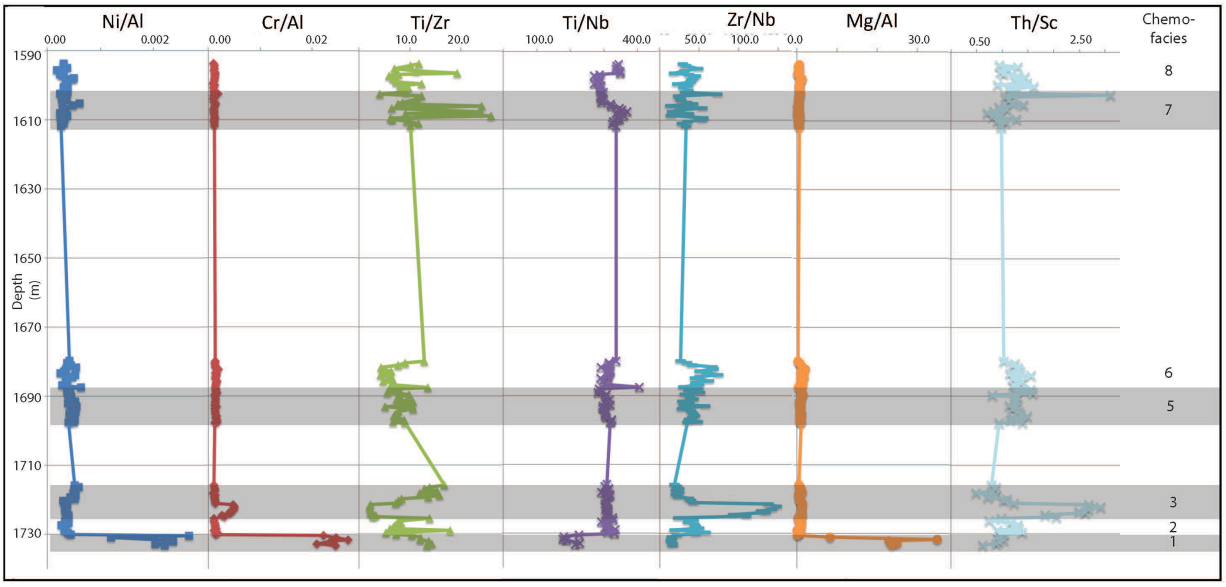

Figure S16: Provenance indicator profiles for well 2-30-070-24W5. Depths are in metres. Chemofacies are numbered on the right. Simplified interpretations of concentrations are labelled at the base with arrows. For references, refer to the Elemental indicators section in the text.

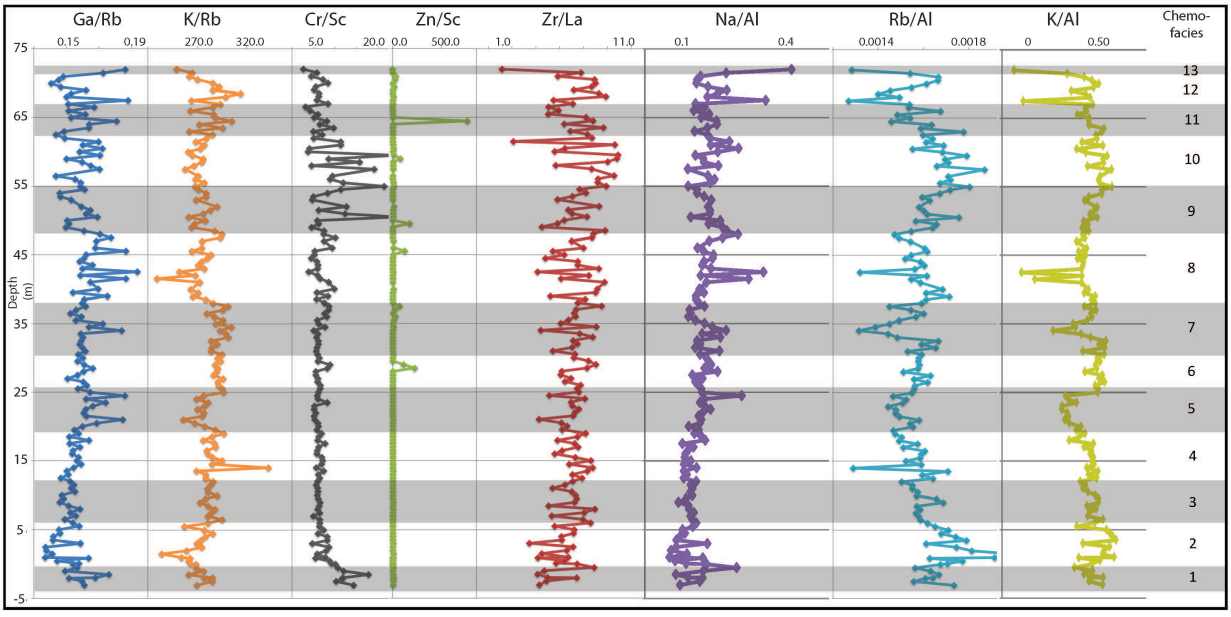

Figure S17: Clay indicator profiles for the outcrop Ursula Creek. Depths are in metres. Chemofacies are numbered on the right. Simplified interpretations of concentrations are labelled at the base with arrows. For references, refer to the Elemental indicators section in the text.

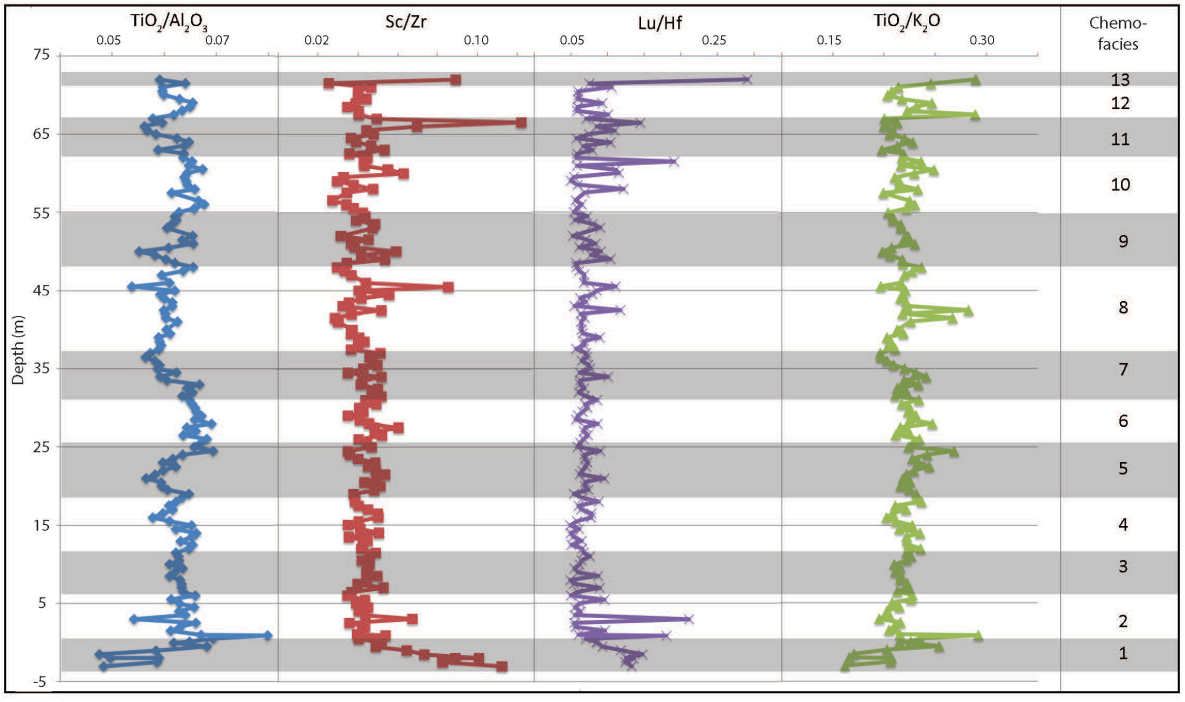

Figure S18: Detrital indicator profiles for the outcrop Ursula Creek. Depths are in metres. Chemofacies are numbered on the right. Simplified interpretations of concentrations are labelled at the base with arrows. For references, refer to the Elemental indicators section in the text.

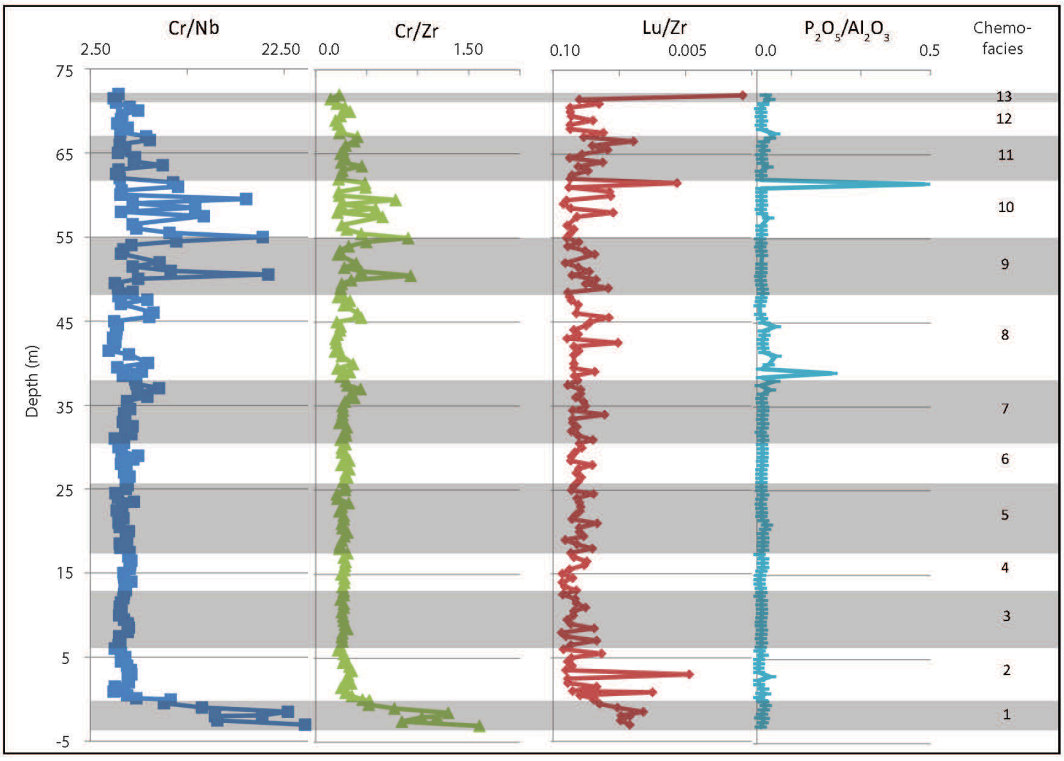

Figure S19: Mineralogical indicator profiles for the outcrop Ursula Creek. Depths are in metres. Chemofacies are numbered on the right. Simplified interpretations of concentrations are labelled at the base with arrows. For references, refer to the Elemental indicators section in the text.

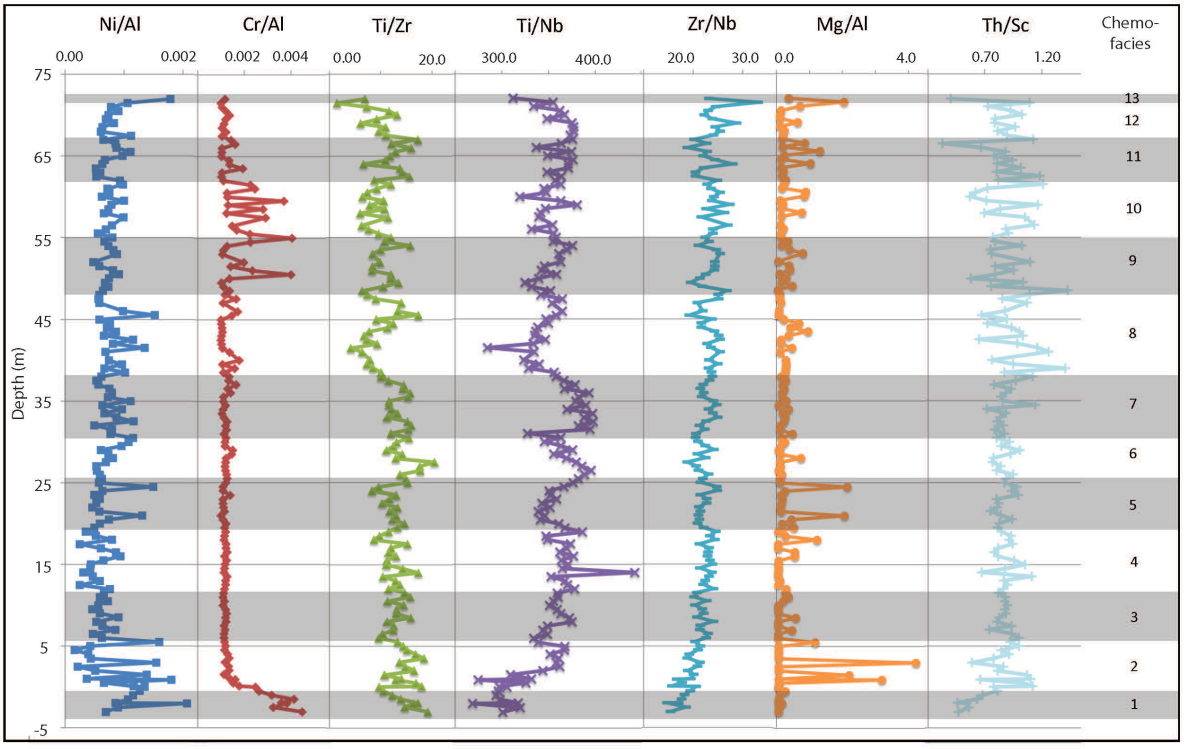

Figure S20: Provenance indicator profiles for the outcrop Ursula Creek. Depths are in metres. Chemofacies are numbered on the right. Simplified interpretations of concentrations are labelled at the base with arrows. For references, refer to the Elemental indicators section in the text.

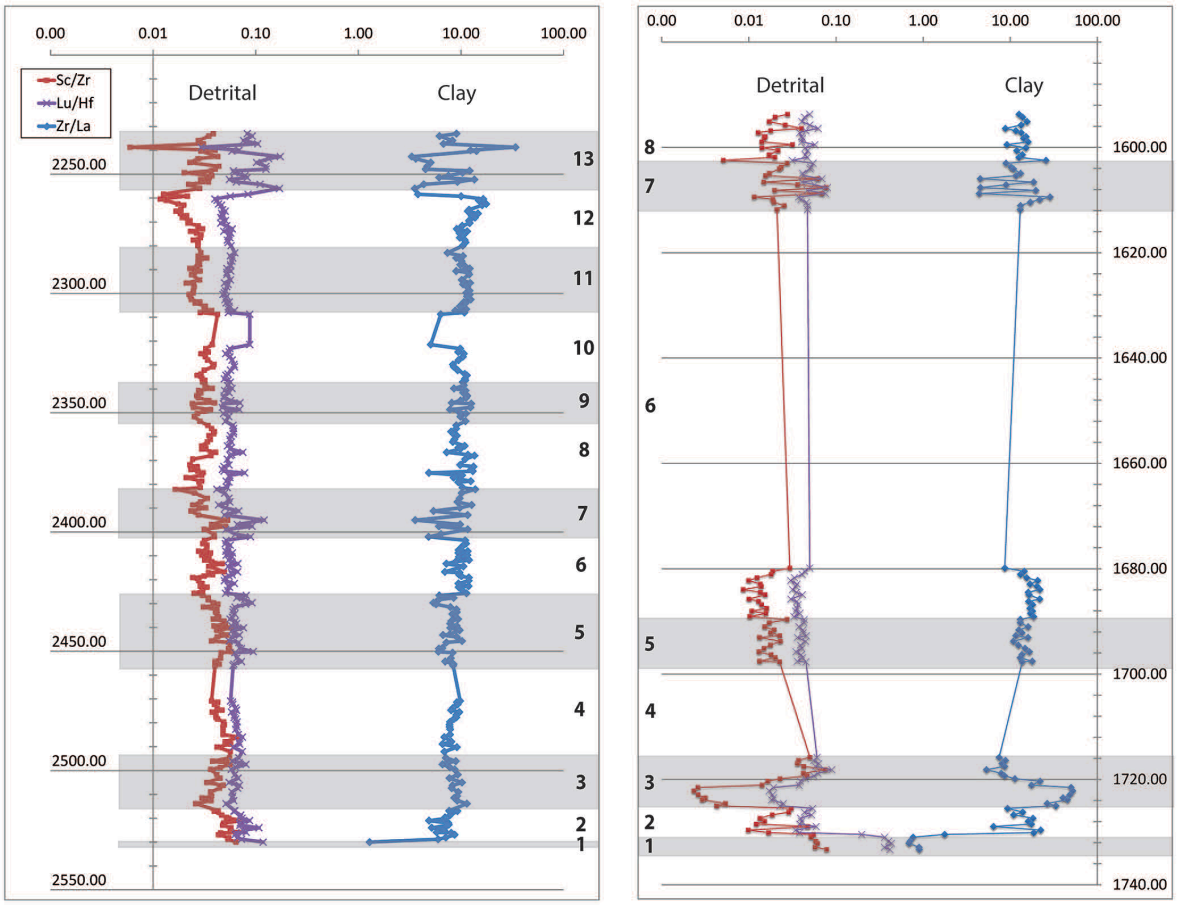

Figure S21: Comparison of select detrital and clay indicators between wells 2-30-070-24W5 (right) and 16-17-083-25W6 (left) illustrating the identification and correlation of chemofacies in well 2-30-070- 24W5.

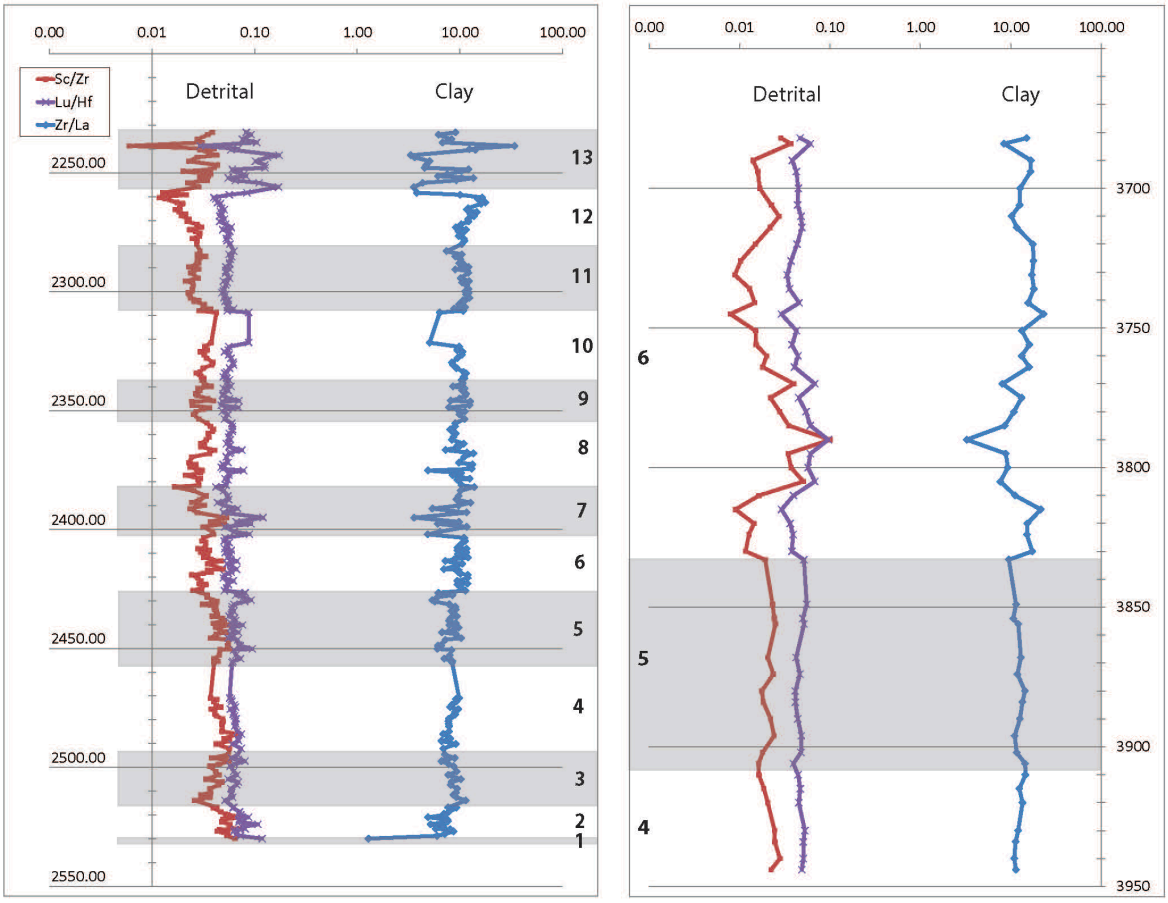

Figure S22: Comparison of select detrital and clay indicators between wells 11-20-082-02W6 (right) and 16-17-083-25W6 (left) illustrating the identification and correlation of chemofacies in well 11-20-082- 02W6.

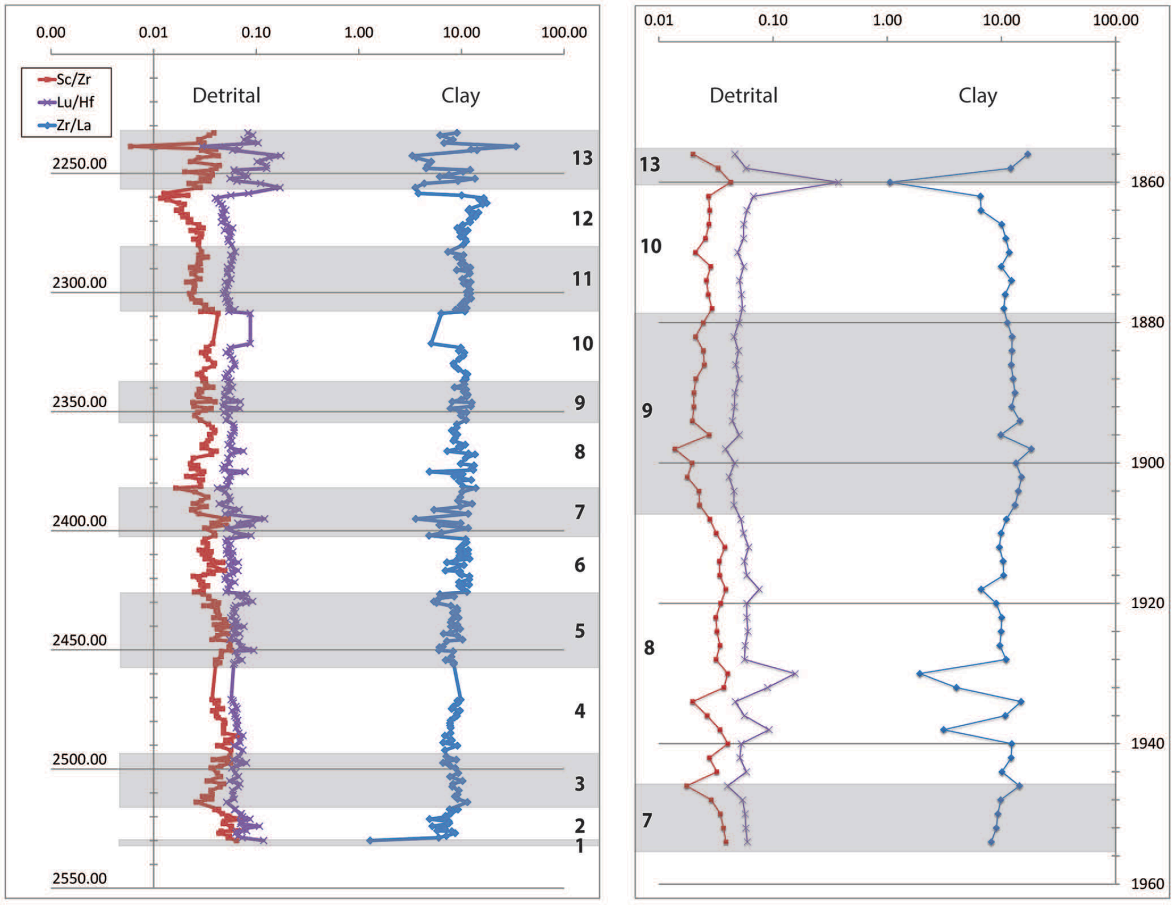

Figure S23: Comparison of select detrital and clay indicators between wells c-74-G/94-B-9 (right) and 16- 17-083-25W6 (left) illustrating the identification and correlation of chemofacies in well c-74-G/94-B-9.

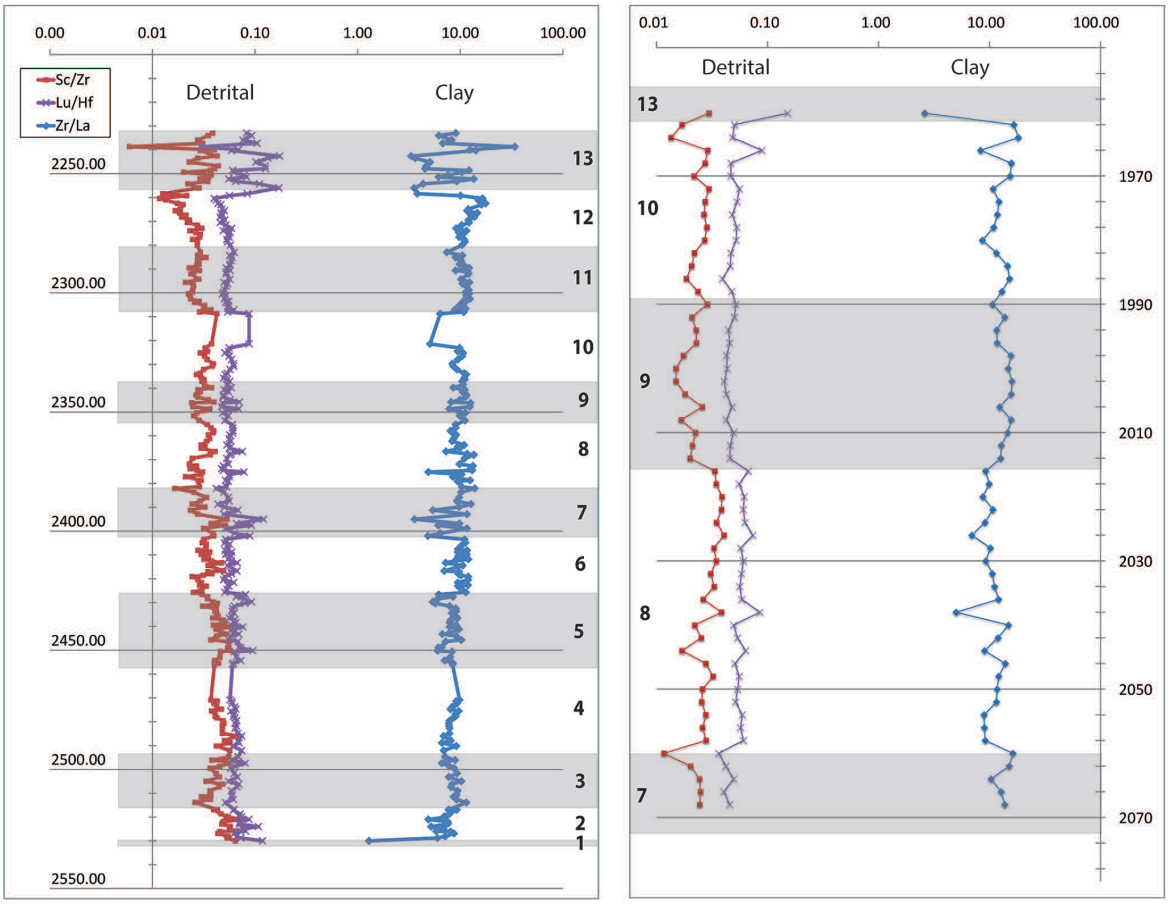

Figure S24: Comparison of select detrital and clay indicators between wells d-48-A/94-B-9 (right) and 16-17-083-25W6 (left) illustrating the identification and correlation of chemofacies in well d-48-A/94-B-9.

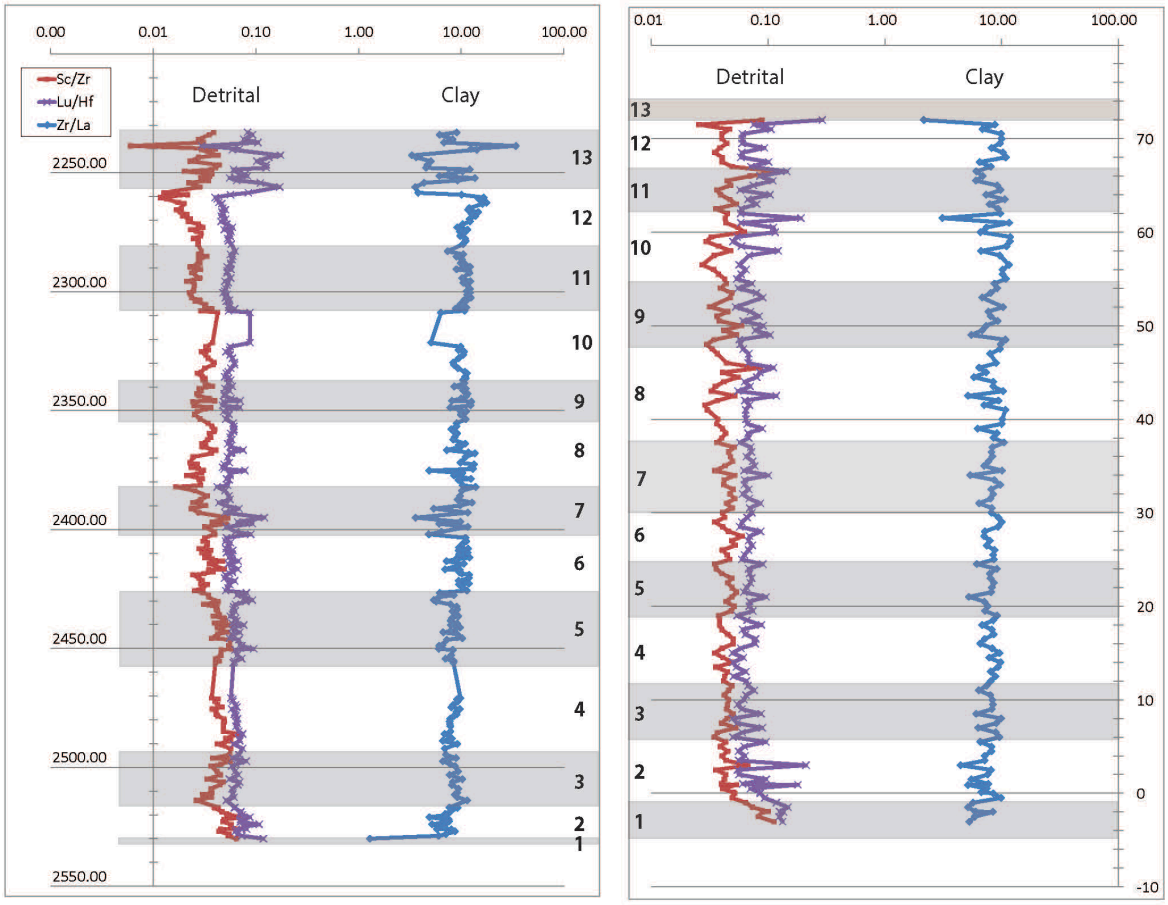

Figure S25: Comparison of select detrital and clay indicators between the outcrop Ursula Creek (right) and 16-17-083-25W6 (left) illustrating the identification and correlation of chemofacies in outcrop Ursula Creek.

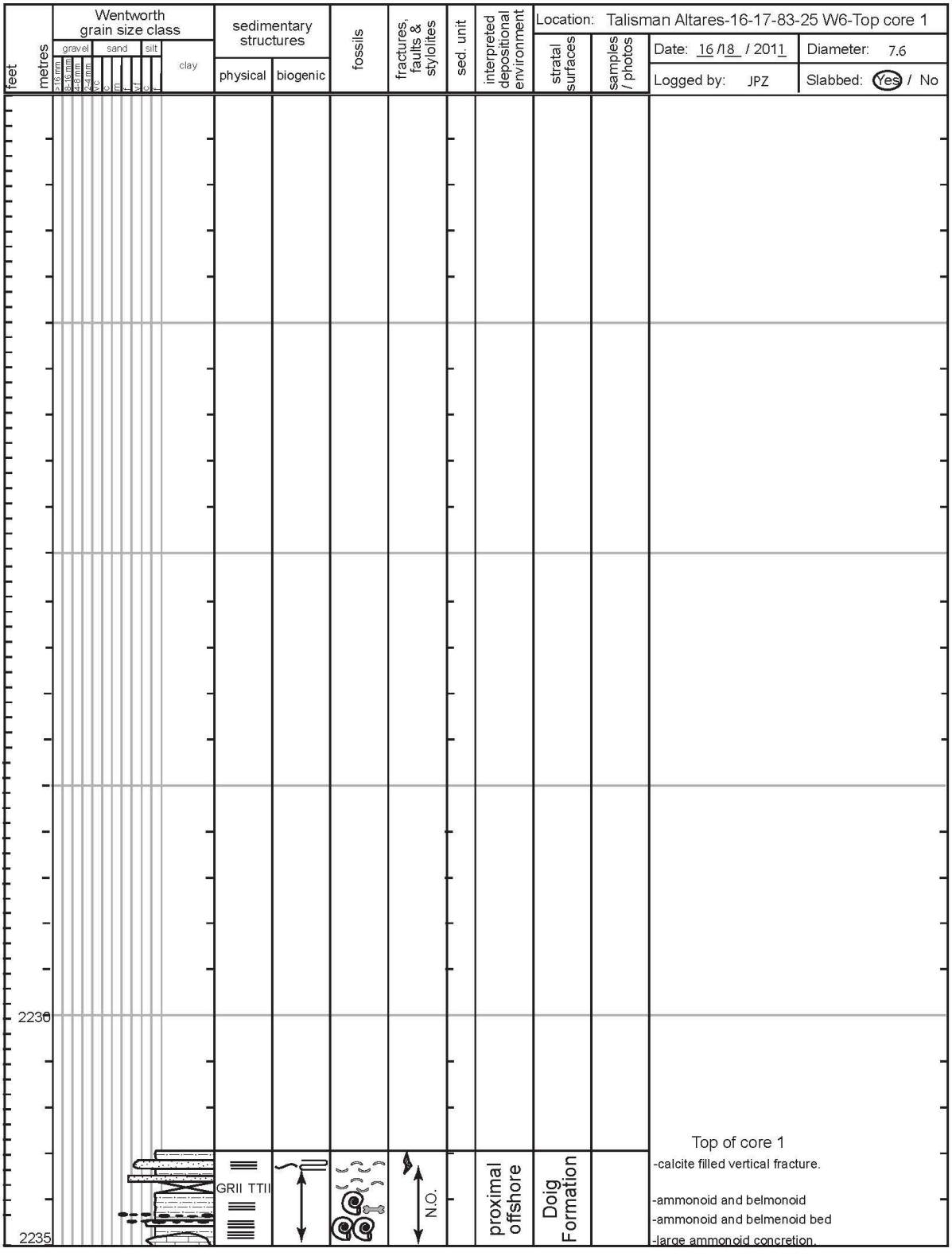
feet
metres
Wentworth grain size class
gravel
sand
silt
clay
>16 mm
8-16 mm
4-8 mm
2-4 mm
v/c
c
m
f
v/f
c
f
sedimentary structures
physical
biogenic
fossils
fractures, faults & stylolites
sed. unit
interpreted depositional environment
Location: Talisman Altares-16-17-83-25 W6-Top core 1
stratal surfaces
samples / photos
Date: 16 /18 / 2011
Diameter: 7.6
Logged by: JPZ
Slabbed: Yes / No
2230
2235
GRII TTII
N.O.
proximal offshore
Doig Formation
Top of core 1
-calcite filled vertical fracture.
-ammonoid and belmonoid
-ammonoid and belmenoid bed
-large ammonoid concretion.

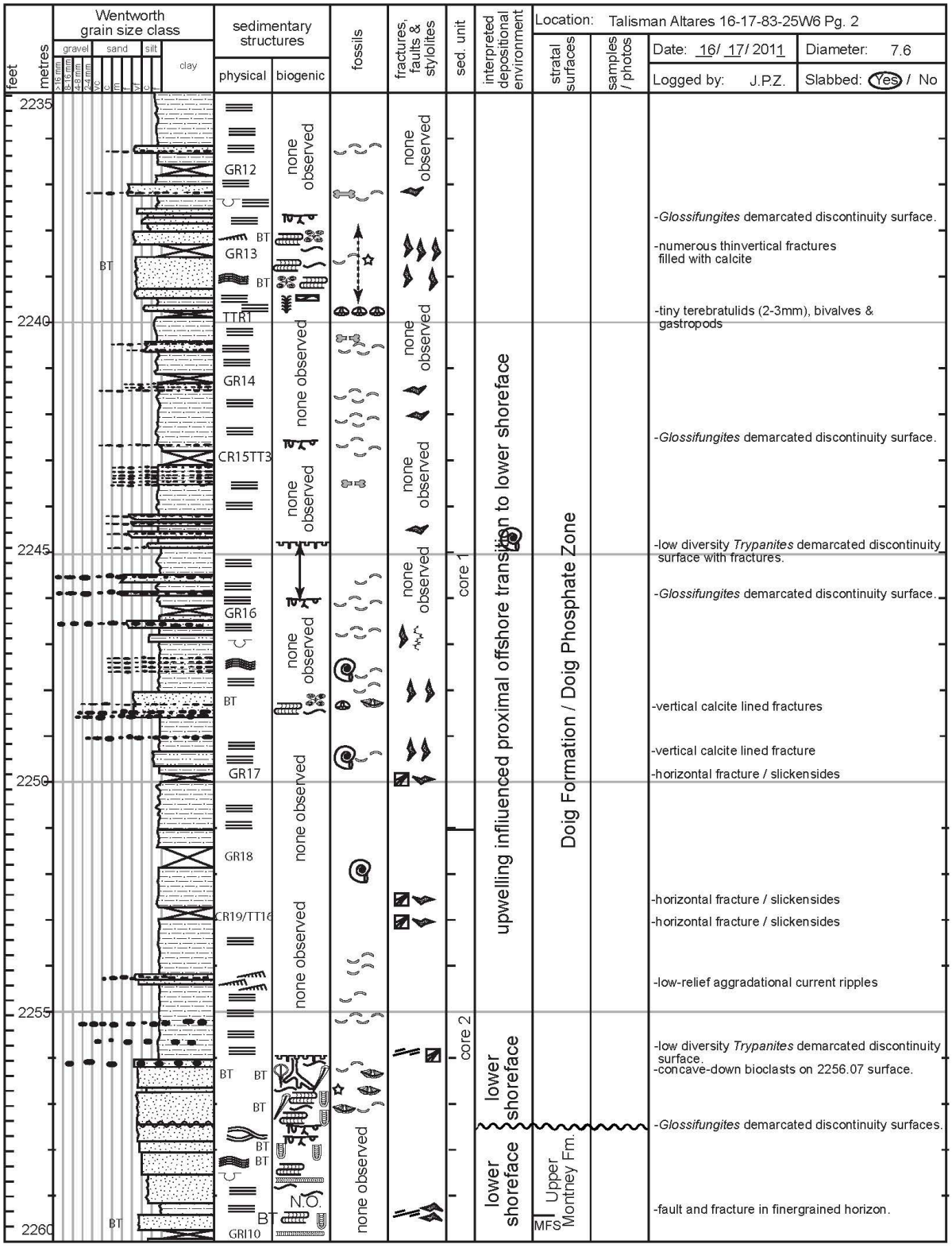
Location: Talisman Altares 16-17-83-25W6 Pg. 2
Date: 16/ 17/ 2011
Diameter: 7.6
Logged by: J.P.Z.
Slabbed: Yes / No
Wentworth grain size class
gravel
sand
silt
clay
sedimentary structures
physical
biogenic
fossils
fractures, faults & stylolites
sed. unit
interpreted depositional environment
stratal surfaces
samples / photos
feet
metres
2235
2240
2245
2250
2255
2260
GR12
GR13
TTRT
GR14
CR15TT3
GR16
GR17
GR18
CR19/TT16
GRI10
BT
none observed
core 1
core 2
upwelling influenced proximal offshore transition to lower shoreface
lower shoreface
Doig Formation / Doig Phosphate Zone
Upper Montney Fm.
MFS
-Glossifungites demarcated discontinuity surface.
-numerous thinvertical fractures filled with calcite
-tiny terebratulids (2-3mm), bivalves & gastropods
-Glossifungites demarcated discontinuity surface.
-low diversity Trypanites demarcated discontinuity surface with fractures.
-Glossifungites demarcated discontinuity surface.
-vertical calcite lined fractures
-vertical calcite lined fracture
-horizontal fracture / slickensides
-horizontal fracture / slickensides
-horizontal fracture / slickensides
-low-relief aggradational current ripples
-low diversity Trypanites demarcated discontinuity surface.
-concave-down bioclasts on 2256.07 surface.
-Glossifungites demarcated discontinuity surfaces.
-fault and fracture in finergrained horizon.

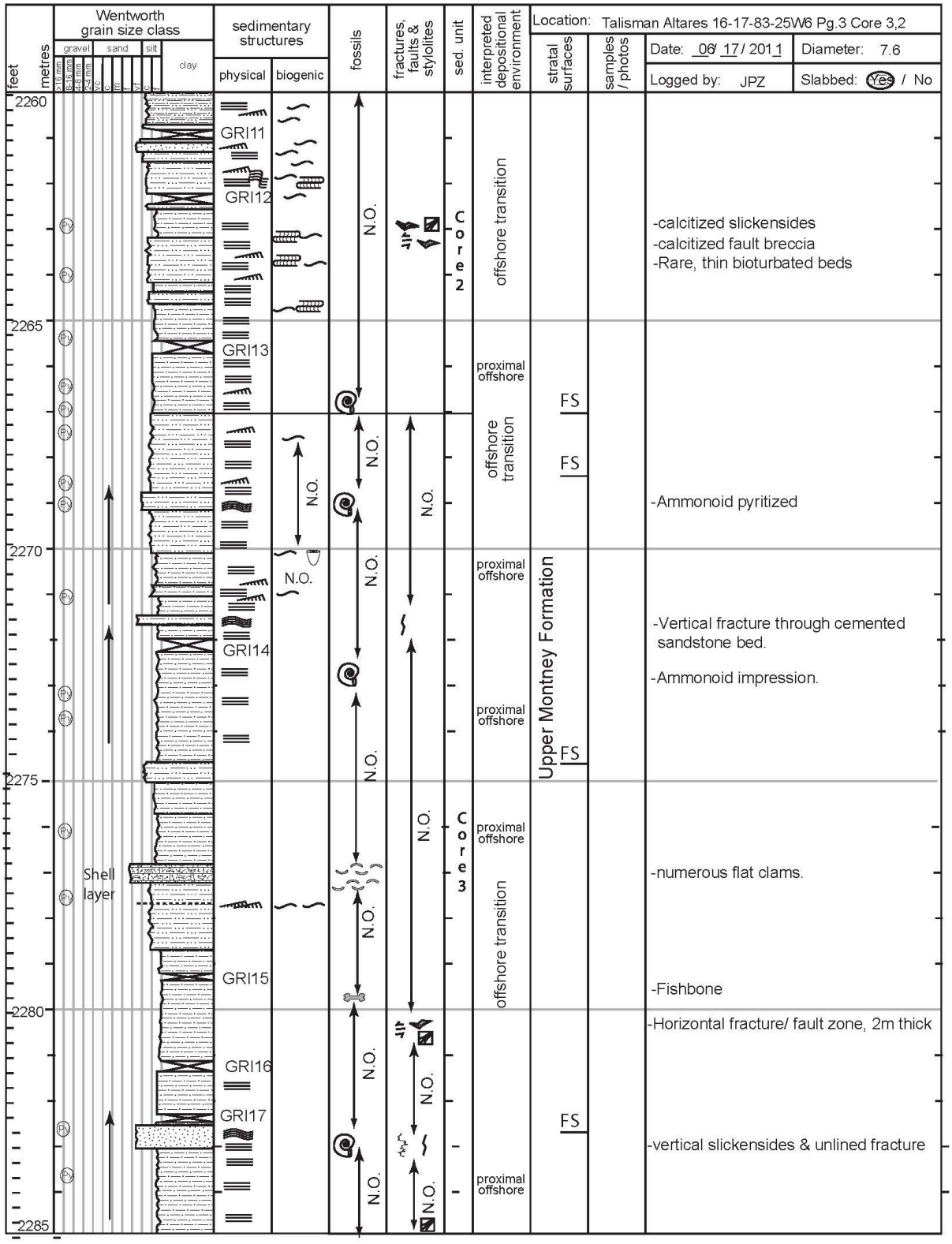
Location: Talisman Altares 16-17-83-25W6 Pg.3 Core 3,2
Date: 09/ 17/ 2011
Diameter: 7.6
Logged by: JPZ
Slabbed: Yes / No
feet
metres
Wentworth grain size class
gravel
sand
silt
clay
sedimentary structures
physical
biogenic
fossils
fractures, faults & stylolites
sed. unit
interpreted depositional environment
stratal surfaces
samples / photos
2260
2265
2270
2275
2280
2285
GRI11
GRI12
GRI13
GRI14
GRI15
GRI16
GRI17
Shell layer
N.O.
Core 2
Core 3
offshore transition
proximal offshore
FS
Upper Montney Formation
-calcitized slickensides
-calcitized fault breccia
-Rare, thin bioturbated beds
-Ammonoid pyritized
-Vertical fracture through cemented sandstone bed.
-Ammonoid impression.
-numerous flat clams.
-Fishbone
-Horizontal fracture/ fault zone, 2m thick
-vertical slickensides & unlined fracture

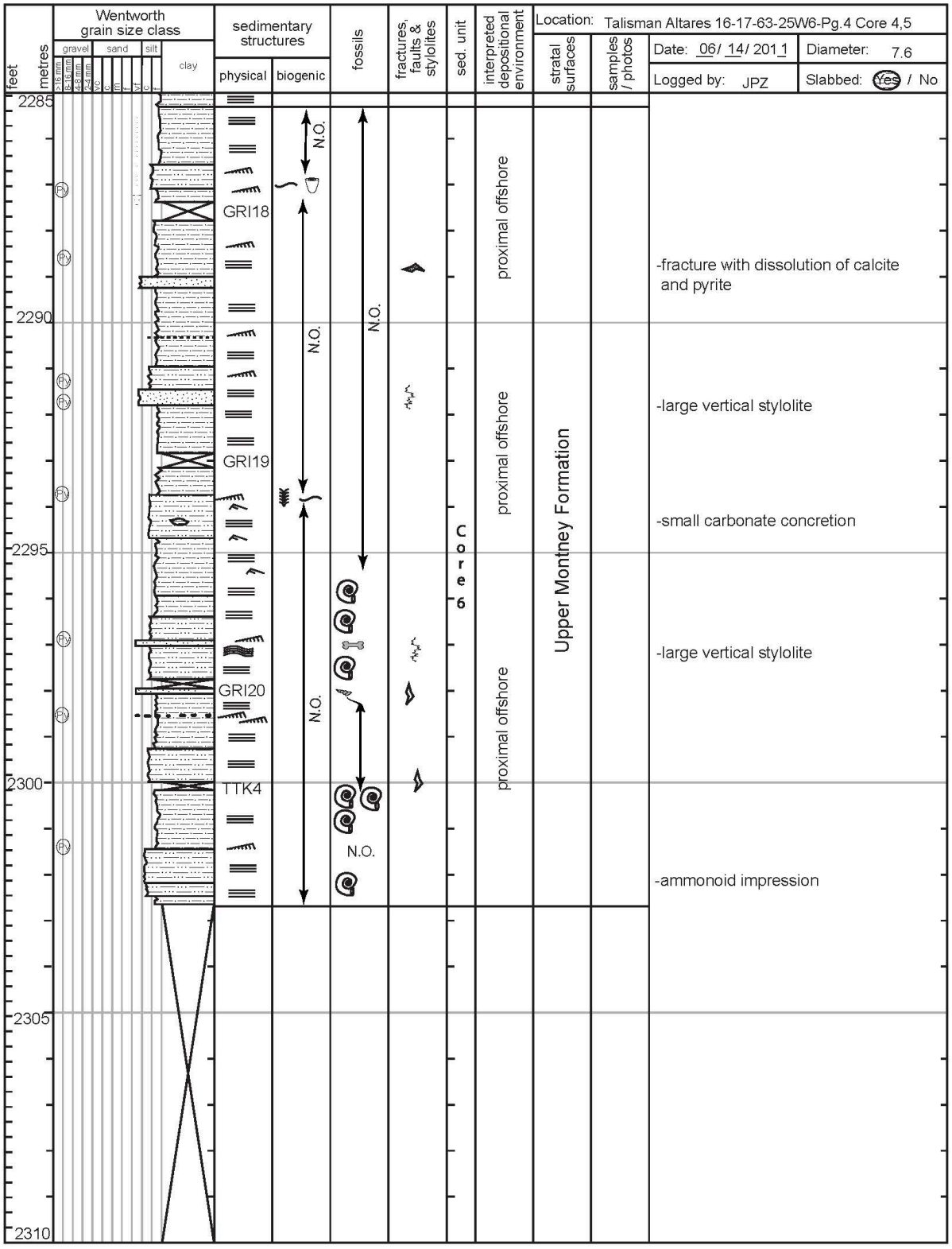
Location: Talisman Altares 16-17-63-25W6-Pg.4 Core 4,5
Date: 06/ 14/ 2011
Diameter: 7.6
Logged by: JPZ
Slabbed: Yes / No
feet
metres
Wentworth grain size class
gravel
sand
silt
clay
>16 mm
2-16 mm
0.5-2 mm
0.25-0.5 mm
0.125-0.25 mm
vc
c
m
f
vf
c
f
sedimentary structures
physical
biogenic
fossils
fractures, faults & stylolites
sed. unit
interpreted depositional environment
stratal surfaces
samples / photos
2285
2290
2295
2300
2305
2310
GRI18
GRI19
GRI20
TTK4
N.O.
N.O.
N.O.
N.O.
N.O.
Core 6
proximal offshore
proximal offshore
proximal offshore
Upper Montney Formation
-fracture with dissolution of calcite and pyrite
-large vertical stylolite
-small carbonate concretion
-large vertical stylolite
-ammonoid impression

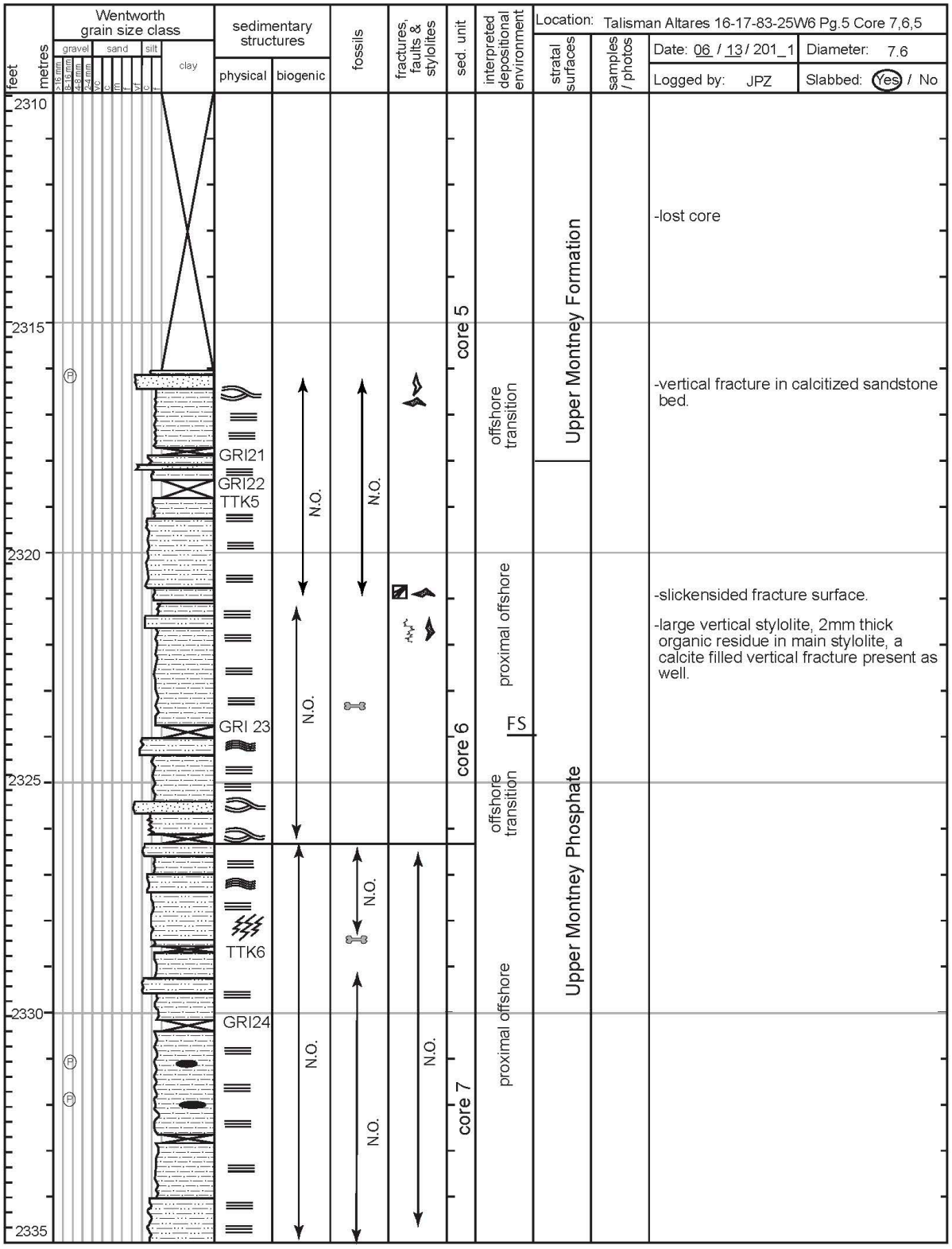
Location: Talisman Altares 16-17-83-25W6 Pg.5 Core 7,6,5
Date: 06 / 13 / 201_1
Diameter: 7.6
Logged by: JPZ
Slabbed: Yes / No
feet
metres
Wentworth grain size class
gravel
sand
silt
clay
sedimentary structures
physical
biogenic
fossils
fractures, faults & stylolites
sed. unit
interpreted depositional environment
strata surfaces
samples / photos
2310
2315
2320
2325
2330
2335
GRI21
GRI22
TTK5
GRI 23
TTK6
GRI24
N.O.
core 5
core 6
core 7
offshore transition
proximal offshore
FS
Upper Montney Formation
Upper Montney Phosphate
-lost core
-vertical fracture in calcitized sandstone bed.
-slickensided fracture surface.
-large vertical stylolite, 2mm thick organic residue in main stylolite, a calcite filled vertical fracture present as well.

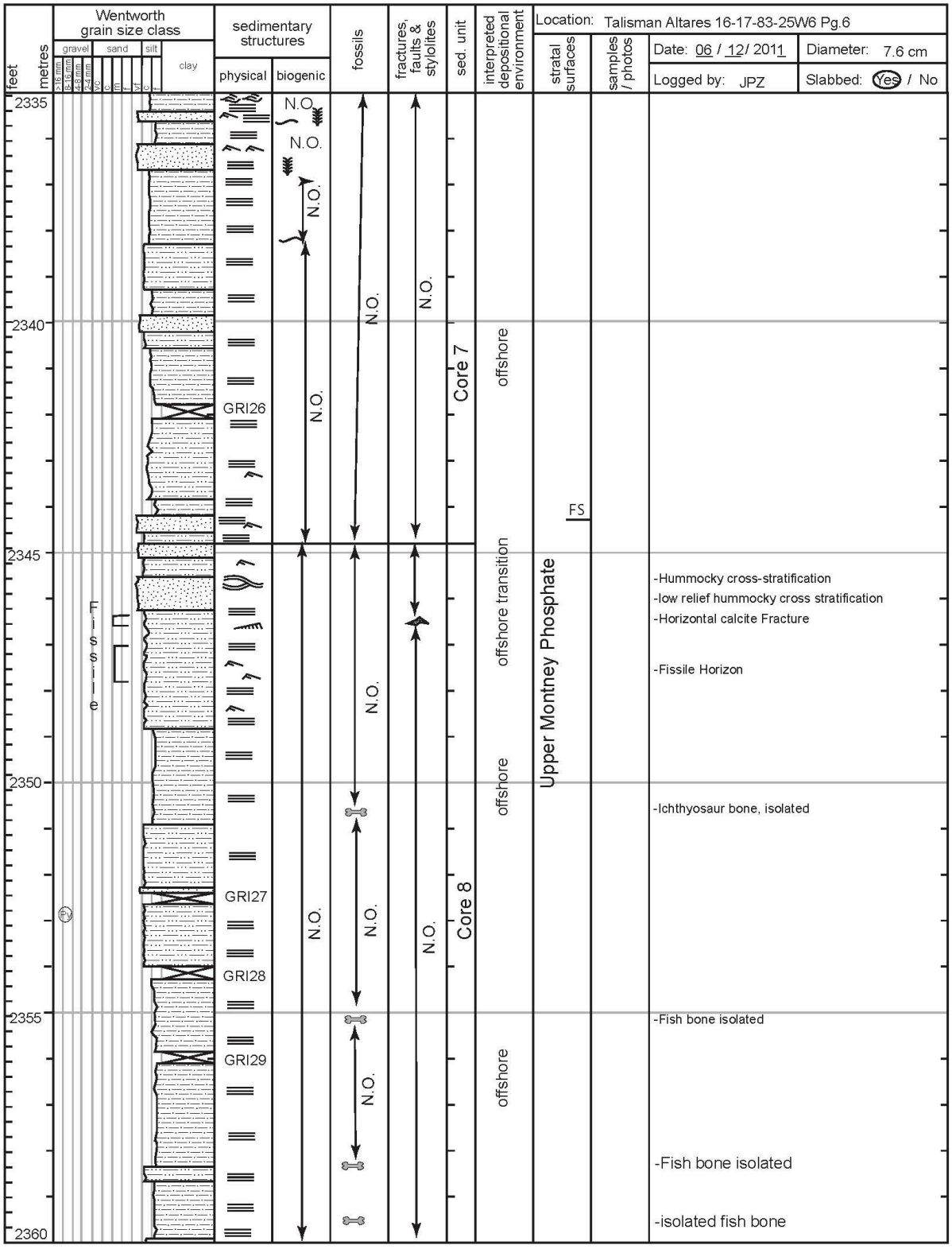
Location: Talisman Altares 16-17-83-25W6 Pg.6
Date: 06 / 12 / 2011
Diameter: 7.6 cm
Logged by: JPZ
Slabbed: Yes / No
feet
metres
Wentworth grain size class
gravel
sand
silt
clay
>16 mm
2-16 mm
0.5-2 mm
0.25-0.5 mm
<0.25 mm
vc
c
m
f
vf
c
f
sedimentary structures
physical
biogenic
fossils
fractures, faults & stylolites
sed. unit
interpreted depositional environment
stratal surfaces
samples / photos
2335
2340
2345
2350
2355
2360
N.O.
GRI26
GRI27
GRI28
GRI29
Core 7
Core 8
offshore
offshore transition
offshore
offshore
FS
Upper Montney Phosphate
-Hummocky cross-stratification
-low relief hummocky cross stratification
-Horizontal calcite Fracture
-Fissile Horizon
-Ichthyosaur bone, isolated
-Fish bone isolated
-Fish bone isolated
-isolated fish bone

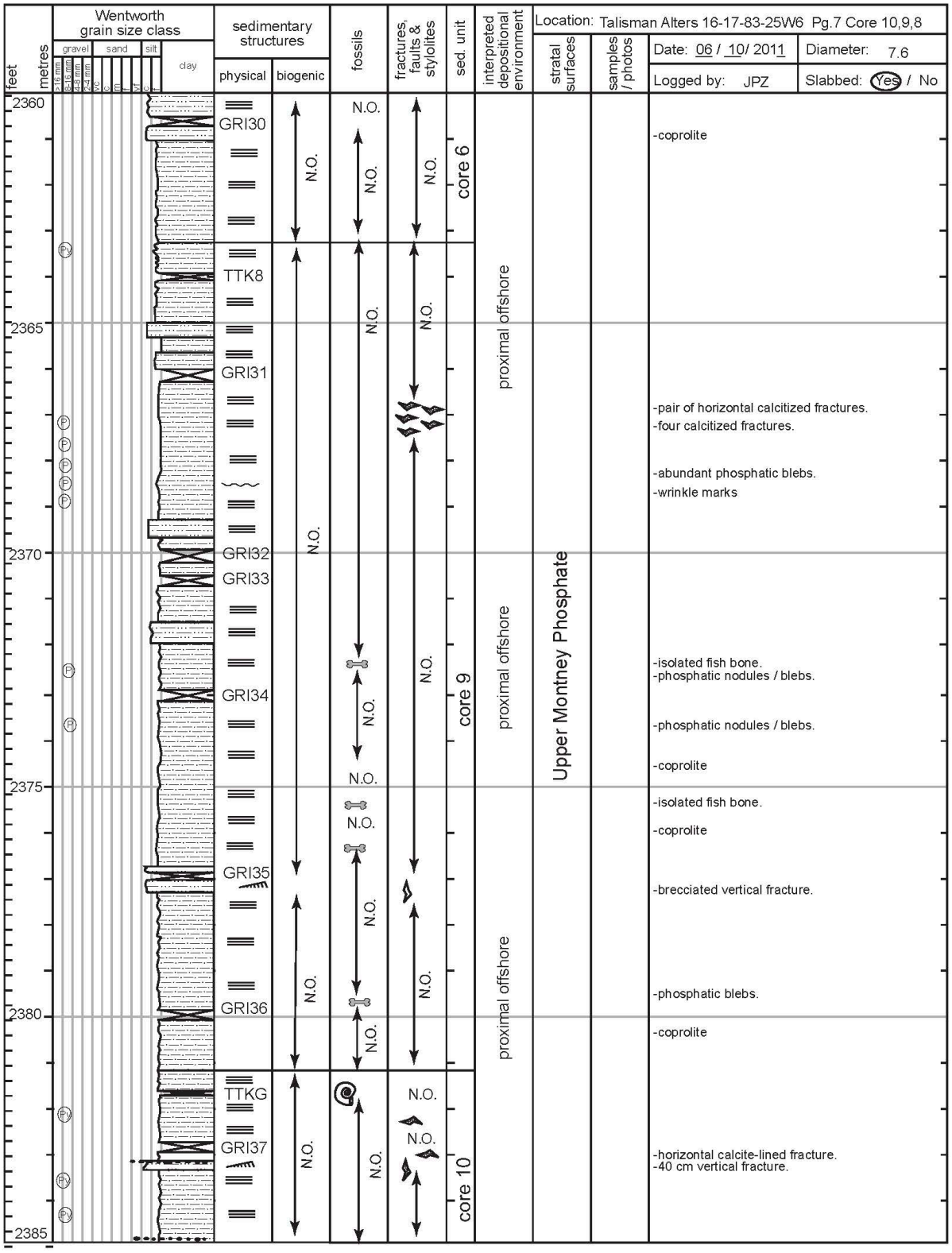
Location: Talisman Alters 16-17-83-25W6 Pg.7 Core 10,9,8
Date: 06 / 10/ 2011
Diameter: 7.6
Logged by: JPZ
Slabbed: Yes / No
feet
metres
Wentworth grain size class
gravel
sand
silt
clay
sedimentary structures
physical
biogenic
fossils
fractures, faults & stylolites
sed. unit
interpreted depositional environment
stratal surfaces
samples / photos
2360
2365
2370
2375
2380
2385
GRI30
TTK8
GRI31
GRI32
GRI33
GRI34
GRI35
GRI36
TTKG
GRI37
N.O.
core 6
core 9
core 10
proximal offshore
Upper Montney Phosphate
-coprolite
-pair of horizontal calcitized fractures.
-four calcitized fractures.
-abundant phosphatic blebs.
-wrinkle marks
-isolated fish bone.
-phosphatic nodules / blebs.
-phosphatic nodules / blebs.
-coprolite
-isolated fish bone.
-coprolite
-brecciated vertical fracture.
-phosphatic blebs.
-coprolite
-horizontal calcite-lined fracture.
-40 cm vertical fracture.

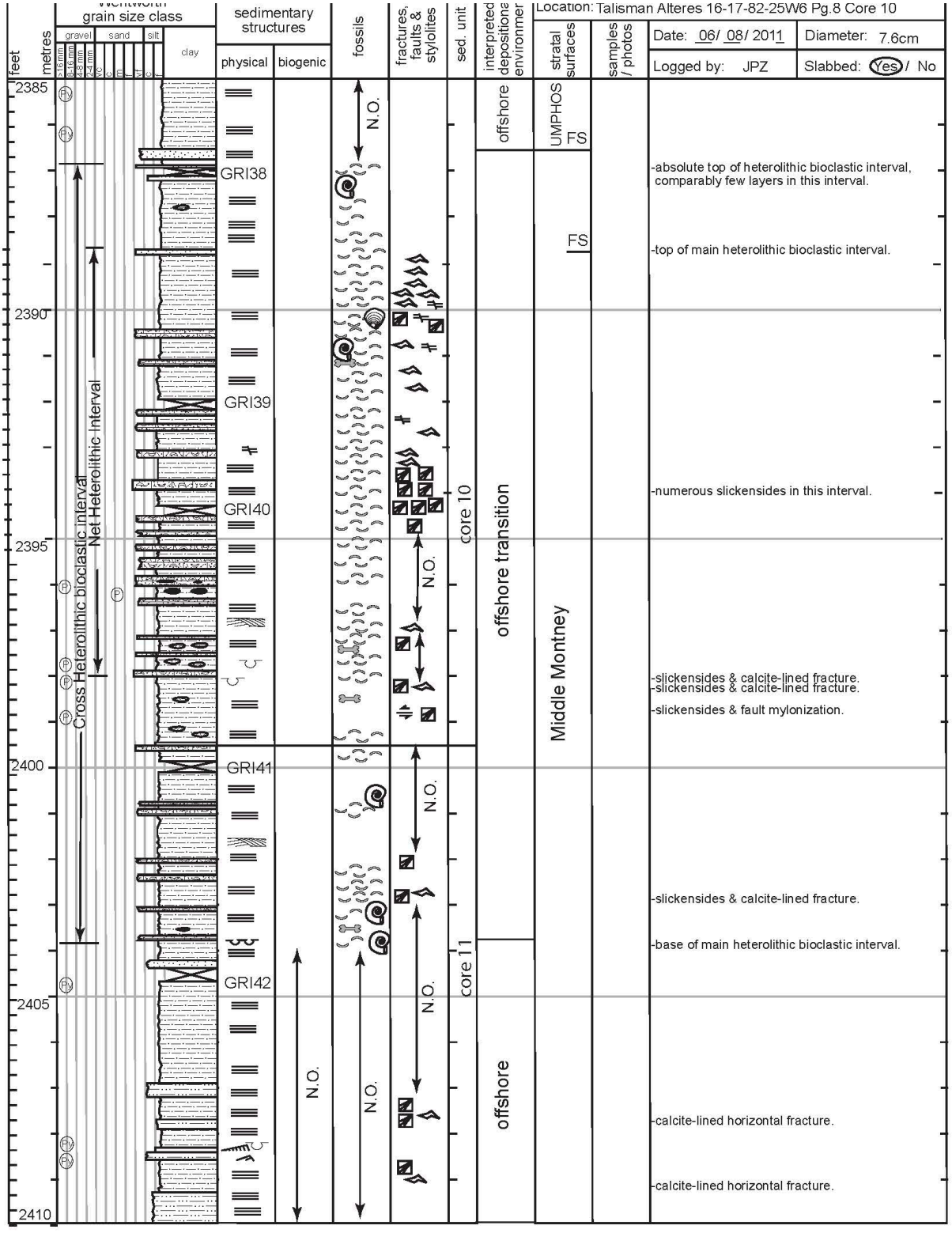
Location: Talisman Alteres 16-17-82-25W6 Pg.8 Core 10
Date: 06/ 08/ 2011
Diameter: 7.6cm
Logged by: JPZ
Slabbed: Yes / No
feet
metres
Wentworth grain size class
gravel
sand
silt
clay
sedimentary structures
physical
biogenic
fossils
fractures, faults & stylolites
sed. unit
interpreted depositional environment
stratal surfaces
samples / photos
2385
2390
2395
2400
2405
2410
GRI38
GRI39
GRI40
GRI41
GRI42
Net Heterolithic Interval
Cross Heterolithic bioclastic interval
N.O.
core 10
core 11
offshore
offshore transition
offshore
UMPHOS
FS
FS
Middle Montney
-absolute top of heterolithic bioclastic interval, comparably few layers in this interval.
-top of main heterolithic bioclastic interval.
-numerous slickensides in this interval.
-slickensides & calcite-lined fracture.
-slickensides & calcite-lined fracture.
-slickensides & fault mylonization.
-slickensides & calcite-lined fracture.
-base of main heterolithic bioclastic interval.
-calcite-lined horizontal fracture.
-calcite-lined horizontal fracture.

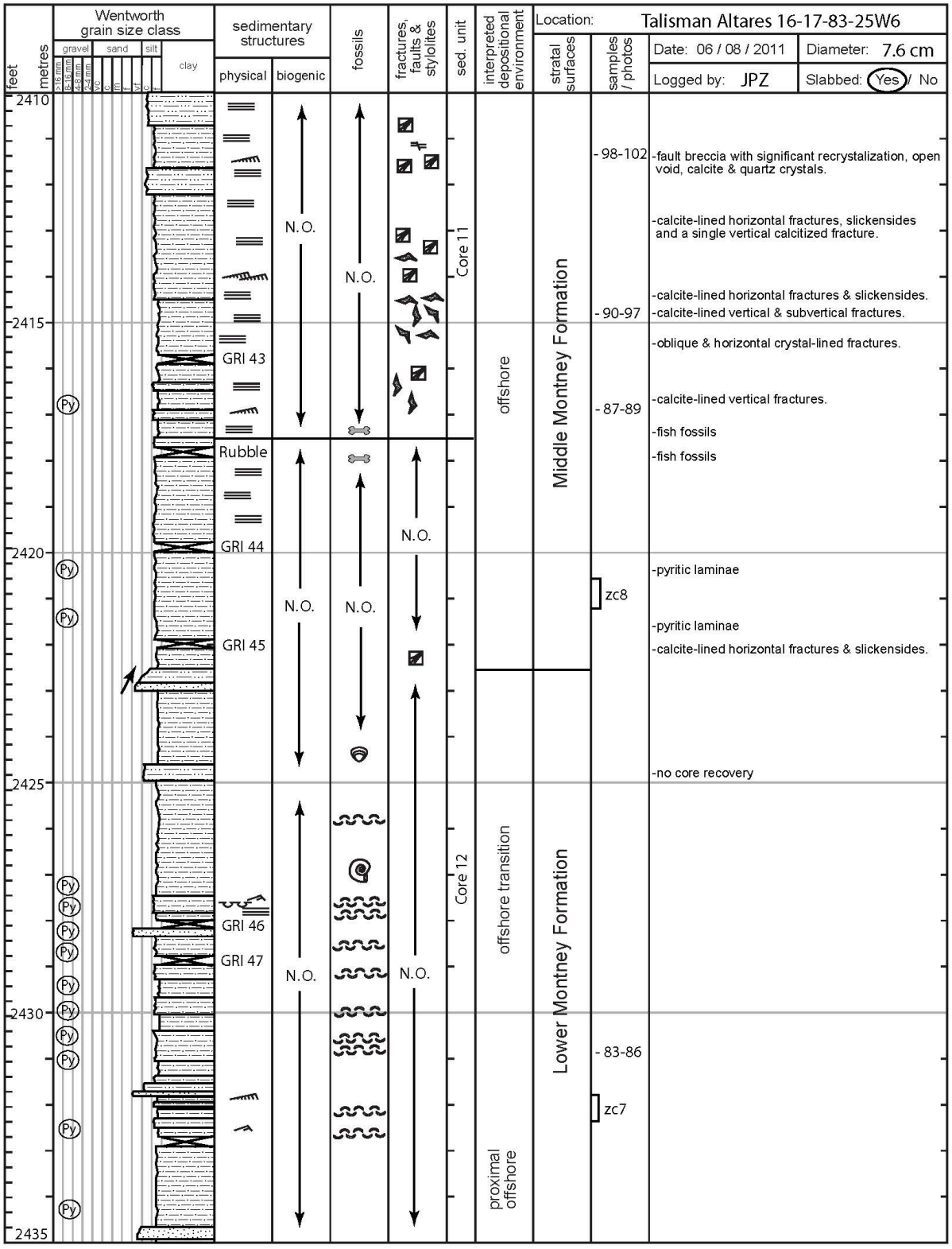
Location: Talisman Altares 16-17-83-25W6
Date: 06 / 08 / 2011
Diameter: 7.6 cm
Logged by: JPZ
Slabbed: Yes / No
feet
metres
Wentworth grain size class
gravel
sand
silt
clay
sedimentary structures
physical
biogenic
fossils
fractures, faults & stylolites
sed. unit
interpreted depositional environment
stratal surfaces
samples / photos
2410
2415
2420
2425
2430
2435
GRI 43
Rubble
GRI 44
GRI 45
GRI 46
GRI 47
N.O.
Py
Core 11
Core 12
offshore
offshore transition
proximal offshore
Middle Montney Formation
Lower Montney Formation
- 98-102
- 90-97
- 87-89
- 83-86
zc8
zc7
-fault breccia with significant recrystalization, open void, calcite & quartz crystals.
-calcite-lined horizontal fractures, slickensides and a single vertical calcitized fracture.
-calcite-lined horizontal fractures & slickensides.
-calcite-lined vertical & subvertical fractures.
-oblique & horizontal crystal-lined fractures.
-calcite-lined vertical fractures.
-fish fossils
-fish fossils
-pyritic laminae
-pyritic laminae
-calcite-lined horizontal fractures & slickensides.
-no core recovery

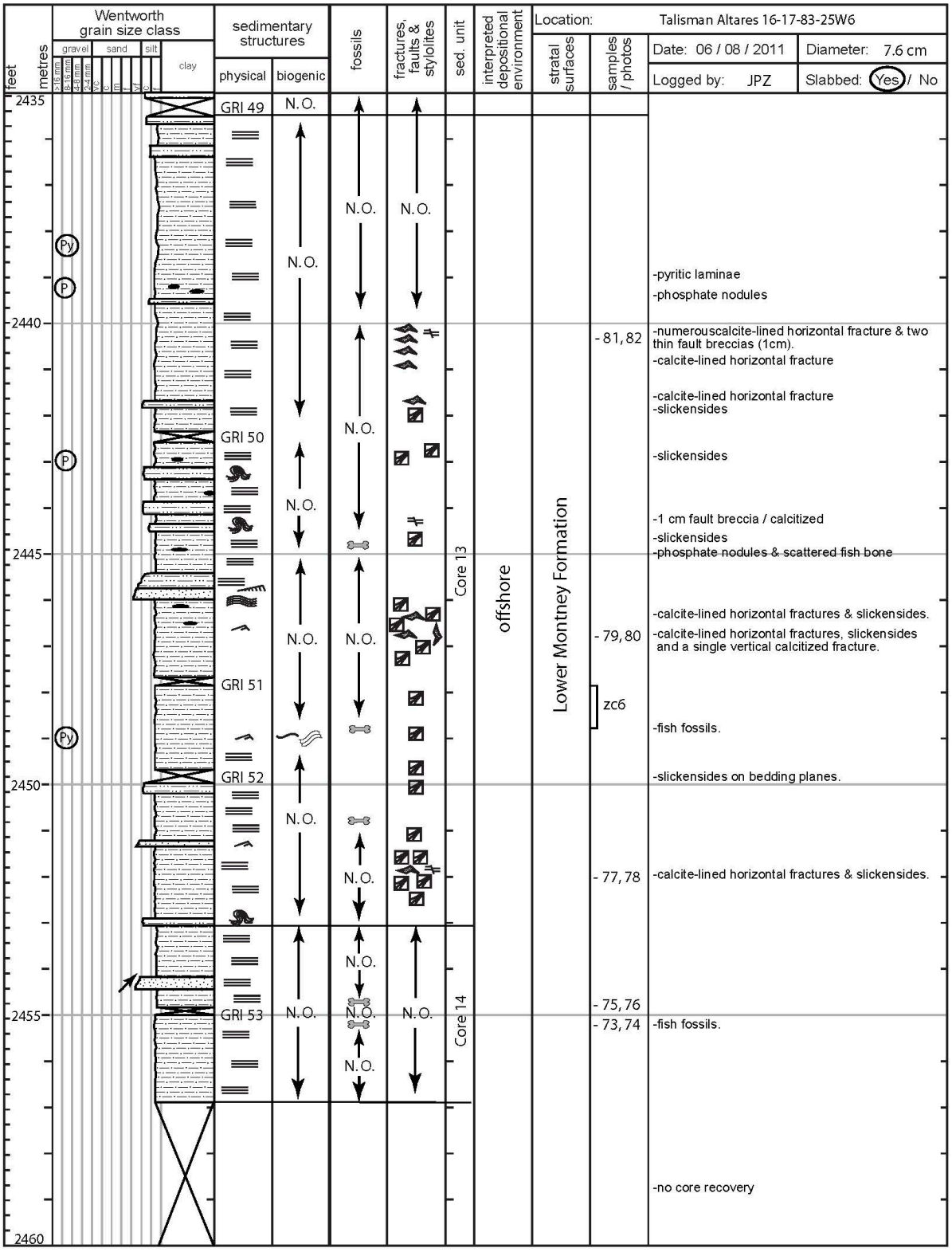
Location: Talisman Altares 16-17-83-25W6
Date: 06 / 08 / 2011
Diameter: 7.6 cm
Logged by: JPZ
Slabbed: Yes / No
feet
metres
Wentworth grain size class
gravel
sand
silt
clay
sedimentary structures
physical
biogenic
fossils
fractures, faults & stylolites
sed. unit
interpreted depositional environment
stratal surfaces
samples / photos
2435
2440
2445
2450
2455
2460
GRI 49
GRI 50
GRI 51
GRI 52
GRI 53
N.O.
Py
P
Core 13
Core 14
offshore
Lower Montney Formation
- 81, 82
- 79, 80
zc6
- 77, 78
- 75, 76
- 73, 74
-pyritic laminae
-phosphate nodules
-numerouscalcite-lined horizontal fracture & two thin fault breccias (1cm).
-calcite-lined horizontal fracture
-calcite-lined horizontal fracture
-slickensides
-slickensides
-1 cm fault breccia / calcitized
-slickensides
-phosphate nodules & scattered fish bone
-calcite-lined horizontal fractures & slickensides.
-calcite-lined horizontal fractures, slickensides and a single vertical calcitized fracture.
-fish fossils.
-slickensides on bedding planes.
-calcite-lined horizontal fractures & slickensides.
-fish fossils.
-no core recovery

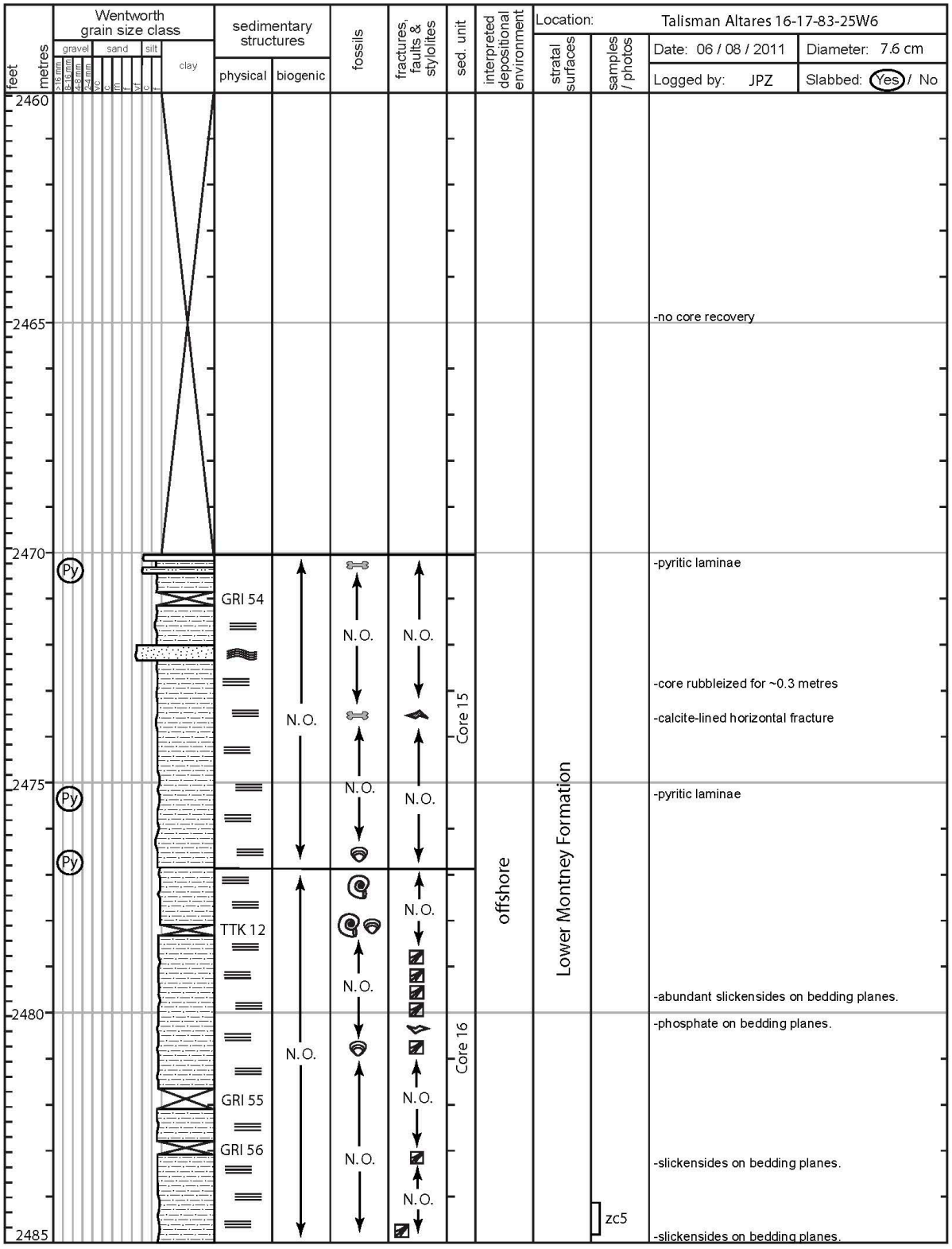
feet
metres
Wentworth grain size class
gravel
sand
silt
clay
>16 mm
2-16 mm
0.5-2 mm
0.25-0.5 mm
<0.25 mm
vc
c
m
f
vf
c
f
sedimentary structures
physical
biogenic
fossils
fractures, faults & stylolites
sed. unit
interpreted depositional environment
Location: Talisman Altares 16-17-83-25W6
stratal surfaces
samples / photos
Date: 06 / 08 / 2011
Diameter: 7.6 cm
Logged by: JPZ
Slabbed: Yes / No
2460
2465
2470
2475
2480
2485
Py
Py
Py
GRI 54
TTK 12
GRI 55
GRI 56
N.O.
N.O.
N.O.
N.O.
N.O.
N.O.
N.O.
N.O.
N.O.
Core 15
Core 16
offshore
Lower Montney Formation
zc5
-no core recovery
-pyritic laminae
-core rubbleized for ~0.3 metres
-calcite-lined horizontal fracture
-pyritic laminae
-abundant slickensides on bedding planes.
-phosphate on bedding planes.
-slickensides on bedding planes.
-slickensides on bedding planes.

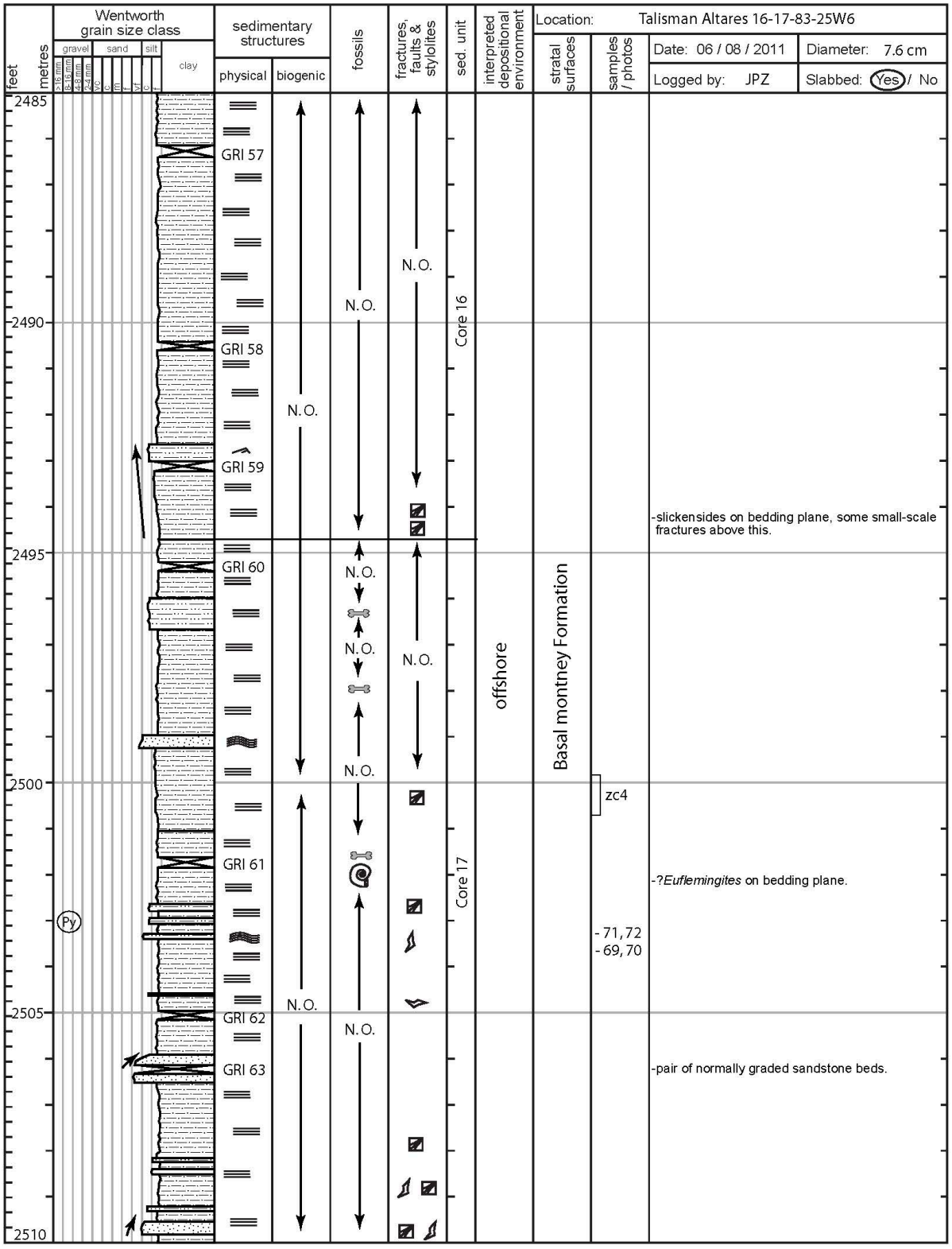
feet
metres
Wentworth grain size class
gravel
sand
silt
clay
>16 mm
2-16 mm
0.25-2 mm
0.4-0.25 mm
vc
c
m
f
vf
c
f
sedimentary structures
physical
biogenic
fossils
fractures, faults & stylolites
sed. unit
interpreted depositional environment
Location: Talisman Altares 16-17-83-25W6
stratal surfaces
samples / photos
Date: 06 / 08 / 2011
Diameter: 7.6 cm
Logged by: JPZ
Slabbed: Yes / No
2485
2490
2495
2500
2505
2510
GRI 57
GRI 58
GRI 59
GRI 60
GRI 61
GRI 62
GRI 63
N.O.
Core 16
Core 17
offshore
Basal montney Formation
Py
zc4
- 71, 72
- 69, 70
-slickensides on bedding plane, some small-scale fractures above this.
-?Euflemingites on bedding plane.
-pair of normally graded sandstone beds.

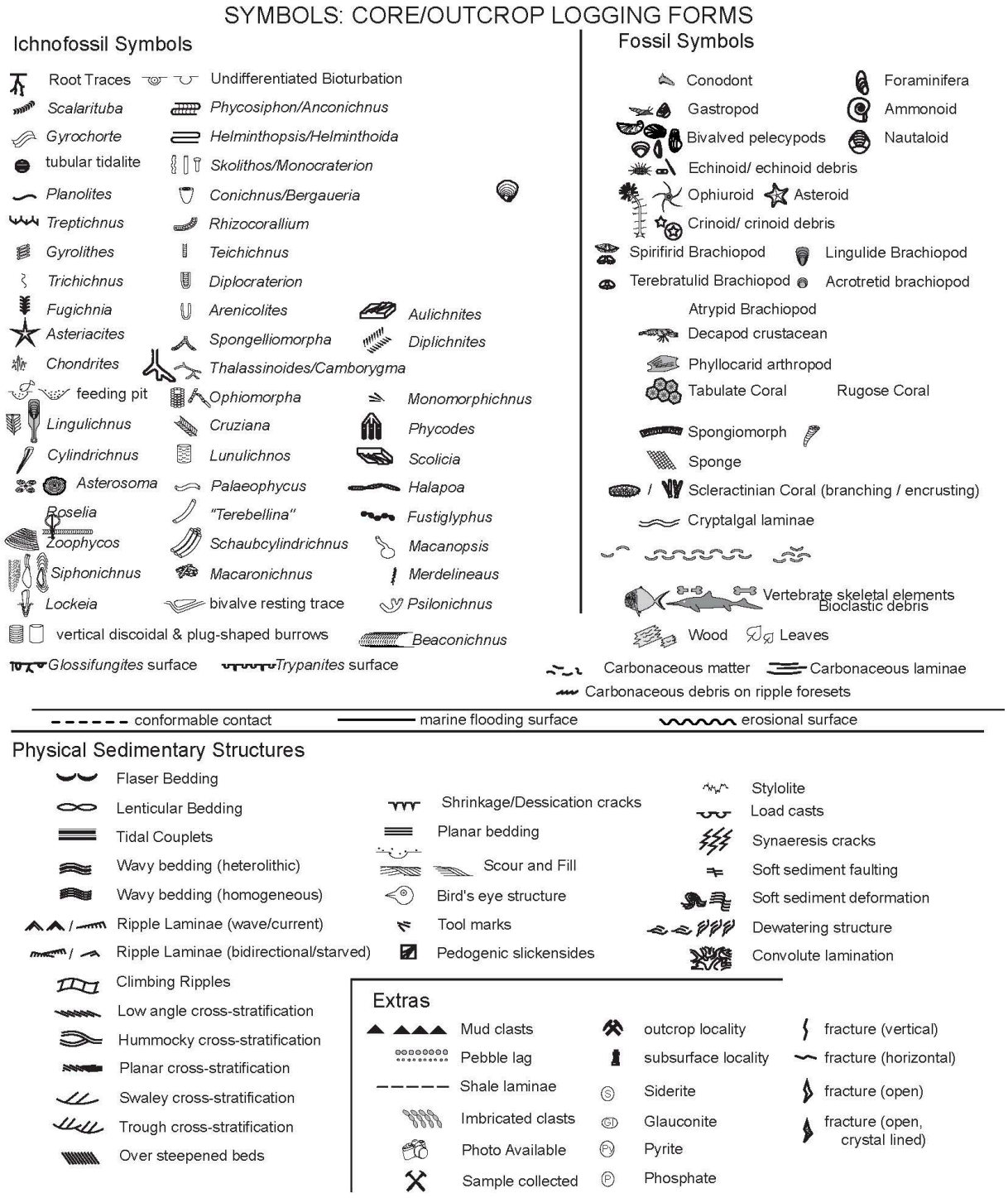

Figure S26: Lithologue for well 16-17-083-25W6. See legend for explanation of symbols used.

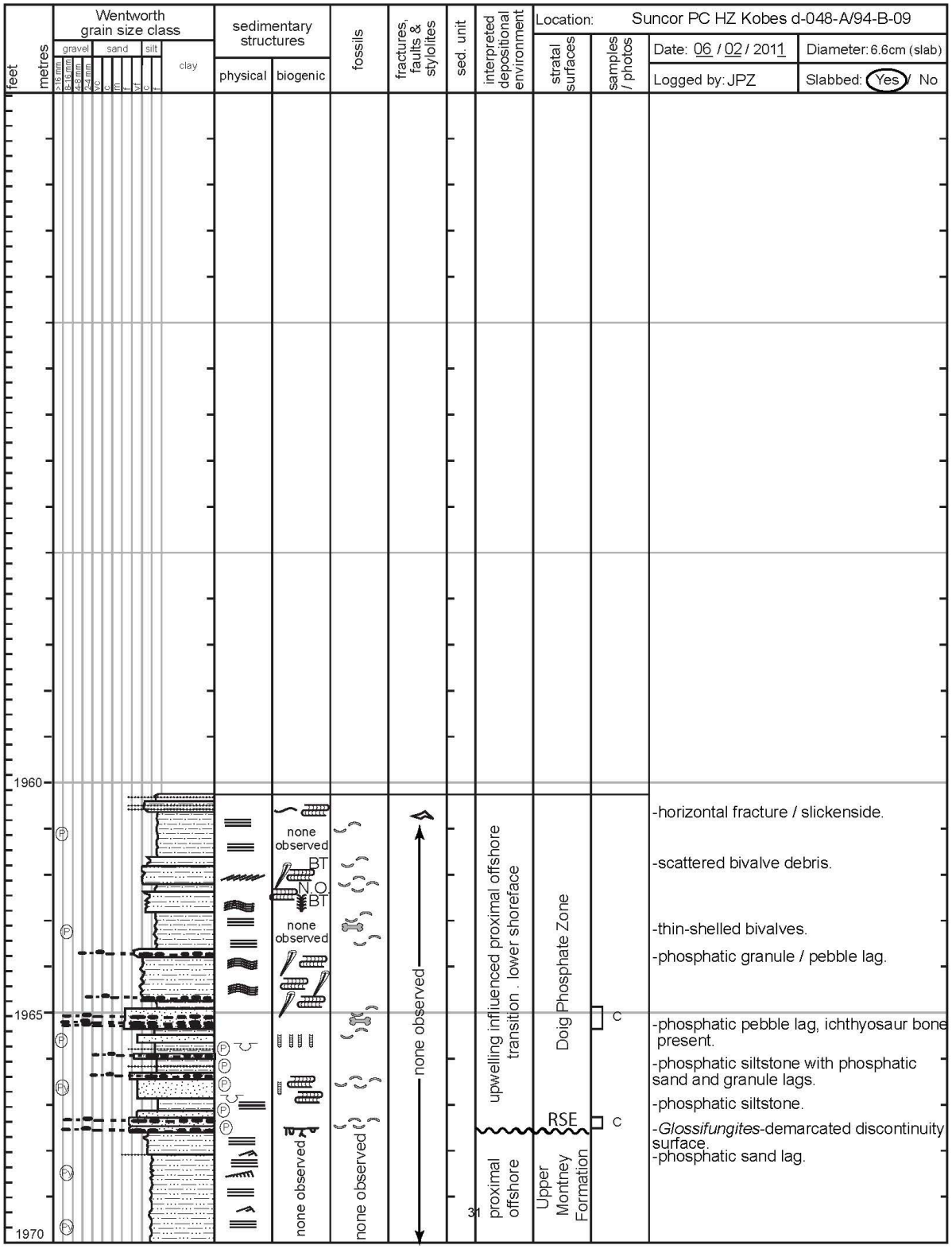
feet
metres
Wentworth grain size class
gravel
sand
silt
clay
>16 mm
2-16 mm
0.5-2 mm
0.25-0.5 mm
<0.25 mm
vc
c
m
f
vf
c
f
sedimentary structures
physical
biogenic
fossils
fractures, faults & stylolites
sed. unit
interpreted depositional environment
Location: Suncor PC HZ Kobes d-048-A/94-B-09
stratal surfaces
samples / photos
Date: 06 / 02 / 2011
Diameter: 6.6cm (slab)
Logged by: JPZ
Slabbed: Yes / No
1960
1965
1970
none observed
BT
N.O
BT
none observed
none observed
none observed
none observed
upwelling influenced proximal offshore transition . lower shoreface
proximal offshore
Doig Phosphate Zone
Upper Montney Formation
RSE
C
C
-horizontal fracture / slickenside.
-scattered bivalve debris.
-thin-shelled bivalves.
-phosphatic granule / pebble lag.
-phosphatic pebble lag, ichthyosaur bone present.
-phosphatic siltstone with phosphatic sand and granule lags.
-phosphatic siltstone.
-Glossifungites-demarcated discontinuity surface.
-phosphatic sand lag.

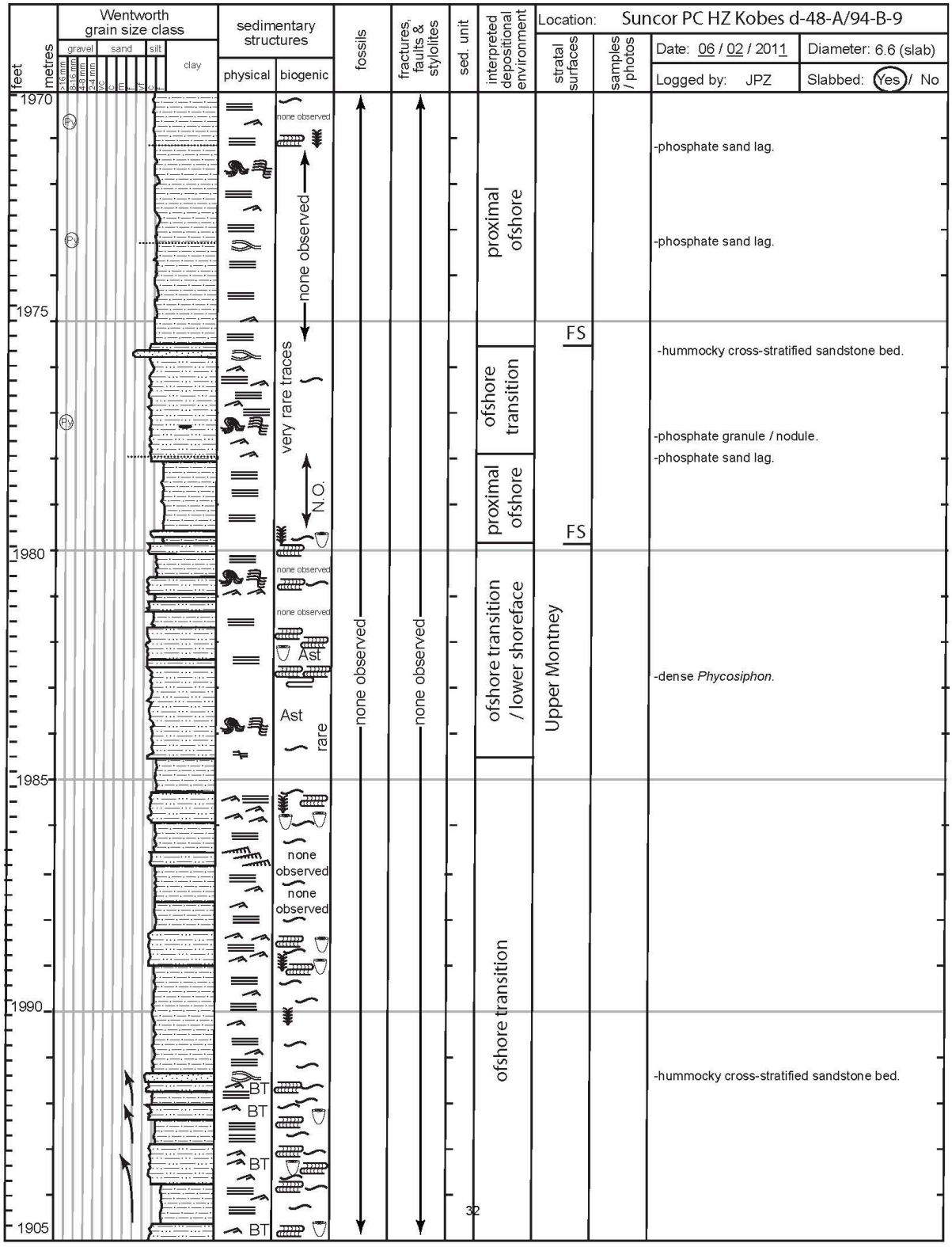
Location: Suncor PC HZ Kobes d-48-A/94-B-9
Date: 06 / 02 / 2011
Diameter: 6.6 (slab)
Logged by: JPZ
Slabbed: (Yes) / No
feet
metres
Wentworth grain size class
gravel
sand
silt
clay
>16 mm
8-16 mm
4-8 mm
2-4 mm
vc
c
m
f
vf
c
f
sedimentary structures
physical
biogenic
fossils
fractures, faults & stylolites
sed. unit
interpreted depositional environment
stratal surfaces
samples / photos
1970
1975
1980
1985
1990
1905
none observed
very rare traces
N.O.
Ast
rare
BT
proximal ofshore
ofshore transition
ofshore transition / lower shoreface
Upper Montney
FS
-phosphate sand lag.
-phosphate sand lag.
-hummocky cross-stratified sandstone bed.
-phosphate granule / nodule.
-phosphate sand lag.
-dense Phycosiphon.
-hummocky cross-stratified sandstone bed.
32

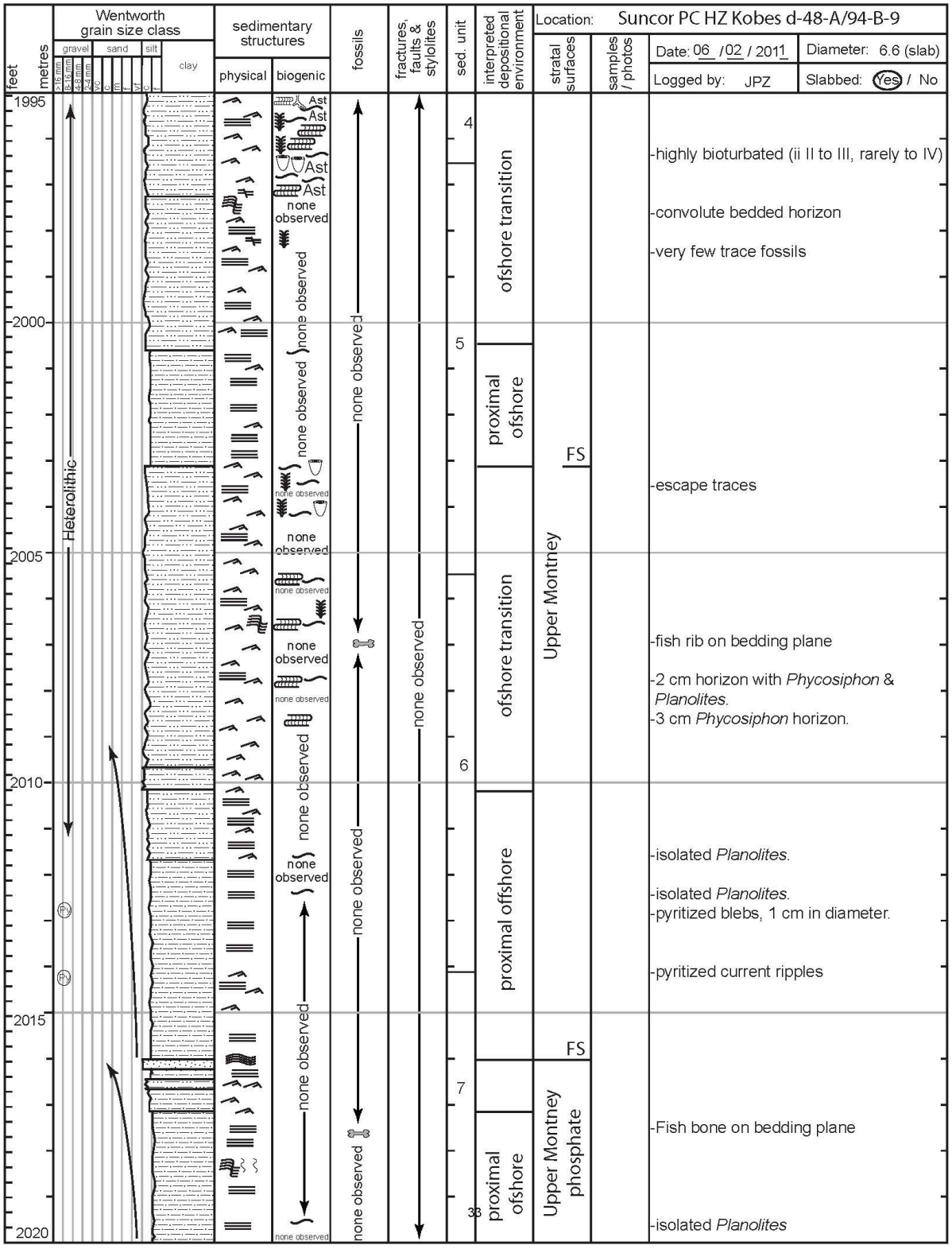
Location: Suncor PC HZ Kobes d-48-A/94-B-9
Date: 06 / 02 / 2011
Diameter: 6.6 (slab)
Logged by: JPZ
Slabbed: Yes / No
feet
metres
Wentworth grain size class
gravel
sand
silt
clay
sedimentary structures
physical
biogenic
fossils
fractures, faults & stylolites
sed. unit
interpreted depositional environment
stratal surfaces
samples / photos
1995
2000
2005
2010
2015
2020
Heterolithic
Ast
none observed
FS
Upper Montney
Upper Montney phosphate
ofshore transition
proximal ofshore
proximal offshore
4
5
6
7
38
-highly bioturbated (ii II to III, rarely to IV)
-convolute bedded horizon
-very few trace fossils
-escape traces
-fish rib on bedding plane
-2 cm horizon with Phycosiphon & Planolites.
-3 cm Phycosiphon horizon.
-isolated Planolites.
-isolated Planolites.
-pyritized blebs, 1 cm in diameter.
-pyritized current ripples
-Fish bone on bedding plane
-isolated Planolites

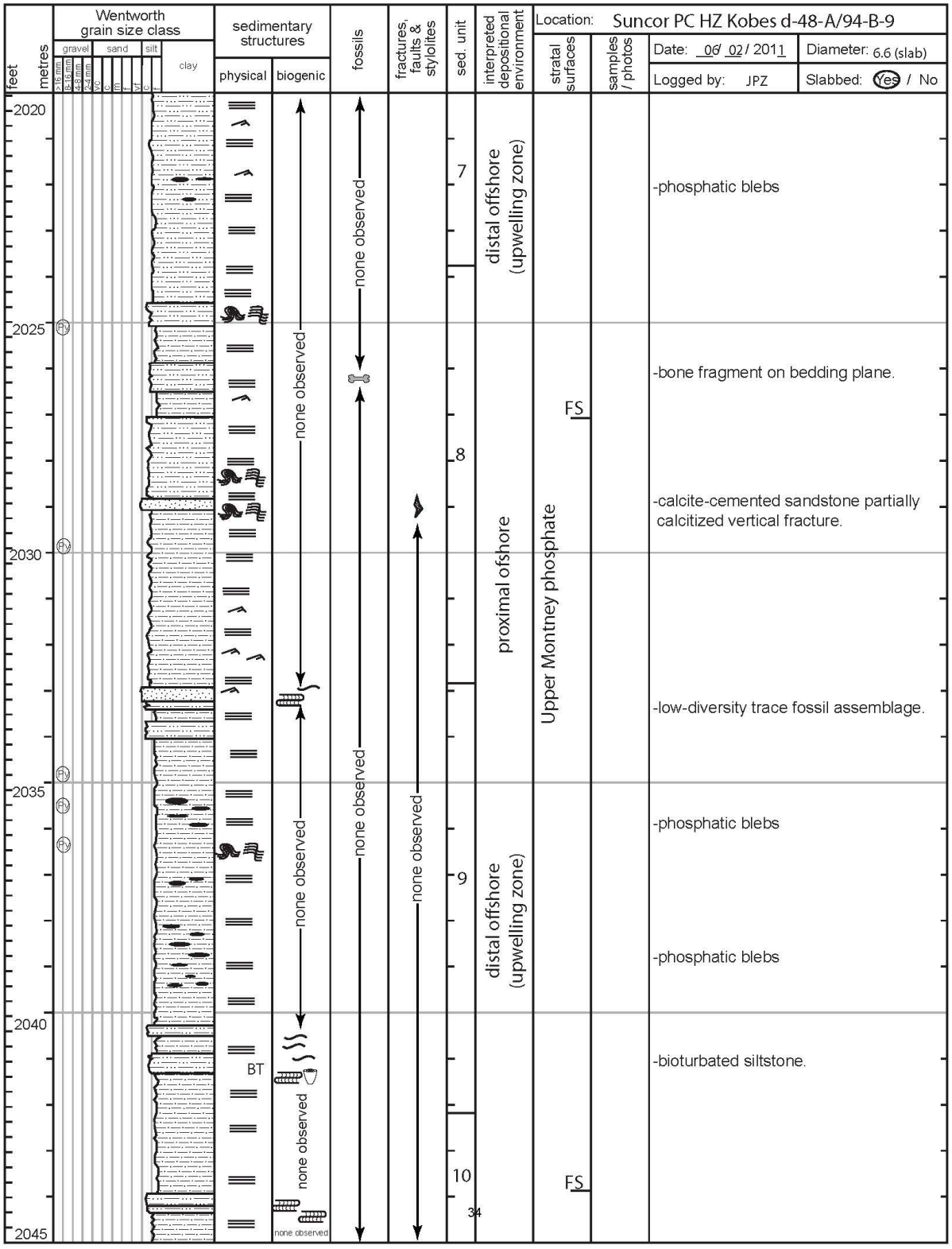
Location: Suncor PC HZ Kobes d-48-A/94-B-9
Date: 06/ 02/ 2011
Diameter: 6.6 (slab)
Logged by: JPZ
Slabbed: Yes / No
feet
metres
Wentworth grain size class
gravel
sand
silt
clay
sedimentary structures
physical
biogenic
fossils
fractures, faults & stylolites
sed. unit
interpreted depositional environment
stratal surfaces
samples / photos
2020
2025
2030
2035
2040
2045
none observed
distal offshore (upwelling zone)
proximal ofshore
Upper Montney phosphate
FS
BT
7
8
9
10
-phosphatic blebs
-bone fragment on bedding plane.
-calcite-cemented sandstone partially calcitized vertical fracture.
-low-diversity trace fossil assemblage.
-phosphatic blebs
-phosphatic blebs
-bioturbated siltstone.
34

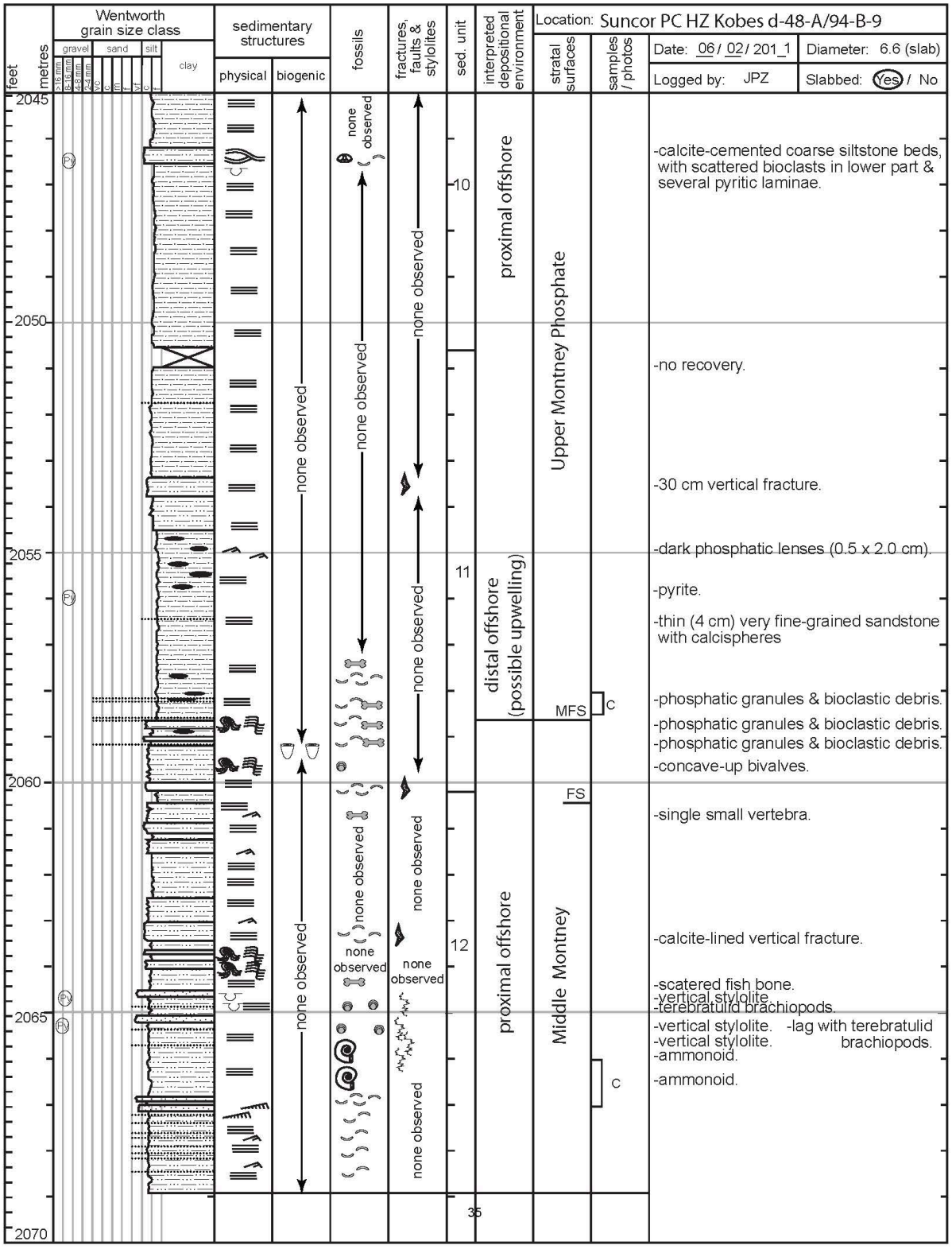
Location: Suncor PC HZ Kobes d-48-A/94-B-9
Date: 06/02/201_1
Diameter: 6.6 (slab)
Logged by: JPZ
Slabbed: Yes / No
feet
metres
Wentworth grain size class
gravel
sand
silt
clay
sedimentary structures
physical
biogenic
fossils
fractures, faults & stylolites
sed. unit
interpreted depositional environment
stratal surfaces
samples / photos
2045
2050
2055
2060
2065
2070
none observed
proximal offshore
distal offshore (possible upwelling)
Upper Montney Phosphate
Middle Montney
MFS
FS
10
11
12
35
-calcite-cemented coarse siltstone beds, with scattered bioclasts in lower part & several pyritic laminae.
-no recovery.
-30 cm vertical fracture.
-dark phosphatic lenses (0.5 x 2.0 cm).
-pyrite.
-thin (4 cm) very fine-grained sandstone with calcispheres
-phosphatic granules & bioclastic debris.
-phosphatic granules & bioclastic debris.
-phosphatic granules & bioclastic debris.
-concave-up bivalves.
-single small vertebra.
-calcite-lined vertical fracture.
-scatered fish bone.
-vertical stylolite.
-terebratulid brachiopods.
-vertical stylolite. -lag with terebratulid brachiopods.
-vertical stylolite.
-ammonoid.
-ammonoid.
C

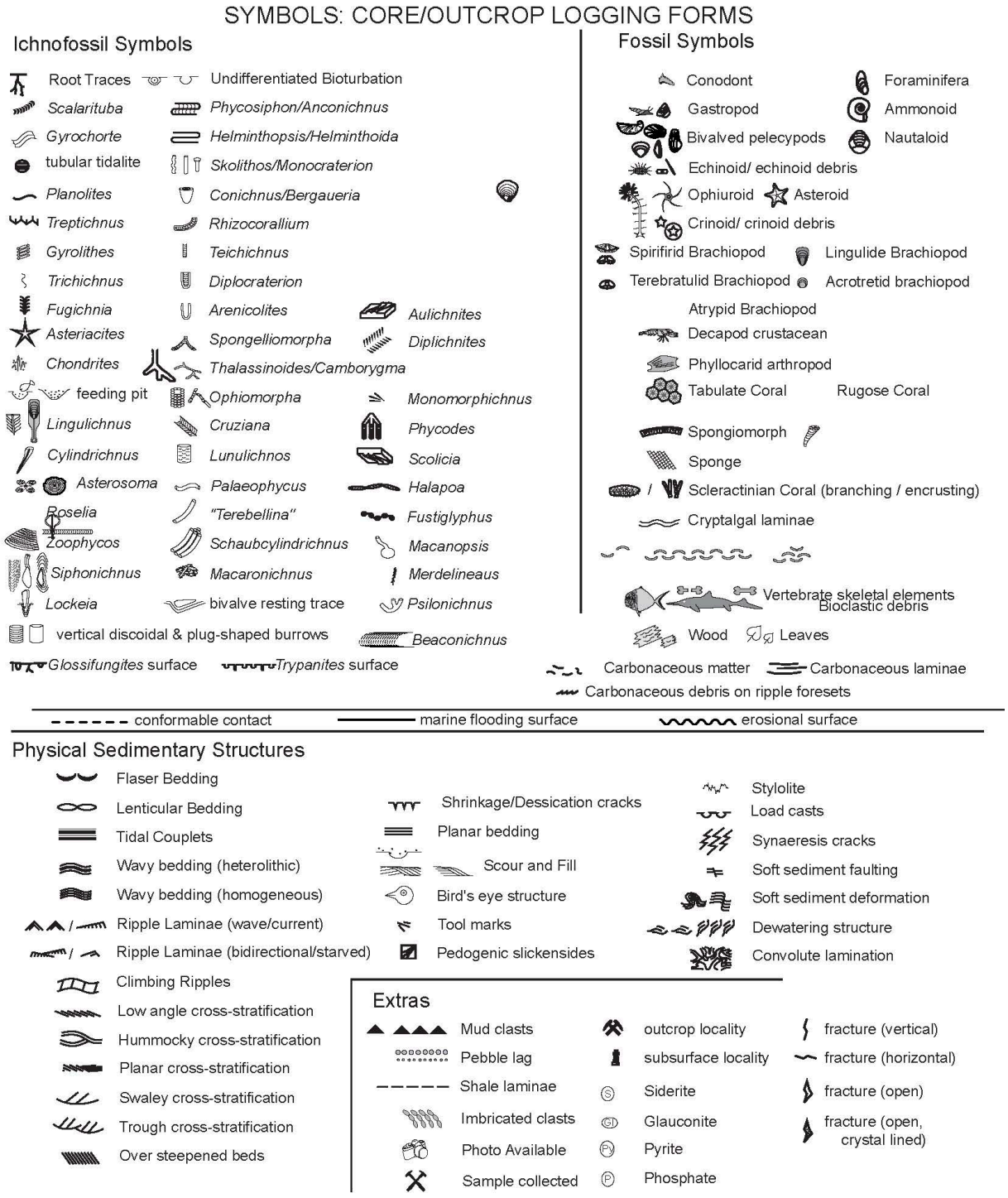

Figure S27: Lithologue for well d-48-A/94-B-9. See legend for explanation of symbols used.

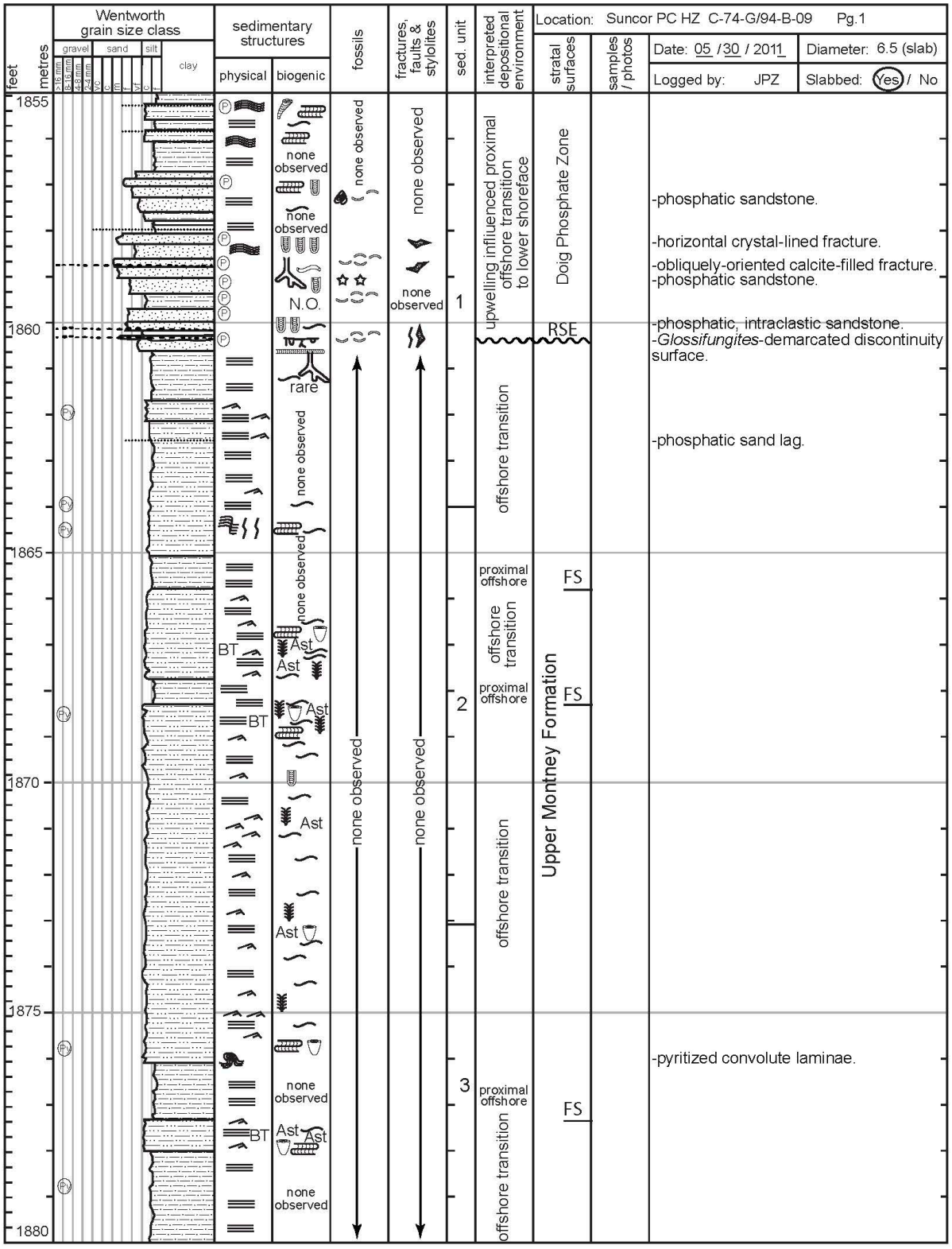
Location: Suncor PC HZ C-74-G/94-B-09 Pg.1
Date: 05 / 30 / 2011
Logged by: JPZ
Diameter: 6.5 (slab)
Slabbed: Yes / No
feet
metres
Wentworth grain size class
gravel
sand
silt
clay
sedimentary structures
physical
biogenic
fossils
fractures, faults & stylolites
sed. unit
interpreted depositional environment
stratal surfaces
samples / photos
1855
1860
1865
1870
1875
1880
none observed
N.O.
rare
BT
Ast
upwelling influenced proximal offshore transition to lower shoreface
offshore transition
proximal offshore
Doig Phosphate Zone
RSE
FS
Upper Montney Formation
-phosphatic sandstone.
-horizontal crystal-lined fracture.
-obliquely-oriented calcite-filled fracture.
-phosphatic sandstone.
-phosphatic, intraclastic sandstone.
-Glossifungites-demarcated discontinuity surface.
-phosphatic sand lag.
-pyritized convolute laminae.

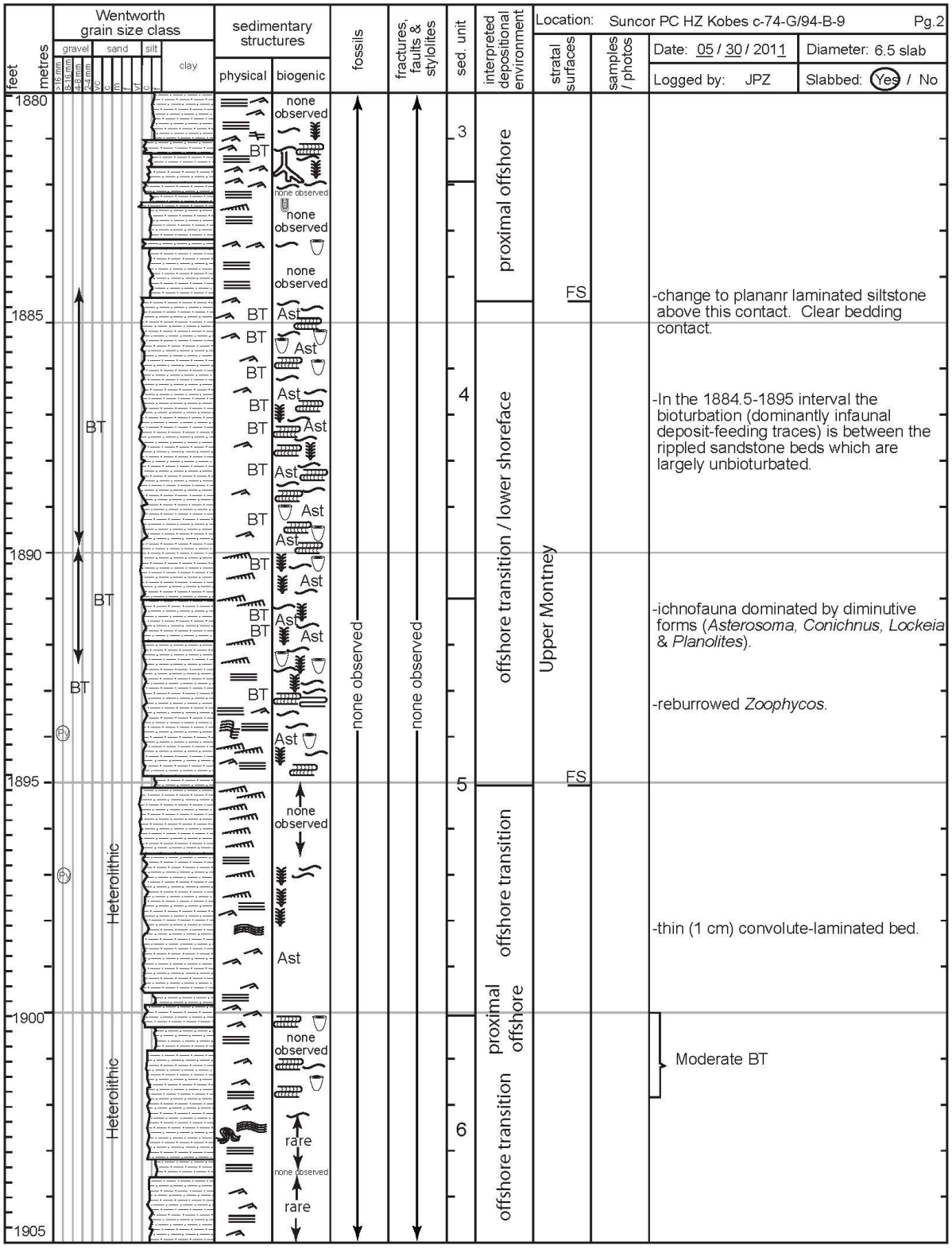
Location: Suncor PC HZ Kobes c-74-G/94-B-9
Pg.2
Date: 05 / 30 / 2011
Diameter: 6.5 slab
Logged by: JPZ
Slabbed: Yes / No
feet
metres
Wentworth grain size class
gravel
sand
silt
clay
sedimentary structures
physical
biogenic
fossils
fractures, faults & stylolites
sed. unit
interpreted depositional environment
stratal surfaces
samples / photos
1880
1885
1890
1895
1900
1905
Heterolithic
Heterolithic
BT
Ast
none observed
rare
FS
Upper Montney
proximal offshore
offshore transition / lower shoreface
offshore transition
proximal offshore
offshore transition
-change to plananr laminated siltstone above this contact. Clear bedding contact.
-In the 1884.5-1895 interval the bioturbation (dominantly infaunal deposit-feeding traces) is between the rippled sandstone beds which are largely unbioturbated.
-ichnofauna dominated by diminutive forms (Asterosoma, Conichnus, Lockeia & Planolites).
-reburrowed Zoophycos.
-thin (1 cm) convolute-laminated bed.
Moderate BT

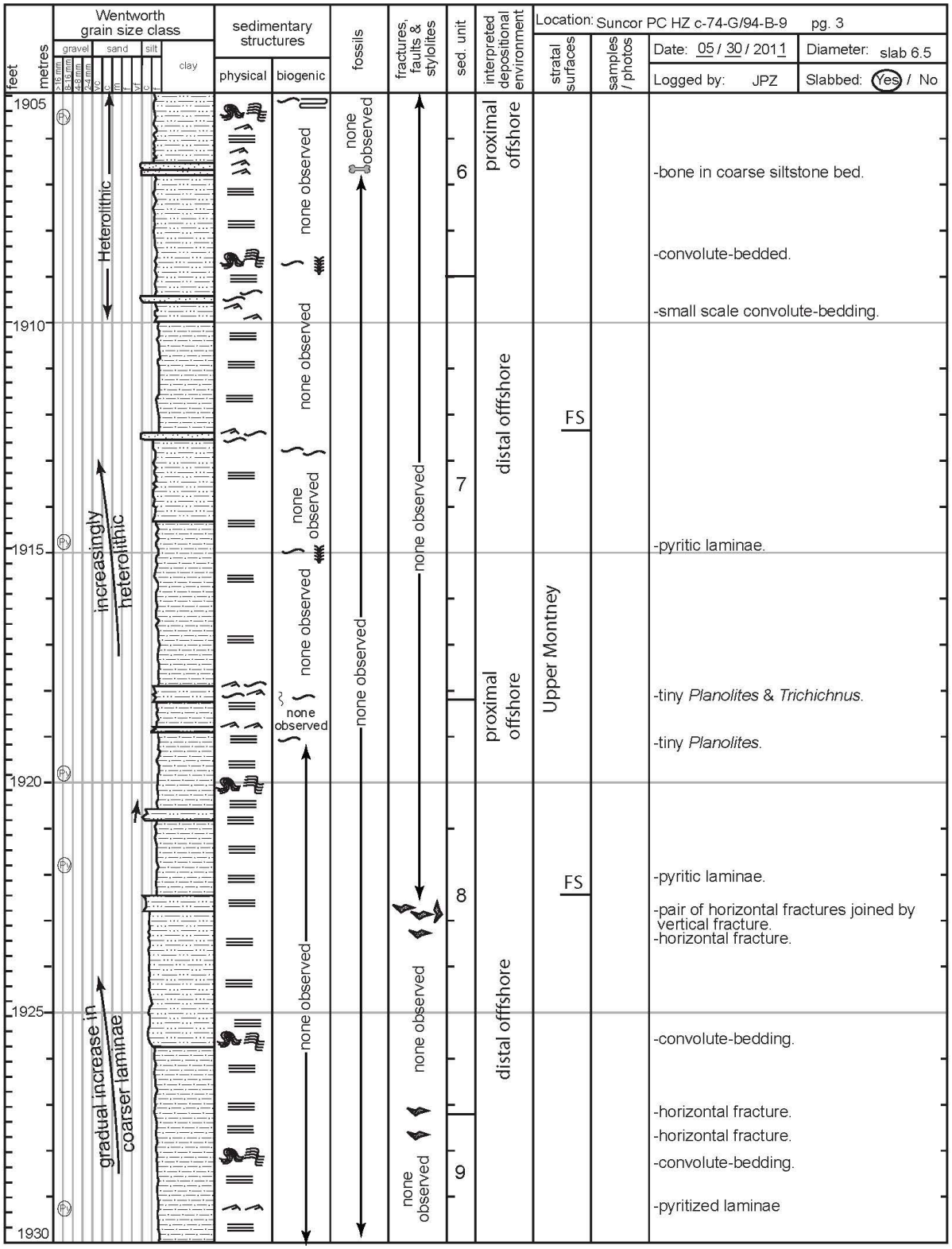
feet
metres
Wentworth grain size class
gravel
sand
silt
clay
>16 mm
2-16 mm
0.5-2 mm
0.25-0.5 mm
<0.25 mm
vc
c
m
f
vf
c
f
sedimentary structures
physical
biogenic
fossils
fractures, faults & stylolites
sed. unit
interpreted depositional environment
Location: Suncor PC HZ c-74-G/94-B-9 pg. 3
Date: 05 / 30 / 2011
Logged by: JPZ
Diameter: slab 6.5
Slabbed: Yes / No
stratal surfaces
samples / photos
1905
1910
1915
1920
1925
1930
Heterolithic
increasingly heterolithic
gradual increase in coarser laminae
none observed
6
7
8
9
proximal offshore
distal offshore
FS
Upper Montney
-bone in coarse siltstone bed.
-convolute-bedded.
-small scale convolute-bedding.
-pyritic laminae.
-tiny Planolites & Trichichnus.
-tiny Planolites.
-pyritic laminae.
-pair of horizontal fractures joined by vertical fracture.
-horizontal fracture.
-convolute-bedding.
-horizontal fracture.
-horizontal fracture.
-convolute-bedding.
-pyritized laminae

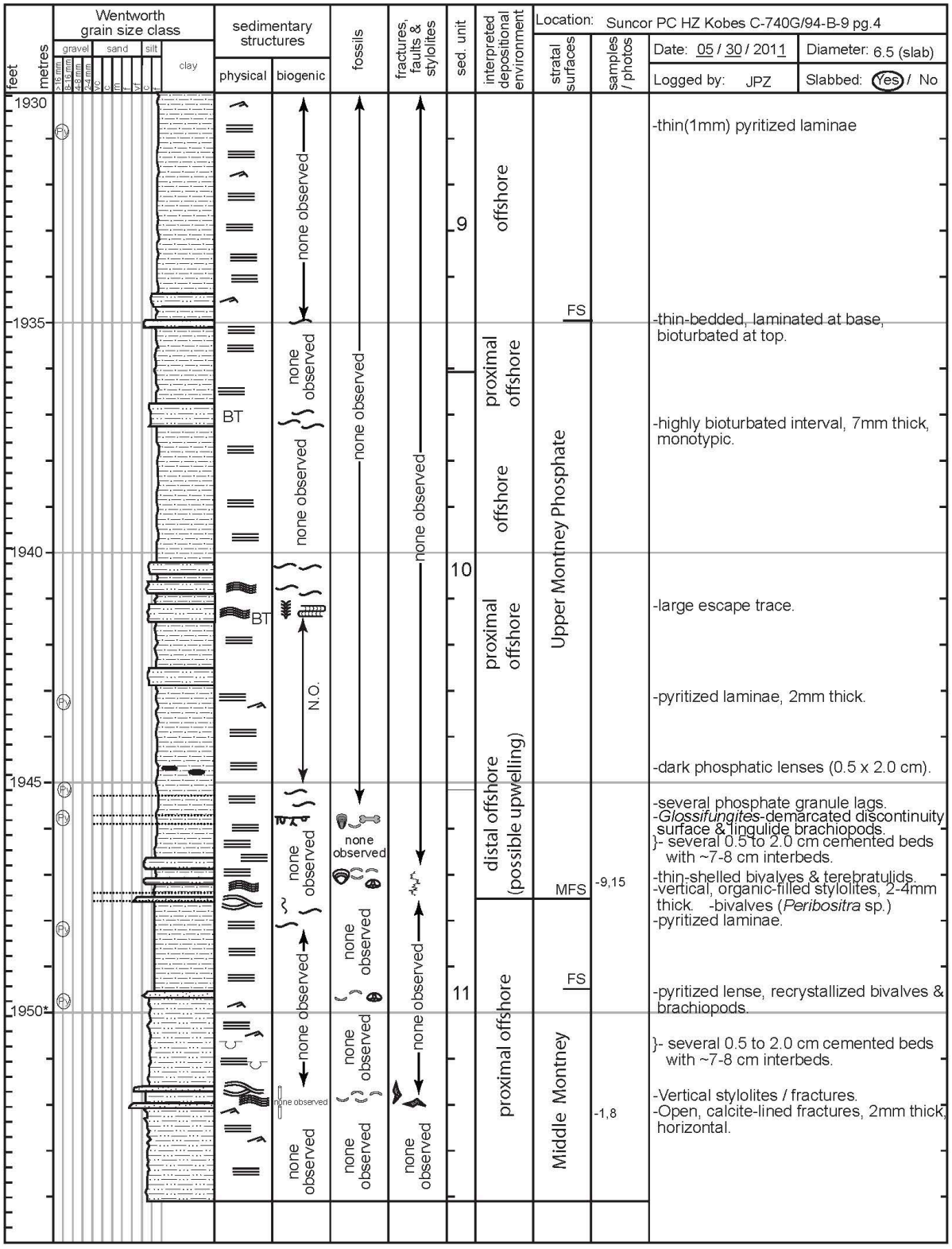
Location: Suncor PC HZ Kobes C-740G/94-B-9 pg.4
Date: 05 / 30 / 2011
Diameter: 6.5 (slab)
Logged by: JPZ
Slabbed: Yes / No
feet
metres
Wentworth grain size class
gravel
sand
silt
clay
>16 mm
2-16 mm
0.5-2 mm
0.25-0.5 mm
vc
c
m
f
vf
c
f
sedimentary structures
physical
biogenic
fossils
fractures, faults & stylolites
sed. unit
interpreted depositional environment
stratal surfaces
samples / photos
1930
1935
1940
1945
1950*
BT
N.O.
none observed
9
10
11
offshore
proximal offshore
distal offshore (possible upwelling)
FS
MFS
Upper Montney Phosphate
Middle Montney
-9,15
-1,8
-thin(1mm) pyritized laminae
-thin-bedded, laminated at base, bioturbated at top.
-highly bioturbated interval, 7mm thick, monotypic.
-large escape trace.
-pyritized laminae, 2mm thick.
-dark phosphatic lenses (0.5 x 2.0 cm).
-several phosphate granule lags.
-Glossifungites-demarcated discontinuity surface & lingulide brachiopods.
}- several 0.5 to 2.0 cm cemented beds with ~7-8 cm interbeds.
-thin-shelled bivalves & terebratulids.
-vertical, organic-filled stylolites, 2-4mm thick. -bivalves (Peribositra sp.)
-pyritized laminae.
-pyritized lense, recrystallized bivalves & brachiopods.
}- several 0.5 to 2.0 cm cemented beds with ~7-8 cm interbeds.
-Vertical stylolites / fractures.
-Open, calcite-lined fractures, 2mm thick, horizontal.

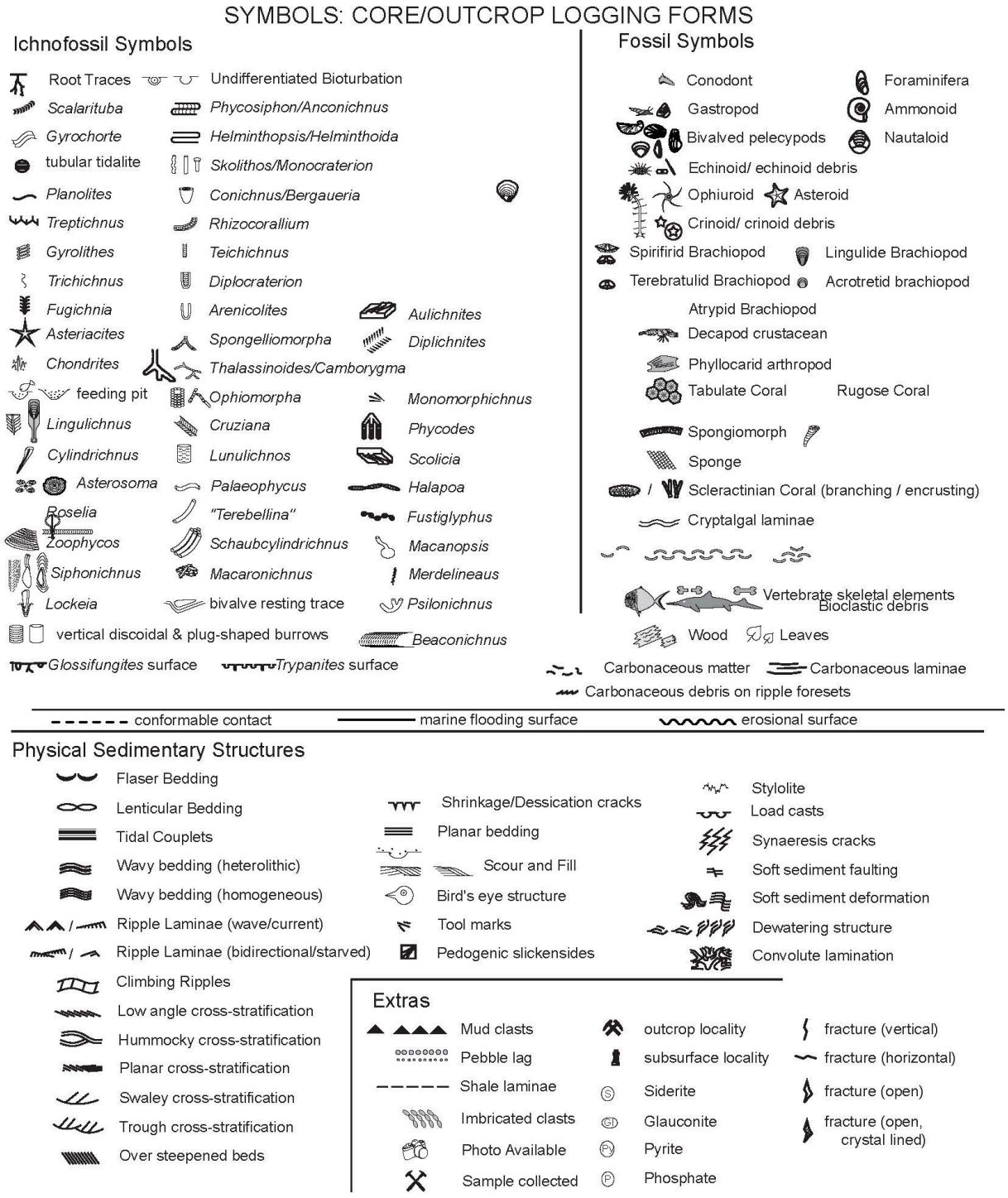

Figure S28: Lithologue for well c-74-G/94-B-9. See legend for explanation of symbols used.

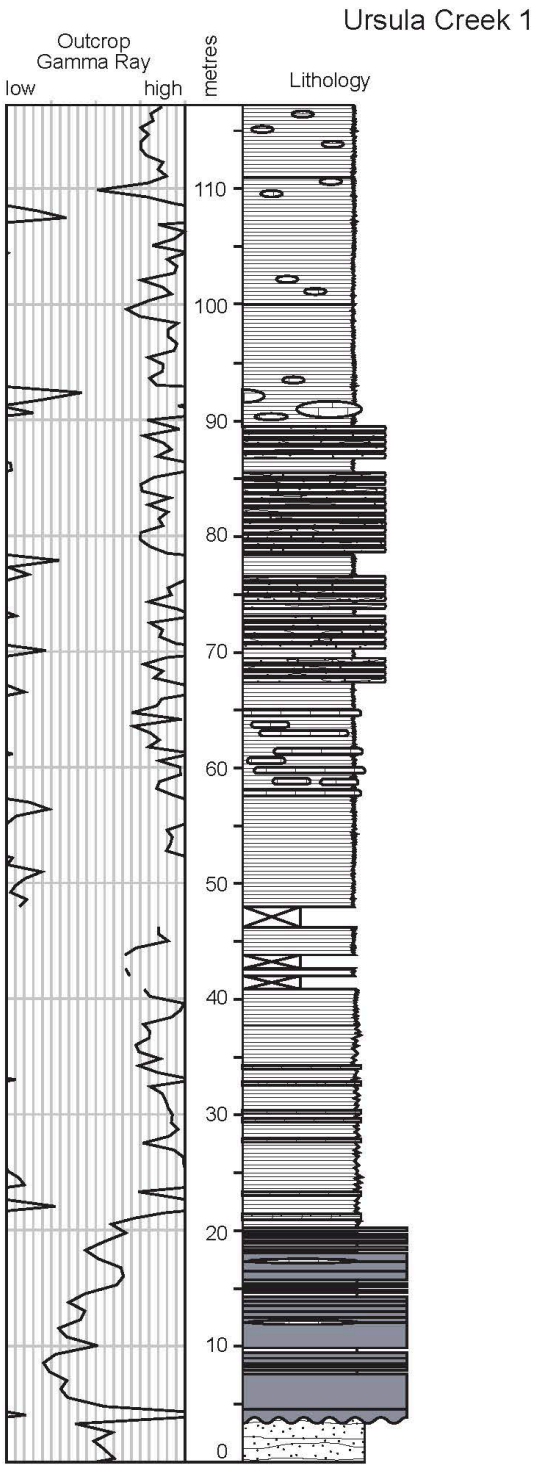

Figure S29: Lithologue for the outcrop Ursula Creek.

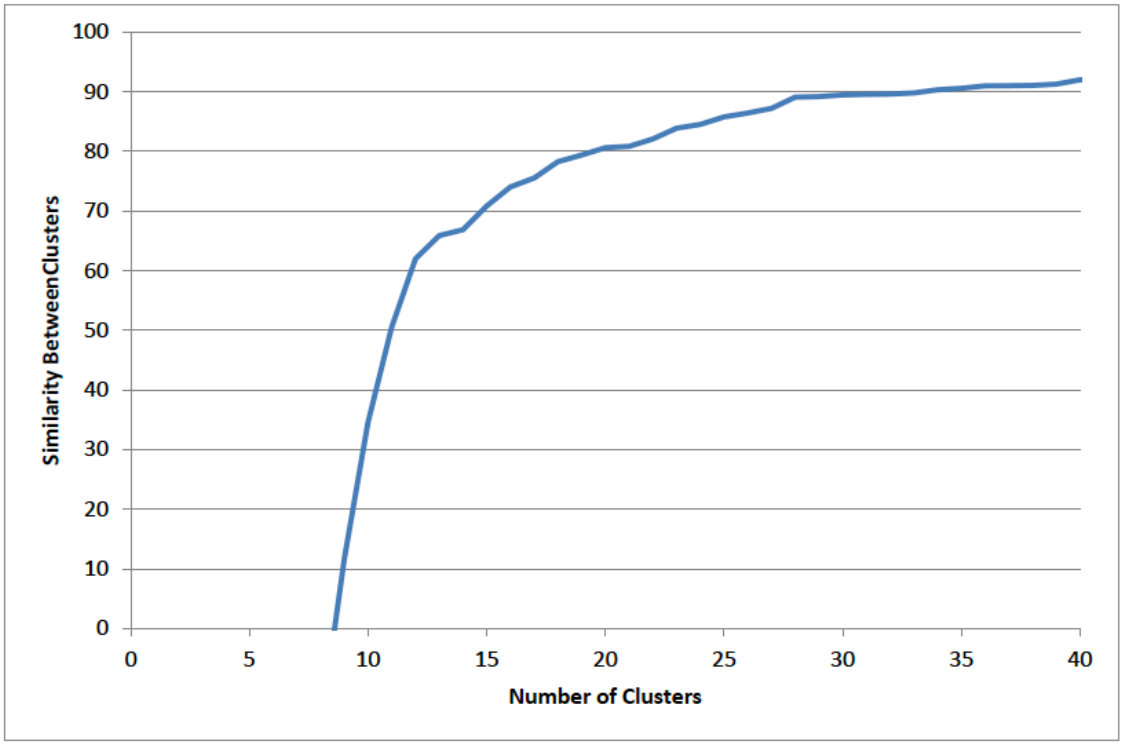

Figure S30: Graph of the number of clusters versus similarity between clusters. An inflection point occurs at 12, which is why 12 statistical divisions were chosen. The Belloy Formation, defined by Golding et al. (2014) within this study's data set, was divided out as an additional subdivision (although the division is not statistically significant).

Table S1: Pearson product-moment values for well 16-17-083-25W6. Table values greater than 0.8 are highlighted in green while values below <0.8 are highlighted in red.

	SiO2 (wt%)	Al2O3 (wt%)	TiO2 (wt%)	Fe2O3 (wt%)	MnO (wt%)	MgO (wt%)	CaO (wt%)	Na2O (wt%)	K2O (wt%)	P2O5 (wt%)	Ba (ppm)	Cr (ppm)	S (ppm)	Sc (ppm)	Sr (ppm)	Zn (ppm)
SiO2 (wt %)	1															
Al2O3 (wt%)	0.88	1														
TiO2 (wt %)	0.91	0.97	1													
Fe2O3 (wt%)	0.27	0.35	0.28	1												
MnO (wt %)	-0.5	-0.39	-0.5	0.125	1											
MgO (wt %)	-0.5	-0.47	-0.5	0.093	0.5	1										
CaO (wt %)	-0.9	-0.9	-0.9	-0.44	0.45	0.32	1									
Na2O (wt %)	0.69	0.62	0.71	0.016	-0.3	-0.3	-0.6	1								
K2O (wt %)	0.81	0.89	0.91	0.166	-0.6	-0.5	-0.8	0.62	1							
P2O5 (wt %)	-0.3	-0.28	-0.3	-0.28	-0.2	-0.1	0.3	-0.21	-0.2	1						
Ba (ppm)	0.01	0.07	0.02	0.513	0.04	-0.1	-0.1	-0.14	0	-0	1					
Cr (ppm)	0.34	0.17	0.11	0.107	-0.3	-0.3	-0.3	-0.1	0.19	0.15	0.04	1				
S (ppm)	0.05	0.11	0.02	0.488	0.32	-0	-0.1	-0.14	-0.2	-0.1	0.37	0.2	1			
Sc (ppm)	0.81	0.95	0.9	0.422	-0.3	-0.4	-0.8	0.49	0.79	-0.3	0.1	0.24	0.27	1		
Sr (ppm)	-0.6	-0.49	-0.6	-0.15	0.2	0.12	0.58	-0.5	-0.5	0.48	0.5	-0.03	0.22	-0.43	1	
Zn (ppm)	-0.1	-0.05	-0.1	-0.22	-0.3	-0.2	0.07	-0.09	0.12	0.25	-0.1	0.3	-0.17	-0.06	0.08	1
Zr (ppm)	0.69	0.53	0.67	-0.08	-0.5	-0.2	-0.6	0.79	0.64	-0.1	-0.1	-0.06	-0.36	0.36	-0.5	-0
Be (ppm)	0.71	0.82	0.79	0.21	-0.5	-0.4	-0.8	0.51	0.86	-0.1	-0	0.37	0.01	0.77	-0.4	0.23
V (ppm)	-0.2	-0.12	-0.1	-0.27	-0.3	-0.1	0.14	-0.16	0.08	0.12	-0.1	0.25	-0.26	-0.13	0.07	0.74
Co (ppm)	0.76	0.85	0.84	0.255	-0.3	-0.4	-0.8	0.52	0.79	-0.3	-0.1	0.05	0.04	0.8	-0.5	-0.1
Ni (ppm)	0.08	0.16	0.17	-0.28	-0.5	-0.3	-0.1	0.03	0.38	0.23	-0.2	0.34	-0.31	0.13	-0	0.69
Cu (ppm)	0.64	0.7	0.71	0.009	-0.5	-0.4	-0.7	0.36	0.78	-0	-0.1	0.27	-0.12	0.67	-0.3	0.21
Ga (ppm)	0.85	0.98	0.96	0.335	-0.4	-0.5	-0.9	0.63	0.89	-0.3	0.04	0.2	0.08	0.94	-0.5	-0
Rb (ppm)	0.8	0.96	0.91	0.389	-0.3	-0.5	-0.8	0.44	0.82	-0.3	0.09	0.25	0.22	0.96	-0.4	-0
Y (ppm)	0.04	-0.01	0.01	-0.2	-0.3	-0.2	-0	0.06	0.1	0.81	-0.1	0.17	-0.17	-0.03	0.24	0.2
Nb (ppm)	0.89	0.95	0.98	0.304	-0.4	-0.4	-0.9	0.74	0.86	-0.3	0.02	0.1	0.07	0.89	-0.6	-0.1
Mo (ppm)	-0	-0.02	0.03	-0.21	-0.3	-0.1	-0	0.1	0.25	0	-0.1	-0.02	-0.43	-0.1	-0.1	0.33
Sn (ppm)	0.61	0.64	0.68	0.16	-0.2	-0.3	-0.6	0.62	0.56	-0.2	-0	0.01	-0.01	0.6	-0.4	-0.1
Cs (ppm)	0.64	0.83	0.74	0.449	-0.2	-0.4	-0.7	0.11	0.65	-0.2	0.17	0.31	0.33	0.88	-0.3	0
La (ppm)	0.46	0.35	0.34	0.063	-0.3	-0.3	-0.4	0.23	0.35	0.5	-0	0.45	0.01	0.35	-0.1	-0
Ce (ppm)	0.64	0.55	0.54	0.205	-0.2	-0.3	-0.6	0.41	0.49	0.1	-0	0.34	0.08	0.54	-0.3	-0.2
Pr (ppm)	0.46	0.33	0.33	0.064	-0.3	-0.3	-0.4	0.28	0.33	0.36	-0	0.38	0.01	0.33	-0.1	-0.1
Nd (ppm)	0.4	0.28	0.29	0.033	-0.3	-0.3	-0.3	0.26	0.3	0.37	-0	0.32	-0.01	0.27	-0.1	-0.1
Sm (ppm)	0.35	0.26	0.27	0.022	-0.2	-0.2	-0.3	0.26	0.29	0.34	-0	0.23	-0.03	0.24	-0	-0.1
Eu (ppm)	0.26	0.2	0.2	0.026	-0.2	-0.2	-0.2	0.18	0.23	0.38	0.17	0.18	0.03	0.19	0.18	-0.1
Gd (ppm)	0.32	0.24	0.25	0.012	-0.2	-0.2	-0.3	0.22	0.26	0.44	-0	0.22	-0	0.23	0.01	-0.1
Tb (ppm)	0.35	0.29	0.3	0.017	-0.3	-0.2	-0.3	0.28	0.3	0.44	-0	0.18	-0.02	0.27	-0	-0
Dy (ppm)	0.35	0.29	0.31	-0.01	-0.3	-0.2	-0.3	0.3	0.33	0.49	-0	0.15	-0.07	0.26	-0	0.01
Ho (ppm)	0.33	0.27	0.3	-0.06	-0.3	-0.2	-0.3	0.29	0.33	0.57	-0.1	0.16	-0.14	0.24	0	0.06
Er (ppm)	0.38	0.32	0.36	-0.05	-0.4	-0.3	-0.3	0.33	0.39	0.58	-0.1	0.16	-0.14	0.29	-0	0.09
Tm (ppm)	0.51	0.46	0.51	-0.01	-0.5	-0.3	-0.5	0.43	0.51	0.5	-0.1	0.18	-0.14	0.42	-0.1	0.1
Yb (ppm)	0.6	0.54	0.6	-0.02	-0.5	-0.3	-0.6	0.53	0.61	0.41	-0.1	0.18	-0.2	0.48	-0.2	0.13
Lu (ppm)	0.62	0.57	0.64	-0.02	-0.6	-0.4	-0.6	0.56	0.66	0.37	-0.1	0.17	-0.24	0.5	-0.2	0.15
Hf (ppm)	0.7	0.54	0.68	-0.07	-0.5	-0.2	-0.7	0.81	0.66	-0.1	-0.1	-0.08	-0.38	0.38	-0.5	-0
Ta (ppm)	0.87	0.93	0.94	0.373	-0.3	-0.4	-0.9	0.63	0.76	-0.3	0.06	0.13	0.24	0.92	-0.5	-0.1
W (ppm)	0.05	0.08	0.11	-0.23	-0.2	-0.1	-0	0.16	0.23	0.12	-0.2	-0.04	-0.4	-0.02	-0.1	0.15
Tl (ppm)	0.25	0.18	0.28	-0.15	-0.4	-0.1	-0.2	0.31	0.36	-0.1	-0.1	-0.08	-0.32	0.08	-0.2	0.15
Pb (ppm)	0.6	0.59	0.59	0.335	-0.1	-0.2	-0.6	0.37	0.37	-0.3	0.12	0.18	0.36	0.62	-0.3	-0.3
Th (ppm)	0.92	0.95	0.97	0.262	-0.5	-0.5	-0.9	0.7	0.9	-0.3	0	0.18	-0.02	0.87	-0.6	-0
U (ppm)	0.01	-0.02	0.02	-0.24	-0.4	-0.2	0	0.01	0.23	0.41	-0.2	0.07	-0.42	-0.08	0.01	0.27

	Zr (ppm)	Be (ppm)	V (ppm)	Co (ppm)	Ni (ppm)	Cu (ppm)	Ga (ppm)	Rb (ppm)	Y (ppm)	Nb (ppm)	Mo (ppm)	Sn (ppm)	Cs (ppm)	La (ppm)	Ce (ppm)	Pr (ppm)	Nd (ppm)
Zr (ppm)	1																
Be (ppm)	0.46	1															
V (ppm)	-0	0.22	1														
Co (ppm)	0.49	0.73	-0.2	1													
Ni (ppm)	0.17	0.49	0.78	0.19	1												
Cu (ppm)	0.42	0.76	0.15	0.75	0.55	1											
Ga (ppm)	0.51	0.87	-0.1	0.86	0.22	0.73	1										
Rb (ppm)	0.37	0.82	-0.1	0.82	0.2	0.7	0.96	1									
Y (ppm)	0.2	0.13	0.15	-0.06	0.31	0.18	-0	-0	1								
Nb (ppm)	0.63	0.76	-0.2	0.83	0.11	0.67	0.95	0.89	-0.03	1							
Mo (ppm)	0.19	0.23	0.47	0.16	0.53	0.28	0.05	-0.1	0.1	0.01	1						

	Zr (ppm)	Be (ppm)	V (ppm)	Co (ppm)	Ni (ppm)	Cu (ppm)	Ga (ppm)	Rb (ppm)	Y (ppm)	Nb (ppm)	Mo (ppm)	Sn (ppm)	Cs (ppm)	La (ppm)	Ce (ppm)	Pr (ppm)	Nd (ppm)
Sn (ppm)	0.47	0.48	-0.1	0.54	0.05	0.45	0.64	0.58	0.05	0.7	0.01	1					
Cs (ppm)	0.12	0.67	-0	0.69	0.17	0.6	0.8	0.93	-0.06	0.7	-0.1	0.4	1				
La (ppm)	0.3	0.39	-0.1	0.27	0.14	0.35	0.35	0.34	0.79	0.32	-0	0.27	0.3	1			
Ce (ppm)	0.4	0.48	-0.2	0.5	-0.01	0.39	0.56	0.51	0.52	0.54	-0	0.41	0.42	0.89	1		
Pr (ppm)	0.32	0.35	-0.1	0.28	0.07	0.29	0.34	0.31	0.73	0.32	-0	0.27	0.24	0.95	0.94	1	
Nd (ppm)	0.3	0.3	-0.1	0.24	0.07	0.25	0.29	0.25	0.75	0.27	0	0.23	0.19	0.91	0.92	0.99	1
Sm (ppm)	0.3	0.28	-0.1	0.22	0.07	0.22	0.27	0.22	0.74	0.26	0.02	0.22	0.15	0.85	0.88	0.96	0.99
Eu (ppm)	0.23	0.21	-0.1	0.16	0.05	0.17	0.2	0.17	0.75	0.18	-0	0.17	0.13	0.8	0.8	0.91	0.94
Gd (ppm)	0.28	0.26	-0.1	0.19	0.08	0.22	0.24	0.21	0.81	0.23	-0	0.2	0.16	0.89	0.86	0.96	0.98
Tb (ppm)	0.33	0.29	-0.1	0.23	0.1	0.25	0.28	0.25	0.82	0.28	-0	0.24	0.18	0.88	0.86	0.95	0.97
Dy (ppm)	0.37	0.31	-0	0.23	0.16	0.29	0.29	0.25	0.87	0.29	0.03	0.26	0.16	0.88	0.83	0.93	0.95
Ho (ppm)	0.39	0.32	0.03	0.21	0.23	0.31	0.27	0.23	0.92	0.27	0.07	0.24	0.14	0.89	0.78	0.9	0.91
Er (ppm)	0.44	0.37	0.04	0.25	0.27	0.37	0.32	0.28	0.92	0.33	0.07	0.29	0.18	0.89	0.75	0.87	0.87
Tm (ppm)	0.54	0.48	0.03	0.36	0.3	0.47	0.46	0.41	0.84	0.47	0.06	0.39	0.29	0.86	0.75	0.82	0.81
Yb (ppm)	0.65	0.57	0.05	0.46	0.36	0.56	0.55	0.48	0.77	0.57	0.13	0.44	0.32	0.81	0.73	0.76	0.74
Lu (ppm)	0.69	0.61	0.09	0.49	0.4	0.6	0.58	0.5	0.72	0.6	0.17	0.47	0.33	0.75	0.66	0.69	0.66
Hf (ppm)	0.99	0.49	-0	0.52	0.18	0.45	0.55	0.39	0.16	0.66	0.22	0.5	0.13	0.29	0.41	0.31	0.29
Ta (ppm)	0.53	0.7	-0.2	0.8	0.04	0.62	0.92	0.92	-0.04	0.95	-0.1	0.63	0.78	0.32	0.53	0.31	0.26
W (ppm)	0.27	0.15	0.2	0.06	0.25	0.12	0.1	0.03	0.23	0.08	0.3	0.16	-0.04	0.15	0.09	0.12	0.13
Tl (ppm)	0.48	0.28	0.2	0.44	0.44	0.4	0.2	0.12	0.06	0.25	0.46	0.18	-0.01	0.04	0.09	0.06	0.06
Pb (ppm)	0.24	0.32	-0.3	0.5	-0.19	0.3	0.54	0.59	-0.11	0.63	-0.3	0.69	0.54	0.27	0.44	0.27	0.22
Th (ppm)	0.7	0.81	-0.1	0.84	0.2	0.71	0.95	0.89	0.09	0.95	0.07	0.66	0.72	0.43	0.63	0.44	0.39
U (ppm)	0.25	0.2	0.37	0.14	0.52	0.36	0.02	-0	0.58	-0.04	0.65	0.05	-0.07	0.39	0.2	0.32	0.33

	Sm (ppm)	Eu (ppm)	Gd (ppm)	Tb (ppm)	Dy (ppm)	Ho (ppm)	Er (ppm)	Tm (ppm)	Yb (ppm)	Lu (ppm)	Hf (ppm)	Ta (ppm)	W (ppm)	Tl (ppm)	Pb (ppm)	Th (ppm)	U (ppm)
Sm (ppm)	1																
Eu (ppm)	0.96	1															
Gd (ppm)	0.99	0.96	1														
Tb (ppm)	0.98	0.95	0.99	1													
Dy (ppm)	0.95	0.93	0.98	0.99	1												
Ho (ppm)	0.91	0.88	0.95	0.96	0.99	1											
Er (ppm)	0.85	0.83	0.9	0.93	0.96	0.99	1										
Tm (ppm)	0.79	0.75	0.83	0.87	0.91	0.95	0.98	1									
Yb (ppm)	0.72	0.67	0.76	0.8	0.85	0.89	0.93	0.98	1								
Lu (ppm)	0.64	0.59	0.67	0.72	0.78	0.83	0.89	0.95	0.98	1							
Hf (ppm)	0.29	0.22	0.27	0.31	0.35	0.37	0.43	0.52	0.64	0.69	1						
Ta (ppm)	0.23	0.17	0.22	0.27	0.27	0.25	0.31	0.45	0.52	0.54	0.55	1					
W (ppm)	0.13	0.1	0.12	0.13	0.17	0.22	0.22	0.23	0.26	0.26	0.28	-0	1				
Tl (ppm)	0.08	0.04	0.05	0.08	0.1	0.12	0.16	0.19	0.27	0.31	0.5	0.15	0.14	1			
Pb (ppm)	0.19	0.15	0.17	0.18	0.16	0.11	0.13	0.22	0.24	0.23	0.25	0.65	-0.15	0.03	1		
Th (ppm)	0.36	0.28	0.34	0.38	0.39	0.38	0.44	0.57	0.67	0.69	0.73	0.92	0.15	0.29	0.56	1	
U (ppm)	0.33	0.31	0.36	0.37	0.43	0.49	0.51	0.46	0.49	0.5	0.25	-0.1	0.36	0.37	-0.3	0.1	1

Table S2: Pearson product-moment values for Ursula Creek. Table values greater than 0.8 are highlighted in green while values below <0.8 are highlighted in red.

	Al2O3	SiO2	TiO2	Fe2O3	MnO	MgO	CaO	Na2O	K2O	P2O5	Al	Ba	Cr
	(wt %)	(wt %)	(wt %)	(wt %)	(wt %)	(wt %)	(wt %)	(wt %)	(wt %)	(wt %)	(ppm)	(ppm)	(ppm)
Al2O3 (wt %)	1												
SiO2 (wt %)	0.61	1											
TiO2 (wt %)	0.98	0.581	1										
Fe2O3 (wt%)	-0.09	-0.43	-0.08	1									
MnO (wt %)	-0.66	-0.89	-0.64	0.505	1								
MgO (wt %)	-0.55	-0.79	-0.54	0.583	0.87	1							
CaO (wt %)	-0.71	-0.93	-0.69	0.219	0.84	0.623	1						
Na2O (wt %)	0.62	0.268	0.63	-0.11	-0.38	-0.36	-0.31	1					
K2O (wt %)	0.99	0.624	0.98	-0.1	-0.68	-0.55	-0.73	0.563	1				
P2O5 (wt %)	0.01	-0.1	0	-0.12	0.03	-0.04	0.12	0.099	0.01	1			
Al ppm	0.01	-0.1	0	-0.12	0.03	-0.04	0.12	0.099	0.01	1	1		
Ba (ppm)	0.29	0.147	0.27	0.029	-0.15	-0.04	-0.24	0.273	0.3	-0.03	-0.03	1	
Cr (ppm)	0.5	0.441	0.47	-0.25	-0.52	-0.43	-0.5	0.21	0.54	0.06	0.063	0.1	1
S (ppm)	-0.13	-0.41	-0.11	0.41	0.21	0.324	0.26	0.254	-0.14	0.03	0.028	0.12	-0.14
Sc (ppm)	0.79	0.53	0.76	0.039	-0.52	-0.45	-0.61	0.473	0.78	-0.02	-0.02	0.26	0.415
Sr (ppm)	-0.56	-0.85	-0.52	0.313	0.8	0.602	0.88	-0.19	-0.58	0.2	0.203	-0.09	-0.44
Zn (ppm)	0.05	0.105	0.05	-0.12	-0.11	-0.08	-0.09	0.156	0.05	-0.02	-0.02	0.29	0.027
Zr (ppm)	0.92	0.484	0.94	-0.06	-0.57	-0.47	-0.61	0.729	0.9	0.03	0.025	0.27	0.447
Be (ppm)	0.77	0.32	0.73	0.065	-0.43	-0.28	-0.5	0.488	0.77	0.1	0.103	0.28	0.661
V (ppm)	0.34	0.194	0.32	-0.21	-0.28	-0.19	-0.22	0.346	0.35	0.05	0.048	0.21	0.252
Co (ppm)	0.5	0.14	0.48	0.267	-0.2	-0.19	-0.26	0.517	0.47	-0.02	-0.02	0.22	0.248
Ni (ppm)	0.39	0.119	0.35	0.031	-0.2	-0.13	-0.21	0.313	0.38	0.06	0.059	0.22	0.407
Cu (ppm)	0.54	0.367	0.5	-0.02	-0.44	-0.36	-0.45	0.336	0.55	0.08	0.077	0.2	0.599
Ga (ppm)	0.97	0.566	0.95	-0.1	-0.66	-0.53	-0.7	0.569	0.97	0.06	0.056	0.29	0.63
Rb (ppm)	0.97	0.595	0.96	-0.09	-0.67	-0.54	-0.72	0.503	0.99	0.02	0.015	0.29	0.575
Y (ppm)	0.09	-0.12	0.1	0.066	0.09	-0	0.13	0.13	0.07	0.87	0.87	0.01	-0.11
Nb (ppm)	0.96	0.586	0.98	-0.08	-0.66	-0.56	-0.71	0.592	0.96	0.01	0.005	0.26	0.505
Mo (ppm)	0.23	0.07	0.21	0.008	-0.17	-0.11	-0.11	0.229	0.22	-0.04	-0.04	0.07	-0.14
Sn (ppm)	0.68	0.527	0.7	-0.1	-0.47	-0.46	-0.55	0.243	0.68	-0.05	-0.05	0.15	0.251
Cs (ppm)	0.87	0.557	0.86	-0.1	-0.62	-0.52	-0.66	0.22	0.9	-0.02	-0.02	0.2	0.511
La (ppm)	0.72	0.243	0.73	0.069	-0.32	-0.34	-0.33	0.459	0.69	0.42	0.42	0.15	0.243
Ce (ppm)	0.69	0.296	0.7	0.035	-0.34	-0.34	-0.37	0.394	0.67	0.49	0.492	0.13	0.162
Pr (ppm)	0.54	0.214	0.54	0.012	-0.25	-0.28	-0.26	0.33	0.52	0.67	0.668	0.1	0.098
Nd (ppm)	0.4	0.133	0.4	0.017	-0.16	-0.21	-0.16	0.258	0.38	0.75	0.75	0.07	0.015
Sm (ppm)	0.21	0.017	0.2	0.037	-0.03	-0.08	-0.04	0.192	0.18	0.79	0.792	0.05	-0.09
Eu (ppm)	0.11	-0.08	0.1	0.067	0.07	-0.01	0.07	0.107	0.08	0.83	0.827	0.07	-0.12
Gd (ppm)	0.2	-0.01	0.19	0.048	-0.01	-0.07	-0.01	0.181	0.17	0.82	0.823	0.04	-0.08
Tb (ppm)	0.16	-0.03	0.16	0.044	0.01	-0.05	0.02	0.163	0.14	0.83	0.825	0.04	-0.1
Dy (ppm)	0.18	-0.02	0.18	0.055	0.01	-0.05	0.01	0.172	0.15	0.82	0.822	0.04	-0.1

	Al2O3	SiO2	TiO2	Fe2O3	MnO	MgO	CaO	Na2O	K2O	P2O5	Al	Ba	Cr
	(wt %)	(wt %)	(wt %)	(wt %)	(wt %)	(wt %)	(wt %)	(wt %)	(wt %)	(wt %)	(ppm)	(ppm)	(ppm)
Ho (ppm)	0.21	-0.01	0.21	0.065	-0	-0.07	-0.01	0.193	0.18	0.83	0.829	0.05	-0.06
Er (ppm)	0.28	0.011	0.29	0.077	-0.04	-0.09	-0.04	0.26	0.25	0.8	0.797	0.11	-0.01
Tm (ppm)	0.4	0.045	0.41	0.118	-0.09	-0.14	-0.11	0.386	0.37	0.68	0.681	0.15	0.113
Yb (ppm)	0.5	0.106	0.5	0.119	-0.16	-0.19	-0.2	0.474	0.47	0.56	0.562	0.2	0.232
Lu (ppm)	0.51	0.109	0.51	0.103	-0.19	-0.21	-0.21	0.52	0.49	0.48	0.478	0.22	0.312
Hf (ppm)	0.93	0.501	0.95	-0.08	-0.59	-0.49	-0.62	0.729	0.91	0.02	0.023	0.27	0.455
Ta (ppm)	0.97	0.572	0.98	-0.09	-0.65	-0.54	-0.7	0.656	0.96	0.04	0.035	0.27	0.498
W (ppm)	0.16	0.212	0.18	-0.1	-0.24	-0.15	-0.23	-0.14	0.2	-0.05	-0.05	-0.03	0.039
Tl (ppm)	0.58	0.326	0.59	-0	-0.4	-0.31	-0.38	0.367	0.58	-0.08	-0.08	0.19	0.039
Pb (ppm)	0.42	0.428	0.44	0.039	-0.32	-0.39	-0.4	0.015	0.43	-0.11	-0.11	0.02	0.247
Th (ppm)	0.9	0.522	0.9	-0.03	-0.59	-0.5	-0.63	0.631	0.89	0.19	0.191	0.32	0.368
U (ppm)	0.38	0.172	0.35	-0.03	-0.27	-0.23	-0.21	0.191	0.38	0.32	0.32	0.12	-0.08

	S	Sc	Sr	Zn	Zr	Be	V	Co	Ni	Cu	Ga	Rb	Y
	(ppm)	(ppm)	(ppm)	(ppm)	(ppm)	(ppm)	(ppm)	(ppm)	(ppm)	(ppm)	(ppm)	(ppm)	(ppm)
S (ppm)	1												
Sc (ppm)	-0.1	1											
Sr (ppm)	0.35	-0.44	1										
Zn (ppm)	0.06	-0.02	-0.08	1									
Zr (ppm)	-0	0.68	-0.45	0.057	1								
Be (ppm)	0.05	0.61	-0.42	-0.01	0.71	1							
V (ppm)	0.07	0.24	-0.2	0.254	0.34	0.39	1						
Co (ppm)	0.15	0.44	-0.23	-0.1	0.5	0.66	0.09	1					
Ni (ppm)	0.06	0.33	-0.21	0.042	0.33	0.66	0.48	0.66	1				
Cu (ppm)	-0	0.53	-0.35	0.189	0.5	0.69	0.48	0.43	0.57	1			
Ga (ppm)	-0.1	0.76	-0.55	0.073	0.89	0.86	0.36	0.51	0.46	0.61	1		
Rb (ppm)	-0.1	0.76	-0.57	0.026	0.89	0.81	0.35	0.48	0.41	0.59	0.98	1	
Y (ppm)	0.03	0.11	0.24	-0.04	0.09	0.09	-0	0.08	0.09	-0.01	0.1	0.06	1
Nb (ppm)	-0.1	0.75	-0.54	0.036	0.93	0.76	0.29	0.5	0.38	0.53	0.95	0.96	0.1
Mo (ppm)	0.21	0.19	-0.15	0.016	0.2	0.19	0.28	0.29	0.4	0.14	0.19	0.22	0
Sn (ppm)	-0.5	0.54	-0.46	0.057	0.64	0.38	-0	0.26	0.15	0.27	0.64	0.67	0.11
Cs (ppm)	-0.2	0.66	-0.53	-0.03	0.73	0.69	0.26	0.33	0.33	0.49	0.88	0.93	0.04
La (ppm)	-0	0.64	-0.1	-0.04	0.69	0.54	0.09	0.39	0.22	0.32	0.7	0.7	0.61
Ce (ppm)	-0.1	0.59	-0.17	-0.04	0.65	0.48	0.04	0.33	0.18	0.23	0.66	0.66	0.7
Pr (ppm)	-0.1	0.47	-0.08	-0.04	0.5	0.38	0.04	0.25	0.16	0.18	0.52	0.51	0.85
Nd (ppm)	-0.1	0.35	-0.02	-0.04	0.36	0.29	0.01	0.19	0.13	0.11	0.39	0.37	0.91
Sm (ppm)	-0	0.19	0.06	-0.03	0.19	0.19	0.02	0.15	0.14	0.05	0.2	0.17	0.93
Eu (ppm)	-0	0.11	0.16	-0.03	0.09	0.13	-0	0.11	0.13	0.01	0.11	0.08	0.95
Gd (ppm)	-0	0.18	0.1	-0.04	0.18	0.18	0	0.14	0.14	0.04	0.19	0.16	0.96
Tb (ppm)	-0	0.16	0.12	-0.02	0.15	0.14	-0	0.12	0.12	0.02	0.16	0.13	0.96
Dy (ppm)	-0	0.18	0.13	-0.04	0.16	0.14	-0	0.12	0.11	0.01	0.17	0.14	0.97

	S (ppm)	Sc (ppm)	Sr (ppm)	Zn (ppm)	Zr (ppm)	Be (ppm)	V (ppm)	Co (ppm)	Ni (ppm)	Cu (ppm)	Ga (ppm)	Rb (ppm)	Y (ppm)
Ho (ppm)	-0	0.22	0.14	-0.03	0.2	0.17	-0	0.13	0.13	0.06	0.2	0.17	0.98
Er (ppm)	0.03	0.3	0.13	-0.04	0.28	0.24	0.02	0.18	0.15	0.12	0.28	0.25	0.97
Tm (ppm)	0.08	0.44	0.1	-0.01	0.43	0.37	0.1	0.28	0.23	0.26	0.41	0.37	0.87
Yb (ppm)	0.11	0.57	0.04	-0.02	0.54	0.47	0.17	0.35	0.29	0.37	0.51	0.47	0.74
Lu (ppm)	0.16	0.59	0.04	-0.04	0.57	0.52	0.2	0.39	0.33	0.44	0.54	0.5	0.63
Hf (ppm)	-0	0.68	-0.48	0.066	1	0.72	0.34	0.51	0.33	0.5	0.9	0.9	0.09
Ta (ppm)	-0.1	0.74	-0.54	0.062	0.96	0.77	0.33	0.52	0.38	0.53	0.95	0.95	0.12
W (ppm)	-0.2	0.1	-0.13	-0.03	0.08	0	-0.1	-0.1	-0.2	-0.02	0.15	0.23	-0
Tl (ppm)	0.03	0.44	-0.33	0.046	0.52	0.43	0.43	0.46	0.59	0.28	0.54	0.56	0.08
Pb (ppm)	-0.6	0.44	-0.31	-0.08	0.38	0.22	-0.2	0.24	0.1	0.25	0.39	0.44	0.02
Th (ppm)	-0.1	0.74	-0.48	0.025	0.88	0.71	0.32	0.53	0.38	0.51	0.88	0.88	0.28
U (ppm)	0.13	0.29	-0.16	0.019	0.28	0.28	0.27	0.21	0.33	0.15	0.36	0.38	0.44

	Nb (ppm)	Mo (ppm)	Sn (ppm)	Cs (ppm)	La (ppm)	Ce (ppm)	Pr (ppm)	Nd (ppm)	Sm (ppm)	Eu (ppm)	Gd (ppm)	Tb (ppm)	Dy (ppm)
Nb (ppm)	1												
Mo (ppm)	0.18	1											
Sn (ppm)	0.73	0.04	1										
Cs (ppm)	0.87	0.2	0.67	1									
La (ppm)	0.73	0.11	0.59	0.65	1								
Ce (ppm)	0.7	0.13	0.61	0.63	0.95	1							
Pr (ppm)	0.55	0.09	0.48	0.48	0.88	0.96	1						
Nd (ppm)	0.4	0.08	0.36	0.34	0.78	0.9	0.98	1					
Sm (ppm)	0.2	0.06	0.17	0.13	0.59	0.74	0.88	0.95	1				
Eu (ppm)	0.1	0.03	0.11	0.06	0.53	0.68	0.83	0.92	0.98	1			
Gd (ppm)	0.19	0.05	0.16	0.12	0.61	0.75	0.89	0.96	0.99	0.98	1		
Tb (ppm)	0.16	0.04	0.15	0.09	0.59	0.73	0.87	0.95	0.99	0.99	1	1	
Dy (ppm)	0.18	0.03	0.18	0.1	0.62	0.75	0.89	0.95	0.98	0.98	0.99	0.99	1
Ho (ppm)	0.22	0.03	0.21	0.14	0.67	0.77	0.9	0.95	0.96	0.96	0.98	0.98	0.99
Er (ppm)	0.29	0.03	0.26	0.19	0.74	0.81	0.92	0.95	0.92	0.92	0.94	0.94	0.96
Tm (ppm)	0.43	0.02	0.32	0.27	0.82	0.82	0.88	0.87	0.8	0.78	0.83	0.82	0.86
Yb (ppm)	0.52	0.05	0.36	0.34	0.84	0.8	0.82	0.77	0.68	0.65	0.7	0.69	0.73
Lu (ppm)	0.54	0.03	0.33	0.34	0.81	0.72	0.72	0.66	0.56	0.53	0.59	0.57	0.61
Hf (ppm)	0.94	0.21	0.65	0.74	0.69	0.65	0.5	0.36	0.19	0.09	0.18	0.15	0.16
Ta (ppm)	0.99	0.19	0.7	0.83	0.74	0.7	0.55	0.41	0.22	0.12	0.21	0.18	0.2
W (ppm)	0.19	-0.1	0.19	0.31	0.14	0.11	0.09	0.03	-0.06	-0.08	-0.06	-0.07	-0.06
Tl (ppm)	0.56	0.62	0.4	0.55	0.4	0.42	0.33	0.26	0.17	0.1	0.15	0.14	0.15
Pb (ppm)	0.5	-0.1	0.81	0.49	0.41	0.4	0.3	0.2	0.03	-0	0.03	0.02	0.06
Th (ppm)	0.91	0.21	0.66	0.75	0.75	0.76	0.67	0.56	0.41	0.32	0.39	0.37	0.38
U (ppm)	0.33	0.61	0.17	0.42	0.44	0.51	0.53	0.54	0.51	0.47	0.49	0.49	0.48

	Ho (ppm)	Er (ppm)	Tm (ppm)	Yb (ppm)	Lu (ppm)	Hf (ppm)	Ta (ppm)	W (ppm)	Tl (ppm)	Pb (ppm)	Th (ppm)	U (ppm)
Ho (ppm)	1											
Er (ppm)	0.99	1										
Tm (ppm)	0.9	0.95	1									
Yb (ppm)	0.79	0.86	0.96	1								
Lu (ppm)	0.68	0.77	0.9	0.97	1							
Hf (ppm)	0.2	0.27	0.42	0.52	0.55	1						
Ta (ppm)	0.23	0.31	0.45	0.54	0.57	0.96	1					
W (ppm)	-0.03	-0.03	-0	-0.03	-0	0.08	0.18	1				
Tl (ppm)	0.15	0.17	0.21	0.25	0.23	0.52	0.55	0.04	1			
Pb (ppm)	0.1	0.13	0.19	0.24	0.23	0.39	0.45	0.2	0.24	1		
Th (ppm)	0.4	0.46	0.55	0.61	0.61	0.88	0.92	0.13	0.54	0.44	1	
U (ppm)	0.47	0.46	0.4	0.35	0.28	0.28	0.32	0.08	0.59	-0.08	0.41	1

Table S3: Pearson product-moment values for well 2-30-070-24W5. Table values greater than 0.8 are highlighted in green while values below <0.8 are highlighted in red.

	Al2O3 (wt %)	SiO2 (wt %)	TiO2 (wt %)	Fe2O3 (wt %)	MnO (wt %)	MgO (wt %)	CaO (wt %)	Na2O (wt %)	K2O (wt %)	P2O5 (wt %)	Ba (ppm)	Cr (ppm)	Sc (ppm)
Al2O3 (%)	1												
SiO2 (%)	-0.18	1											
TiO2 (%)	0.92	-0.07	1										
Fe2O3(%)	0.591	-0.25	0.508	1									
MnO (%)	-0.41	-0.25	-0.44	-0.32	1								
MgO (%)	-0.27	-0.77	-0.31	-0.29	0.48	1							
CaO (%)	-0.53	-0.64	-0.6	-0.24	0.41	0.83	1						
Na2O (%)	0.531	-0.06	0.601	0.208	-0.7	-0.13	-0.32	1					
K2O (%)	0.973	-0.11	0.908	0.531	-0.4	-0.34	-0.6	0.45	1				
P2O5 (%)	-0.28	-0.2	-0.32	0.428	-0.2	0.1	0.39	-0.06	-0.4	1			
Ba (ppm)	0.866	0.12	0.835	0.418	-0.4	-0.45	-0.69	0.49	0.87	-0.41	1		
Cr (ppm)	0.451	-0.2	0.423	0.856	-0.3	-0.22	-0.12	0.12	0.36	0.6	0.28	1	
Sc (ppm)	0.976	-0.22	0.893	0.633	-0.4	-0.26	-0.48	0.48	0.95	-0.23	0.83	0.5	1
Sr (ppm)	0.753	-0.21	0.674	0.516	-0.1	-0.13	-0.3	0.18	0.71	-0.18	0.67	0.46	0.75
Zr (ppm)	-0	0.51	0.289	-0.13	-0.3	-0.37	-0.46	0.22	0.03	-0.2	0.14	0.01	-0
Be (ppm)	0.922	-0.22	0.803	0.623	-0.3	-0.23	-0.42	0.38	0.86	-0.16	0.76	0.56	0.91
V (ppm)	0.619	-0.26	0.516	0.931	-0.3	-0.29	-0.24	0.13	0.57	0.4	0.43	0.91	0.66
Co (ppm)	0.464	-0.22	0.412	0.92	-0.3	-0.32	-0.23	0.17	0.42	0.48	0.29	0.83	0.51
Ni (ppm)	0.838	-0.33	0.758	0.8	-0.2	-0.21	-0.36	0.26	0.82	-0	0.63	0.66	0.85
Cu (ppm)	0.52	-0.26	0.544	0.622	-0.2	-0.16	-0.26	0.15	0.53	0.05	0.38	0.44	0.52
Zn (ppm)	0.266	-0.16	0.216	0.211	-0.2	-0.03	-0.04	0.11	0.25	-0.07	0.17	0.15	0.27
Ga (ppm)	0.971	-0.23	0.87	0.619	-0.4	-0.25	-0.48	0.46	0.93	-0.23	0.82	0.51	0.95
Rb (ppm)	0.968	-0.17	0.865	0.586	-0.3	-0.3	-0.53	0.38	0.96	-0.3	0.84	0.47	0.95
Y (ppm)	0.221	-0.16	0.328	0.567	-0.5	-0.07	-0	0.4	0.12	0.63	0.05	0.67	0.28
Nb (ppm)	0.901	-0.09	0.985	0.491	-0.5	-0.31	-0.6	0.64	0.89	-0.32	0.82	0.41	0.87
Mo(ppm)	0.097	-0.11	0.097	0.733	-0.3	-0.22	-0.04	0.24	0.04	0.61	0.02	0.56	0.12
Sn (ppm)	0.355	-0.37	0.321	0.288	-0.2	0.18	0.12	0.2	0.3	0.1	0.26	0.33	0.35
Cs (ppm)	0.906	-0.24	0.764	0.619	-0.3	-0.22	-0.41	0.23	0.88	-0.18	0.74	0.56	0.9
La (ppm)	0.801	-0.25	0.787	0.757	-0.5	-0.23	-0.35	0.5	0.71	0.19	0.61	0.75	0.81
Ce (ppm)	0.841	-0.04	0.876	0.617	-0.5	-0.39	-0.58	0.59	0.81	-0.13	0.73	0.5	0.84
Pr (ppm)	0.734	-0.05	0.771	0.696	-0.6	-0.37	-0.47	0.56	0.68	0.11	0.6	0.63	0.76
Nd (ppm)	0.656	0	0.704	0.68	-0.6	-0.39	-0.46	0.55	0.6	0.17	0.53	0.61	0.69
Sm (ppm)	0.54	0.11	0.613	0.592	-0.6	-0.42	-0.46	0.54	0.5	0.16	0.44	0.51	0.59
Eu (ppm)	0.51	0.12	0.547	0.624	-0.6	-0.45	-0.44	0.49	0.47	0.22	0.41	0.53	0.57
Gd (ppm)	0.456	0.11	0.544	0.566	-0.6	-0.38	-0.4	0.54	0.41	0.24	0.36	0.5	0.52
Tb (ppm)	0.447	0.12	0.561	0.531	-0.6	-0.38	-0.41	0.55	0.41	0.2	0.36	0.47	0.5
Dy (ppm)	0.475	0.08	0.61	0.529	-0.6	-0.35	-0.41	0.58	0.44	0.18	0.39	0.48	0.52
Ho (ppm)	0.486	0.03	0.632	0.527	-0.6	-0.3	-0.38	0.6	0.44	0.2	0.38	0.51	0.53
Er (ppm)	0.516	-0	0.68	0.512	-0.6	-0.28	-0.38	0.62	0.47	0.17	0.41	0.52	0.55
Tm (ppm)	0.562	0.01	0.743	0.47	-0.6	-0.29	-0.43	0.64	0.52	0.07	0.48	0.49	0.58
Yb (ppm)	0.57	0.03	0.765	0.428	-0.6	-0.29	-0.46	0.64	0.54	0.01	0.5	0.46	0.58
Lu (ppm)	0.546	0.05	0.756	0.393	-0.6	-0.3	-0.46	0.63	0.52	-0.02	0.49	0.44	0.55
Hf (ppm)	-0	0.49	0.289	-0.14	-0.3	-0.37	-0.46	0.22	0.03	-0.21	0.13	0.01	-0
Ta (ppm)	0.886	-0.08	0.973	0.464	-0.5	-0.3	-0.6	0.7	0.87	-0.32	0.82	0.37	0.85
W (ppm)	0.663	0.06	0.66	0.437	-0.5	-0.43	-0.47	0.21	0.7	-0.16	0.62	0.47	0.66
Tl (ppm)	0.715	-0.21	0.658	0.789	-0.3	-0.25	-0.34	0.29	0.68	0.07	0.55	0.59	0.74
Pb (ppm)	0.385	-0.09	0.408	0.509	-0.4	-0.25	-0.28	0.41	0.37	0.15	0.25	0.39	0.38
Th (ppm)	0.821	-0	0.931	0.483	-0.5	-0.36	-0.61	0.63	0.81	-0.26	0.75	0.42	0.8
U (ppm)	0.185	-0.14	0.232	0.785	-0.4	-0.22	-0.05	0.23	0.09	0.77	0.05	0.84	0.24

	Sr (ppm)	Zr (ppm)	Be (ppm)	V (ppm)	Co (ppm)	Ni (ppm)	Cu (ppm)	Zn (ppm)	Ga (ppm)	Rb (ppm)	Y (ppm)	Nb (ppm)	Mo (ppm)
Sr (ppm)	1												
Zr (ppm)	-0.1	1											
Be (ppm)	0.76	-0.06	1										
V (ppm)	0.54	-0.19	0.67	1									
Co (ppm)	0.4	-0.12	0.48	0.92	1								
Ni (ppm)	0.71	-0.14	0.84	0.83	0.76	1							
Cu (ppm)	0.44	-0.05	0.47	0.57	0.7	0.79	1						
Zn (ppm)	0.24	-0.06	0.3	0.22	0.19	0.3	0.26	1					
Ga (ppm)	0.76	-0.05	0.98	0.67	0.5	0.87	0.53	0.32	1				
Rb (ppm)	0.74	-0.02	0.95	0.65	0.47	0.86	0.53	0.27	0.98	1			
Y (ppm)	0.18	0.29	0.2	0.51	0.58	0.34	0.34	0.09	0.2	0.13	1		
Nb (ppm)	0.63	0.31	0.77	0.5	0.42	0.74	0.54	0.23	0.86	0.85	0.36	1	
Mo(ppm)	-0	-0.03	0.09	0.54	0.71	0.34	0.43	0.09	0.1	0.06	0.57	0.12	1
Sn (ppm)	0.29	-0.12	0.36	0.31	0.22	0.36	0.22	0.19	0.37	0.35	0.21	0.31	0.12
Cs (ppm)	0.75	-0.11	0.96	0.71	0.5	0.87	0.5	0.27	0.95	0.97	0.14	0.73	0.05
La (ppm)	0.69	0.14	0.83	0.75	0.67	0.82	0.59	0.28	0.83	0.78	0.68	0.8	0.39
Ce (ppm)	0.66	0.36	0.78	0.57	0.54	0.75	0.56	0.27	0.82	0.8	0.55	0.89	0.28
Pr (ppm)	0.6	0.35	0.7	0.64	0.64	0.71	0.55	0.26	0.72	0.68	0.73	0.79	0.42

	Sr	Zr	Be	V	Co	Ni	Cu	Zn	Ga	Rb	Y	Nb	Mo
	(ppm)	(ppm)	(ppm)	(ppm)	(ppm)	(ppm)	(ppm)	(ppm)	(ppm)	(ppm)	(ppm)	(ppm)	(ppm)
Nd (ppm)	0.53	0.38	0.61	0.61	0.63	0.65	0.51	0.23	0.63	0.59	0.78	0.72	0.46
Sm (ppm)	0.4	0.44	0.45	0.5	0.57	0.52	0.43	0.18	0.49	0.45	0.77	0.63	0.46
Eu (ppm)	0.36	0.36	0.43	0.53	0.61	0.52	0.43	0.16	0.46	0.43	0.75	0.56	0.49
Gd (ppm)	0.32	0.45	0.37	0.46	0.55	0.45	0.4	0.15	0.4	0.36	0.82	0.57	0.49
Tb (ppm)	0.3	0.5	0.34	0.43	0.53	0.43	0.39	0.13	0.38	0.34	0.82	0.59	0.46
Dy (ppm)	0.32	0.52	0.35	0.44	0.52	0.45	0.41	0.13	0.41	0.37	0.84	0.64	0.45
Ho (ppm)	0.33	0.52	0.37	0.45	0.52	0.45	0.41	0.13	0.42	0.38	0.86	0.67	0.44
Er (ppm)	0.34	0.55	0.4	0.45	0.5	0.47	0.41	0.14	0.46	0.42	0.85	0.72	0.4
Tm (ppm)	0.36	0.6	0.44	0.43	0.45	0.48	0.4	0.13	0.5	0.48	0.78	0.79	0.33
Yb (ppm)	0.36	0.63	0.45	0.4	0.41	0.46	0.38	0.13	0.51	0.49	0.73	0.81	0.28
Lu (ppm)	0.34	0.67	0.43	0.36	0.37	0.43	0.34	0.13	0.5	0.47	0.7	0.8	0.26
Hf (ppm)	-0.1	1	-0.06	-0.2	-0.11	-0.13	-0	-0.1	-0	-0.02	0.28	0.32	-0
Ta (ppm)	0.59	0.33	0.76	0.46	0.39	0.7	0.49	0.21	0.84	0.83	0.36	0.99	0.13
W (ppm)	0.46	0.19	0.63	0.54	0.39	0.62	0.43	0.21	0.67	0.73	0.22	0.66	0.06
Tl (ppm)	0.61	-0.02	0.69	0.69	0.68	0.83	0.77	0.39	0.72	0.69	0.47	0.64	0.51
Pb (ppm)	0.19	0.14	0.29	0.44	0.57	0.49	0.6	0.36	0.37	0.34	0.55	0.48	0.5
Th (ppm)	0.57	0.48	0.73	0.47	0.41	0.66	0.47	0.19	0.79	0.78	0.46	0.95	0.17
U (ppm)	0.16	0.08	0.22	0.75	0.84	0.44	0.45	0.08	0.21	0.15	0.83	0.25	0.78

	Sn	Cs	La	Ce	Pr	Nd	Sm	Eu	Gd	Tb	Dy	Ho	Er	Tm
	(ppm)	(ppm)	(ppm)	(ppm)	(ppm)	(ppm)	(ppm)	(ppm)	(ppm)	(ppm)	(ppm)	(ppm)	(ppm)	(ppm)
Sn (ppm)	1													
Cs (ppm)	0.37	1												
La (ppm)	0.39	0.77	1											
Ce (ppm)	0.25	0.72	0.91	1										
Pr (ppm)	0.25	0.63	0.93	0.96	1									
Nd (ppm)	0.21	0.54	0.88	0.93	0.99	1								
Sm (ppm)	0.12	0.38	0.75	0.85	0.93	0.97	1							
Eu (ppm)	0.1	0.37	0.7	0.79	0.89	0.94	0.98	1						
Gd (ppm)	0.09	0.29	0.7	0.79	0.9	0.95	0.99	0.98	1					
Tb (ppm)	0.09	0.27	0.68	0.79	0.89	0.94	0.98	0.97	0.99	1				
Dy (ppm)	0.12	0.29	0.72	0.81	0.9	0.94	0.97	0.94	0.98	0.99	1			
Ho (ppm)	0.15	0.3	0.75	0.81	0.9	0.93	0.95	0.9	0.96	0.97	0.99	1		
Er (ppm)	0.19	0.33	0.77	0.83	0.89	0.91	0.91	0.85	0.91	0.94	0.97	0.99	1	
Tm (ppm)	0.2	0.38	0.77	0.84	0.87	0.88	0.86	0.79	0.86	0.88	0.93	0.96	0.98	1
Yb (ppm)	0.2	0.39	0.76	0.84	0.85	0.85	0.82	0.74	0.81	0.85	0.9	0.93	0.97	0.99
Lu (ppm)	0.19	0.37	0.73	0.82	0.83	0.82	0.8	0.71	0.79	0.82	0.88	0.91	0.95	0.99
Hf (ppm)	-0.1	-0.1	0.15	0.36	0.35	0.37	0.43	0.34	0.43	0.48	0.5	0.51	0.54	0.6
Ta (ppm)	0.3	0.7	0.78	0.89	0.78	0.72	0.64	0.56	0.58	0.6	0.65	0.68	0.73	0.8
W (ppm)	0.25	0.7	0.6	0.6	0.54	0.48	0.39	0.37	0.32	0.33	0.37	0.38	0.42	0.48
Tl (ppm)	0.31	0.67	0.79	0.75	0.77	0.73	0.66	0.65	0.61	0.58	0.58	0.57	0.55	0.52
Pb (ppm)	0.28	0.25	0.57	0.58	0.63	0.64	0.62	0.6	0.61	0.61	0.62	0.62	0.61	0.57
Th (ppm)	0.26	0.68	0.82	0.94	0.86	0.81	0.74	0.65	0.68	0.7	0.75	0.77	0.82	0.88
U (ppm)	0.18	0.18	0.6	0.41	0.59	0.63	0.6	0.63	0.64	0.62	0.62	0.64	0.62	0.56

	Yb	Lu	Hf	Ta	W	Tl	Pb	Th	U
	(ppm)	(ppm)	(ppm)	(ppm)	(ppm)	(ppm)	(ppm)	(ppm)	(ppm)
Yb (ppm)	1								
Lu (ppm)	1	1							
Hf (ppm)	0.64	0.68	1						
Ta (ppm)	0.82	0.81	0.34	1					
W (ppm)	0.5	0.49	0.19	0.63	1				
Tl (ppm)	0.49	0.46	-0	0.62	0.51	1			
Pb (ppm)	0.54	0.51	0.15	0.47	0.36	0.68	1		
Th (ppm)	0.9	0.9	0.48	0.96	0.62	0.61	0.47	1	
U (ppm)	0.5	0.48	0.08	0.24	0.2	0.49	0.5	0.31	1

Table S4: Pearson product-moment values for well 11-20-082-02W6. Table values greater than 0.8 are highlighted in green while values below <0.8 are highlighted in red.

		SiO2	Al2O3	Fe2O3	MgO	CaO	Na2O	K2O	TiO2	P2O5	MnO	Sc	Ba	Co	Cs
		(wt %)	(wt %)	(wt %)	(wt %)	(wt %)	(wt %)	(wt %)	(wt %)	(wt %)	(wt %)	(ppm)	(ppm)	(ppm)	(ppm)
SiO2	(wt %)	1													
Al2O3	(wt %)	-0.53	1												
Fe2O3	(wt %)	-0.53	0.863	1											
MgO	(wt %)	-0.66	-0.27	-0.2	1										
CaO	(wt %)	-0.44	-0.52	-0.41	0.96	1									
Na2O	(wt %)	-0.27	0.56	0.335	-0.21	-0.36	1								
K2O	(wt %)	-0.52	0.987	0.816	-0.25	-0.51	0.63	1							
TiO2	(wt %)	-0.37	0.899	0.702	-0.36	-0.57	0.72	0.92	1						
P2O5	(wt %)	0.58	-0.15	0.05	-0.55	-0.4	-0.55	-0.2	-0.2	1					
MnO	(wt %)	-0.55	-0.34	-0.28	0.93	0.94	-0.38	-0.4	-0.4	-0.3	1				
Sc	(ppm)	-0.5	0.965	0.885	-0.29	-0.52	0.52	0.94	0.88	-0.1	-0.3	1			
Ba	(ppm)	-0.4	0.854	0.602	-0.29	-0.52	0.82	0.89	0.87	-0.4	-0.4	0.77	1		
Co	(ppm)	-0.43	0.927	0.893	-0.33	-0.54	0.36	0.88	0.8	0.09	-0.3	0.93	0.72	1	
Cs	(ppm)	-0.48	0.962	0.891	-0.3	-0.54	0.39	0.92	0.81	-0	-0.4	0.93	0.75	0.94	1
Ga	(ppm)	-0.48	0.979	0.874	-0.31	-0.55	0.44	0.94	0.85	-0	-0.3	0.94	0.79	0.95	0.99
Hf	(ppm)	0.56	-0.28	-0.35	-0.38	-0.27	-0.05	-0.3	0.05	0.2	-0.3	-0.3	-0.2	-0.3	-0.3
Nb	(ppm)	-0.35	0.858	0.673	-0.35	-0.55	0.75	0.88	0.99	-0.2	-0.4	0.83	0.85	0.76	0.76
Rb	(ppm)	-0.5	0.99	0.877	-0.3	-0.54	0.48	0.97	0.86	-0.1	-0.4	0.95	0.82	0.94	0.99
Sr	(ppm)	-0.32	0.914	0.731	-0.43	-0.64	0.53	0.89	0.88	-0	-0.4	0.86	0.83	0.87	0.89
Ta	(ppm)	-0.27	0.712	0.51	-0.32	-0.5	0.64	0.73	0.82	-0.3	-0.4	0.69	0.73	0.62	0.64
Th	(ppm)	-0.07	0.764	0.677	-0.61	-0.76	0.52	0.74	0.87	0.12	-0.6	0.78	0.68	0.75	0.75
U	(ppm)	0.14	0.549	0.56	-0.67	-0.75	0.38	0.52	0.69	0.32	-0.7	0.61	0.45	0.61	0.55
Zr	(ppm)	0.57	-0.31	-0.37	-0.37	-0.25	-0.07	-0.3	0.03	0.22	-0.3	-0.3	-0.2	-0.3	-0.3
Y	(ppm)	0.24	0.487	0.489	-0.72	-0.76	0.26	0.45	0.66	0.39	-0.7	0.55	0.38	0.55	0.51
La	(ppm)	-0.01	0.786	0.741	-0.7	-0.83	0.35	0.74	0.8	0.33	-0.7	0.8	0.63	0.82	0.82
Ce	(ppm)	0.06	0.725	0.713	-0.72	-0.84	0.34	0.68	0.77	0.37	-0.7	0.76	0.56	0.77	0.76
Pr	(ppm)	0.01	0.742	0.7	-0.68	-0.81	0.32	0.69	0.78	0.32	-0.7	0.77	0.58	0.78	0.78
Nd	(ppm)	0.06	0.715	0.705	-0.71	-0.83	0.29	0.67	0.74	0.37	-0.7	0.76	0.54	0.77	0.76
Sm	(ppm)	0.11	0.635	0.655	-0.71	-0.8	0.28	0.59	0.7	0.38	-0.7	0.69	0.46	0.71	0.67
Eu	(ppm)	0.08	0.676	0.728	-0.71	-0.8	0.23	0.63	0.68	0.45	-0.7	0.74	0.47	0.76	0.72
Gd	(ppm)	0.2	0.565	0.577	-0.75	-0.81	0.21	0.52	0.65	0.47	-0.7	0.63	0.4	0.65	0.6
Tb	(ppm)	0.23	0.533	0.548	-0.76	-0.82	0.32	0.5	0.67	0.4	-0.8	0.6	0.42	0.6	0.55
Dy	(ppm)	0.21	0.496	0.502	-0.7	-0.76	0.29	0.47	0.66	0.37	-0.7	0.57	0.38	0.56	0.51
Ho	(ppm)	0.21	0.513	0.478	-0.71	-0.77	0.43	0.5	0.72	0.28	-0.7	0.57	0.45	0.53	0.5
Er	(ppm)	0.17	0.536	0.473	-0.68	-0.75	0.41	0.52	0.74	0.24	-0.7	0.58	0.47	0.55	0.53
Tm	(ppm)	0.18	0.498	0.388	-0.65	-0.72	0.49	0.5	0.75	0.14	-0.7	0.53	0.49	0.48	0.45
Yb	(ppm)	0.17	0.482	0.354	-0.63	-0.69	0.48	0.48	0.76	0.12	-0.6	0.52	0.5	0.47	0.43
Lu	(ppm)	0.18	0.452	0.355	-0.61	-0.68	0.5	0.46	0.73	0.11	-0.7	0.49	0.46	0.43	0.4
Mo	(ppm)	0.25	0.101	0.325	-0.46	-0.44	0.2	0.08	0.18	0.26	-0.5	0.21	0.08	0.24	0.14

		SiO2	Al2O3	Fe2O3	MgO	CaO	Na2O	K2O	TiO2	P2O5	MnO	Sc	Ba	Co	Cs
		(wt %)	(wt %)	(wt %)	(wt %)	(wt %)	(wt %)	(wt %)	(wt %)	(wt %)	(wt %)	(ppm)	(ppm)	(ppm)	(ppm)
Cu	(ppm)	-0.19	0.744	0.831	-0.49	-0.64	0.42	0.72	0.7	0.1	-0.6	0.79	0.56	0.78	0.75
Pb	(ppm)	0.04	0.292	0.258	-0.41	-0.46	0.52	0.26	0.37	-0	-0.4	0.32	0.5	0.28	0.28
Zn	(ppm)	-0.28	0.392	0.482	-0.09	-0.17	0.39	0.39	0.43	-0.1	-0.2	0.49	0.35	0.4	0.31
Ni	(ppm)	-0.5	0.942	0.923	-0.27	-0.5	0.43	0.91	0.81	-0	-0.3	0.93	0.75	0.97	0.93
V	(ppm)	-0.45	0.963	0.91	-0.35	-0.58	0.41	0.92	0.83	0.03	-0.4	0.96	0.75	0.96	0.99
Cr	(ppm)	-0.36	0.939	0.882	-0.43	-0.64	0.43	0.9	0.86	0.07	-0.5	0.93	0.75	0.93	0.95
W	(ppm)	-0.02	0.16	0.11	-0.22	-0.25	0.45	0.14	0.27	-0.2	-0.3	0.19	0.37	0.13	0.11
Sn	(ppm)	-0.35	0.89	0.838	-0.37	-0.57	0.4	0.85	0.77	0.14	-0.4	0.87	0.69	0.92	0.88
S	(ppm)	-0.24	0.786	0.911	-0.47	-0.63	0.39	0.75	0.72	0.23	-0.5	0.82	0.56	0.84	0.81
Tl	(ppm)	0.34	0.128	0.556	-0.48	-0.46	0.06	0.09	0.16	0.42	-0.5	0.25	-0	0.36	0.28

		Ga	Hf	Nb	Rb	Sr	Ta	Th	U	Zr	Y	La	Ce	Pr	Nd
		(ppm)	(ppm)	(ppm)	(ppm)	(ppm)	(ppm)	(ppm)	(ppm)	(ppm)	(ppm)	(ppm)	(ppm)	(ppm)	(ppm)
Ga	(ppm)	1													
Hf	(ppm)	-0.3	1												
Nb	(ppm)	0.81	0.07	1											
Rb	(ppm)	0.99	-0.3	0.81	1										
Sr	(ppm)	0.92	-0.1	0.85	0.91	1									
Ta	(ppm)	0.67	0.1	0.8	0.69	0.69	1								
Th	(ppm)	0.77	0.29	0.87	0.77	0.81	0.74	1							
U	(ppm)	0.56	0.37	0.71	0.55	0.6	0.58	0.86	1						
Zr	(ppm)	-0.3	0.99	0.05	-0.3	-0.09	0.08	0.26	0.35	1					
Y	(ppm)	0.52	0.5	0.66	0.5	0.58	0.51	0.86	0.89	0.48	1				
La	(ppm)	0.83	0.17	0.78	0.81	0.84	0.64	0.94	0.85	0.15	0.86	1			
Ce	(ppm)	0.76	0.23	0.75	0.75	0.78	0.61	0.93	0.9	0.21	0.9	0.98	1		
Pr	(ppm)	0.79	0.23	0.76	0.77	0.82	0.61	0.92	0.86	0.21	0.89	0.98	0.97	1	
Nd	(ppm)	0.76	0.22	0.72	0.75	0.76	0.6	0.92	0.87	0.2	0.89	0.97	0.98	0.98	1
Sm	(ppm)	0.68	0.3	0.69	0.66	0.69	0.55	0.89	0.9	0.28	0.9	0.94	0.97	0.96	0.98
Eu	(ppm)	0.72	0.16	0.66	0.71	0.71	0.52	0.86	0.85	0.14	0.88	0.94	0.97	0.95	0.97
Gd	(ppm)	0.61	0.35	0.64	0.59	0.64	0.5	0.87	0.88	0.34	0.93	0.92	0.95	0.95	0.96
Tb	(ppm)	0.56	0.42	0.68	0.55	0.61	0.54	0.89	0.92	0.4	0.96	0.9	0.94	0.92	0.94
Dy	(ppm)	0.52	0.46	0.67	0.5	0.56	0.55	0.87	0.91	0.44	0.95	0.86	0.91	0.88	0.9
Ho	(ppm)	0.52	0.48	0.73	0.51	0.6	0.57	0.89	0.9	0.46	0.93	0.85	0.89	0.87	0.88
Er	(ppm)	0.55	0.52	0.75	0.54	0.63	0.64	0.92	0.91	0.5	0.93	0.86	0.89	0.88	0.88
Tm	(ppm)	0.49	0.58	0.77	0.49	0.6	0.65	0.89	0.88	0.55	0.9	0.8	0.83	0.82	0.81
Yb	(ppm)	0.47	0.56	0.78	0.46	0.59	0.65	0.87	0.84	0.54	0.89	0.77	0.79	0.79	0.78
Lu	(ppm)	0.44	0.61	0.76	0.44	0.55	0.62	0.85	0.87	0.58	0.87	0.74	0.78	0.76	0.75
Mo	(ppm)	0.09	0.14	0.19	0.11	0.09	0.14	0.37	0.56	0.13	0.5	0.37	0.45	0.36	0.42
Cu	(ppm)	0.74	-0.1	0.67	0.75	0.65	0.6	0.72	0.68	-0.2	0.63	0.76	0.76	0.73	0.76
Pb	(ppm)	0.27	0.13	0.39	0.28	0.39	0.31	0.46	0.45	0.12	0.4	0.4	0.42	0.43	0.41
Zn	(ppm)	0.33	-0.1	0.44	0.34	0.28	0.31	0.39	0.34	-0.1	0.37	0.32	0.36	0.35	0.36

		Ga	Hf	Nb	Rb	Sr	Ta	Th	U	Zr	Y	La	Ce	Pr	Nd
		(ppm)	(ppm)	(ppm)	(ppm)	(ppm)	(ppm)	(ppm)	(ppm)	(ppm)	(ppm)	(ppm)	(ppm)	(ppm)	(ppm)
Ni	(ppm)	0.94	-0.3	0.76	0.94	0.85	0.61	0.72	0.58	-0.3	0.5	0.78	0.74	0.74	0.72
V	(ppm)	0.98	-0.3	0.78	0.98	0.89	0.66	0.78	0.6	-0.3	0.56	0.84	0.79	0.8	0.79
Cr	(ppm)	0.96	-0.1	0.82	0.95	0.91	0.68	0.84	0.68	-0.1	0.65	0.89	0.85	0.86	0.84
W	(ppm)	0.11	0.12	0.29	0.13	0.26	0.22	0.26	0.27	0.12	0.25	0.19	0.22	0.25	0.19
Sn	(ppm)	0.9	-0.3	0.74	0.89	0.83	0.55	0.71	0.58	-0.3	0.52	0.79	0.75	0.73	0.74
S	(ppm)	0.79	-0.1	0.71	0.79	0.71	0.51	0.78	0.77	-0.2	0.67	0.84	0.85	0.79	0.81
Tl	(ppm)	0.18	0.19	0.2	0.19	0.15	0.1	0.43	0.65	0.18	0.55	0.54	0.6	0.51	0.56

		Sm	Eu	Gd	Tb	Dy	Ho	Er	Tm	Yb	Lu	Mo	Cu	Pb	Zn
		(ppm)	(ppm)	(ppm)	(ppm)	(ppm)	(ppm)	(ppm)	(ppm)	(ppm)	(ppm)	(ppm)	(ppm)	(ppm)	(ppm)
Sm	(ppm)	1													
Eu	(ppm)	0.96	1												
Gd	(ppm)	0.97	0.96	1											
Tb	(ppm)	0.97	0.93	0.97	1										
Dy	(ppm)	0.93	0.9	0.95	0.97	1									
Ho	(ppm)	0.91	0.84	0.91	0.95	0.94	1								
Er	(ppm)	0.89	0.84	0.9	0.94	0.94	0.95	1							
Tm	(ppm)	0.83	0.75	0.83	0.9	0.9	0.94	0.96	1						
Yb	(ppm)	0.79	0.72	0.8	0.88	0.88	0.91	0.94	0.96	1					
Lu	(ppm)	0.78	0.69	0.78	0.86	0.86	0.93	0.93	0.97	0.96	1				
Mo	(ppm)	0.46	0.45	0.45	0.52	0.49	0.46	0.42	0.4	0.39	0.42	1			
Cu	(ppm)	0.73	0.76	0.67	0.68	0.65	0.63	0.61	0.57	0.53	0.55	0.53	1		
Pb	(ppm)	0.4	0.36	0.4	0.44	0.39	0.44	0.42	0.44	0.42	0.43	0.48	0.37	1	
Zn	(ppm)	0.38	0.37	0.36	0.38	0.36	0.4	0.37	0.37	0.34	0.37	0.33	0.52	0.41	1
Ni	(ppm)	0.66	0.71	0.59	0.54	0.51	0.49	0.5	0.45	0.42	0.41	0.28	0.81	0.32	0.45
V	(ppm)	0.71	0.76	0.65	0.61	0.56	0.54	0.56	0.49	0.48	0.45	0.24	0.81	0.33	0.38
Cr	(ppm)	0.78	0.81	0.72	0.69	0.64	0.64	0.65	0.6	0.58	0.56	0.27	0.83	0.39	0.38
W	(ppm)	0.2	0.16	0.21	0.25	0.24	0.29	0.28	0.33	0.34	0.34	0.34	0.23	0.87	0.42
Sn	(ppm)	0.66	0.73	0.62	0.57	0.53	0.53	0.51	0.45	0.44	0.42	0.22	0.74	0.25	0.35
S	(ppm)	0.8	0.85	0.74	0.73	0.69	0.68	0.65	0.58	0.53	0.55	0.52	0.88	0.35	0.47
Tl	(ppm)	0.58	0.64	0.55	0.59	0.56	0.5	0.46	0.42	0.38	0.41	0.87	0.57	0.26	0.17

		Ni	V	Cr	W	Sn	S	Tl
		(ppm)	(ppm)	(ppm)	(ppm)	(ppm)	(ppm)	(ppm)
Ni	(ppm)	1						
V	(ppm)	0.96	1					
Cr	(ppm)	0.94	0.97	1				
W	(ppm)	0.18	0.17	0.21	1			

		Ni	V	Cr	W	Sn	S	Tl
		(ppm)	(ppm)	(ppm)	(ppm)	(ppm)	(ppm)	(ppm)
Sn	(ppm)	0.91	0.91	0.88	0.13	1		
S	(ppm)	0.86	0.85	0.86	0.17	0.83	1	
Tl	(ppm)	0.35	0.38	0.39	0.09	0.33	0.72	1

Table S5: Pearson product-moment values for well d-48-A/94-B-9. Table values greater than 0.8 are highlighted in green while values below <0.8 are highlighted in red.

	Al2O3	SiO2	TiO2	Fe2O3	MnO	MgO	CaO	Na2O	K2O	P2O5	Ba	Cr	S	Sc	Sr	Zn	Zr	Be	V
	(wt%)	(wt%)	(wt%)	(wt%)	(wt%)	(wt%)	(wt%)	(wt%)	(wt%)	(wt%)	(ppm)	(ppm)	(ppm)	(ppm)	(ppm)	(ppm)	(ppm)	(ppm)	(ppm)
Al2O3 (wt %)	1																		
SiO2 (wt %)	0.84	1																	
TiO2 (wt %)	0.95	0.93	1																
Fe2O3 (wt %)	0.18	0.08	0.16	1															
MnO (wt %)	-0.43	-0.4	-0.4	0.326	1														
MgO (wt %)	-0.55	-0.6	-0.6	0.329	0.71	1													
CaO (wt %)	-0.87	-1	-0.9	-0.25	0.34	0.51	1												
Na2O (wt %)	0.67	0.93	0.81	0.06	-0.3	-0.6	-0.9	1											
K2O (wt %)	0.94	0.78	0.9	0.231	-0.4	-0.5	-0.8	0.57	1										
P2O5 (wt %)	-0.28	-0.4	-0.3	-0.32	-0.1	-0.1	0.4	-0.4	-0.2	1									
Ba (ppm)	-0.2	-0.3	-0.2	0.142	0.39	0.47	0.2	-0.2	-0.2	0.14	1								
Cr (ppm)	0.67	0.43	0.61	0.003	-0.4	-0.4	-0.5	0.19	0.71	0.1	-0.21	1							
S (ppm)	0.08	-0.1	0.04	0.711	0.22	0.26	-0.1	-0.1	0.13	-0.2	-0.09	-0.1	1						
Sc (ppm)	0.93	0.77	0.89	0.2	-0.4	-0.6	-0.8	0.6	0.92	-0.1	-0.18	0.67	0.15	1					
Sr (ppm)	-0.64	-0.8	-0.7	-0.36	0.07	0.23	0.8	-0.7	-0.6	0.81	0.3	-0.2	-0.2	-0.5	1				
Zn (ppm)	-0.06	-0.2	-0.1	-0.2	-0.2	-0.1	0.2	-0.4	-0.1	0.62	-0.04	0.53	-0.2	-0	0.45	1			
Zr (ppm)	0.39	0.71	0.59	-0.1	-0.2	-0.5	-0.6	0.75	0.27	-0.2	-0.29	0.15	-0.1	0.33	-0.5	-0.13	1		
Be (ppm)	0.85	0.54	0.75	0.187	-0.4	-0.4	-0.7	0.32	0.84	-0.1	-0.17	0.81	0.16	0.79	-0.4	0.22	0.2	1	
V (ppm)	0.36	0.09	0.24	-0.08	-0.3	-0.2	-0.2	-0.1	0.28	0.25	-0.14	0.73	-0.2	0.32	0.05	0.75	-0	0.5	1
Co (ppm)	0.11	0.4	0.23	-0.13	-0.1	-0.1	-0.4	0.56	-0	-0.3	-0.03	-0.2	-0.2	0.02	-0.4	-0.34	0.49	-0.1	-0.2
Ni (ppm)	0.15	-0.1	0.03	-0.29	-0.4	-0.2	0.1	-0.3	0.13	0.68	-0.08	0.66	-0.2	0.2	0.43	0.89	-0.1	0.38	0.8
Cu (ppm)	0.45	0.26	0.38	-0.16	-0.4	-0.4	-0.3	0.04	0.47	0.4	-0.07	0.76	-0.2	0.48	0.03	0.64	0.18	0.6	0.66
Ga (ppm)	0.96	0.75	0.92	0.221	-0.3	-0.5	-0.8	0.58	0.96	-0.2	-0.14	0.75	0.13	0.93	-0.6	0.03	0.32	0.91	0.37
Rb (ppm)	0.95	0.73	0.9	0.196	-0.3	-0.5	-0.8	0.53	0.95	-0.2	-0.17	0.8	0.1	0.92	-0.6	0.07	0.29	0.93	0.44
Y (ppm)	-0.07	-0.2	-0.1	-0.3	-0.3	-0.2	0.2	-0.2	-0	0.95	0.06	0.3	-0.2	0.1	0.64	0.64	-0.1	0.05	0.33
Nb (ppm)	0.92	0.94	0.98	0.148	-0.4	-0.6	-1	0.85	0.85	-0.4	-0.24	0.54	0.07	0.85	-0.7	-0.17	0.65	0.73	0.17
Mo (ppm)	0.35	0.08	0.24	0.042	-0.3	-0.2	-0.2	-0.1	0.29	0.19	-0.11	0.54	0.14	0.28	0.05	0.53	0.01	0.56	0.61
Sn (ppm)	0.62	0.67	0.65	-0.23	-0.4	-0.5	-0.6	0.71	0.46	-0.3	-0.12	0.22	-0.3	0.51	-0.4	-0.23	0.4	0.29	0.1

	Al2O3 (wt%)	SiO2 (wt%)	TiO2 (wt%)	Fe2O3 (wt%)	MnO (wt%)	MgO (wt%)	CaO (wt%)	Na2O (wt%)	K2O (wt%)	P2O5 (wt%)	Ba (ppm)	Cr (ppm)	S (ppm)	Sc (ppm)	Sr (ppm)	Zn (ppm)	Zr (ppm)	Be (ppm)	V (ppm)
Cs (ppm)	0.79	0.43	0.68	0.237	-0.2	-0.3	-0.5	0.18	0.81	-0.1	-0.14	0.84	0.18	0.78	-0.3	0.26	0.05	0.93	0.58
La (ppm)	0.2	0.1	0.15	-0.2	-0.3	-0.3	-0.1	-0	0.21	0.81	0.05	0.38	-0.2	0.35	0.42	0.44	0.1	0.22	0.26
Ce (ppm)	0.56	0.55	0.56	0.004	-0.2	-0.4	-0.5	0.44	0.55	0.23	-0.11	0.46	-0	0.62	-0.2	0.03	0.41	0.44	0.14
Pr (ppm)	0.3	0.23	0.26	-0.17	-0.3	-0.4	-0.2	0.11	0.31	0.64	-0.06	0.48	-0.1	0.42	0.21	0.39	0.19	0.3	0.29
Nd (ppm)	0.25	0.19	0.2	-0.19	-0.3	-0.3	-0.1	0.08	0.26	0.66	-0.07	0.46	-0.1	0.37	0.25	0.41	0.17	0.26	0.28
Sm (ppm)	0.25	0.2	0.21	-0.18	-0.3	-0.3	-0.2	0.09	0.25	0.6	-0.11	0.47	-0.1	0.36	0.19	0.4	0.19	0.26	0.29
Eu (ppm)	0.15	0.09	0.09	-0.2	-0.3	-0.3	-0.1	-0	0.16	0.73	-0.07	0.41	-0.1	0.28	0.33	0.49	0.09	0.19	0.3
Gd (ppm)	0.17	0.11	0.12	-0.23	-0.3	-0.3	-0.1	0	0.18	0.72	-0.08	0.45	-0.1	0.3	0.32	0.49	0.14	0.22	0.31
Tb (ppm)	0.21	0.15	0.17	-0.23	-0.3	-0.3	-0.1	0.03	0.22	0.72	-0.07	0.48	-0.2	0.34	0.31	0.5	0.15	0.25	0.35
Dy (ppm)	0.2	0.13	0.15	-0.22	-0.3	-0.3	-0.1	0.02	0.21	0.74	-0.07	0.47	-0.2	0.34	0.33	0.52	0.15	0.24	0.35
Ho (ppm)	0.17	0.11	0.13	-0.23	-0.3	-0.3	-0.1	-0	0.18	0.79	-0.04	0.44	-0.2	0.32	0.38	0.54	0.14	0.22	0.36
Er (ppm)	0.19	0.13	0.15	-0.23	-0.4	-0.4	-0.1	0.02	0.19	0.8	-0.05	0.45	-0.2	0.34	0.38	0.57	0.17	0.24	0.37
Tm (ppm)	0.27	0.21	0.24	-0.22	-0.4	-0.4	-0.2	0.1	0.25	0.76	-0.06	0.5	-0.2	0.4	0.3	0.57	0.25	0.3	0.4
Yb (ppm)	0.38	0.33	0.36	-0.17	-0.5	-0.5	-0.3	0.21	0.35	0.66	-0.12	0.56	-0.1	0.5	0.17	0.55	0.35	0.39	0.43
Lu (ppm)	0.41	0.36	0.4	-0.17	-0.5	-0.5	-0.3	0.24	0.37	0.61	-0.13	0.58	-0.1	0.52	0.13	0.54	0.4	0.44	0.44
Hf (ppm)	0.4	0.72	0.59	-0.1	-0.2	-0.5	-0.6	0.76	0.27	-0.2	-0.28	0.12	-0.1	0.33	-0.5	-0.16	0.99	0.21	-0
Ta (ppm)	0.34	0.65	0.48	-0.08	-0.3	-0.4	-0.6	0.76	0.19	-0.3	-0.22	-0.1	-0.1	0.25	-0.5	-0.29	0.73	0.09	-0.2
W (ppm)	0.21	0.52	0.34	-0.14	-0.2	-0.3	-0.5	0.66	0.05	-0.3	-0.18	-0.2	-0.1	0.11	-0.4	-0.29	0.65	-0	-0.2
Tl (ppm)	0.19	-0.1	0.07	-0.2	-0.4	-0.1	0	-0.3	0.14	0.44	-0.08	0.6	-0.1	0.17	0.29	0.8	-0.1	0.44	0.81
Pb (ppm)	0.32	0.53	0.4	-0.19	-0.3	-0.3	-0.4	0.63	0.13	-0.3	-0.19	-0.1	-0.2	0.21	-0.4	-0.2	0.53	-0.1	0.08
Th (ppm)	0.92	0.87	0.96	0.186	-0.3	-0.6	-0.9	0.71	0.91	-0.3	-0.24	0.7	0.05	0.89	-0.7	-0.07	0.57	0.78	0.3
U (ppm)	-0.17	-0.3	-0.3	-0.23	-0.2	-0.1	0.3	-0.4	-0.1	0.95	0.08	0.19	-0.1	-0	0.74	0.69	-0.2	0.03	0.37

	Co (ppm)	Ni (ppm)	Cu (ppm)	Ga (ppm)	Rb (ppm)	Y (ppm)	Nb (ppm)	Mo (ppm)	Sn (ppm)	Cs (ppm)	La (ppm)	Ce (ppm)	Pr (ppm)	Nd (ppm)	Sm (ppm)	Eu (ppm)	Gd (ppm)	Tb (ppm)	Dy (ppm)
Co (ppm)	1																		
Ni (ppm)	-0.3	1																	
Cu (ppm)	-0.2	0.74	1																
Ga (ppm)	0.01	0.21	0.52	1															

	Co (ppm)	Ni (ppm)	Cu (ppm)	Ga (ppm)	Rb (ppm)	Y (ppm)	Nb (ppm)	Mo (ppm)	Sn (ppm)	Cs (ppm)	La (ppm)	Ce (ppm)	Pr (ppm)	Nd (ppm)	Sm (ppm)	Eu (ppm)	Gd (ppm)	Tb (ppm)	Dy (ppm)
Rb (ppm)	-0	0.26	0.54	0.99	1														
Y (ppm)	-0.2	0.74	0.54	-0	-0	1													
Nb (ppm)	0.37	-0	0.34	0.89	0.85	-0.1	1												
Mo (ppm)	-0.1	0.61	0.47	0.38	0.41	0.28	0.23	1											
Sn (ppm)	0.45	-0.1	0.06	0.49	0.46	-0.2	0.65	0.08	1										
Cs (ppm)	-0.3	0.43	0.61	0.87	0.92	0.1	0.6	0.53	0.18	1									
La (ppm)	-0.2	0.61	0.6	0.25	0.23	0.93	0.13	0.27	-0	0.26	1								
Ce (ppm)	0.07	0.2	0.48	0.55	0.53	0.48	0.56	0.18	0.28	0.42	0.73	1							
Pr (ppm)	-0.1	0.54	0.59	0.32	0.32	0.83	0.24	0.26	0.05	0.32	0.94	0.88	1						
Nd (ppm)	-0.1	0.55	0.56	0.27	0.27	0.85	0.19	0.26	0.01	0.28	0.93	0.85	1	1					
Sm (ppm)	-0.1	0.53	0.54	0.26	0.27	0.8	0.2	0.27	0.02	0.27	0.87	0.85	0.98	0.99	1				
Eu (ppm)	-0.2	0.61	0.55	0.17	0.17	0.9	0.08	0.27	-0.1	0.21	0.92	0.75	0.96	0.98	0.97	1			
Gd (ppm)	-0.1	0.61	0.58	0.2	0.21	0.89	0.12	0.29	-0	0.24	0.93	0.78	0.98	0.99	0.98	0.99	1		
Tb (ppm)	-0.1	0.63	0.6	0.24	0.24	0.89	0.15	0.29	-0	0.27	0.94	0.79	0.98	0.99	0.98	0.99	1	1	
Dy (ppm)	-0.1	0.65	0.6	0.23	0.23	0.91	0.14	0.31	-0	0.26	0.94	0.76	0.97	0.98	0.97	0.98	0.99	1	1
Ho (ppm)	-0.1	0.67	0.6	0.2	0.21	0.94	0.12	0.31	-0	0.24	0.96	0.73	0.96	0.97	0.94	0.97	0.98	0.99	0.99
Er (ppm)	-0.1	0.7	0.61	0.23	0.22	0.94	0.15	0.31	-0	0.25	0.96	0.7	0.94	0.94	0.91	0.96	0.96	0.97	0.98
Tm (ppm)	-0.1	0.7	0.65	0.3	0.29	0.91	0.24	0.33	0.05	0.29	0.94	0.7	0.92	0.92	0.89	0.92	0.94	0.95	0.96
Yb (ppm)	-0	0.69	0.66	0.4	0.39	0.83	0.37	0.39	0.11	0.37	0.89	0.72	0.88	0.88	0.86	0.88	0.89	0.91	0.93
Lu (ppm)	-0	0.68	0.67	0.43	0.42	0.79	0.41	0.41	0.14	0.39	0.84	0.69	0.85	0.85	0.82	0.84	0.86	0.88	0.89
Hf (ppm)	0.52	-0.1	0.15	0.32	0.29	-0.1	0.66	-0	0.44	0.04	0.07	0.4	0.17	0.15	0.18	0.08	0.12	0.13	0.13
Ta (ppm)	0.85	-0.3	-0	0.23	0.18	-0.2	0.62	-0.1	0.56	-0.1	-0.1	0.27	0.02	-0.01	0.01	-0.1	-0	-0	-0
W (ppm)	0.88	-0.3	-0.1	0.1	0.04	-0.2	0.48	-0.1	0.5	-0.2	-0.1	0.2	-0.03	-0.04	-0	-0.1	-0.1	-0.1	-0.1
Tl (ppm)	-0.3	0.89	0.63	0.25	0.3	0.46	0.03	0.72	-0.1	0.47	0.33	-0	0.25	0.26	0.25	0.32	0.33	0.35	0.37
Pb (ppm)	0.58	-0.1	-0	0.14	0.11	-0.2	0.43	-0	0.75	-0.2	-0.1	0.14	-0.04	-0.06	-0	-0.1	-0.1	-0.1	-0.1
Th (ppm)	0.08	0.11	0.48	0.92	0.92	-0	0.92	0.26	0.51	0.76	0.24	0.63	0.36	0.31	0.31	0.19	0.23	0.27	0.25
U (ppm)	-0.3	0.76	0.47	-0.1	-0.08	0.91	-0.3	0.44	-0.3	0.08	0.78	0.22	0.61	0.63	0.58	0.71	0.69	0.7	0.73

	Ho	Er	Tm	Yb	Lu	Hf	Ta	W	Tl	Pb	Th	U
	(ppm)	(ppm)	(ppm)	(ppm)	(ppm)	(ppm)	(ppm)	(ppm)	(ppm)	(ppm)	(ppm)	(ppm)
Ho (ppm)	1											
Er (ppm)	0.99	1										
Tm (ppm)	0.98	0.99	1									
Yb (ppm)	0.93	0.95	0.98	1								
Lu (ppm)	0.9	0.93	0.96	0.98	1							
Hf (ppm)	0.11	0.15	0.23	0.33	0.39	1						
Ta (ppm)	-0	-0	0.07	0.13	0.16	0.76	1					
W (ppm)	-0.1	-0.1	0.02	0.06	0.08	0.69	0.98	1				
Tl (ppm)	0.39	0.42	0.44	0.47	0.49	-0.1	-0.2	-0.24	1			
Pb (ppm)	-0.1	-0	0.02	0.08	0.09	0.56	0.65	0.63	-0.07	1		
Th (ppm)	0.22	0.24	0.31	0.42	0.46	0.55	0.35	0.2	0.1	0.26	1	
U (ppm)	0.77	0.79	0.75	0.69	0.65	-0.2	-0.3	-0.3	0.57	-0.3	-0.17	1

Table S6: Pearson product-moment values for well c-74-G/94-B-9. Table values greater than 0.8 are highlighted in green while values below <0.8 are highlighted in red.

	Al2O3 (wt %)	SiO2 (wt %)	TiO2 (wt %)	Fe2O3 (wt %)	MnO (wt %)	MgO (wt %)	CaO (wt %)	Na2O (wt %)	K2O (wt %)	P2O5 (wt %)	Ba (ppm)	Cr (ppm)	S (ppm)	Sc (ppm)	Sr (ppm)
Al2O3 (wt %)	1														
SiO2 (wt %)	0.89	1													
TiO2 (wt %)	0.96	0.95	1												
Fe2O3 (wt %)	0.58	0.36	0.43	1											
MnO (wt %)	-0.05	-0.16	-0.16	0.379	1										
MgO (wt %)	-0.43	-0.46	-0.47	0.132	0.41	1									
CaO (wt %)	-0.88	-0.88	-0.91	-0.46	0.07	0.23	1								
Na2O (wt %)	0.77	0.93	0.89	0.152	-0.2	-0.51	-0.8	1							
K2O (wt %)	0.97	0.83	0.9	0.639	-0.03	-0.39	-0.85	0.67	1						
P2O5 (wt %)	-0.61	-0.63	-0.63	-0.45	-0.11	-0.29	0.85	-0.53	-0.58	1					
Ba (ppm)	0.68	0.7	0.67	0.54	0.1	-0.24	-0.55	0.6	0.66	-0.4	1				
Cr (ppm)	0.72	0.61	0.66	0.329	-0.21	-0.63	-0.43	0.43	0.74	-0.1	0.55	1			
S (ppm)	0.35	0.29	0.27	0.729	0.34	0.2	-0.25	0.12	0.4	-0.3	0.39	0.21	1		
Sc (ppm)	0.91	0.74	0.83	0.586	-0.07	-0.4	-0.75	0.6	0.9	-0.5	0.58	0.75	0.332	1	
Sr (ppm)	-0.65	-0.66	-0.67	-0.44	-0.05	-0.19	0.89	-0.56	-0.63	0.98	-0.36	-0.12	-0.26	-0.54	1
Zn (ppm)	0.18	0.21	0.18	-0.07	-0.13	-0.25	-0.13	0.12	0.2	-0	0.17	0.46	-0.09	0.41	-0
Zr (ppm)	0.52	0.78	0.71	0.066	-0.24	-0.31	-0.64	0.82	0.42	-0.5	0.46	0.28	0.191	0.35	-0.5
Be (ppm)	0.87	0.65	0.76	0.664	-0.05	-0.22	-0.73	0.47	0.89	-0.5	0.52	0.67	0.465	0.83	-0.6
V (ppm)	0.3	0.31	0.31	-0.02	-0.27	-0.35	-0.15	0.18	0.25	-0	0.23	0.64	0.076	0.32	-0
Co (ppm)	0.39	0.58	0.47	0.111	-0.1	-0.25	-0.37	0.57	0.32	-0.3	0.4	0.26	0.217	0.3	-0.2
Ni (ppm)	0.06	0.08	0.05	-0.05	-0.24	0.02	0	-0.11	0.07	-0.1	-0.05	0.44	0.054	0.13	-0
Cu (ppm)	0.57	0.55	0.55	0.273	-0.12	-0.34	-0.48	0.37	0.58	-0.3	0.51	0.72	0.037	0.56	-0.3
Ga (ppm)	0.98	0.81	0.91	0.603	-0.01	-0.4	-0.86	0.69	0.96	-0.6	0.63	0.7	0.334	0.92	-0.6
Rb (ppm)	0.97	0.77	0.88	0.64	0.04	-0.35	-0.83	0.62	0.95	-0.6	0.61	0.71	0.362	0.9	-0.6
Y (ppm)	-0.17	-0.24	-0.22	-0.23	-0.18	-0.34	0.38	-0.25	-0.11	0.59	-0.01	0.39	-0.051	-0.09	0.54
Nb (ppm)	0.93	0.95	0.98	0.376	-0.17	-0.47	-0.92	0.91	0.85	-0.7	0.63	0.59	0.224	0.8	-0.7
Mo (ppm)	0.07	0.06	0.07	0.214	-0.16	0.16	-0.1	-0.04	0.09	-0.2	-0.11	0.01	0.285	0.1	-0.2
Sn (ppm)	0.75	0.81	0.76	0.332	0.17	-0.4	-0.64	0.77	0.68	-0.4	0.7	0.57	0.264	0.67	-0.4
Cs (ppm)	0.81	0.53	0.67	0.744	0.08	-0.19	-0.6	0.29	0.83	-0.4	0.55	0.71	0.442	0.8	-0.5
La (ppm)	0.05	-0.05	-0.01	-0.08	-0.16	-0.35	0.15	-0.1	0.11	0.39	0.14	0.52	0.016	0.1	0.32
Ce (ppm)	0.24	0.14	0.17	0.051	-0.11	-0.25	-0.11	0.05	0.29	0.08	0.27	0.56	0.121	0.24	0.02
Pr (ppm)	0.16	0.05	0.08	0.048	-0.13	-0.25	0.01	-0.05	0.23	0.17	0.2	0.57	0.138	0.22	0.13
Nd (ppm)	0.13	0.02	0.05	0.007	-0.14	-0.26	0.04	-0.07	0.19	0.21	0.19	0.56	0.114	0.18	0.16
Sm (ppm)	0.09	0.01	0.03	-0.04	-0.12	-0.23	0.05	-0.07	0.15	0.21	0.17	0.5	0.083	0.12	0.16
Eu (ppm)	0.06	-0.03	-0.01	-0.07	-0.13	-0.24	0.09	-0.1	0.11	0.27	0.15	0.48	0.067	0.09	0.21
Gd (ppm)	0.04	-0.06	-0.02	-0.09	-0.14	-0.24	0.1	-0.12	0.1	0.27	0.12	0.47	0.041	0.08	0.21
Tb (ppm)	0.08	-0.01	0.01	-0.05	-0.15	-0.26	0.08	-0.08	0.14	0.26	0.16	0.52	0.076	0.12	0.2
Dy (ppm)	0.07	-0.02	0.01	-0.06	-0.15	-0.29	0.1	-0.09	0.13	0.29	0.16	0.52	0.066	0.12	0.23
Ho (ppm)	0.02	-0.06	-0.03	-0.11	-0.16	-0.32	0.15	-0.11	0.08	0.36	0.13	0.49	0.026	0.07	0.3

	Al2O3 (wt %)	SiO2 (wt %)	TiO2 (wt %)	Fe2O3 (wt %)	MnO (wt %)	MgO (wt %)	CaO (wt %)	Na2O (wt %)	K2O (wt %)	P2O5 (wt %)	Ba (ppm)	Cr (ppm)	S (ppm)	Sc (ppm)	Sr (ppm)
Er (ppm)	0.03	-0.05	-0.02	-0.12	-0.19	-0.36	0.16	-0.09	0.08	0.4	0.13	0.51	0.011	0.07	0.33
Tm (ppm)	0.08	0.02	0.04	-0.1	-0.22	-0.43	0.13	-0.02	0.12	0.4	0.18	0.56	0.033	0.12	0.33
Yb (ppm)	0.14	0.1	0.12	-0.09	-0.26	-0.5	0.07	0.07	0.17	0.38	0.24	0.6	0.048	0.17	0.31
Lu (ppm)	0.21	0.19	0.22	-0.08	-0.3	-0.57	-0.01	0.18	0.23	0.33	0.27	0.63	0.049	0.23	0.25
Hf (ppm)	0.52	0.78	0.72	0.044	-0.22	-0.32	-0.66	0.84	0.42	-0.5	0.47	0.26	0.158	0.35	-0.5
Ta (ppm)	0.58	0.81	0.7	0.113	-0.2	-0.39	-0.59	0.82	0.46	-0.4	0.56	0.37	0.152	0.45	-0.4
W (ppm)	0.47	0.73	0.59	0.076	-0.21	-0.34	-0.48	0.72	0.36	-0.4	0.5	0.32	0.146	0.37	-0.3
Tl (ppm)	0.21	0.32	0.27	-0.11	-0.29	-0.22	-0.2	0.21	0.14	-0.2	0.08	0.38	-0.041	0.18	-0.2
Pb (ppm)	0.3	0.47	0.41	-0.14	0.04	-0.18	-0.32	0.59	0.17	-0.3	0.22	0.1	-0.013	0.18	-0.2
Th (ppm)	0.92	0.91	0.97	0.398	-0.18	-0.51	-0.89	0.85	0.86	-0.6	0.62	0.67	0.226	0.79	-0.6
U (ppm)	-0.37	-0.46	-0.43	-0.07	-0.21	0.01	0.55	-0.52	-0.31	0.56	-0.35	0.09	0.109	-0.23	0.55

	Zn (ppm)	Zr (ppm)	Be (ppm)	V (ppm)	Co (ppm)	Ni (ppm)	Cu (ppm)	Ga (ppm)	Rb (ppm)	Y (ppm)	Nb (ppm)	Mo (ppm)	Sn (ppm)	Cs (ppm)	La (ppm)
Zn (ppm)	1														
Zr (ppm)	0.1	1													
Be (ppm)	0.12	0.31	1												
V (ppm)	0.32	0.17	0.3	1											
Co (ppm)	0.19	0.57	0.19	0.18	1										
Ni (ppm)	0.29	0.03	0.28	0.68	-0.02	1									
Cu (ppm)	0.49	0.39	0.57	0.49	0.27	0.47	1								
Ga (ppm)	0.2	0.41	0.9	0.29	0.31	0.06	0.55	1							
Rb (ppm)	0.17	0.36	0.92	0.33	0.27	0.13	0.57	0.99	1						
Y (ppm)	0.1	-0.27	-0.02	0.37	-0.2	0.31	0.17	-0.1	-0.13	1					
Nb (ppm)	0.17	0.73	0.73	0.28	0.51	0.02	0.5	0.89	0.85	-0.26	1				
Mo (ppm)	-0.11	0.05	0.29	0.18	-0.09	0.49	-0.01	0.07	0.1	-0.17	0.05	1			
Sn (ppm)	0.32	0.52	0.45	0.33	0.53	0.02	0.5	0.68	0.64	-0.18	0.74	-0.1	1		
Cs (ppm)	0.13	0.12	0.9	0.38	0.15	0.28	0.57	0.86	0.91	-0	0.61	0.2	0.43	1	
La (ppm)	0.13	-0.17	0.19	0.41	-0.15	0.32	0.3	0.09	0.09	0.96	-0.06	-0.17	-0	0.18	1
Ce (ppm)	0.13	-0.04	0.37	0.44	-0.09	0.37	0.41	0.27	0.28	0.84	0.13	-0.12	0.1	0.33	0.95
Pr (ppm)	0.14	-0.11	0.28	0.5	-0.05	0.4	0.31	0.19	0.21	0.76	0.04	-0.14	0.12	0.3	0.82
Nd (ppm)	0.14	-0.13	0.27	0.49	-0.1	0.42	0.33	0.16	0.18	0.86	0	-0.14	0.06	0.27	0.92
Sm (ppm)	0.13	-0.12	0.25	0.44	-0.15	0.4	0.34	0.13	0.14	0.91	-0.02	-0.11	-0	0.22	0.97
Eu (ppm)	0.1	-0.15	0.21	0.44	-0.15	0.39	0.3	0.09	0.11	0.93	-0.05	-0.13	-0	0.19	0.98
Gd (ppm)	0.11	-0.16	0.21	0.43	-0.18	0.39	0.3	0.08	0.09	0.93	-0.06	-0.13	-0.1	0.18	0.97
Tb (ppm)	0.13	-0.13	0.23	0.46	-0.13	0.41	0.32	0.11	0.13	0.92	-0.03	-0.13	-0	0.21	0.97
Dy (ppm)	0.13	-0.14	0.22	0.47	-0.13	0.4	0.32	0.11	0.12	0.94	-0.04	-0.13	-0	0.21	0.98
Ho (ppm)	0.12	-0.15	0.17	0.44	-0.15	0.37	0.3	0.06	0.07	0.96	-0.07	-0.14	-0	0.15	0.99
Er (ppm)	0.13	-0.14	0.16	0.44	-0.14	0.36	0.3	0.06	0.06	0.97	-0.07	-0.15	-0	0.15	0.99
Tm (ppm)	0.14	-0.07	0.19	0.46	-0.08	0.34	0.33	0.1	0.1	0.96	-0	-0.15	0.02	0.17	0.98
Yb (ppm)	0.16	0.03	0.22	0.48	-0.02	0.32	0.35	0.15	0.14	0.93	0.09	-0.14	0.08	0.19	0.96

	Zn	Zr	Be	V	Co	Ni	Cu	Ga	Rb	Y	Nb	Mo	Sn	Cs	La
	(ppm)	(ppm)	(ppm)	(ppm)	(ppm)	(ppm)	(ppm)	(ppm)	(ppm)	(ppm)	(ppm)	(ppm)	(ppm)	(ppm)	(ppm)
Lu (ppm)	0.17	0.14	0.25	0.5	0.05	0.3	0.39	0.21	0.19	0.88	0.19	-0.15	0.15	0.2	0.92
Hf (ppm)	0.1	0.99	0.31	0.17	0.57	0	0.36	0.43	0.38	-0.27	0.75	0.02	0.54	0.11	-0.2
Ta (ppm)	0.16	0.78	0.32	0.29	0.77	0.08	0.39	0.48	0.44	-0.29	0.76	-0.01	0.68	0.24	-0.2
W (ppm)	0.19	0.73	0.23	0.28	0.82	0.1	0.38	0.36	0.33	-0.28	0.65	-0.03	0.61	0.17	-0.2
Tl (ppm)	0.31	0.27	0.18	0.8	0.21	0.62	0.48	0.18	0.21	0	0.27	0.37	0.29	0.2	0.04
Pb (ppm)	0.11	0.46	0.02	0.23	0.36	0.03	0.2	0.23	0.18	-0.25	0.4	-0.03	0.66	-0.1	-0.2
Th (ppm)	0.2	0.74	0.76	0.33	0.44	0.07	0.6	0.89	0.86	-0.13	0.97	0.02	0.68	0.66	0.07
U (ppm)	-0.07	-0.36	-0.01	0.19	-0.26	0.55	-0.04	-0.3	-0.3	0.57	-0.47	0.5	-0.5	-0	0.44

	Ce	Pr	Nd	Sm	Eu	Gd	Tb	Dy	Ho	Er	Tm	Yb	Lu	Hf	Ta
	(ppm)	(ppm)	(ppm)	(ppm)	(ppm)	(ppm)	(ppm)	(ppm)	(ppm)	(ppm)	(ppm)	(ppm)	(ppm)	(ppm)	(ppm)
Ce (ppm)	1														
Pr (ppm)	0.83	1													
Nd (ppm)	0.93	0.97	1												
Sm (ppm)	0.98	0.84	0.94	1											
Eu (ppm)	0.97	0.84	0.94	1	1										
Gd (ppm)	0.97	0.85	0.95	1	1	1									
Tb (ppm)	0.97	0.89	0.97	0.99	0.99	1	1								
Dy (ppm)	0.97	0.89	0.97	0.99	0.99	0.99	1	1							
Ho (ppm)	0.95	0.83	0.93	0.99	0.99	0.99	0.99	0.99	1						
Er (ppm)	0.94	0.83	0.92	0.97	0.98	0.98	0.98	0.99	1	1					
Tm (ppm)	0.93	0.81	0.91	0.96	0.97	0.96	0.96	0.97	0.99	0.99	1				
Yb (ppm)	0.9	0.79	0.88	0.92	0.93	0.93	0.93	0.94	0.96	0.97	0.99	1			
Lu (ppm)	0.87	0.76	0.84	0.88	0.89	0.88	0.89	0.9	0.92	0.94	0.97	0.99	1		
Hf (ppm)	-0	-0.1	-0.1	-0.12	-0.14	-0.2	-0.13	-0.1	-0.15	-0.13	-0.06	0.04	0.15	1	
Ta (ppm)	-0.1	-0.1	-0.1	-0.17	-0.19	-0.2	-0.17	-0.2	-0.19	-0.18	-0.1	-0.01	0.09	0.8	1
W (ppm)	-0.1	-0.1	-0.2	-0.2	-0.21	-0.2	-0.19	-0.2	-0.21	-0.19	-0.12	-0.04	0.05	0.74	0.98
Tl (ppm)	0.09	0.12	0.1	0.07	0.06	0.06	0.08	0.08	0.06	0.06	0.08	0.09	0.13	0.26	0.34
Pb (ppm)	-0.1	-0.1	-0.1	-0.18	-0.19	-0.2	-0.17	-0.2	-0.2	-0.19	-0.16	-0.13	-0.1	0.47	0.51
Th (ppm)	0.25	0.15	0.13	0.11	0.07	0.06	0.1	0.09	0.06	0.07	0.13	0.22	0.31	0.75	0.68
U (ppm)	0.29	0.32	0.37	0.4	0.42	0.43	0.42	0.43	0.46	0.47	0.46	0.42	0.36	-0.4	-0.4

	W	Tl	Pb	Th	U
	(ppm)	(ppm)	(ppm)	(ppm)	(ppm)
W (ppm)	1				
Tl (ppm)	0.35	1			
Pb (ppm)	0.45	0.36	1		
Th (ppm)	0.57	0.28	0.33	1	
U (ppm)	-0.31	0.06	-0.38	-0.39	1

	Total Variance Explained		
Component	Variance	% of Total Variance	Cumulative %
1	**27.600**	**32.86**	**32.86**
2	**14.320**	**17.05**	**49.90**
3	**11.040**	**13.14**	**63.05**
4	**7.509**	**8.94**	**71.99**
5	**4.257**	**5.07**	**77.06**
6	**2.656**	**3.16**	**80.22**
7	2.447	2.91	83.13
8	1.935	2.30	85.43
9	1.681	2.00	87.44
10	1.483	1.77	89.20

Table S7: Summary of the first ten principal components used for statistically defining the chemofacies.

Appendix 2

Clinoform identification and correlation in fine-grained sediments: A case study using the Triassic Montney Formation

Supplimentary Methods

A total of 641 samples were analyzed and include core samples (wells c-74-G/94-b-09, d-48-A/94-b-09, 02-30-070-24W5, 16-17-083-25W6, and 11-20-082-02W6) and outcrop samples (Ursula Creek, British Columbia; Fig. 1). The wells and outcrop were chosen to create a transect perpendicular to the Triassic paleoshorline. The sampling interval was 0.5 or 1 m, depending on the length of the well or outcrop. Sampling at this resolution will inherently miss laminar-scale as well as thin-bed variation; however, because our study is at the basin-scale, we feel that the general, basin-wide trends will be captured sufficiently at this interval of sampling. Sample size varied between 2 and 5 cm_2, but only 0.25 g is required for analysis by lithium metaborate fusion.

As sample collection and analysis took place over a significant length of time, samples were analyzed in batches at two different laboratories (Chemostrat Laboratories and Bureau Veritas Mineral Laboratories). Samples from wells c-74-G/94-b-09, d-48-A/94-b-09, 02-30-070-24W5, 16-17-083-25W6 and the Ursula Creek outcrop were analyzed using both inductively coupled plasma mass spectrometry (ICP-MS) and inductively coupled plasma optical emission spectrometry (ICP-OES) at Chemostrat laboratories in Houston, Texas, a laboratory accredited to ISO 17025:2005 (equivalent to ISO 9000). ICPMS analysis was conducted using a Thermo Scientific XSERIES 2 mass spectrometer while ICP-OES analysis was completed using a Scientific iCAP

7000 Series ICP-OES mass spectrometer. Outcrop samples were selected to exclude surface weathering and only fresh, unexposed rock was sampled.

Following procedures outlined in Hildred et al. (2010), all samples were cleaned using water and solvent to remove surface contamination. Subsequently, samples analyzed at Chemostrat laboratory were pulverized using an agate mortar and subjected to a Limetaborate digestion (Jarvis and Jarvis, 1992). Major elements analyzed for include: SiO_2, TiO_2, Al_2O_3, Fe_2O_3, MgO, MnO, CaO, Na_2O, K_2O, and P_2O_5. Data was also collected for 25 trace elements (Ba, Cr, S, Sc, Sr, Zn, Zr, Be, V, Co, Ni, Cu, Ga, Rb, Y, Nb, Mo, Sn, Cs, Ta, W, Tl, Pb, Th, and U) and 14 rare earth elements (REE: La, Ce, Pr, Nd, Sm, Eu, Gd, Tb, Ho, Dy, Er, Tm, Yb, and Hf). Major-element data and high-abundance trace elements (e.g., Cr, Sc, Sr, and Zr) were determined using ICP-OES. Precision, measured by running select samples in triplicate, is estimated to be ±2% for major elements run on ICP-OES for the major-element data, and approximately ±3% for high abundance trace elements. Low-abundance trace element data collected via ICP-MS, is estimated to have a precision of ±5%. The accuracy, measured by using an internal standard, of major element analysis is ±1%. Additionally, in order to assess external reproducibility, 11 batches of five certified reference materials were analyzed in duplicate. The associated two-sigma uncertainty is 5-7% for major elements and 7-12% for trace elements. Trace element accuracy ranges from ± 3- 7 ppm, decreasing with higher abundance.

Samples from well 11-20-082-02W6 were analyzed by Bureau Veritas Mineral Laboratories (formerly Acme labs) using $LiBO_2$ digestion followed by ICP-MS conducted

with a Perkin Elmer Elan 6000 ICP mass spectrometer (SiO_2, Al_2O_3, Fe_2O_3, MgO, CaO, Na_2O, K_2O, TiO_2, P_2O_5, MnO, Cr_2O_3, Sc, Ba, Be, Co, Cs, Ga, Hf, Nb, Rb, Sn, Sr, Ta, Th, U, W, Zr, Y, La, Ce, Pr, Nd, Sm, Eu, Gd, Tb, Dy, Ho, Er, Tm, Yb, Lu). Detection limits vary from 0.01 to 1 ppm. Error values and reproducibility for geochemical data (by element) from this lab are available within Rukhlov and Pawlowicz (2011).

Select samples (18 in total) from 02-30-070-24W5 were analyzed by a Bruker AXS D8Advance X-ray Diffractometer at SGS Mineral Services Lakefield, Ontario, a lab accredited to ISO/IEC 17025. A Co radiation source operating at 40 kV and 35 mA was used. Scans were taken stepwise at 0.02° intervals, with a step time of 0.2s, and a 2Θ range from 3-70°. Spectral interpretations were made using PDF2/PDF4 powder diffraction databases issued by the International Center for Diffraction Data (ICDD), and DiffracPlus Eva® software. The detection limit is 0.5-2% (dependent on crystallinity).

A statistical evaluation of the correlation between mineralogical and elemental data was conducted using Pearson product-moment correlation (PPMC) and eigenvector analyses (EA) on DataDesk®6.3.1. Principal component analysis was used as an indicator for mineralogy during chemostratigraphic analysis (Pearce et al., 2005; Svendsen, et al., 2007; Ellwood et al., 2008; Ratcliffe et al., 2010, 2015). Additionally, to investigate sediment provenance, abiotic carbonate input and hydrothermal influence, plots of La/Sm versus Yb/Sm, log (Fe_2O_3/K_2O) and log (SiO_2/Al_2O_3), Th/Sc versus Cr/Th, and Sr versus Mg cross-plots were created using DataDesk®6.3.1 and Microsoft Excel ®2010. Plots of Fe/S and P/Fe were also produced using this software, as well as rare earth element plots (REE plots) normalized to chondrite abundance.

Chemostratigraphic packages were defined using principle component analysis and cluster analysis on the most complete core data set (16-17-083-25W6), which was used as the type section. In total, 84 variables were considered, as summarized in Table I. The variables used fall into eight categories: the first and second categories, referred to as oxides and trace elements comprise the unaltered data provided by the lab; the third category, oxide elements, contains the calculated elemental portion of the oxides converted to ppm; the final categories, indicators, comprise ratios of elements or oxides. Select samples (18 in total) from 02-30-070-24W5 were analyzed by a Bruker AXS D8

The 84 variables have a variety of relationships and correlations to one another. To condense the data set and reduce the redundancy between variables, principal component analysis was applied (Johnson and Wichern, 1988; Schlens, 2014). This method is a multivariate transformation that reduces the dimension of the data set while retaining most of the variance of the original data. Supplimentary Table VII shows a summary of the first ten principal components, the variance in the data set explained by each component, and the cumulative percentage of the variance explained. The first six components account for over 80% of the variance; these six were retained and used for cluster analysis.

The six principal components were used with depth as a seventh variable to divide the 238 data points into clusters (Tan et al., 2006). Hierarchical clustering was used to merge the data points into clusters, with the multidimensional distance between clusters calculated by Ward's method (Ward, 1963). Supplementary Figure 30 defines the relationship between the number of clusters and the corresponding similarity

between the clusters. As more clusters are merged with one another, more dissimilar data points must be combined and there is therefore less similarity between the remaining clusters. Supplementary Figure 30 highlights an inflection point at 12 clusters, where reducing the number of clusters rapidly decreases similarity. For this reason, 12 clusters were retained in the results. Although only occurring in the basal data point (and thus statistically insignificant), a thirteenth division was added based on the published contact between the Permian Belloy Formation and the Montney Formation in this data set (Golding et al., 2014).

Chemofacies were then analyzed and summarized using clay indicator ratios (Cr/Sc, Zr/La, Zn/Sc, SiO_2/Al_2O_3, Ga/Rb, K_2O/Al_2O_3, K_2O/Rb, Na_2O/Al_2O_3, Rb/Al); provenance ratios (Ni/Al, Cr/Al, Th/Sc, Ti/Zr, MgO/Al_2O_3, and Ti/Nb); detrital input indicators (TiO_2/Al_2O_3,TiO_2/K_2O, Lu/Hf, Sc/Zr) and mineralogical indicators (P_2O_5/Al_2O_3, Cr/Nb, Lu/Zr, and Cr/Zr). Further details of each are provided in the following section. An average value of each ratio was determined from the type section. These overall average values were compared to the averaged values generated from within each chemofacies in order to make interpretations. Due to the low elemental immobility, and the relation to detrital input, subsequent data sets were correlated primarily using the signatures of Sc/Zr, Lu/Hf, and Zr/La (see the section entitled ‘Elemental Indicators’ for a more detailed explanation of the ratios used in this study).